RALT–008

FIRST MEASUREMENTS OF THE NEUTRAL CURRENT DEEP INELASTIC CROSS-SECTIONS AND THE PROTON STRUCTURE FUNCTION $F_2(x, Q^2)$ AT HERA

Tanwir Ahmed

Thesis submitted for the degree of
Doctor of Philosophy

School of Physics and Space Research
Faculty of Science
University of Birmingham

February 1994

Synopsis

The proton structure function, $F_2(x, Q^2)$, and the total cross-section, σ_t, have been measured from the first data collected in 1992 with the H1 detector. In this thesis, a detailed account describing the various theoretical predictions for $F_2(x, Q^2)$ in the kinematic regime accessible at HERA is presented. The criteria used to select candidate events for this study are based on a novel approach to the identification of the scattered electron in neutral current deep inelastic interactions. The experimental aspects of the use of this algorithm and the subsequent selection of events is discussed in detail.

In the kinematic range $Q^2 \geq 5\,\mathrm{GeV}^2$, $0.025 \leq y \leq 0.6$ and $\theta_e \leq 174^o$, the total cross-section σ_t is measured to be:

$$\sigma_t = 130 \pm 24(\text{sys.}) \pm 4(\text{sta.})\,\text{nb}.$$

In the same kinematic region, two independent $F_2(x, Q^2)$ measurements are made using the electron and mixed kinematic variables. The above σ_{tot} value and $F_2(x, Q^2)$ measurements are in agreement with theoretical predictions which assume a strong rise in the gluon density of the proton as $x \rightarrow 0$. A comparison between the observed hadronic deep inelastic final state and Monte Carlo predictions is also presented. Initial results indicate that none of the models is able to accurately reproduce the data, although the Colour Dipole Model is in reasonable agreement.

To my parents and Ulrike

Acknowledgements

I would like to thank Professors George Morrison and John Dowell for allowing me the opportunity of working in the School of Physics and Space Research. I acknowledge the financial support of the Science and Engineering Research Council during my studentship.

I am very grateful to my supervisor John Garvey for his help, advice and continued support during my studentship. I would like to extend my thanks to John Garvey and John Dowell for being very patient with me and letting me pursue my research interests.

I must express my deep gratitude to Lawrie Lowe for always answering my computing problems (no matter how trivial!) and Alan Watson for always having the time to answer my computing and physics questions. Without their help writing this thesis may have taken even longer!

During my studentship at Birmingham and DESY, I have had the pleasure of meeting a lot of staff members (post-docs included!) and students who have all made time as a student very enjoyable. Therefore, I feel it is only fair that they get a mention! Firstly, I would like to thank all the members of staff in the B'ham HEP group for presenting a pleasant working atmosphere and for always answering my trivial queries. In particular, I would like to thank Ian Kenyon for his help on the many HERA physics topics and 'one and only' Frank Votruba for his very enlightening discussions on Quantum Mechanics and 'this bloody' Pomeron! Thanks, Frank for convincing me that I didn't have to be a (senior) staff member not to understand the Pomeron! Thanks also to the technicians Dennis, Roger, Ian and Richard, and our secretaries, Frances Brown and Murial Mason, for their help over the past few years.

I am greatly indebted to my fellow H1'ers, Lee-the man mountain-West and Hywel Phillips who were the only people who could understand my constant gripes regarding physics analysis outside of DESY. Thanks, guys for listening and helping me! I am extremely grateful to Lee for reading this thesis and correcting my English!

Thanks also to Nigel Watson, Dave Rees, Mark Nikitas, Matty Couch, John Walker, Nick Thackray and Ian Fensome for their help and friendship during the early years of my Ph.D. I would also like to thank the 'scousers' Mick and Damian for keeping me sane during our summer school in Alushta! During my time at DESY, I had the pleasure of knowing Bill-the red devil-Haynes, Andy-the owl-Sirous and the 'gooners' Julian and Ash, who between them always kept me informed about the British football scene! Thanks, lads you made my stay at DESY really worth while. A big thanks to the DESY football team and the Anglo St. Pauli fan club for providing me with hours of fun, you know who you are! Thanks to Alan Goodall and Lindsay Wormersley for being good mates. Thanks also to the 'Brum boys on tour', John-cakehead-Sutton, Stuart-five bellies-Robbo and Paul-not the actor-Newman, keep up the good work lads. I would like to send a special thanks to all the people of the Uni. of Davis H1 group who I knew whilst at DESY.

Now to the people, to whom I owe a lot and who have helped me through the last year. First, I would like to thank Roland Martin, who always had time to answer my DIS physics queries, no matter how trivial. Without his help, my work may have been even harder, thanks a million Roly. I will always be grateful to Camille Kaufmann and 'liebe' Hella for their friendship and help while I was as at DESY. To all the following people at B'ham, I cannot express in words how much I have enjoyed your company so I hope you don't mind me just mentioning your names! Thanks, (in no particular order!) to Mike-007-Haben, Rich-the runner-Carney, Chris-hands of steel-Dodenhoff, Steve-not welsh enough-Clewer, Andy-the boy-Bayes, Mark-the socialist revolutionary-Whalley, Paul-the long-haired layabout-Davies, Mike-the bavarian-Natusch, and finally, our new first years, Vicky, Tim, Keith and Dave. To all you lot I wish you all the best for your futures, whatever

they may be. Thanks, also to the physics football players, in particular 'big' George Karban, Frank-the manager-Macdonald and Gron-lets play in triangles-Jones.

I would like to say a big thank you to my flatmates Ish Badr (and Judith) and Richard Barnes for being excellent friends and more than just flatmates. I will always look back at my time in The triangle, Siskin Drive and Balden Road with fond memories...thanks for making it great time, and keep up the home brewing! I hope all your future wishes come true. Similarly, I will always be grateful to Salim and Grace Sabri for being very special friends and always putting me up when I came down to London. Also, thanks must go to Phil the only Barnet F.C. fan I have ever known!

During the past two years I have been very fortunate to know Ulrike Büchler (and her paps). Out of all the people I meet at DESY, my relationship with Ulrike is very special, and a large part of this thesis would not have been possible without her love, support and encouragement. Thanks, Ulrike, the past two years have been great and I hope it will continue, you are a very special person and I am very lucky to know you. Finally, I am deeply grateful to my family for their continual love, support and encouragement. They have given up so much to give me the opportunities that I've had. Without them none of this work would have been possible. It is to my parents and Ulrike that I dedicate this thesis, because a large part of it belongs to them.

Once again, to all the people that I've mentioned thanks for everything. My last words to you are, *'Quidquid agis, prudenter agas et respice finem'*.

Tanwir Ahmed
Birmingham
February 1994

Aber Wissenschaft von der Realität geht von vornherein über die unmittelbaren Interessen des Daseins hinaus. Sie hat in der Praxis, die immer zugleich Kampf ist, in dieser Erfahrung, der Meisterung der Widerstände nur einen ihrer Ursprünge. Der Mensch will wissen was wirklich ist, unabhängig von allem praktischen Interesse. Ein tieferer Urprung der Wissenschaften ist die reine, hinebende Kontemplation, das schende Sichvertiefen, das Hören auf die Antworten aus der Welt.

– Karl Jaspers

Now the smallest Particles of Matter may cohere by the strongest Attractions, and compose bigger Particles of weaker Virtue.... There are therefore Agents in Nature able to make the Particles of Bodies stick together by very strong Attractions. And it is the Business of experimental Philosophy to find them out.

– Issac Newton

Contents

1 The Standard Model of Particle Physics **1**

1.1 Historical Prelude to the Standard Model 1

1.2 Overview of the Standard Model 2

1.2.1 The Fundamental Fermions 3

1.2.2 The Fundamental Bosons and their Interactions 4

1.2.3 Overview of Gauge Field Theories 5

1.2.4 Electro-weak theory 7

1.2.5 Perturbative Quantum Chromodymanics 10

2 The HERA Physics Programme **14**

2.1 Introduction 14

2.2 Event Kinematics 16

2.3 Deep Inelastic Scattering at HERA 17

2.3.1 Review of the Quark-Parton Model 17

2.3.2 Cross-sections and Structure Functions 19

2.3.3 QCD and DIS: Q^2 Evolution of $F_2(x, Q^2)$ 24

2.3.4 The Alterelli-Parisi Evolution Equations 27

2.3.5 The Lipatov Evolution Equation 31

2.3.6 QCD at Low x: Parton Saturation 33

2.3.7 QCD at low x: Predictions for DIS at HERA 36

2.3.8 QCD at Low x: Summary 41

2.4 Low Q^2 Physics: Photoproduction at HERA 42

2.5 Electroweak tests at HERA 46

2.6 Exotic Physics at HERA 47
2.7 Summary 50

3 HERA and the H1 Detector **51**
3.1 Introduction to HERA 51
3.2 The H1 Detector: General Overview 55
3.3 Calorimetery: Introduction 57
  3.3.1 The Liquid Argon Calorimeter 58
  3.3.2 The Backward Electromagnetic Calorimeter 61
  3.3.3 The Plug Calorimeter 64
  3.3.4 The Instrumented Iron 64
  3.3.5 The Electron and Photon taggers 66
3.4 The Time-of-Flight Device and the Veto Walls 68
3.5 Tracking: Introduction 68
  3.5.1 The Central Tracking Detector 70
  3.5.2 The Forward Tracking Detector 72
  3.5.3 The Backward Proportional Chamber 73
3.6 The Forward Muon Detector 74
3.7 Triggering and Data Acquisition 75
3.8 The H1 Software Chain 76

4 Electron Identification in NC DIS Events **79**
4.1 Introduction 79
4.2 Description of the Jet-Finding Algorithm, QJELEC 80
  4.2.1 Jet Parameters and Electron Identification 81
4.3 Monte-Carlo Tuning for Electron Identification 84
  4.3.1 MC Analysis Chain and Reconstructed Jet Profiles 84
4.4 Reconstructed Properties of the Selected Electron 89
  4.4.1 Electron Energy Reconstruction 89
  4.4.2 Energy Reconstruction in the BEMC 90
  4.4.3 Energy Reconstruction in the LAr Calorimeter 93

4.4.4 θ Reconstruction 96
4.5 Electron Identification Efficiencies 99
4.6 False e Candidates and Final e Selection Criteria 101
4.7 Concluding Remarks 104

5 Event Selection & Kinematic Reconstruction **105**
5.1 Introduction 105
5.2 Event Classification at the DST Level 106
5.3 Vertex Reconstruction 108
5.4 Reconstruction of the Event Kinematics 113
5.4.1 Reconstruction from the Scattered Electron 114
5.4.2 Reconstruction from the Hadronic Final State 117
5.4.3 Reconstruction using the Mixed Method 122
5.5 Study of Photoproduction Background 123
5.6 Event Selection Summary & Global Uncertainties 130
5.7 First Look at the Selected Data 132

6 Measurement of the Total Cross-section(s) & the Proton Structure Function $F_2(x, Q^2)$ **138**
6.1 Introduction 138
6.2 Cross-section and Structure Function Determination 139
6.2.1 Bin Centre Corrections 142
6.2.2 Comparison between Monte Carlo and Data 143
6.2.3 The Measurable Kinematic Domain and Bin Sizes 145
6.2.4 Radiative Corrections, $\delta(x, Q^2)$ 147
6.3 Measurement of the Total DIS Cross-section σ_t 154
6.4 Extraction of the $F_2(x, Q^2)$ Structure Function 163
6.5 DIS Events with Large Rapidity Gaps 173
6.6 Discussion 173
6.7 Summary 176

7 Measurements of the Hadronic Final State **180**

7.1 Introduction 180

7.2 QCD Models and Simulation 181

7.3 Results and Discussion 183

7.4 Concluding Remarks 187

8 Summary & Conclusions **188**

A $F_2(x, Q^2)$ Values **190**

List of Figures

2.1 The deep inelastic kinematical plane accessible at HERA assuming incoming energies of 30 and 820 GeV for the electron and proton beams, respectively. 15

2.2 Basic diagram for *ep* scattering without assumptions about the structure of the initial proton and final hadronic system. 16

2.3 Typical quark-parton model picture a deep inelastic scattering event. The line of 'colour flow' illustrates the hadronization process. 18

2.4 Two examples of a first order NC DIS radiative event, (a) an initial-state radiated γ and, (b) a final-state radiated γ. 20

2.5 Relative size of the cross-sections from pure γ, pure Z^o and their interference as a function of Q^2. 22

2.6 Symbolic picture of the nucleon, as probed in lepton scattering, as the wavelength $\lambda = \frac{1}{Q}$ of the virtual boson is decreased and more structure is revealed. 24

2.7 Graphical illustration of scaling violations of F_2. 26

2.8 Graphical representation of the Alterelli-Parisi equations. 29

2.9 QCD ladder diagram describing the evolution of the gluon density in the LLA($\frac{1}{x}$). 32

2.10 Diagram showing the (x, Q^2) regions of validity of the two evolution equations. The resulting parton density of the proton (in the transverse plane) is also indicated. 35

2.11 A typical fan diagram which forms the basis of the GLR equation. . . 36

2.12 Theoretical regimes describing the small x behaviour of the proton structure function $F_2(x, Q^2)$: standard QCD evolution verses two possible alternatives for the true QCD evolution. 37
2.13 The x evolution of the proton structure function $F_2(x, Q^2)$ at $Q^2 = 5$, 15, 30 and 100 GeV^2, using the D− (including screening corrections) and D0 distributions. 39
2.14 Two dedicated processes sensitive to saturation effects. The first (a) is a simple illustration of a 'hot spot' event with an identified jet. The second (b) figure shows a typical diffractive DIS event characterised by a Pomeron exchange. 40
2.15 Lowest order QCD Feynman diagrams for photon-gluon fusion (a) and QCD compton (b) processes. 43
2.16 Photoproduction diagrams via the VDM process for elastic (a) and inelastic diffractive scattering (b), nondiffractive processes (c) and hard scattering (d). 44
2.17 Three diagrams illustrating the resolved photon process. 45
2.18 Dominant diagrams in W^+ production at HERA. 46
2.19 Diagrams showing direct channel production of leptoquarks LQ (a) and leptogluons LG (b) in ep scattering. 48
2.20 Illustration of the production and decay of heavy Majorana neutrinos. 49

3.1 The general layout of the HERA accelerator and pre-accelerators. Also shown are the three intersection regions housing the H1, ZEUS and HERMES detectors. 52
3.2 A perspective view of the H1 detector. 56
3.3 A longitudinal view of the H1 detector also showing the position of the scintillator walls. 57
3.4 Radial view of a single wheel of the LAr calorimeter. 60
3.5 Transverse view of the BEMC (a), and a side view of a quadratic stack. 63
3.6 Arrangement of the streamer tubes, readout pads (P) and strips (S) in the barrel region. The point structure of the pads is also shown. . . 65

3.7 The layout of the H1 luminosity monitoring system. 66
3.8 The H1 tracking system ($r - z$ view). 69
3.9 Radial view of the H1 central tracking detector. 71

4.1 General shower properties (a) and a typical shower $r - z$ shower profile in the LAr calorimeter (b), for an electron. 83
4.2 Simple diagram illustrating the meaning of the jet variable EFN. . . 84
4.3 ΔRe distribution, wrt. the generated e, for all reconstructed jets. . . 86
4.4 Correlation between ΔRe and the number of (η,ϕ) bins, N_{bin}, for each jet. 86
4.5 Correlation between ΔRe and the electromagnetic fraction, EMF, for each jet. 87
4.6 Correlation between ΔRe and the energy fraction in the jet's initiator and neighbouring bins, EFN 87
4.7 ΔRe of jets before and after e selection 88
4.8 ΔR distribution between the MC scattered e and final state radiated γ (a) and the energy resolution $\frac{\Delta E}{E}$ of the selected e cluster (b). . . . 91
4.9 Dependence of $\frac{\Delta E}{E}$ wrt. the e scattering angle, θ_e. 92
4.10 $\frac{\Delta E}{E}$ distribution (a) and dependence of $\frac{\Delta E}{E}$ wrt. θ_e (b) for LAr clusters. 94
4.11 Simulated event in which the e scatters in the backward region of the BBE. 95
4.12 Angular resolution, $\Delta\theta$, for the BEMC clusters when θ_e is calculated from the e energy 4-vector (a) and linked tracking data (b). 97
4.13 Angular resolution, $\Delta\theta$, for the LAr e clusters when θ_e is calculated from the e energy 4-vector (a) and linked CJC track (b). 98
4.14 Acceptance of the refined QJELEC algorithm as a function of $\log_{10} Q^2$ (a) and $\log_{10} x$ (b). 103

5.1 Typical background event due to an upstream proton interaction. The proton triggers the BEMC and subsequently passes the L1 and L4-L5 data selection levels. 109

5.2 Vertex reconstruction efficiencies (ϵ_{vtx}) as a function of E'_e for the three given angular regions. The solid line indicate the MC values and the solid points correspond to the data. 111

5.3 Correlation between the reconstructed and generated variables y_e ((a)-(b)), and Q^2_e ((c)-(d)). 116

5.4 Correlation between the reconstructed and generated Jacquet-Blondel variables y_{JB} and Q^2_{JB}, for all events ((a) and (c)) and events with a reconstructed vertex ((b) and (d)). 120

5.5 Correlation between reconstructed and generated x^{mix}. Only the events satisfying the vertex criteria are plotted. 123

5.6 Correlation between kinematic variables y_{JB} and y_e for MC γp (a)-(b) and DIS (c) events. The dashed lines mark the region where event are rejected by the y cut; $y_{JB} < \frac{1}{2} y_e$ for $y_e \geq 0.6$. 128

5.7 $x - Q^2$ distribution of the 1809 DIS event distributions. Also shown on the figure are the lines of constant E'_e and θ_e. 134

5.8 A deep inelastic scattering event at $Q^2 = 1935\,\mathrm{GeV}^2$ and $x = 0.046$, as seen in the H1 detector. 135

5.9 This figure shows the deep inelastic scattering event that was reconstructed with the lowest x value. 135

5.10 Distribution of the ratio $\frac{y_e}{y_{JB}}$. The solid histogram corresponds to the Monte Carlo prediction. 136

5.11 Reconstructed z_{vtx} distribution for MC and data. 137

6.1 Distributions of the scattered electron's energy E'_e and (b) polar angle θ_e for Monte Carlo and data. 144

6.2 Predicted γp background rates in the selected data sample in bins of y_e (a) and $\log_{10} x$ (b). 146

6.3 One-loop (a) and single-photon bremsstrahlung (b) diagrams showing the $\mathcal{O}(\alpha)$ corrections to the NC DIS cross-section. 148

6.4 Photon energy E_γ spectrum for DIS events with colinear initial-state bremsstrahlung, as detected by the photon tagging calorimeter. . . . 149

6.5 Kinematic dependence of the leptonic and mixed radiative corrections using the TERAD91 (TE) and HELIOS (HL) programs for $Q^2 = 7.5$ (a), 15 (b), 30 (c) and 60 GeV^2 (d). 151

6.6 F_2 measurement uncertainty due to the difference between the TERAD91 and HELIOS radiative corrections at four Q^2 values. 152

6.7 Differential cross-sections $\frac{d\sigma_t}{dQ^2}$ (a) and $\frac{d\sigma_t}{d\log_{10}(x)}$ (b) in the kinematic region $Q_e^2 \geq 5\,\text{GeV}^2$, $\theta_e \leq 174^o$ and $0.025 \leq y_e \leq 0.6$. 164

6.8 $F_2(x,Q^2)$ measurements, from analysis I and II, for six values of Q^2. . 170

6.9 A typical 'rapidity gap' event candidate as seen in the H1 detector. . 174

6.10 (a) Q^2 and (b) $\log_{10}(x)$ distributions for the 65 'rapidity gap' event candidates. 175

6.11 The $F_2(x,Q^2)$ measurements for six values of Q^2, compared to several parameterizations which are fitted to recent low energy data from the muon proton scattering experiments. 177

6.12 The $F_2(x,Q^2)$ measurements as a function of Q^2 for fixed values of x, compared to several recent structure function parameterizations. . . . 178

7.1 Transverse energy flow ($E_\perp$) as a function of the pseudo-rapidity (η) for the data. Also shown are the fully reconstructed QCD model predictions. 185

7.2 Transverse energy flow ($E_\perp$) as a function of the azimuthal angle (ϕ) defined wrt. the scattered electron, for data and QCD model predictions. 185

7.3 Energy flow (E^*) in the hadronic center-of-mass frame as a function of θ^*, for data and the model predictions. 186

7.4 Seagull plot showing the mean $p_\perp^2$ in the hadronic centre-of-frame ($< p_\perp^{*2} >$) as a function of Feynman-x (x_F), for data and model predictions. 186

List of Tables

4.1 Table showing e selection cuts. 88

4.2 Scattered e identification probabilities in the BEMC and LAr calorimeter. 100

5.1 Table summarizing the expected rate of e candidates from DIS and γp events. 125

5.2 Expected number of DIS and γp events remaining after each rejection criteria have been applied 129

6.1 The total cross-sections, determined from the Autumn 1992 data (σ_t) and the HERACLES event generator, in the kinematic region $Q_e^2 \geq 5\,\mathrm{GeV}^2$, $\theta_e \leq 174^o$ and $0.025 \leq y_e \leq 0.6$. 161

6.2 Measured cross-sections in bins of Q^2. 162

6.3 Measured cross-sections in bins of $\log_{10}(x)$. 163

6.4 The proton structure function $F_2(x,Q^2)$, as measured from the first HERA data, for $Q^2 \leq 30\,\mathrm{GeV}^2$. 171

6.5 Similar to previous table, except that the $F_2(x,Q^2)$ measurements are made at $Q^2 \geq 60\,\mathrm{GeV}^2$. 172

Chapter 1

The Standard Model of Particle Physics

1.1 Historical Prelude to the Standard Model

Elementary particle physics is concerned with providing a description of the building blocks and forces of nature at the most fundamental level. The origin of particle physics can be traced back to the early 19^{th} century with the famous Maxwell's equations of electricity and magnetism, in which the two fundamental forces of nature, at that time, were unified within an elegant mathematical framework. During the late 19^{th} and early 20^{th} centuries, the foundations for the theoretical description of the elementary world was laid down by the beautiful formulation of quantum mechanics and Einstein's theory of relativity. In parallel with these theoretical developments, the basic constituents of matter were being investigated by the pioneering experiments of Thompson, Rutherford, and Chadwick. By the late 1930's the original unit of matter, the atom, had been successively broken down. The atomic nucleus was found to be a composite object made up of two particles of similar mass, the positively charged proton, and the electrically neutral neutron. It is at this point that the concept of elementary particle physics, as a physical science, began.

During the last fifty years, technological and theoretical advancements in particle physics have successfully pushed the fundamental level of nature further and further back. Out of the vast, and confusing, profusion of particles and their interactions observed from experimental data, an elegant theory known as the 'Standard Model' has emerged. Over the last two decades, the Standard Model has been subject to stringent, high precision tests by many experimental groups at various laboratories around the world. In particular, it has recently survived intensive tests at the large Large-Electron-Positron Collider (LEP) at the CERN laboratory. To date no experimental phenomenon has been observed which is inconsistent with this theory.

In the spring of 1992 the worlds first electron-proton collider HERA (Hadronen-Elecktronen-Ring-Anlage), situated at the DESY (Deutsches Electronen-Synchrotron) laboratory in Hamburg, started producing collisions for physics studies. This has opened a new era of high precision tests of the Standard Model and so it is appropriate that before the HERA physics programme is discussed the Standard Model is briefly previewed[1].

1.2 Overview of the Standard Model

The Standard Model [4] is based on the principle that the fundamental forces of nature can be described by quantum field theories which possess gauge symmetry and are constructed in such a way as to be renormalizable, *i.e.* they remain finite and give physical predictions. At present, the fundamental building blocks of matter are thought to be structureless (pointlike) spin $\frac{1}{2}$ fermions[2]. Interactions between these fundamental fermions are mediated by spin 1 particles called (gauge) bosons.

The current elementary forces of nature are thought to be the strong, weak, electromagnetic and gravitational forces. The Standard Model successfully describes the effects of the first three forces in terms of two gauge field theories down to a scale of $\mathcal{O}(10^{-17}\,\mathrm{m})$. The first gauge theory describes both the electromagnetic and

---

[1] The intention here is not to describe the Standard Model in detail, as it is the subject of very many published articles and textbooks; for example, see [1, 2, 3].

[2] The spin value is quoted in 'natural units', and this convention will be used in this thesis. In this convention, the speed of light c is dimensionless and equal to unity, and also the fundamental constants $\hbar$ and ϵ_o are set to unity.

weak interactions in a unified gauge group, known as the electroweak interaction of Glashow-Weinberg-Salam [4], and the second describes the strong force.

The gravitational force is not included in the theory due to problems arising in its formulation as a quantum field theory. At the energies available with present particle accelerators, the strength of the gravitational interaction between the fundamental fermions is so small compared with the other forces that its inclusion in Standard Model can be safely neglected.

1.2.1 The Fundamental Fermions

The fundamental fermions can be organized into two groups, the leptons and the quarks, the difference being that the leptons do not interact via the strong force. Neglecting the fermion anti-particles (particles with the same mass but opposite charge) a total of twelve fermions have been observed or implied by experimental results and theory. There are six flavours of leptons, three massive charged leptons (e^-, μ^-, τ^-), and their associated electrically neutral neutrinos (ν_e, ν_μ, ν_τ) which are assumed to be massless. There are six flavours of quarks, three of which have a fractional charge of $+\frac{2}{3}$ (u, c, t) with the remaining three having a fractional charge of $-\frac{1}{3}$ (d, s, b). There is a symmetry between the different quarks and leptons which is evident when they are grouped together to form 'generations'. Each fermion, in successive generations, has greater mass than their partner of the previous generation. The grouping of these generations are:

$$(e, \nu_e; u,\ d) \quad (\mu,\ \nu_\mu; c,\ s) \quad (\tau, \nu_\tau; t, b) \tag{1.1}$$

The top quark (t) is included here to complete the symmetry between the generations, although it has not yet been experimentally observed. It is assumed that the top quark exists but its mass is outside the energy region explored by the current accelerators. The lightest fermions[3], (e,u,d), make up the stable matter in nature. The

---

[3] Excluding the massless neutrinos.

more massive particles in the other generations are unstable and eventually decay to the lightest fermions, via the weak interactions. In nature the matter particles termed 'hadrons' are composite states of quarks (q) and anti-quarks ($\bar{q}$). Hadrons can either consist of three quarks known as baryons or consist of q$\bar{q}$ pairs known as mesons (see Section 1.2.5).

The first important results to come from LEP was to limit the number of neutrinos generations to three [5], *i.e.* those already shown above. Although, the Standard Model does not restrict the number of generations, the LEP results imply that if each generation has a neutrino, then there can only be three generations.

1.2.2 The Fundamental Bosons and their Interactions

The force or interaction between two fermions can be described by the exchange of gauge particles (see Section 1.2.3) known as bosons. In Gauge Field Theories (GFT) interactions between fermions are interpreted as the exchanged of virtual bosons which carry momentum and particular quantum numbers. Therefore, not only it is possible to describe interactions, such as scattering, when only the momentum of the particles are changed, but also interactions where the particles decay. At the heart of these interactions is the fact that the coupling of the gauge bosons to the fermions have a universal strength through out the three generations; this is how the symmetry of the fermions first became apparent. This universality is a fundamental property of the GFT used to describe the forces.

The electromagnetic interaction is mediated by the massless photon (γ), the weak interaction is mediated by three massive gauge bosons, W^+, W^- and Z^o, and the strong interaction is mediated by an octet of massless, and chargeless, gluons (g). These interaction will be described in the forthcoming sections. The fact that the $W^\pm$ and Z^o gauge bosons are massive ($M_W \sim$ 80 GeV/c and $M_Z \sim$ 90 GeV/c) can be inferred from the relatively short range of the weak force, typically 10^{-17} m. In contrast, the electromagnetic interaction has an infinite range (due to the γ having zero mass). The exchange of a W has the effect of changing a fermion into its partner of a doublet (of the same generation) *e.g.* $e \rightarrow \nu_e$ or $c \rightarrow s$. These interactions are generally referred to as 'charged current' interactions because the charge is different for the initial and final state fermion. When a Z^o is exchanged there is no change in the charge or fermion and so it is referred to as a 'neutral current' interaction.

1.2.3 Overview of Gauge Field Theories

In the Standard Model, the fundamental interactions (described above) are described by elegant theories known as Gauge Field Theories (GFT). The first such theory was Quantum Electrodynamics (QED) which describes the electromagnetic interaction. Since its formulation over two decades ago, it has been tested to very high precision and is currently the most accurate theory known. The success of QED has lead to the application of Gauge Theories to describe all the elementary forces.

In Quantum Field Theories (QFT), the fundamental fermions are represented by complex fields, which are then used to construct the Langrangian (an expression describing the energy-momentum dynamics of the system). At the heart of these theories is the fact that the (fermionic) fields have a quantum mechanical phase which is physically unobservable.

At this stage, a basic postulate of GFT is introduced, namely the principle of 'local gauge invariance'. It is postulated that the Lagrangian is invariant under a arbitrary change in the phase of the fermionic field, at any point in space and time, *i.e.* the physics must remain invariant or symmetrical. This phase transformations is called a 'local' transformation as opposed to a 'global' transformation which is a constant shift at all space-time point; under a 'global' transformation the Langrangian would naturally remain unchanged. For historical reasons, such transformations are called 'gauge' transformations.

Applying such arbitrary transformations to the original QFT Lagrangian has the effect of introducing extra terms, *i.e.* it is not invariant. However, the invariance of the Langrangian can be restored by adding new fields to the Lagrangian, which behave in a different way to the original fermionic fields under the gauge transformations. The addition of these gauge fields into the original Lagrangian introduces new interaction terms which predict the dynamics of the fundamental interactions; the particles described by these new gauge fields are the gauge bosons (described in Section 1.2.2). It is this formulation for an interaction that is generally referred to as a Gauge Theory.

It is remarkable that the interactions in the SM can be described by Gauge Theories. There is *a priori* no reason why this should be so, but the way in which all the forces fall out from a demand of invariance, or symmetry, at the fundamental level suggests some underlying simplicity in nature. The many different aspects of the elementary interactions are derived from demanding gauge invariance under operations of various symmetry groups. The properties of the gauge fields that are introduced depend on the way in which the fermionic fields transform. The precise symmetry transformations which describe a particular gauge group depend on the type of interaction concerned.

One very striking feature of the SM Gauge Theories is that they are all *'renormalizable'* [6], *i.e.* the interaction cross-sections are well behaved. Once an interaction has been formulated in terms of a QFT, perturbation theory is used to obtain 'physical' predictions. Unfortunately, this simple technique leads to a large number of intermediate states which give divergent terms (infinities or singularities) in the calculations. In order to make a physical prediction all possible intermediate states must be accounted for, and so these divergent terms must be somehow be cancelled out of all the physical observables.

By imposing an arbitrary cut-off in the calculations these intermediate states cause the solution of these terms to converge, thus yielding a finite results. In QED the divergent terms are absorbed into a redefinition of the 'bare' lepton charges and masses, which are in any case arbitrary, so that the new definition (cut-off) is equal to the physically measured values. This is renormalization; a theory is renormalizable if the singularities can be removed by introducing by introducing a finite number of experimentally observable parameters. In QED these parameters are the well known constants h, e and m_e (electron mass). A proper treatment of renormalization is beyond the scope of this thesis. Detailed discussions can be found in [1, 3].

1.2.4 Electro-weak theory

In the late 1960's the biggest advance towards the unification of all forces came with the with the unification of the electromagnetic and weak interactions into one gauge theory. The Glashow-Weinberg-Salam (GWS) electroweak theory manages to combine two very different interactions under one framework and also make completely new predictions which have been confirmed by experiments. The GWS theory requires that the appropriate Langrangian be invariant under the transformations of the non-abelian (see below) product group $SU(2)_L \times U(1)_Y$, where $SU(2)_L$ and $U(1)_Y$ are the gauge groups of weak isospin and the weak hypercharge (Y) respectively.

Experimentally, the weak charged current interaction was found to couple to left-handed fermions only. In order to construct a weak gauge theory this parity-violating nature is accounted for by treating the left and right-handed fermions differently. The left-handed fermions are grouped into weak isospin doublets, and the right-handed fermions are left as weak isospin singlets. The weak gauge theory is then constructed by requiring that the left-handed fermion doublets are allowed to transform according to the gauge group of weak isospin $SU(2)_L$. The left-handed fermion doublets and right-handed singlets for the three generations of leptons[4]:

$$\begin{pmatrix} \nu_e \\ e \end{pmatrix}_L , \begin{pmatrix} \nu_\mu \\ \mu \end{pmatrix}_L , \begin{pmatrix} \nu_\tau \\ \tau \end{pmatrix}_L , e_R \, , \mu_R \, , \tau_R$$

Similarly, for the quarks:

$$\begin{pmatrix} u \\ d' \end{pmatrix}_L , \begin{pmatrix} c \\ s' \end{pmatrix}_L , \begin{pmatrix} t \\ b' \end{pmatrix}_L , u_R \, , c_R \, , t_R \, , d_R \, , s_R \, , b_R$$

---

[4] In the GWS theory, it is assumed that left and right-handed helicity states exist for all fermions, except the massless neutrinos which only exist in left-handed states (or right-handed states for anti-neutrinos).

where d', s' and b' are orthogonal combinations of the physical eigenstates of the d, s and b quarks, respectively. This quark mixing is described by the unitary Cabibbo-Kobayashi-Maskawa matrix, $\mathbf{V}$, which is defined as:

$$\begin{pmatrix} d' \\ s' \\ b' \end{pmatrix} = \mathbf{V} \cdot \begin{pmatrix} d \\ s \\ b \end{pmatrix} = \begin{pmatrix} V_{ud} & V_{us} & V_{ub} \\ V_{cd} & V_{cs} & V_{cb} \\ V_{td} & V_{ts} & V_{tb} \end{pmatrix} \cdot \begin{pmatrix} d \\ s \\ b \end{pmatrix}$$

By convention the u, c and t quarks are unmixed, and the matrix is expressed in terms of three angles and one complex phase. The current limits on the magnitude of the matrix elements are [7]:

$$\begin{pmatrix} 0.9747 \text{ to } 0.9759 & 0.218 \text{ to } 0.224 & 0.002 \text{ to } 0.007 \\ 0.218 \text{ to } 0.224 & 0.9735 \text{ to } 0.9751 & 0.032 \text{ to } 0.054 \\ 0.003 \text{ to } 0.018 & 0.030 \text{ to } 0.054 & 0.9985 \text{ to } 0.9995 \end{pmatrix}$$

In the weak gauge group local gauge invariance means that the weak interaction is invariant under $SU(2)$ 'rotations' between the two states of a doublet,*e.g.* an electron rotates to a electron-neutrino and *vice versa.* Maintaining invariance under $SU(2)_L$ transformations results in the introduction of three gauge fields W^i_μ; two charged fields, W^1_μ and W^2_μ, and one neutral field W^3_μ. The two charged members of this weak isotriplet can be arranged in suitable linear combinations, which reproduce the charged current properties. The linear combinations which describe the two charged weak bosons $W^\pm$ are:

$$W^\pm_\mu = \frac{1}{\sqrt{2}}(W^1_\mu \mp iW^2_\mu)$$

Since the W^i_μ are carriers of weak isospin, the requirement that the weak theory be locally gauge invariant leads to extra terms which correspond to the W^i_μ being able to interact with each other. It is this property, known as self-interaction, which makes the weak theory non-abelian[5].

The weak neutral current interaction is known to couple to both left and right-handed helicity states so the neutral field of the $SU(2)_L$ gauge transformation (W^3_μ)

---

[5] This is not the case in QED, since the γ does not carry charge and so cannot interact with itself.

cannot be used alone to describe the neutral currents. In additional the neutral field of QED is also observed to couple to both helicity states. Therefore, in order to describe the neutral currents of the weak and electromagnetic interactions a $U(1)$ gauge transformation is introduced and invariance under the combined $SU(2)_L \times U(1)_Y$ gauge transformation is required. The $U(1)_Y$ transformation gives a neutral field B_μ that couples to *weak hypercharge* (the conserved quantum number associated with the field) defined by:

$$Q = T_3 + \frac{Y}{2}$$

where Q is the electric charge, T_3 is the third component of weak isospin ($\frac{1}{2}$ for ν_e and -$\frac{1}{2}$ for e_L^-) and Y is the weak hypercharge.

The physical fields Z_μ and A_μ, which correspond to the Z^o and γ boson respectively, are now defined as two orthogonal linear combinations of the W_μ^3 and B_μ fields:

$$\begin{aligned} Z_\mu &= W_\mu^3 \cos\theta_W \; - \; B_\mu \sin\theta_W \\ A_\mu &= W_\mu^3 \sin\theta_W \; + \; B_\mu \cos\theta_W \end{aligned}$$

where θ_W is the weak mixing angle. This mixing angle then governs the relative strength of the weak and electromagnetic forces by the relation:

$$g \sin\theta_W \; = \; e \; = \; g' \cos\theta_W$$

where the coupling constant g measures the strength by which the weak isotriplet vector fields W_μ^i couple to weak isospin. Similarly, the strength of the B_μ and weak hypercharge coupling is given by g'.

A consequence of the above $SU(2)_L \times U(1)_Y$ gauge invariance is that the $W^\pm$, Z^o and γ gauge bosons are assumed to be massless, whereas the observed short range of the weak interaction indicate that the weak bosons are of $\mathcal{O}(100$ GeV$)$. If mass terms are added into the basic $SU(2)_L \times U(1)_Y$ Lagrangian its invariance is lost and the theory would no longer be renormalizable[6]. This mass problem was solved (by Weinberg and Salam) by introducing of an isoscaler field, Φ, consisting of four *Higgs* fields, which allows the possibility of having a 'spontaneously broken symmetry'. Therefore, by adding the Higgs fields, the Langrangian still remains invariant under local $SU(2)_L \times U(1)$ transformations, but in the vacuum state (ground state) the gauge invariance is broken allowing the particles to have mass [8]. The fact that the Langrangian still remains invariant makes the theory renormalizable. These Higgs field all carry non-zero weak isospin and hypercharge quantum numbers, and three of these fields then couple to the $W^{\pm}$ and Z^o generating the required mass. This is referred to as the *Higgs mechanism* [8, 1, 3].

Thus, the Higgs model provides a mechanism by which the weak bosons can acquire mass, although there is no prediction of what these masses should be. The only mass relation given by the standard model is that between the weak bosons:

$$M_W = M_Z \cos\theta_W$$

This relation has been experimentally tested and found to be satisfied. One remnant from this mechanism is that it introduces an extra neutral boson (fourth Higgs field) into the theory. There is no mass prediction for this boson in the SM but the fermion mass is governed by the strength by which the Higgs boson couples to the fermions.

During the last four years, the SM has been subject to very precise tests at the LEP collider. Results from the LEP experiments, all show significant agreement with SM predictions, however, the Higgs boson and top quark are still to be experimentally observed; the mass of the Higgs boson is has a lower limit of 65 GeV/c. A more detailed review of the LEP electroweak measurements can be found in [9].

1.2.5 Perturbative Quantum Chromodymanics

Quantum Chromodynamics (QCD) is the gauge theory describing the strong interaction which is responsible for binding quarks into hadrons. QCD is a non-Abelian

---

[6] For a theory to be renormalizable, it must have local gauge invariance [6].

theory based on the symmetry group $SU(3)$ of colour. At the heart of theory lies the fact that all quarks posses an additional degree of freedom known as colour. This colour is a 'charge-like' quantum number, and each quark may exist in the one of the following coloured states: Red (R), Green (G) and Blue (B). Quarks have never been observed in isolation, *i.e.* in single coloured states, they are always confined within hadrons. To explain this observation, it is postulated that only particles which are colour singlets, *i.e. 'colourless' or 'white'*, can be observed directly. This is a special property of QCD and it is termed colour confinement.

The gauge bosons of QCD are massless particles called gluons. The requirement that the gauge theory be invariant under transformations by the SU(3) group lead to an octet of bi-coloured gluons in QCD; *i.e.* the gluons carry colour-anticolour quantum numbers. The fact that the gluons carry colour implies that they may interact with each other illustrating the non-Abelian nature of the theory. These eight gluons can be expressed as the following colour-anticolour states[7]:

$$R\bar{B},\ R\bar{G},\ B\bar{G},\ B\bar{R},\ G\bar{R},\ G\bar{B},\ \frac{R\bar{R}-B\bar{B}}{\sqrt{2}},\ \frac{R\bar{R}+B\bar{B}-2G\bar{G}}{\sqrt{6}}.$$

The strength of the strong interaction is characterized by the strong coupling constant α_s. One feature of non-Abelian gauge theories is that the gluon-gluon interactions lead to an increase in the effective colour charge, experienced by an interacting quark, as the momentum transfer Q^2 (see Chapter 2) of the process is lowered. This means that for large momentum transfers, the quarks behave as they are only weakly interacting whereas at lower Q^2 the converse it true. Since, the inter-quark distance is proportional to $\frac{1}{Q^2}$ the above statement implies that at small inter-quark separations (large Q^2) the strong force is small, whereas at larger separations the strong forces is large, which is exactly the kind of behaviour that is required to explain colour confinement.

This decrease in α_s as $Q^2 \to \infty$ is known as *asymptotic freedom* and it is a very important property of QCD; it also lies at the heart of deep inelastic lepton-hadron

---

[7] In actual fact there exists a ninth state which is a colour singlet state and has no colour changing properties.

scattering experiments, and will be discussed in Chapter 2. This behaviour leads to the important concept of a running coupling constant, *i.e.* α_s varies with Q^2. Although this concept came into prominence only with the advent of QCD, it is equally valid in other field theories such as QED.

In the leading logarithmic approximation the running coupling constant of QCD is expressed as:

$$\alpha_s(Q^2) = \frac{12\pi}{(33 - 2n_f)\ln(Q^2/\Lambda^2_{QCD})} \tag{1.2}$$

where, n_f is the number of quark flavours. The constant Λ_{QCD} characterises the point at which α_s becomes sufficiently large that perturbative QCD breaks down. This constant represents the boundary between the world of free quarks (and gluons) and the physical world of hadrons, *i.e.* it is scale at which colour confinement begins to set in.

It can be seen from the above equation, that asymptotic freedom can only occur provided $n_f \leq 16$. The value of Λ_{QCD} is not predicted by QCD; it is a free parameter to be determined from experiment. Perturbative QCD cannot predict the value of α_s, it can only predict the running of α_s. From experiment, Λ_{QCD} is found to line in the range 0.2-0.4 GeV, thus QCD perturbation theory breaks down for a Q^2 of less than a few GeV^2. This means that the hadronization of quarks and gluons occurs at too low a Q^2 to be treated perturbatively. As a result phenomenological models are needed to describe the fragmentation and hadronization of the quark and gluon into multi-hadron final states.

In the case of QED, if an electron is probed by another charged particle, the electron can continually emit virtual photons which form e^+e^- pairs (vacuum polarization). These e^+e^- pairs act to screen the original electron charge and thus, reduce the effective charge experienced by the interacting particle. As the Q^2 of the interaction is increased, the dielectric cloud of the original electron is penetrated and the interacting particle 'sees' more of the electron's 'bare' or original charge. Thus, as Q^2 increases, the QED coupling constant $\alpha(Q^2)$ also increases. In the leading logarithmic approximation $\alpha(Q^2)$ is expressed as:

$$\alpha(Q^2) = \frac{\alpha(\mu^2)}{1 - \frac{\alpha(\mu^2)}{3\pi}\ln(Q^2/\mu^2)} \tag{1.3}$$

where, μ^2 is a reference Q^2 at which α has been measured[8]

For all experimentally attainable Q^2, this variation in α is very small; at the scale of the masses of the $W^\pm$ and Z^o bosons ($Q^2 \sim 90\,\mathrm{GeV}^2$) its values is only 6% greater than that at low Q^2. This behaviour is opposite to that of α_s.

It is important to remark that the phenomena of screening is typical of renormalizable gauge theories, and that the different behaviours of $\alpha_s(Q^2)$ and $\alpha(Q^2)$ cover the two possible types of theory. Since $\alpha(Q^2) \ll \alpha_s(Q^2)$, higher order terms in perturbative expansions are much more significant in QCD than in QED.

The major physics processes that will be studied at HERA will be dominated by QCD processes. For this reason, perturbative QCD will be discussed further in the next chapter.

---

[8] When $Q^2 = \mu^2$, $\alpha = \frac{e^2}{4\pi}$ (in natural units). This is termed the fine-structure constant; numerically $\alpha \sim \frac{1}{137}$.

Chapter 2

The HERA Physics Programme

2.1 Introduction

Deep inelastic lepton-nucleon scattering has been one of the key testing grounds in the development of the Standard Model (SM), particularly in the understanding of the sub-nuclear world and the short distance properties of QCD. As a result the nucleons can now be well described by constituent quarks bound by exchange gluons. In the electroweak sector fixed target lepton-nucleon scattering has provided one of the major quantative tests of the SM through measurements of the weak neutral currents (NC) and charged currents (CC). The kinematic area that has been explored to date in fixed target lepton-nucleon scattering is Q^2 in the region up to a few hundred GeV^2 and x above 0.05 (see Section 2.2), where x is defined as the fraction of the incoming proton four-momentum carried by the struck quark.

The HERA collider is designed to collide electrons or positrons (e) with protons (p). With the planned beam energies of E_e between 15 and 30 GeV (electron beam) and E_p between 300 and 820 GeV (proton beam), centre-of-mass (cms) energies ranging between $\sqrt{s}$ = 134 GeV and $\sqrt{s}$ = 314 GeV will be available. For the data analysed in this thesis, HERA operated with beam energies of E_e = 26.7 GeV and E_p = 820 GeV, corresponding to a cms energy of $\sqrt{s}$ = 296 GeV. The maximum possible momentum transfer is $Q^2_{max} = s \simeq 10^5$ GeV^2, although the range will be restricted by event statistics to $Q^2 \sim 10^4$. As a result of the large cms energies available at HERA, deep inelastic events down to x values of 10^{-5} will be possible. In practice, as a result of detector acceptance and beam-pipe losses, x values down to 10^{-4} will be directly measurable. Thus, HERA will extend the previously accessible kinematic regions by two orders of magnitude, as illustrated in Figure 2.1.

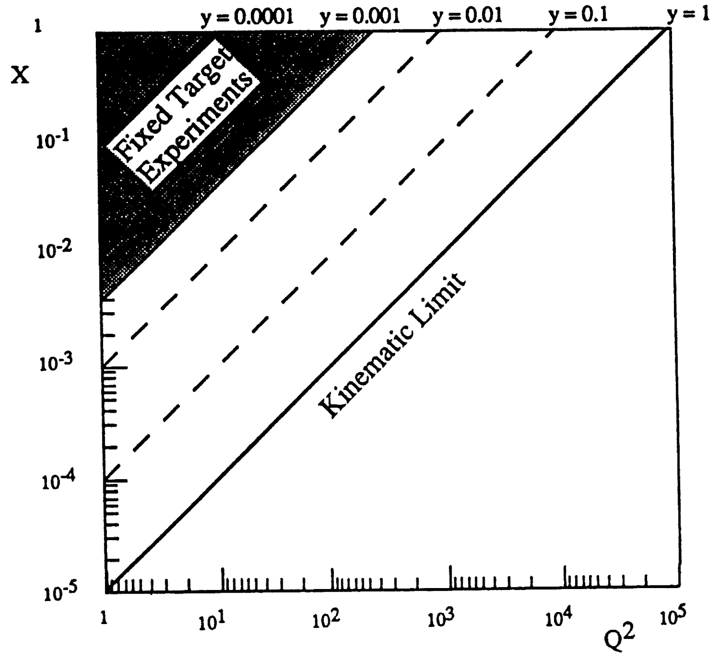

Figure 2.1: The deep inelastic kinematical plane accessible at HERA assuming incoming energies of 30 and 820 GeV for the electron and proton beams, respectively. Also shown is the kinematic plane (shaded area) covered by fixed target experiments before the advent of HERA.

The main part of this chapter will be concerned with deep inelastic physics (DIS) that will be studied at HERA, since it is the main topic of this thesis. This discussion will be mainly be concentrated on the DIS physics that is predicted in the new low x region. The various theoretical scenarios describing this low x physics are presented.

In the latter part of this chapter, the low Q^2 physics programme (photoproduction) are briefly discussed, together will possible 'exotic' physics processes that may be detectable at HERA. However, before the HERA physics programme can be presented, it is important to understand the meaning of the ep event kinematic variables.

2.2 Event Kinematics

The basic inelastic scattering process $e + p \rightarrow l + X$, where l is the scattered lepton and X is the final hadronic system, is depicted in Figure 2.2. The kinematics of this process can be determined from measurements of the scattered lepton or the final hadronic system. To determine the basic interaction kinematics let p_l, $p_{l'}$ be the four-vectors of the incoming and scattered lepton, respectively, and p_p, p_X that of the incoming (proton) and outgoing hadronic system, respectively.

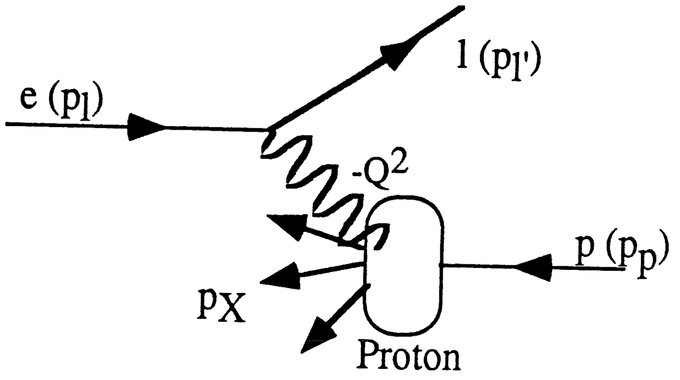

Figure 2.2: Basic diagram for *ep* scattering without assumptions about the structure of the initial proton and final hadronic system.

Using the above four-vector definitions, the kinematical variables determined at the leptonic vertex are expressed as:

$$Q^2 = -(p_l - p_{l'})^2 \quad x = \frac{Q^2}{2p_p \cdot (p_l - p_{l'})} \quad y = \frac{p_p \cdot (p_l - p_{l'})}{p_p \cdot p_l} \tag{2.1}$$

Similarly, the kinematic variables at the hadronic vertex are described by:

$$Q^2 = -(p_X - p_p)^2 \quad x = \frac{Q^2}{2p_p \cdot (p_X - p_p)} \quad y = \frac{p_p \cdot (p_X - p_p)}{p_p \cdot p_l} \tag{2.2}$$

Here, Q^2 is the momentum transfer variable and x and y are the dimensionless scaling variables; their kinematically allowed regions are $0 \leq x, y \leq 1$. From the above definitions it can be shown that:

$$Q^2 \simeq sxy \tag{2.3}$$

where s is defined as the total centre-of-mass energy squared; $s = (p_p + p_l)^2 \simeq 4E_pE_e$. The '$\simeq$' sign indicates that the masses of the electron, proton and scattered lepton are neglected; an excellent approximation at HERA energies.

For hadronization processes, and also for QCD effects, an important variable is the invariant mass, W, of the final hadronic system which is defined as:

$$W^2 = (q + p_p)^2 = Q^2\frac{1 - x}{x} + m_p^2 \tag{2.4}$$

where, m_p^2 is the mass of the proton and is non-negligible for low W^2 processes.

2.3 Deep Inelastic Scattering at HERA

2.3.1 Review of the Quark-Parton Model

In the quark-parton model (QPM) of deep inelastic scattering, the complicated process of inelastic scattering of hadrons is viewed as a two stage process. The first stage consists of quasi-elastic scattering of the lepton by one of the proton constituents, called partons (quarks), carrying a fraction x (defined above) of the nucleon four-momentum. The corresponding DIS cross-sections are then governed by the nucleon 'structure functions' $F_1(x, Q^2)$, $F_2(x, Q^2)$ and $F_3(x, Q^2)$ which describe the density distributions of the charged partons of fractional momentum x.

The second stage of the DIS process consists of the recombination of the partons to form secondary hadrons. This process is normally referred to as *hadronization* or *fragmentation* between the struck parton and the proton remnant partons. This hadronization process is a direct consequence of the colour confinement property of QCD; the struck parton is a coloured object and thus, it cannot be observed in isolation. The hadronic final state consists of the 'current jet' from fragmentation of the struck parton, and the 'target jet' formed from the spectator (proton remnant) partons. This two stage QPM DIS process is illustrated in Figure 2.3.

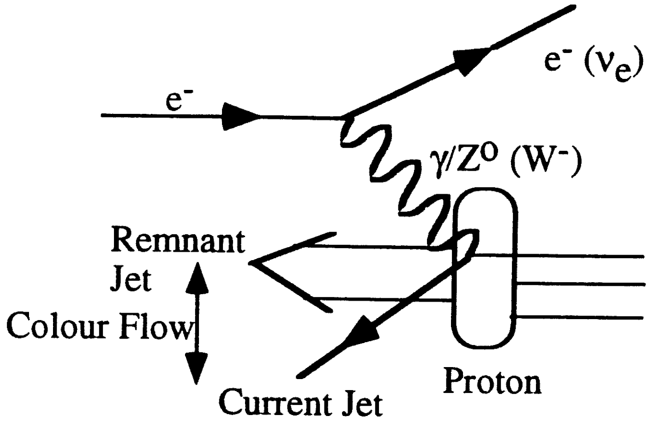

Figure 2.3: Typical quark-parton model picture a deep inelastic scattering event. The line of 'colour flow' illustrates the hadronization process.

The basis for the QPM was that virtual photons scatter off a 'free' quark, *i.e.* there was no interaction between the quarks over the short-time scale during the scattering; this was known as the 'impulse' approximation. QCD provides the theoretical justification for the QPM insofar that over the short distance-time scales involved, the strong coupling α_s becomes very small, *i.e.* the quarks are asymptotically free. However, over longer time-scales (lower Q^2), α_s becomes large enough such that the quarks cannot be treated as 'free' (noninteracting) partons. Therefore, the absolute scaling of the QPM is really a weak (logarithmic) dependence on Q^2 and so, within the framework of perturbative QCD, the structure functions evolve logarithmically with Q^2, independently of x. This variation is known as *scaling violations* and will be subject of discussion in Section 2.3.4.

Many measurements have been made of the proton structure functions in *ep*-scattering, νp- and $\bar{\nu}p$-fixed target experiments. Due to the low cms energies of these experiments, the kinematic plane was restricted to the region $x \geq 0.03$. The main results can be summarized as:

- The 'valence quark' composition of the proton is (u u d) and the valence quark momentum distributions peak around $x = \frac{1}{3}$.

- At small x there is a 'sea' of quarks and antiquarks of all flavours, due to the decay $g \rightarrow q\bar{q}$. The momentum distribution of these 'sea' quarks increases towards small x.
- Since these quarks can interact with each other, momentum is constantly redistributed and the momentum distribution is a continuous function.
- Roughly 50% of the nucleon momentum can be attributed to the charged partons. Therefore, it is postulated that the remaining 50% of the momentum is attributed to the gluons of the proton. The gluon distributions increase towards low x, which give rise to the presence of the 'sea' (and quark interactions).

2.3.2 Cross-sections and Structure Functions

The total differential neutral current deep inelastic (NC DIS) cross-section observable at HERA can be expressed by:

$$\frac{d^2\sigma_{tot}}{dxdQ^2} = \frac{d^2\sigma_o}{dxdQ^2} + \frac{\alpha}{2\pi}\frac{d^2\sigma_1}{dxdQ^2} + \mathcal{O}(\alpha^2) \tag{2.5}$$

where, the first term is known as the Born cross-section and the and the second and third terms represent the electroweak radiative corrections in first and second order, respectively.

The largest radiative contributions come from events in which the incoming or scattered electron radiates a real photon. These first order radiative corrections are illustrated Figures 2.4(a) and 2.4(b). Radiative contributions to the observed cross-sections are expected to be large at HERA energies, and are discussed in detail in Sections 6.2 and 6.2.4. In order to extract any structure function measurements, it is imperative that these radiative contributuions are accurately determined such that the Born cross-section can be extracted from the observed cross-section.

In the lowest order of electroweak coupling the differential NC cross-section (*i.e.* the Born cross-section) is given by:

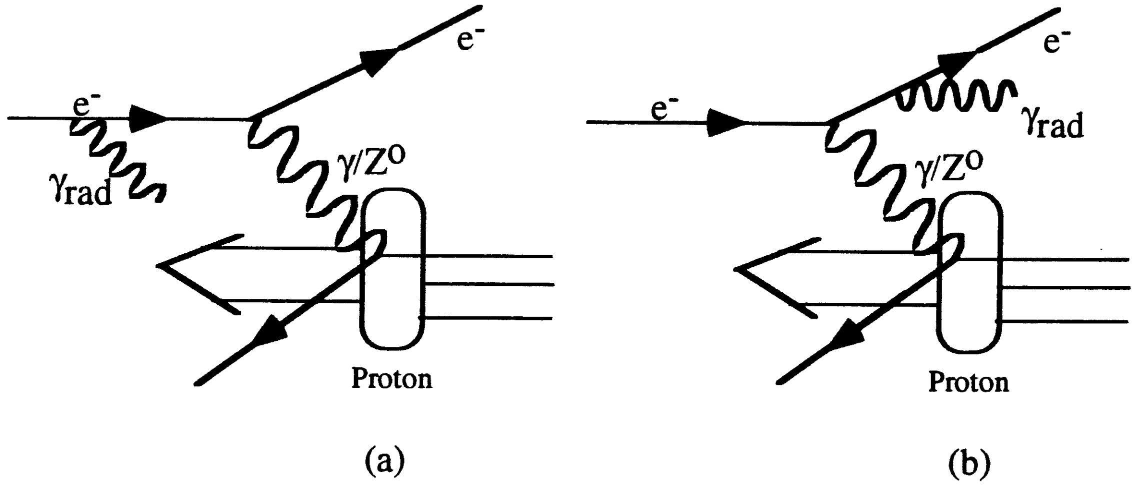

(a) (b)

Figure 2.4: Two examples of a first order NC DIS radiative event, (a) an initial-state radiated γ and, (b) a final-state radiated γ.

$$\frac{d\sigma_{NC}(e^{\mp})}{dxdQ^2} = \frac{4\pi\alpha^2}{xQ^4}\left[y^2xF_1(x,Q^2) + (1-y)F_2(x,Q^2) \pm \left(y - \frac{y^2}{2}\right)xF_3(x,Q^2)\right] \tag{2.6}$$

in terms of the structure functions F_1, F_2 and F_3. In the high x region, F_1 and F_2 can be related through the Callan-Gross relation, $2xF_1 = F_2$, which holds for spin $\frac{1}{2}$ quarks[1]. However, in the small x region accessible at HERA, this relation breaks down due to QCD effects and the longitudinal structure function $F_L = F_2 - 2xF_1$ becomes sizeable. By defining $R(x,Q^2)$ as $\frac{F_L(x,Q^2)}{F_2(x,Q^2) - F_L(x,Q^2)}$, equation 2.6 can be re-expressed as:

$$\frac{d\sigma_{NC}(e^{\mp})}{dxdQ^2} = \frac{2\pi\alpha^2}{xQ^4}\left[2(1-y)F_2(x,Q^2) + \frac{y^2F_2(x,Q^2)}{1+R(x,Q^2)} \pm (1-(1-y)^2)xF_3(x,Q^2)\right] \tag{2.7}$$

The ratio R is known as the photoabsorbtion ratio, and is discussed in more detail in Section 6.2. Taking the lepton polarization into account is an important testing ground for the SM electroweak theory. For left- (L) and right-handed (R) electrons, the structure functions, in the QPM model, are given by:

---

[1] Neglecting quark masses and intrinsic transverse momenta.

$$F_2^{L,R}(x,Q^2) = \sum_f \left[xq_f(x,Q^2) + x\bar{q}_f(x,Q^2)\right] A_f^{L,R}(Q^2) \quad (2.8)$$
$$xF_3^{L,R}(x,Q^2) = \sum_f \left[xq_f(x,Q^2) - x\bar{q}_f(x,Q^2)\right] B_f^{L,R}(Q^2) \quad (2.9)$$

where the sum is over all flavours f in the proton and q_f ($\bar{q}_f$) is the probability to find a quark (antiquark) carrying the momentum fraction x of the proton. The xq_f ($x\bar{q}_f$) are normally referred to as the parton density (or distribution) functions. The coefficients A_f and B_f depend on the coupling of the quark flavour f to the neutral current:

$$A_f^{L,R}(Q^2) = e_f^2 - 2e_f(v_e \pm a_e)v_f P_Z + (v_e \pm a_e)^2(v_f^2 + a_f^2)P_Z^2 \quad (2.10)$$
$$B_f^{L,R}(Q^2) = \mp 2e_f(v_e \pm a_e)a_f P_Z \pm 2(v_e \pm a_e)^2 v_f a_f P_Z^2 \quad (2.11)$$

where e_f is the electric charge of the quark f, v_f (v_e) and a_f (a_e) are the NC axial and vector couplings of the quark (electron), respectively. For a given fermion F (*i.e.* quark or lepton) they are defined as $v_F = [T_{3F} - 2e_F sin^2\theta_W]/\sin 2\theta_W$ and $a_F = T_{3F}/sin2\theta_W$, where, T_{3F} is the third component of weak isospin and θ_W is the Weinberg angle. P_Z is the propagator ratio $\frac{Q^2}{Q^2+M_Z^2}$.

The corresponding cross-sections for left- and right-handed positrons ($e^+_{L,R}$) are obtained from the above e^- formulae by replacing $F_2^{L,R} \rightarrow F_2^{R,L}$ and $xF_3^{L,R} \rightarrow -xF_3^{R,L}$.

At Q^2 values below the scale of the electroweak physics, *i.e.* $Q^2 \ll M_z^2 \Rightarrow P_Z \sim 0$, F_2 is due to electromagnetic scattering (γ) hence, $xF_3(x,Q^2)$ is small and can be neglected. At higher Q^2 electroweak effects such as γ/Z^o interference and pure Z^o exchange become dominant and xF_3 can no longer be neglected.

In the high Q^2 region the F_2 and xF_3 structure functions can only be disentangled by combining the electron and positron measurements:

$$F_2(x,Q^2) = \frac{1}{2}[\tilde{\sigma}_{NC}(e^-) + \tilde{\sigma}_{NC}(e^+)] \tag{2.12}$$

$$xF_3(x,Q^2) = \frac{1}{2}\frac{1+(1-y)^2}{1-(1-y)^2}[\tilde{\sigma}_{NC}(e^-) - \tilde{\sigma}_{NC}(e^+)] \tag{2.13}$$

where

$$\tilde{\sigma}_{NC}(e^{\pm}) = \frac{xQ^4}{2\pi\alpha^2[1+(1-y)^2]}\frac{d^2\sigma_{NC}(e^{\pm})}{dxdQ^2} \tag{2.14}$$

The ratio R is set to zero as this is a good approximation at at high Q^2 (high x).

At low Q^2, it is the pure γ exchange term in $A_f^{L,R}$ which dominates the cross-section measurements since the P_Z term is very small. This statement is illustrated in Figure 2.5. For the $F_2(x,Q^2)$ measurements presented in Chapter 6, the electroweak contributions to the cross-sections are neglected, since $Q^2 \leq 200\,\mathrm{GeV}^2$.

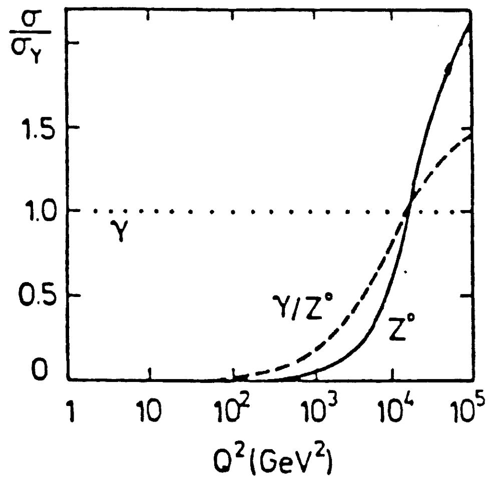

Figure 2.5: Relative size of the cross-sections from pure γ, pure Z^o and their interference as a function of Q^2, all normalized to the γ-exchange cross-section.

The corresponding differential cross-sections for charged current (CC) interactions are given by:

$$\frac{d\sigma_{CC}(e^-p)}{dxdQ^2} = \frac{\pi\alpha^2}{4\sin^4(\theta_W)(Q^2+M_W^2)^2}\sum_{i,j}\left(|V u_i d_j|^2 u_i(x,Q^2) + (1-y)^2|V_{u_j d_i}|^2\bar{d}_i(x,Q^2)\right)$$

$$\frac{d\sigma_{CC}(e^+p)}{dxdQ^2} = \frac{\pi\alpha^2}{4\sin^4(\theta_W)(Q^2 + M_W^2)^2}\sum_{i,j}\left(|V_{u_id_j}|^2\bar{u}_i(x,Q^2) + (1 - y)^2|V_{u_jd_i}|^2 d_i(x,Q^2)\right) \quad (2.15)\,(2.16)\,(2.17)$$

where $V_{u_id_j}$ are elements of the Cabbibo-Kabayashi-Maskawa matrix, u_i and d_j denote up-type and down-type quark flavours, respectively, and i, j are family indices.

Considering only four massless quark flavours (u, d, s, c) and using the the unitary relation $\sum_j |V_{u_id_j}|^2 = \sum_i |V_{u_jd_i}|^2 = 1$, the CC cross-section becomes:

$$\frac{d\sigma_{CC}(ep)}{dxdQ^2} \simeq \frac{G_F^2}{\pi}\left(1 + \frac{Q^2}{M_W^2}\right)^{-2}\begin{cases}(u + c) + (1 - y)^2(\bar{d} + \bar{s}) & for \quad e_L^- \\ (\bar{u} + \bar{c}) + (1 - y)^2(d + s) & for \quad e_L^+ \\ 0 & for \quad e_L^+, e_R^-\end{cases} \quad (2.18)$$

where, the Fermi coupling constant $G_F = \pi\alpha/\sqrt{2}\sin^2(\theta_W)M_W^2$, M_W is the W boson mass and u corresponds to the u-quark density $u(x, Q^2)$ *etc.*

The individual valence and sea quark distributions can only be disentangled by combining the NC and CC cross-section measurements. The method of unfolding the parton distributions from the above cross-sections can be found in [10]. The extraction of the gluon structure function $xg(x, Q^2)$ is non-trivial and will be discussed during the course of this chapter. One method has been proposed where $xg(x, Q^2)$ can be extracted from measurements of $F_L(x, Q^2)$ (see Section 6.2). There are currently two ways in which $F_L(x, Q^2)$ can be measured at HERA [11]:

1. $F_L(x, Q^2)$ can be extracted from measurements of the photoabsorbtion ratio $R(x, Q^2)$. To extract $R(x, Q^2)$ from the NC cross-sections, HERA will be required to run at different cms energies. This method is discussed in detail in [78].
2. $F_L(x, Q^2)$ can be extracted from NC DIS events with initial state photon radiation. As above, this method is based on the fact that the emission of photons in the direction close to the incoming e^- can be interpreted as

a reduction in the effective cms energy. $R(x, Q^2)$ can then be extracted from the measured initial state radiation cross-sections. For more details see [12].

2.3.3 QCD and DIS: Q^2 Evolution of $F_2(x, Q^2)$

Historically, the first experimental evidence in support of QCD came from the observation of scaling violations in the DIS structure functions. It was found that independently of x, the nucleon structure functions evolved slowly with Q^2 indicating small deviations from the pure parton-like behaviour of non-interacting, free quark constituents.

Within the framework of (perturbative) QCD, the quarks can interact with each other, via the exchange of gluons, or they can simply radiate gluons (gluon bremsstrahlung) which in turn can form quark-antiquark pairs. Therefore, as the Q^2 of the DIS process is increased, the exchanged boson probes smaller and smaller distances, and more nucleon 'structure' is revealed. This is illustrated in Figure 2.6 (taken from [2]):

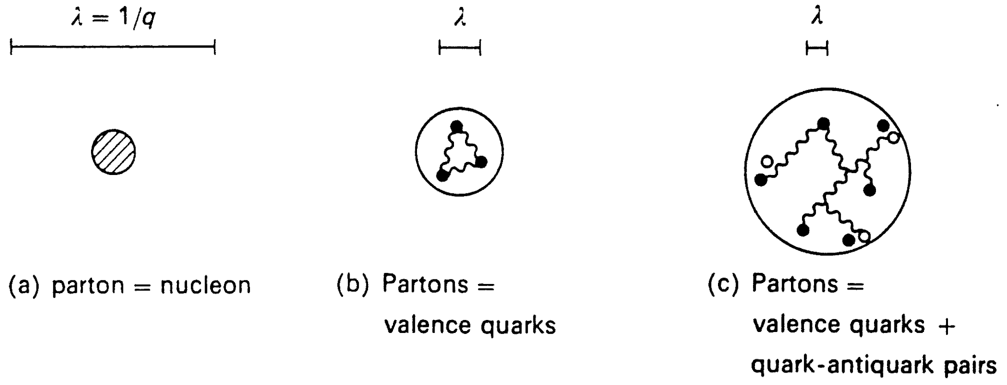

(a) parton = nucleon (b) Partons = valence quarks (c) Partons = valence quarks + quark-antiquark pairs

Figure 2.6: Symbolic picture of the nucleon, as probed in lepton scattering, as the wavlength $\lambda = \frac{1}{Q}$ of the virtual boson is decreased and more structure is revealed.

In order to see what this means in terms of the structure functions, it is worth considering the varying Q^2 dependence of the valence and sea quark distributions inside the nucleon. The valence quarks can only radiate gluons, and therefore they will lose a fraction of their momentum, which in turn is given to the gluon and sea-quark distributions. Thus as Q^2 increases, the valence quark structure functions decrease towards large x. Alternatively, the sea quark distribution is influenced by gluon radiation and $g \longrightarrow q\bar{q}$ processes. Therefore, at low x the increasing number of gluons leads to an increase in the sea-quark distribution as Q^2 is increased.

Since the F_2 structure function is determined from the summation over the valence and sea quark distributions (equation 2.8) the Q^2 evolution of F_2 is that of 'Q^2 contraction' shown in Figure 2.7(a). Alternatively, for constant values of x, perturbative QCD predicts that F_2 increases with Q^2 at low x and decreases with Q^2 at large x. This 'scale breaking' is a well established experimental fact, as shown in Figure 2.7(b) [2]:

To date the Q^2 dependence of the nucleon structure functions are well described by perturbative QCD. However, in the very low x region accessible at HERA the x and Q^2 dependence of the proton structure function (or parton distributions) will allow an important test of QCD dynamics in the region where the low x partons will be dominated by soft gluon emissions[2].

At present the theoretical predictions for the possible behaviour of the proton structure function (and parton distributions) are governed by evolution equations which are valid in different kinematic regimes. In order to appreciated the kinematic differences between the following evolution equations, it is worth remembering that if $F_2(x, Q^2)$ is determined from all possible Feynman diagrams it can be expressed in the following form:

$$F_2(x, Q^2) = \sum_n \alpha_s^n \sum_{k,m=0} \ln^k \left(\frac{1}{x}\right) \ln^m(Q^2) \qquad (2.19)$$

where the summation is over all orders of perturbation theory.

The different evolution equations sum different terms in the perturbative expansion of $F_2(x, Q^2)$.

---

[2] At very low x the dominant processes are $q \longrightarrow qg$ and $g \longrightarrow gg$.

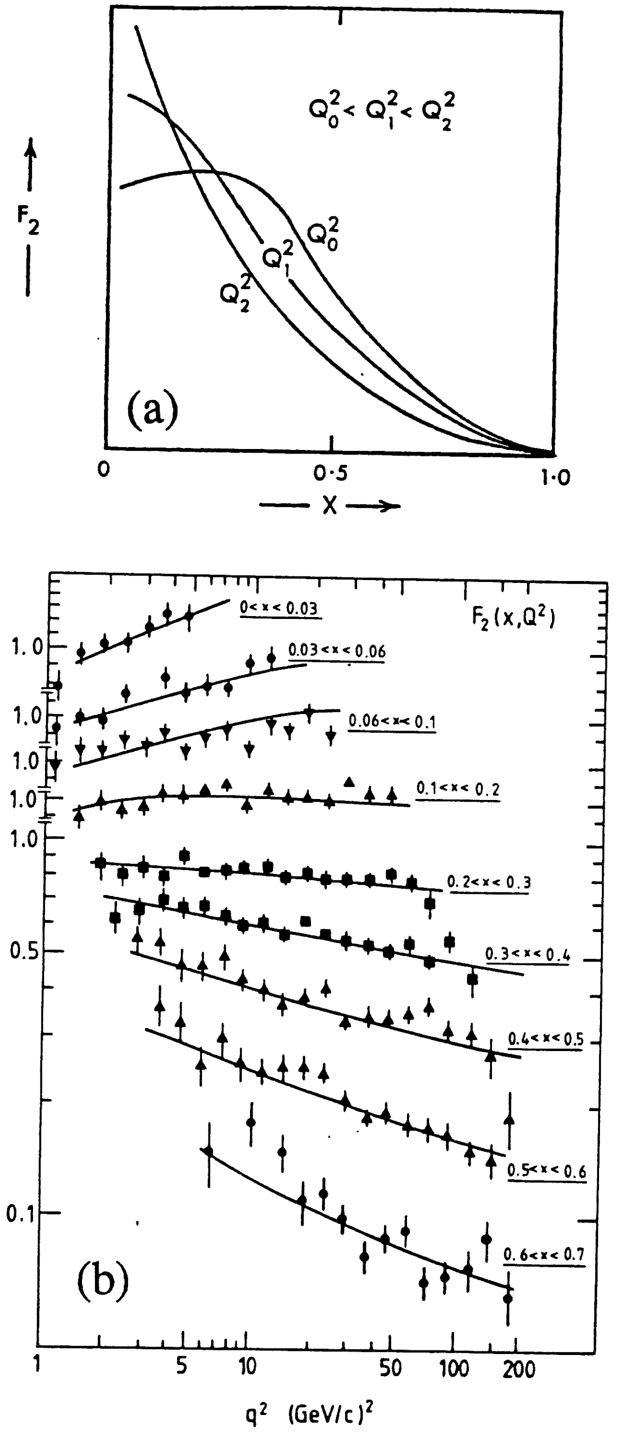

Figure 2.7: Graphical illustration of the scale breaking nature of $F_2(x,Q^2)$, as a function of x (a) and Q^2 (b).

2.3.4 The Alterelli-Parisi Evolution Equations

In the kinematic domain that has been accessible to fixed target DIS experiments (*i.e.* $x > 0.05$ for $Q^2 = 10\,\mathrm{GeV}^2$), the observed Q^2 dependence of the structure functions is described by the perturbative QCD evolution equations of Gribov, Lipatov, Alterelli and Parisi (GLAP) [14, 15]. In describing the way in which scaling is broken in QCD, it is convieniant to define non-singlet quark distributions q^{NS} (*i.e.* non flavour symmetric) and singlet quark distributions q^S (*i.e.* flavour symmetric):

$$q^{NS}(x,Q^2) = q_i(x,Q^2) - q_j(x,Q^2), \qquad q^S(x,Q^2) = \sum_i^{n_f}(q_i(x,Q^2) + \bar{q}_i(x,Q^2))$$

where $i \neq j$. The non-singlet distributions have non-zero values of flavour quantum numbers such as isospin or baryon number. The non-singlet distributions simply correspond to the unpaired valence quark distributions.

As described in Section 2.3.3, the Q^2 evolution of the non-singlet (valence quark) structure functions involves only one term, corresponding to gluon radiation. The singlet distributions correspond to the valence and sea distributions which evolve in Q^2 as a result of gluon radiation and quark pair production.

Thus, the complete GLAP evolution equations, in the leading logarithmic approximation[3] LLA(Q^2) are:

$$\frac{dq^{NS}(x,t)}{dt} = \frac{\alpha_s(t)}{2\pi}\int_x^1 \frac{dy}{y}\left[q(y,t)^{NS}P_{qq}^{NS}\left(\frac{x}{y}\right)\right] \tag{2.20}$$

$$\frac{dq^S(x,t)}{dt} = \frac{\alpha_s(t)}{2\pi}\int_x^1 \frac{dy}{y}\left[q^S(y,t)P_{qq}\left(\frac{x}{y}\right) + 2n_f g(y,t)P_{qg}\left(\frac{x}{y}\right)\right] \tag{2.21}$$

$$\frac{dG(x,t)}{dt} = \frac{\alpha_s(t)}{2\pi}\int_x^1 \frac{dy}{y}\left[q^S(y,t)P_{gq}\left(\frac{x}{y}\right) + 2n_f g(y,t)P_{gg}\left(\frac{x}{y}\right)\right] \tag{2.22}$$

where, $t = \ln\frac{Q^2}{Q_o^2}$. P_{qq}, P_{gq}, P_{qg} and P_{gg} are known as the Alterelli-Parisi splitting functions, n_f is the number of flavours and $yg(y,Q^2)$ is the gluon distribution. Q_o^2 is some arbitrarily chosen reference value of Q^2.

---

[3] In the LLA(Q^2) only the Feynman diagrams that contain the maximum power of $\ln Q^2$ are selected to all orders of perturbation theory.

Equation 2.20 expresses the fact that a (valence) quark with momentum fraction x could have come from a parent quark with a larger momentum fraction y which has radiated a gluon. The probability that this happens is proportional to $\alpha_s P_{qq}(\frac{x}{y})$; the integral corresponds to the sum over all possible momentum fractions of the parent quark.

Similarly, equation 2.21 describes the evolution of the 'sea' quark distribution. In this equation, a new term is included (second term) which corresponds to the possibility that a quark with momentum fraction x is the result of $q\bar{q}$ pair creation by a parent gluon with momentum fraction $y\,(> x)$. The probability for this to happen is $\alpha_s P_{qg}\left(\frac{x}{y}\right)$.

The final equation (equation 2.22) describes the evolution of the gluon density. The first term corresponds to the possibility that a gluon of momentum fraction x is the result of a quark of momentum fraction y radiating the gluon. The second term accounts for the fact the gluons can interact amongst themselves and share momentum. It is assumed that the quark masses are negligible such that P_{gq} is independent of quark flavour.

These evolution equations are graphically illustrated in Figure 2.8 where each equation is represented in terms of the basic QCD splitting diagrams.

In leading-order QCD, the Alterelli-Parisi splitting functions are given by:

$$\begin{aligned}
P_{qq}(z) &= \frac{4}{3}\left[\frac{1+z^2}{(1-z)_+} + 2\delta(1-z)\right] && (2.23)\\
P_{qg}(z) &= \frac{1}{2}\left[z^2 + (1-z)^2\right] && (2.24)\\
P_{gq}(z) &= \frac{4}{3}\left[\frac{1+(1-z)^2}{z}\right] && (2.25)\\
P_{gg}(z) &= 6\left[\frac{1-z}{z} + z(1-z) + \left(\frac{z}{1-z}\right)_+ + \frac{11}{12}\delta(1-z)\right] \\
&\quad - \frac{n_f}{3}\delta(1-z) && (2.26)
\end{aligned}$$

where $z = \frac{x}{y}$ and $1/(1-z)_+$ means:

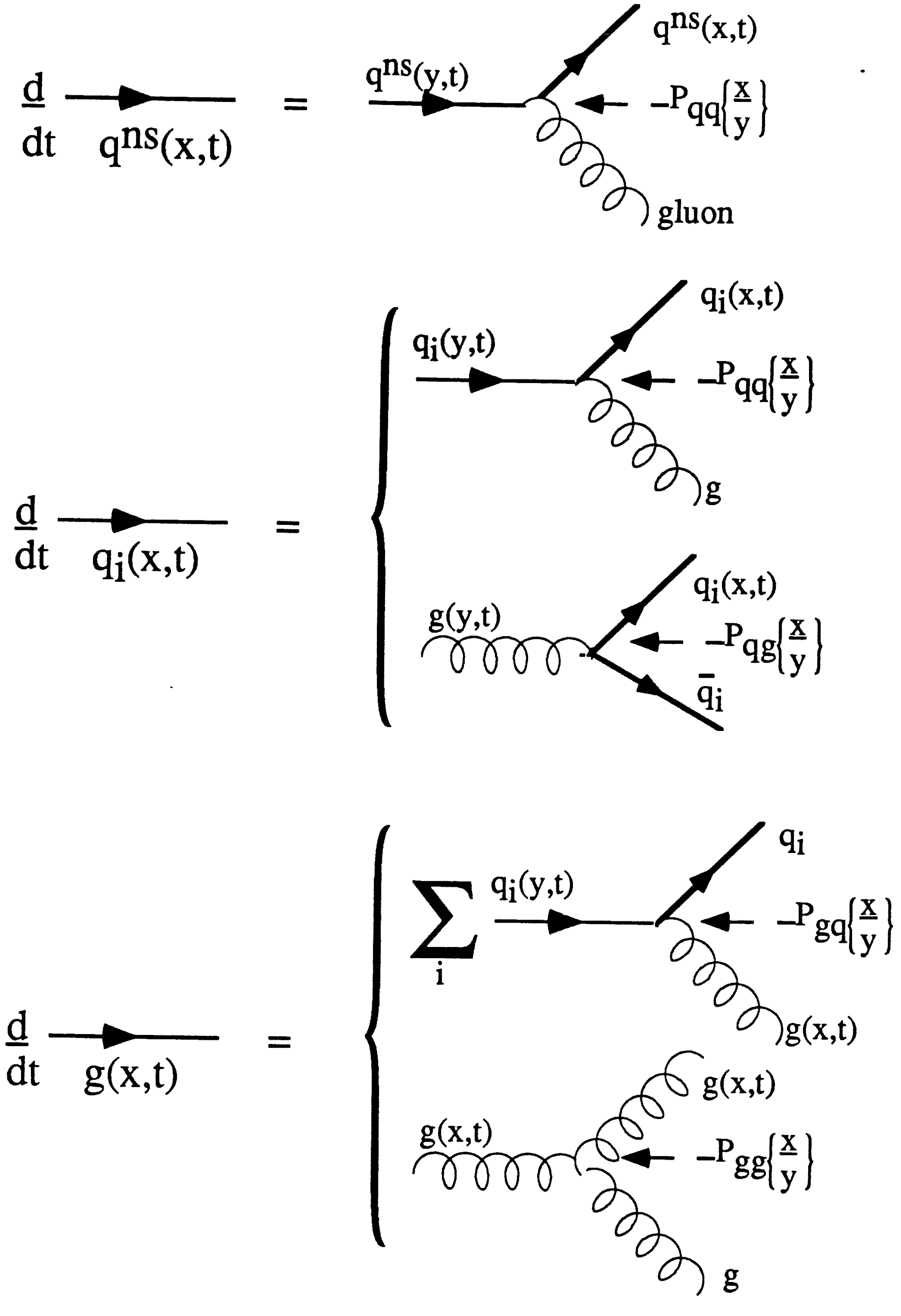

Figure 2.8: Graphical representation of the Alterelli-Parisi equations.

$$\int_0^1 dz \frac{f(z)}{(1-z)_+} = \int_0^1 \frac{f(z)-f(1)}{(1-z)} dz$$

This integral is introduced to cancel the singularities occurring at $z = 1$ when virtual gluon diagrams are included in the GLAP equations [1]. The $\delta(1-z)$ term corresponds to there being no change in $q(x, Q^2)$.

The experimentally measured structure function $F_2(x, Q^2)$ is given by:

$$F_2(x, Q^2) = \frac{5}{18} F_2^S(x, Q^2) + \frac{3}{18} F_2^{NS}(x, Q^2)$$

where F_2^S and F_2^{NS} are the singlet and non-singlet structure functions:

$$\begin{aligned} F_2^S &= \sum_i^{n_f} x[q_i(x, Q^2) + \bar{q}_i(x, Q^2) \\ F_2^{NS} &= \sum_i^{n_f/2} x[(u_i(x, Q^2) - d_i(x, Q^2)) + (\bar{u}_i(x, Q^2) - \bar{d}_i(x, Q^2))] \end{aligned}$$

Thus, the evolution of the F_2 structure function can be expressed in terms of F_2^{NS} and F_2^S using the above evolution equations. It should be noted that the only constraint on the gluon distribution $g(x, Q^2)$ comes from conservation of momentum:

$$\int_0^1 dx\, F^{NS}(x, Q^2) + \int_0^1 dx\, xg(x, Q^2) = 1$$

for all Q^2.

Perturbative QCD only describes how the parton distributions change with Q^2, given their values at one particular Q^2 scale, Q_o^2, it does not predict the actual values of the parton distributions. Therefore, in order to perform any QCD analysis on the measured structure functions, the parton distributions are parameterized for all x at a low value of Q_o^2. These parameterizations take a simple analytic form, for example:

$$\begin{aligned} xu_v(x, Q_o^2) &\sim x^a(1-x)^b \\ xg(x, Q_o^2) &\sim (1-x)^{n_G} \end{aligned}$$

and Λ_{QCD} is a free parameter. These parameterizations are then evolved to higher Q^2 via the Alterelli-Parisi equations, and fitted to the experimental data. The precise form of the gluon density in the low x limit ($x \rightarrow 0$) is determined from QCD predictions and will be the subject of discussion in the forthcoming sections. A good description on the QCD analysis of the nucleon structure functions can be found in [13].

In summary, perturbative QCD predicts the breakdown of Bjorken scaling which has now been extensively verified, as shown in Figure 2.7. The scaling violations arise from a resummation of the term $\alpha_s(Q^2)\ln Q^2$ (occurring in the perturbative part of F_2) which is *a priori* only valid in the kinematical domain of the LLA(Q^2) defined by:

$$\begin{aligned}\alpha_s(Q^2)\ln\frac{Q^2}{Q_o^2} &\sim 1\\ \alpha_s(Q^2)\ln\frac{1}{x} &\ll 1\\ \alpha_s(Q^2) &\ll 1\end{aligned} \tag{2.27}$$

From the above equations it can be seen that the LLA should hardly hold at $Q^2 = 10\,\mathrm{GeV}^2$ and $x = 0.01$ where $\alpha_s(Q^2)\ln\frac{1}{x} \sim 1.2$. Thus, in the very low x region accessible at HERA, the LLA(Q^2) approach no longer seems to be applicable.

2.3.5 The Lipatov Evolution Equation

In the low x limit the relevant framework for calculating the parton distributions, in perturbative QCD, is the leading $\log(\frac{1}{x})$ approximation (LLA($\frac{1}{x}$)). It corresponds to the sum of those terms which contain the maximal power of $\ln\frac{1}{x}$ at each order of perturbation expansion (this is in contrast to the GLAP equations which are in LLA(Q^2)). The basic quantity in this approximation is the non-integrated gluon distribution $f(x, k^2)$ which is related to the conventional gluon distribution $g(x, Q^2)$, in the following way [11]:

$$xg(x,Q^2) = \int_0^{Q^2} \frac{dk^2}{k} f(x,k^2) \tag{2.28}$$

where k represents the virtuality along the gluon decay chain, as shown in Figure 2.9.

In the LLA($\frac{1}{x}$) the $f(x,k^2)$ satisfies the following equation:

$$\begin{aligned} x\frac{\delta f(x,k^2)}{\delta x} &= \frac{3\alpha_s(k^2)}{\pi}k^2 \int_{k_0^2}^{\infty} \frac{dk'^2}{k'^2} \left\{ \frac{f(x,k'^2) - f(x,k^2)}{|k'^2 - k^2|} + \frac{f(x,k^2)}{\sqrt{4k'^4 + k^4}} \right\} \\ &\equiv K_L \otimes f \end{aligned} \tag{2.29}$$

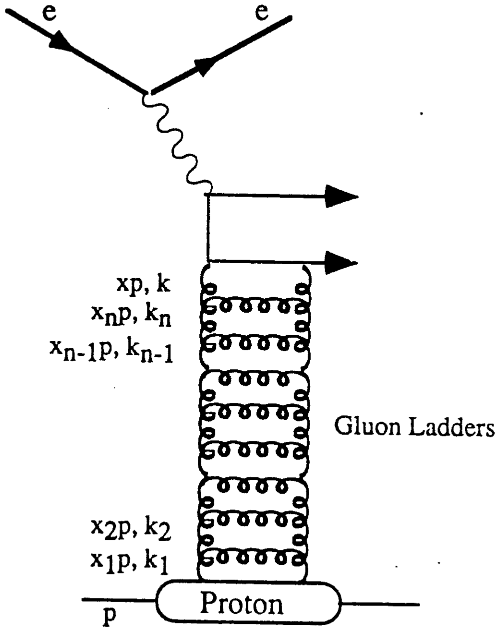

Figure 2.9: QCD ladder diagram describing the evolution of the gluon density in the LLA($\frac{1}{x}$).

This equation is known at the Balitskiǐ-Kuraev-Fadin-Lipatov (BKFL) equation or, in short, the Lipatov equation. It formally sums all terms of type $(\alpha_s(Q^2)\ln\frac{1}{x})^n$ corresponding to the ladder diagrams shown in Figure 2.9. The kernel K_L of equation 2.29 contains both the real gluon emission terms (proportional to $f(x,k'^2)$) and virtual gluon terms (proportional to $f(x,k^2)$); as above k^2 and k'^2 correspond to the transverse momenta (virtualities) of the gluons. The parameter k_o^2 is the infrared cut-off which is needed if the running coupling constant ($\alpha_s(k^2)$) effects are taken into account.

Similar to the GLAP evolution equations (LLA(Q^2)), the small x evolution can be described as a branching process in the initial state. However, in this case, along the parton decay chain there is no strong ordering in the transverse momenta k_n of the gluons, but a strong ordering in x_n:

$$x \ll x_n \ll x_{n-1} \ll \cdots x_2 \ll x_1$$

$$Q^2 \geq k^2 \geq k_n^2 \geq k_{n-1}^2 \cdots k_2^2 \geq k_1^2 \geq Q_o^2$$

Thus, the BKFL evolution equation is best suited for the behaviour of the parton distributions in the very low x region. The different orderings in the GLAP and BKFL (gluon) evolution equations result in clear differences, in the multiplicity and distributions of the emitted gluons in the HERA domain [11]; these differences may be observable in studies of the DIS hadronic final state. The validity of the BKFL equation is restricted to the region:

$$\begin{aligned} \alpha_s(Q^2)\ln\frac{Q^2}{Q_o^2} &\ll 1 \\ \alpha_s(Q^2)\ln\frac{1}{x} &\sim 1 \\ \alpha_s(Q^2) &\ll 1 \end{aligned} \tag{2.30}$$

where Q_o^2 is some moderate scale ($Q_o^2 \gg \Lambda_{QCD}^2$).

2.3.6 QCD at Low x: Parton Saturation

In the asymptotic limit $x \rightarrow 0$, the behaviour of the gluon distribution $xg(x, Q^2)$ can be derived from the GLAP and BFKL equations. It has been shown in [18], that the low x behaviour of the gluon (and sea quark) distributions can be expressed as:

$$\lim_{x\to 0} xg(x, Q^2) \sim \exp\left[2\left(\xi \ln\frac{1}{x}\right)^{\frac{1}{2}}\right]$$

where,

$$\xi = \int_{Q_o^2}^{Q^2} \frac{dk^2}{k^2}\frac{3\alpha_s(k^2)}{\pi}$$

and hence,

$$\lim_{x\to 0} xg(x,Q^2) \sim \exp\left[\left(\frac{144}{33 - n_f}\ln\left(\frac{\ln(Q^2/\Lambda^2_{QCD})}{\ln(Q^2_o/\Lambda^2_{QCD})}\right)\ln\frac{1}{x}\right)^{\frac{1}{2}}\right] \tag{2.31}$$

Similarly, the small x gluon behaviour from the BKFL equation is given by the following formula:

$$\lim_{x\to 0} xg(x,Q^2) \sim h(Q^2)x^{\beta} \tag{2.32}$$

where $\beta \sim -0.5$.

It can be seen from both gluon equations that as x decreases the gluon density rapidly increases. This rise in the gluon density is more rapid for the BKFL equation. Thus, it follows that in this low x limit $F_2(x,Q^2)$ rises in accordance with the increasing gluon (sea quark) density.

However, this rapid rise in the parton density cannot continue forever since *unitary* requires that the total cross-section for virtual photon absorption should be smaller than the size of the proton radius, *i.e.*

$$\sigma(\gamma^* p) = \frac{4\pi\alpha}{Q^2}F_2(x,Q^2) \leq 2\pi R_p^2 \tag{2.33}$$

where R_p is the proton radius[4].

Therefore, in this low x limit, the rise of the gluon density must be damped by a new mechanism. It has been proposed that in this low x region, at some critical value of x (x_{crit}) the partons densities become so large, that the partons begin to spatially overlap. Such a scenario is depicted in Figure 2.10. Beyond this point annihilation and recombination of parton pairs must dominate the low x processes. Such 'screening' or 'shadowing' effects damp the fast growth of the parton density. These saturation effects have been incorporated in the evolution equations of Gribov, Levin and Ryskin (GLR) [19].

Although the BKFL and GLAP equations are valid in different kinematic regions, the GLR equations allow a smooth transition between these two regimes.

---

[4] Strictly speaking the hadron radius varies slowly with the cms energy s, $R(s)_p \sim const. \ln s$

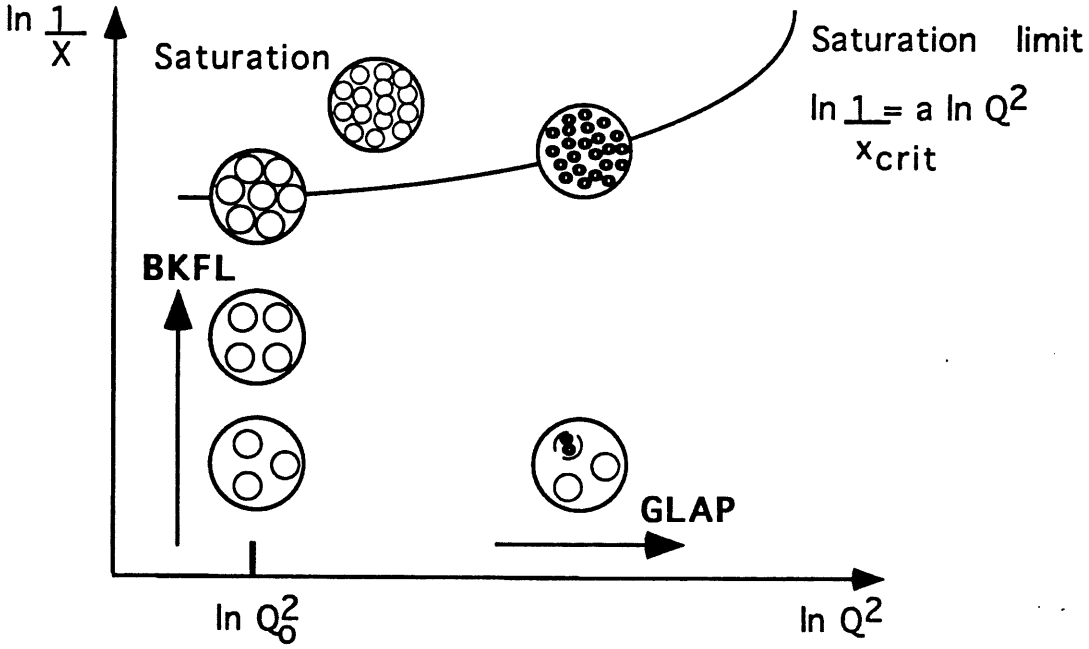

Figure 2.10: Diagram showing the (x, Q^2) regions of validity of the two evolution equations. The resulting parton density of the proton (in the transverse plane) is also indicated.

The GLR equations formally sums all terms of the type $(\alpha_s \ln Q^2)^n$, $(\alpha_s \ln \frac{1}{x})^n$ and $(\alpha_s \ln Q^2 \ln \frac{1}{x})^n$; this is called the double leading logarithmic approximation since both terms are large. The GLR evolution equation for the gluon is expressed as:

$$x\frac{\delta f(x,k^2)}{\delta x} = \int_{k_0^2}^{\infty} dk'^2 \tilde{K}(k,k')f(x,k'^2) - \frac{81\alpha_s(k^2)}{16R_a^2k^2}[xg(x,k^2)]^2 \tag{2.34}$$

where, $f(x, k^2)$ is defined in equation 2.28 and the kernel $\tilde{K}$ is modified to include the BKFL kernal (K_L) and the gluonic part of the GLAP equation. The second (non-linear) term in the GLR equation represents the correction due to parton screening. The free parameter R_a depends on the locality of the screening region (see Section 2.3.7). A simple derivation of this shadowing term can be found in [11].

The origin of this shadowing term lies in the interaction between different gluon ladders (fan diagrams) as shown in Figure 2.11. However, these fan diagrams only act to suppress the rate at which the gluon density grows; they do not describe the saturation mechanism. Therefore, it is expected that validity of the GLR equation must break down before parton saturation is reached.

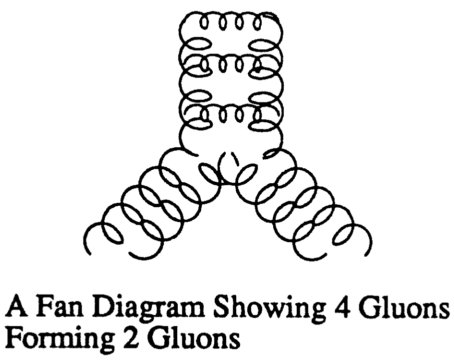

Figure 2.11: A typical fan diagram which forms the basis of the GLR equation.

2.3.7 QCD at low x: Predictions for DIS at HERA

Using the results discussed in the previous sections, the evolution of the proton structure function $F_2(x, Q^2)$ can be described by three different theoretical regimes A,B and C:

- A: The evolution is described by the standard QCD evolution equations of GLAP and BKFL.
- B: The start of the parton-parton recombination or annihilation with the x evolution described by the GLR equation(s).
- C: The parton density has reached saturation and the partons cannot be considered to be free, although $\alpha_s(Q^2) \ll 1$. At this point, the LLA must break down and non-perturbative confinement effect will become important. However, this region is still not well understood and no solid theoretical tools are available yet. For example see [20].

The resulting $F_2(x, Q^2)$ evolution, and theoretical regimes, are illustrated in Figure 2.12. It is assumed that region C is beyond the reach of HERA. However, the experimental observation on the x evolution of $F_2(x, Q^2)$ will allow detailed tests to be made of the standard evolution equations. If $F_2(x, Q^2)$ is observed to rise towards low x, then region B may be detectable at HERA.

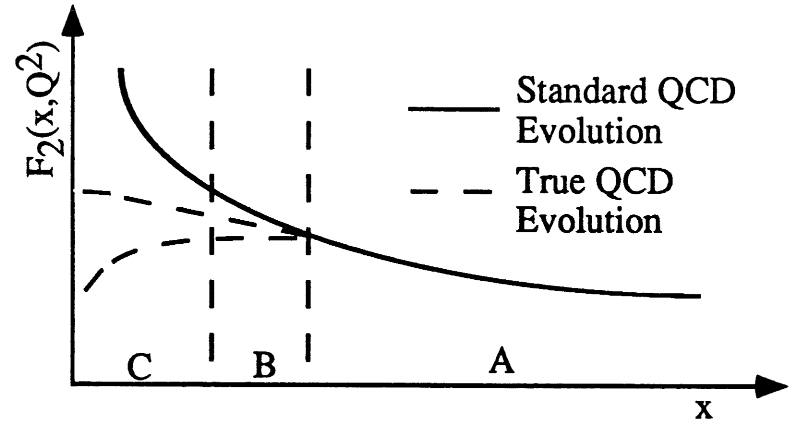

Figure 2.12: Theoretical regimes describing the small x behaviour of the proton structure function $F_2(x,Q^2)$: standard QCD evolution verses two possible alternatives for the true QCD evolution.

However, the size of the non-linear term in the GLR equation, which governs region B, is very strongly dependent on the assumptions made on the gluon distribution and the locality of the screening region R_a. At present there exists two possible scenarios for the value of R_a:

- The large increase in the gluon density is localized in small regions called 'hot spots'. The transverse size of the 'hot spots' is uncertain but it is generally assumed to be equal to the (transverse) size of the valence quark, *i.e.* $R_a \sim 2\,\mathrm{GeV}^{-1}$.
- The large increase in the gluon density is spread uniformly over the full transverse size of the proton, in which case $R_a \sim 5\,\mathrm{GeV}^{-1}$.

Similarly, two main scenarios exist for the shape of the gluon density in the $x \longrightarrow 0$ limit:

- At Q_o^2 the gluon density $xg(x,Q_o^2)$ can assume either the Lipatov type behaviour (equation 2.32) or the GLAP behaviour (equation 2.31).
- In the naive Regge-parton model $xg(x,Q_o^2) \sim x^{1-\alpha_{P(0)}}$, where the Pomeron intercept $\alpha_{P(0)} \simeq 1$, implying that the gluon density, $xg(x,Q_o^2)$, remains approximately constant.

In either case the parton densities are evolved in Q^2 via the GLAP equations.

The 'hot spot' scenario assumes that saturation starts close to one of the valence quarks, and is normally referred to as 'strong' screening since the non-linear GLR term (see equation 2.34) is greater for $R_a = 2$ than $R_a = 5$ (scenario 2, 'weak' screening). These two screening effects are illustrated in Figure 2.13, using the parton distribution parameterizations of Martin, Roberts and Sterling (MRS) [66]. The MRS parameterization assumes a Lipatov (D$-$) and Regge (D0) type behaviour for the gluon density at low x at a Q_o^2 scale of 4 GeV^2.

From Figure 2.13 it can be seen that if $F_2(x,Q^2)$ is observed to rise, it will be difficult to distinguish the weak screening prediction from the Lipatov behaviour at HERA. Similarly, if $F_2(x,Q^2)$ rises slowly it will be difficult to distinguish the strong screening and Regge-parton model predictions. Specific studies [21] have shown that the strong screening evolution may be distinguishable provided the systematic errors on the $F_2(x,Q^2)$ measurements are kept below 5%.

It should be noted that $F_2(x,Q^2)$ measures the parton density, averaged over the full transverse size of the hadron. Therefore, it is desirable to look for experiments in which the small x behaviour of QCD can be studied which directly measure the localization of partons ('hot spots') within the hadron.

One method has been proposed [22] in which the presence of 'hot spots' can be detected by studying low x DIS events[5] which contain an identified jet (x_j, k_1^2), where $x \ll x_j$ and $Q^2 \simeq k_1^2$. This process is illustrated in Figure 2.14(a) where the jet arises from parton 'a' (quark or gluon). Since events are chosen with $Q^2 \simeq k_1^2$ the QCD evolution (over the parton chain) is neutralised and attention is focused on the small $\frac{x}{x_j}$ behaviour. The differential cross-section for this process can be expressed as:

$$x_j k_1^2 \frac{\delta F_2(x_j, k_1^2)}{\delta x_j \delta k_1^2} \quad = \quad C\alpha_s(Q^2)\left[xg(x_j, k_1^2) \; + \; \frac{4}{9}(xq(x_j, k_1^2) \; + \; x\bar{q}(x_j, k_1))\right]$$

---

[5] Here, the kinematics are defined at the leptonic vertex.

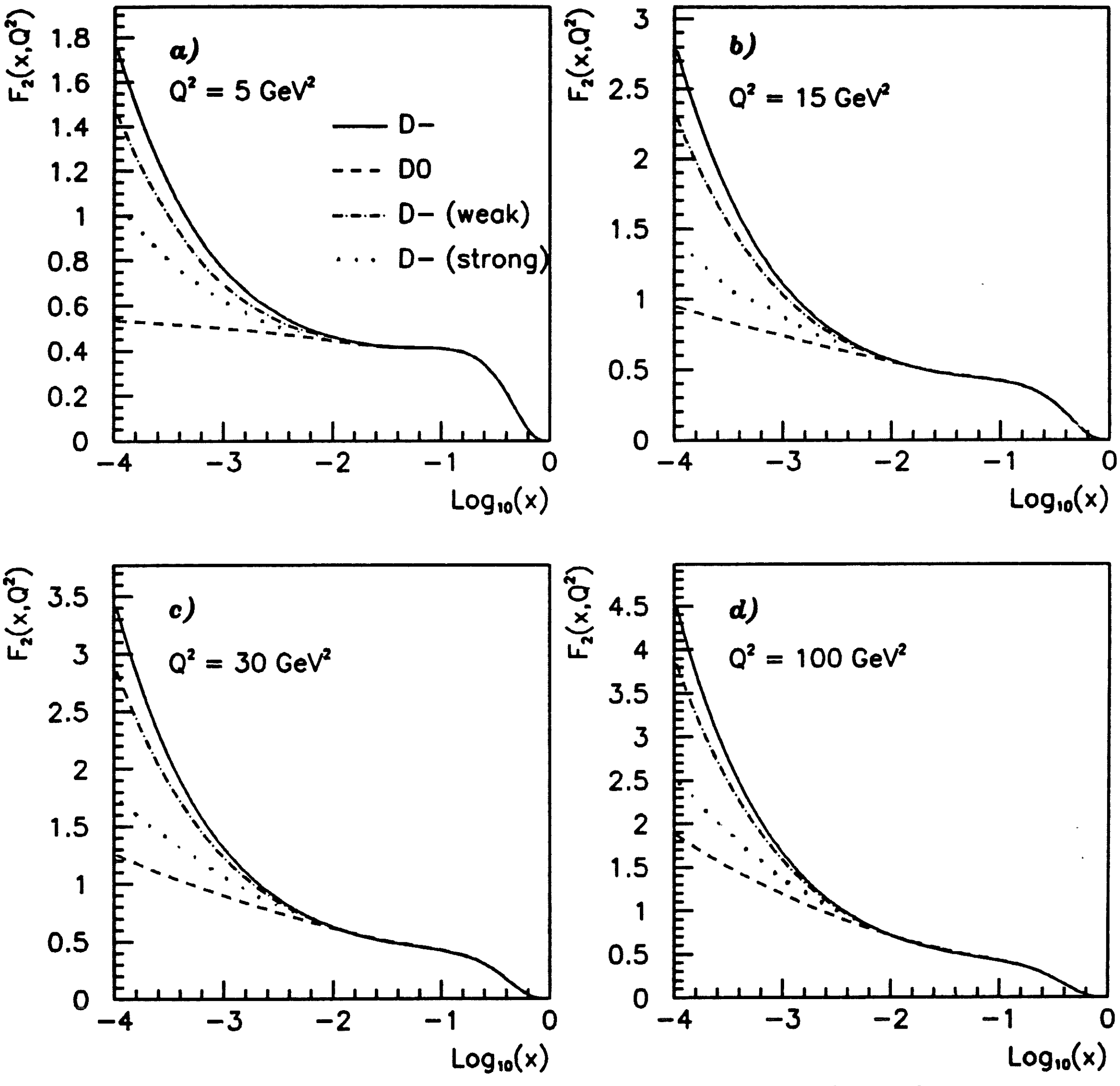

Figure 2.13: The x evolution of the proton structure function $F_2(x,Q^2)$ at $Q^2 = 5$, 15, 30 and 100 GeV^2, using the $D-$ (including screening corrections) and $D0$ distributions.

$$\times \frac{\exp\left(\frac{12\alpha_s(Q^2)}{\pi} \ln 2 \ln \frac{x_j}{x}\right)}{\sqrt{\ln \frac{x_j}{x}}} \tag{2.35}$$

where C is a calculable normalization constant.

It can be seen that the above cross-section rapidly increases as $\frac{x_j}{x} \rightarrow 0$ (as expected from pure BKFL evolution). However, in the prescence of 'hot spots', as $\frac{x}{x_j}$ decreases, the saturation effects result in a suppression of the above inclusive jet cross-section. One of the pleasant features of this method is that since x_j is taken to be large (≥ 0.05) the parton distributions are in a well measured region, and no additional assumptions need to be made. More details on searches for 'hot spots' at HERA can be found in [23].

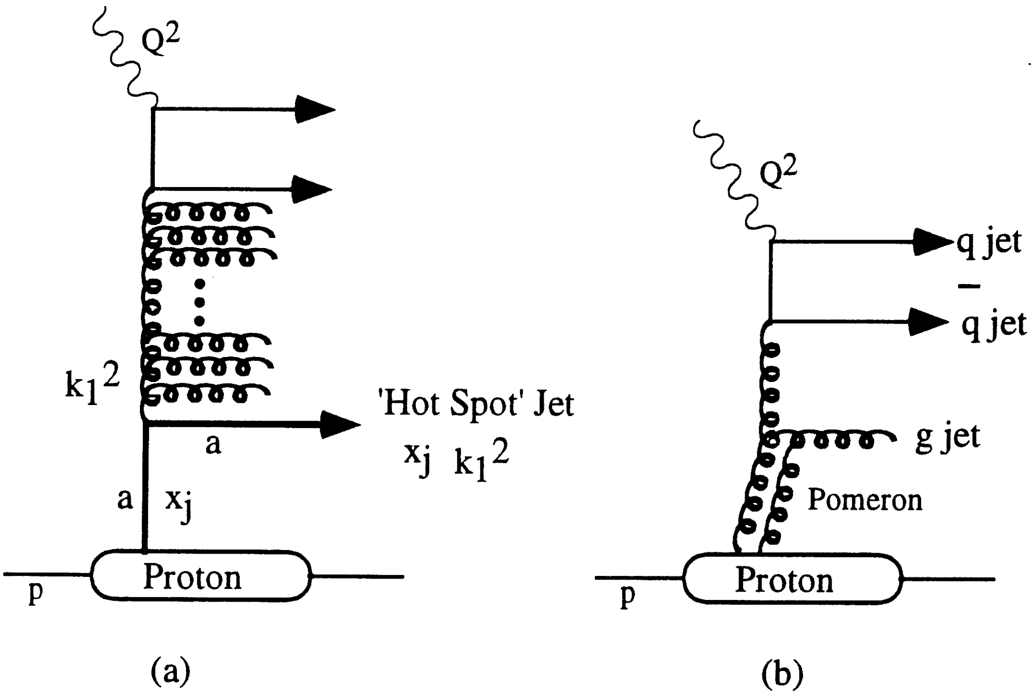

Figure 2.14: The first (a) is a simple illustration of a 'hot spot' event with an identified jet. The second (b) figure shows a typical diffractive DIS event characterised by a Pomeron exchange.

Another method based upon the existence of such 'hot spots' has been proposed by Ryskin [24]. It has been suggested that the observation of diffractive dissociation of the virtual photon into three jets originating from $q\bar{q}g$, will allow a good test of the saturation mechanism. The virtual photon dissociates into a $q\bar{q}$ pair which then interact with the proton via the exchange of a Pomeron exchange, as shown in Figure 2.14(b). Since the Pomeron is a colourless object there is no colour flow (hadronization) between the proton and Pomeron. This results in a large rapidity gap between the forward going proton and gluon jet.

The important aspect of this process is that the cross-section is proportional gluon density ($x_k g(x_k, k^2)$) and is therefore, very sensitive to saturation effects. With saturation effects the cross-section should be substantially smaller, than the standard linear evolution predictions; for example, the cross-section without screening amounts to about $2 - 10$ nb which can be reduced to 0.01 nb when saturation sets in.

2.3.8 QCD at Low x: Summary

So far, only a brief account has been given for the possible theoretical scenarios that might be accessible in the new low x limit opened up by HERA. It should be noted that besides looking for new QCD effects, such as saturation, studies of the DIS hadronic final state will allow quantative tests of standard perturbative QCD and the hadronization mechanism. For example, the observation of jets in DIS (excluding the proton remnant) will allow the determination of α_s and hence, Λ_{QCD}.

Observation of diffractive DIS events (with large rapidity gaps) will allow a new test of QCD dynamics relating to the Pomeron. In modern QCD language, the Pomeron is thought of as a strongly interacting (non-perturbative) partonic system, similar to a hadron. Therefore, observations of these events will not only yield important information about the partonic nature of the Pomeron[6], it will open up the opportunity to study the longer range, and thus the softer non-perturbative, regions of QCD.

In summary, if $F_2(x, Q^2)$ is observed to rise then at some point new physics must set in. Whether these new QCD effects will be visible at HERA is subject to various theoretical and experimental uncertainties. The results from HERA will certainly be instrumental in the understanding of the physics of the next generation of high

---

[6] *i.e.* determine the quark and gluon content of the Pomeron.

energy hadron-hadron and hadron-lepton colliders.

2.4 Low Q^2 Physics: Photoproduction at HERA

Electron-proton collisions at low Q^2 are the most dominant processes at HERA. These photoproduction event are characterised by $Q^2 \sim 0$ where the electron is scattered at very low angles. This gives a unique opportunity to study the high energy scattering of quasi-real photons with protons. Similar to the DIS case, the interest in using HERA for studying photoproduction processes comes from the large cms energies obtainable in the γp system. It will be possible to measure the total γp cross-section up to a cms energy $\sqrt{s_{\gamma p}} \sim 300$ GeV.

In the single photon exchange process, using the Weizsäcker-Williams approximation (WWA), the ep photoproduction cross-section at a fixed cms energy can be written as [60]:

$$\frac{d\sigma_{ep}}{dy} = \sigma_{tot}(\sqrt{s_{\gamma p}}) \frac{\alpha}{2\pi} \frac{1 + (1 - y)^2}{y} \ln \frac{Q^2_{max}(y)}{Q^2_{min}(y)} \tag{2.36}$$

where $\sqrt{s_{\gamma p}} = 2\sqrt{yE_eE_p}$ and $Q^2_{min}(y) = (m_e y)^2/(1 - y)$. The value of $Q^2_{max}(y)$ is defined by the experimental conditions. The definition for y is given in equation 2.1. $\sigma_{tot}(\sqrt{s_{\gamma p}})$ is the total photoproduction cross-section.

It should be noted that the validity of the WWA is limited to the very small Q^2 region, $Q^2 \ll 1$. In the region where $Q^2_{max} \sim 4\,\mathrm{GeV}^2$, corrections of the order of 10 - 15% need to be applied to the WWA. As a result of the large γp cross-section(s), photoproduction processes form the largest background to DIS physics. This is discussed in detail in Chapters 5 and 6.

The total photoproduction cross-section contains contributions from processes where the photon couples pointlike to the partons in the proton and from subprocesses involving the photon structure function. The processes based on the pointlike coupling are QCD compton, $\gamma q \rightarrow gq$, and photon-gluon fusion, $\gamma q \rightarrow q\bar{q}$. These processes are sometimes referred to as direct photon interactions, and are illustrated in Figure 2.15.

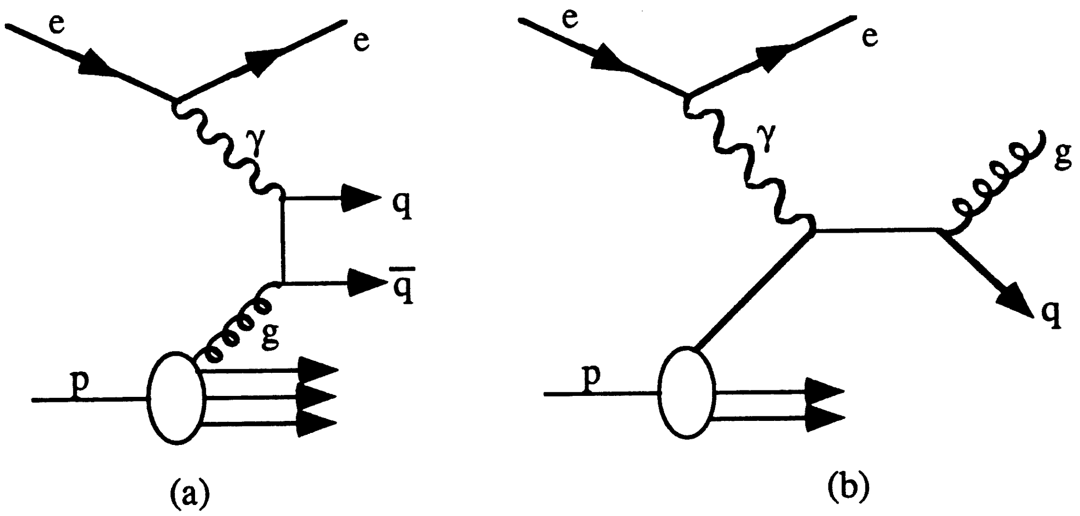

Figure 2.15: Lowest order QCD Feynman diagrams for photon-gluon fusion (a) and QCD compton (b) processes.

Production of the heavy flavour quarks (c and b)[7] predominantly occur through the photon-gluon fusion processes. The cross-section for these processes (to $\mathcal{O}(\alpha_s)$) is written as:

$$\sigma(ep \rightarrow q\bar{q}X) = \int dx_g G(x_g, \hat{s})\hat{\sigma}(eg \rightarrow q\bar{q}) \tag{2.37}$$

where X represents the remaining final state partons, excluding the quark-antiquark pair. $\hat{\sigma}$ is the QCD parton level cross-section and $G(x_g, \hat{s})$ is the probability to find a gluon of momentum $x_g p_p$ at a mass scale $\hat{s}$ (the invariant mass squared of the $q\bar{q}$ system).

The important aspect of this process is that measurements of the cross-section will allow measurements to be made of the gluon density. This could be studied using the process $\gamma g \rightarrow J/\psi + g$ where the J/ψ ($c\bar{c}$) decays to two leptons e^+e^- or $\mu^+\mu^-$ [25]. It should be noted that in such a process the pointlike coupling of the photon directly probes the partons, and can give complementary information to the usual DIS structure functions.

---

[7] The t quark is now assumed to be beyond the reach of HERA.

The photoproduction processes which probe the hadronic nature of the photon are described by the photon structure function, which is given by the sum of a vector-meson dominance model (VDM) component and of a resolved photon component.

In the VDM process the photon couples to a vector meson **V** (ρ, ϕ, ω, ...), which then interacts with the proton. Typical diffractive and nondiffractive VDM processes are shown in Figure 2.16.

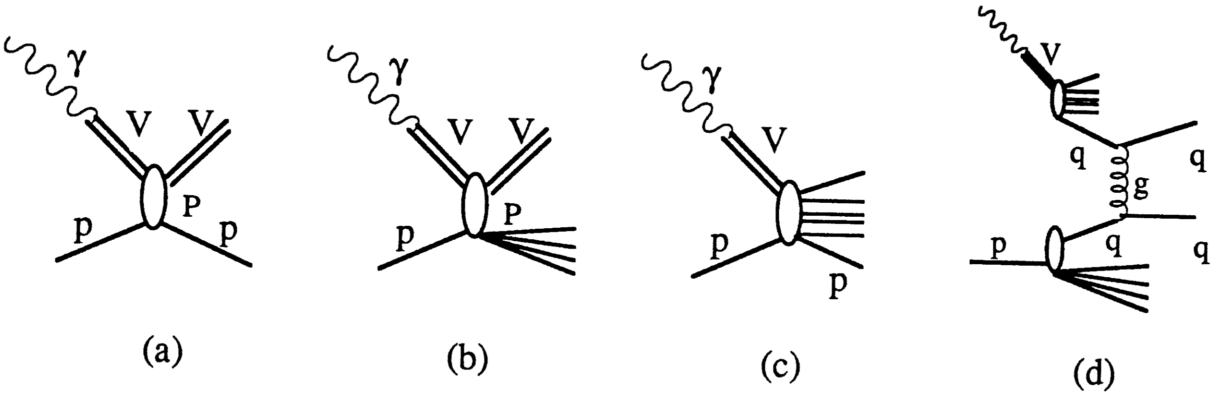

Figure 2.16: Photoproduction diagrams via the VDM process for elastic (a) and inelastic diffractive scattering (b), nondiffractive processes (c) and hard scattering (d).

In the resolved photon processes, shown in Figure 2.17, the photon couples to a $q\bar{q}$ pair (pair production) which in turn interact with a gluon. Higher order processes involve gluons being radiated from the $q\bar{q}$ pair which may also interact with the protons constituents. These resolved photon process provide the best environment to probe the partonic nature of the photon.

In addition to deep inelastic scattering these photoproduction processes provide an ideal testing ground for perturbative QCD. Hard scattering processes (direct or resolved) will give rise to high transverse momentum ($p_\perp$) parton jets, sometimes referred to as 'minijets'. Measurements of these high $p_\perp$ jets and of the hard scattering cross-sections can be compared with QCD predictions, thus giving a better understanding of the QCD dynamics of the proton and photon.

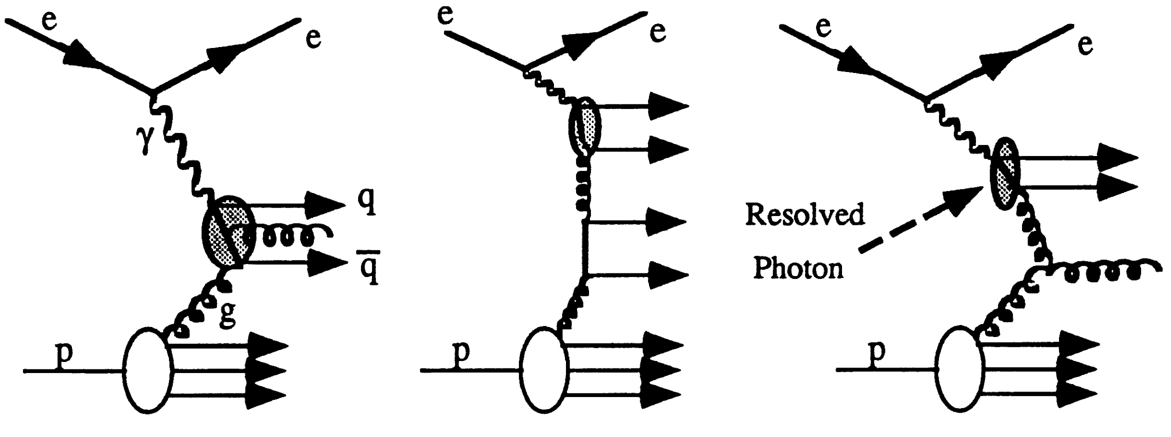

Figure 2.17: Three diagrams illustrating the resolved photon process.

,

Before the advent of HERA, measurements of $\sigma_{tot}(\sqrt{s_{\gamma p}})$ were restricted to cms energies below less than 50 GeV. In the cms energy range accessible at HERA ($90 \leq \sqrt{s_{\gamma p}} \leq 300$ GeV) the value of $\sigma_{tot}(\sqrt{s_{\gamma p}})$ is subject to various theoretical uncertainties. The predictions for $\sigma_{tot}(\sqrt{s_{\gamma p}})$ are based on two approaches:

- The Regge Approach: In this prediction σ_{tot} increases slowly with the γp cms energy.
- The Minijet Approach: The total inelastic cross-section is built up of a soft part (independent of $s_{\gamma p}$) and a QCD part describing the hard interactions. This latter contribution is dependent on the photon and proton structure functions and the scale $\hat{p_\perp}$ describing the $p_\perp$ of the hard interaction in the cms system. This method predicts a rise in σ_{tot} with $s_{\gamma p}$ which is strongly dependent on the value of $\hat{p}_\perp^{min}$, the minimum value of $p_\perp$ where the QCD part becomes applicable. There is no precise theoretical prediction for $\hat{p}_\perp^{min}$.

Thus, the aim of the photoproduction studies at HERA will be to extensively test the validity of both scenarios in the HERA energy range. A more detailed description on the theoretical and experimental issues facing photoproduction physics at HERA can be found in [26]. Early results from HERA [27, 70] indicate that σ_{tot} at $\sqrt{s_{\gamma p}} \sim$ 200 GeV is in agreement with the Regge prediction and the minijets model provided $\hat{p}_{\perp}^{min}$ is about 2 GeV/c. There is no physics reason why $\hat{p}_{\perp}^{min}$ should be this value and will require further studies.

2.5 Electroweak tests at HERA

Despite the large Q^2 range accessible in NC and CC DIS processes, production of the SM electroweak bosons Z^o and $W^{\pm}$ will be very limited as result of the low cross-sections. The $W^{\pm}$ and Z^o bosons can be produced by bremsstrahlung from a quark or lepton and by boson fusion, γW, WW, WZ, exhibiting a triple gauge boson vertex. A few leading order diagrams for W^+ production are shown in Figure 2.18 (similar diagrams exist for W^- and Z^o production).

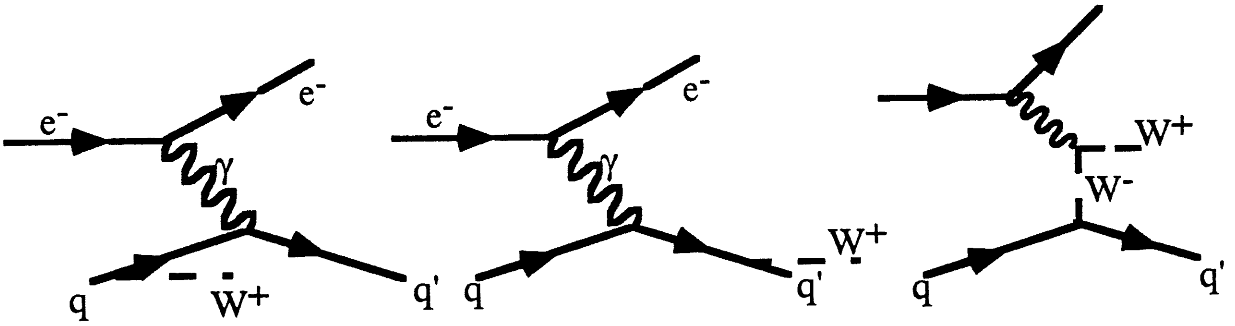

Figure 2.18: Dominant diagrams in W^+ production at HERA.

It is estimated that about 50 W^-, 40 W^+ and 25 Z^o events can be expected from an integrated luminosity of 100 pb^{-1} [28]. Despite the small number, measurement of these cross-sections will allow an important test of the non-Abelian nature of the SM, *i.e.* the triple boson vertex.

In addition to the production of the pure gauge bosons, precision tests of SM parameters will be made by running HERA with longitudinally polarized e^+ and e^-

beams. Studies of cross-section asymmetries and cross-section ratios (*i.e.* $\frac{\sigma_{NC}}{\sigma_{CC}}$) with the polarized beams will allow measurements to be made of the electroweak terms in the A_f and B_f coefficients of the $F_2(x,Q^2)$ and $F_3(x,Q^2)$ structure functions (see equations 2.10 and 2.11). A brief account of the electroweak tests at HERA can be found in [29]. A more detailed account covering the theoretical and experimental issues at HERA is presented in [30].

2.6 Exotic Physics at HERA

The large kinematic domain that will be explored at HERA provides a unique opportunity to search for new phenomena beyond the Standard Model. In this section a very brief review is given for a few examples of new physics that may be accessible at HERA. A more detailed account on the exotic physics predicted at HERA can be found in [31].

The search for new physics can be divided in two parts:

- Detecting new particles, such as leptoquarks, leptogluons and heavy Majorana neutrinos.
- Detection of new interactions, through the appearance of small systematic deviations from the expected SM cross-sections. Examples of new dynamics are exchange of new bosons W' and Z' or compositeness (substructure) of leptons and quarks via the observation of excited leptons and quarks.

Leptoquarks are new particles which have the quantum numbers of both leptons and quarks, and are ideal exotic candidates for HERA. Leptoquarks arise in a number of theoretical scenarios (composite models, grand unified theories and superstring inspired model), while leptogluons are more speculative and are thought to be exotic bound states of leptons and gluons. The particles appear directly as resonance formation in the incident eq and eg systems, as shown in Figure 2.19.

It can be seen that the production of these particles leads to final states that are similar to NC DIS events. If the masses are well within the reach of HERA then

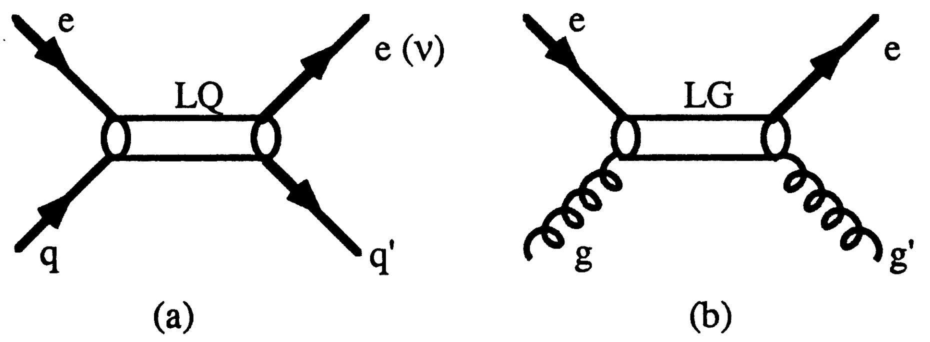

Figure 2.19: Diagrams showing direct channel production of leptoquarks LQ (a) and leptogluons LG (b) in *ep* scattering.

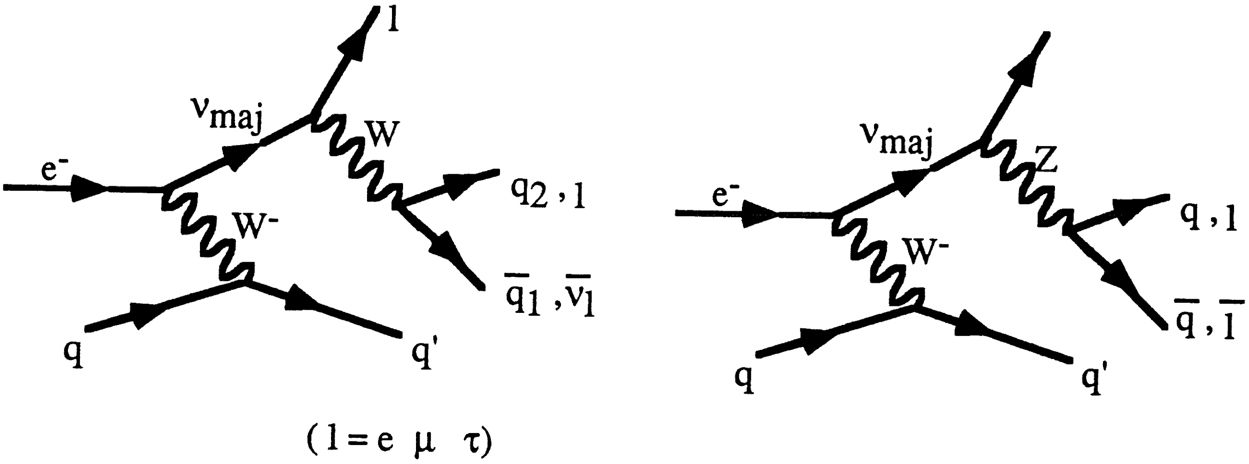

Figure 2.20: Illustration of the production and decay of heavy Majorana neutrinos.

the observation of these exotic particles, amidst NC DIS background, will appear as an excess population at fixed x value equal to $\frac{m_{LQ}^2}{s}$ where m_{LQ} is the mass of the leptoquark or leptogluon. The mass of these particles are *a priori* not known, but it is expected that the leptoquark mass may be of the order 100 GeV.

In classical theories, lepton number conservation is only valid when the usual SM neutrinos, described in Section 1.2.1, are exactly massless. However, in a number of unified theories these neutrinos acquire a very small mass and right-handed Majorana neutrinos are introduced to the SM fermions. In *ep* collisions these massive Majorana neutrinos may be produced in CC interactions through their mixing with the light neutrinos. The signature for such processes are very spectacular as shown in Figure 2.20. Depending on the mixing parameters it is expected that heavy neutrinos with masses up to 160 GeV can be discovered at HERA.

Extensions to the SM predict additional gauge bosons W' and Z' with masses greater than the conventional W and Z bosons. Therefore, direct production and detection of these new bosons may be beyond the reach of HERA. However, they may be detectable by looking for deviations in the standard electroweak cross-sections due to $Z - Z'$ and $W - W'$ mixing. One example of these new bosons would be the existence of a right-handed W_R' which couple to a right handed neutrino such as the above Majorana neutrino. Possible couplings of these bosons may also lead to the existence of new right-handed fermion states.

New interactions have been proposed called 'contact' interactions which are remnants of a new confining force associated with a further level of fermonic substructure (compositeness). These interactions may be mediated by new massive vector bosons, sometimes referred to as preons, down to scales of 10^{-18} m.

The mass scales (or compositeness) scale for these contact interactions are predicted to be of the order of a few TeV, well beyond the reach of HERA. However, evidence for fermonic substructure can be provided by the direct observation of excited leptonic states, e^*,ν^*, via the decays[8]:

$$\begin{array}{lllll}
e^* & \longrightarrow & e\,\gamma & & \\
e^* & \longrightarrow & \nu\,W & \longrightarrow & \nu\,e\,\nu \\
e^* & \longrightarrow & e\,Z & \longrightarrow & e\,e\,e \\
e^* & \longrightarrow & e\,Z & \longrightarrow & e\,\mu\,\mu \\
e^* & \longrightarrow & e\,Z & \longrightarrow & e\,\nu\,\nu \\
\nu^* & \longrightarrow & \nu\,\gamma & & \\
\nu^* & \longrightarrow & e\,W & \longrightarrow & e\,e\,\nu \\
\nu^* & \longrightarrow & e\,W & \longrightarrow & e\,\mu\,\nu \\
\nu^* & \longrightarrow & e\,Z & \longrightarrow & e\,e\,e
\end{array}$$

---

[8] Excited quark states q^* may also exist although, they may be more difficult to observe experimentally, since the decay particles get 'absorbed' into the DIS hadronic final state.

For simplicity, the gauge boson and final state particle charges are not shown. The accessible mass range for these excited fermions is limited by the cms energy to ≤ 250 GeV.

2.7 Summary

In many ways the physics potential at HERA is unique and will provide a challenging environment to experimental and theoretical physicists. In DIS physics the large x domain domain accessible at HERA will allow detailed tests to be made in the low x region where the standard linear evolution equations (*i.e.* standard perturbative QCD) are expected to break down possibly leading to new QCD effects. The huge increase in the γp cms energy together with the large photoproduction cross-sections will open up a new window for precise photon structure function measurements and QCD tests. Over a longer time scale, as a results of the large Q^2 region available at HERA, the Standard Model will be subject to stringent tests which will include searches for new physics beyond the Standard Model.

Chapter 3

HERA and the H1 Detector

3.1 Introduction to HERA

The HERA machine [32] is the first electron proton collider to be built, accelerating electrons (or positrons) and protons in two independent accelerators (storage rings). It is designed to store 210 bunches of protons up to an energy of 820 GeV and 210 bunches of electrons (or positrons) up to an energy of 30 GeV. The HERA rings are housed in a tunnel of circumference 6.3 km and depth between 15 and 20 m. The electron and proton bunches counter-circulate in their respective storage rings and the two rings are arranged to intersect at four points. At these intersection points, the two bunches (beams) are forced to collide head-on (*i.e.* zero crossing angle between beams) every 96 ns[1] producing a luminosity of $1.5 \times 10^{31}\,\mathrm{cm}^{-2}\,\mathrm{s}^{-1}$. The overall layout of the HERA machine including the pre-accelerators to inject the electron and protons beams into HERA is shown in Figure 3.1. The four interaction regions are shown as the North, South, East and West experimental halls.

In the proton storage ring the proton bunches are accelerated by a series of warm 52 and 208 MHz RF cavities, and they are guided around the ring by 104 superconducting magnet 'cells' of length 47 m. The 52 MHz cavity system accelerates proton bunches of 1.15 m length at an RF voltage of 280 kV, and the 208 MHz system leads to a bunch length of 0.27 m at proton energies of 820 GeV. Each magnet cell

---

[1] This time interval is usually referred to as the *bunch crossing* interval.

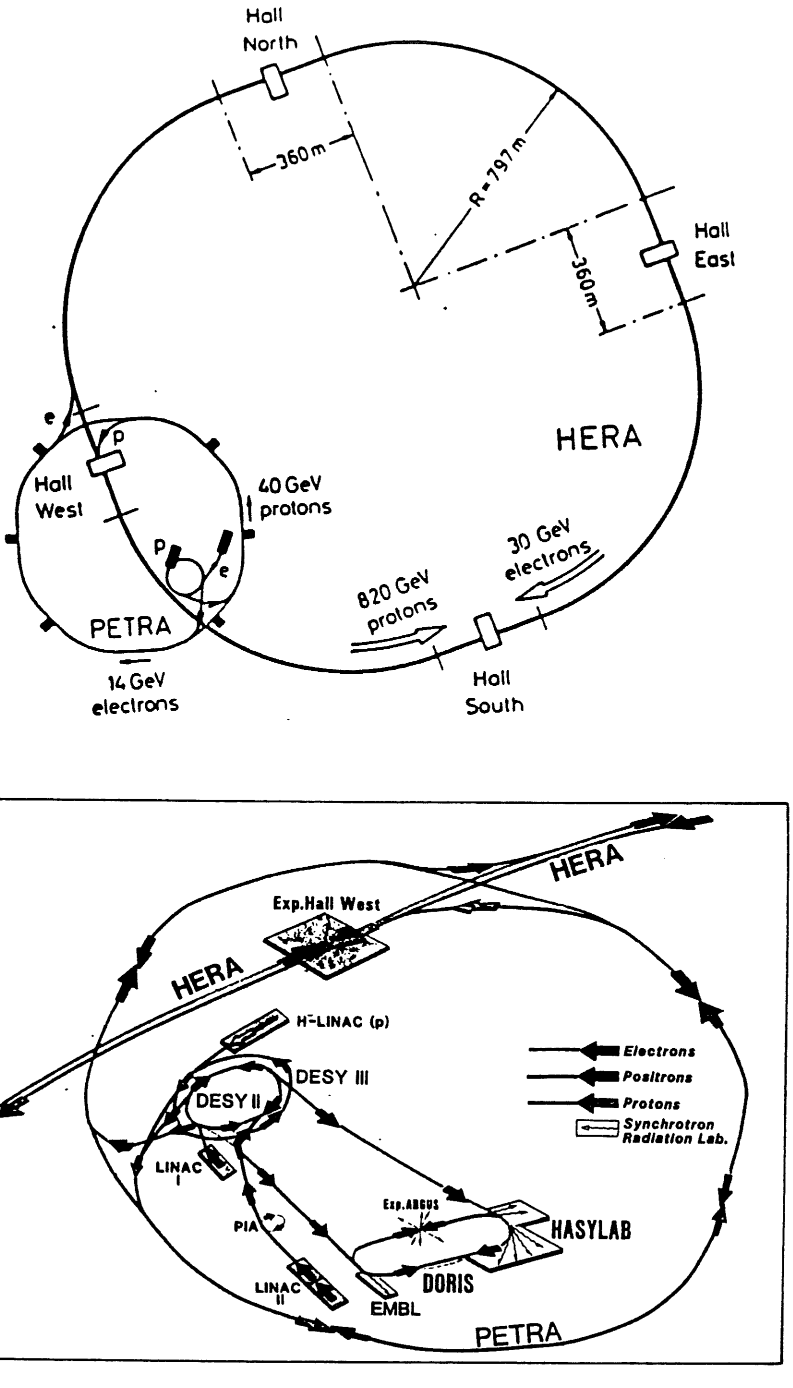

Figure 3.1: The general layout of the HERA accelerator and pre-accelerators. Also shown are the three intersection regions housing the H1, ZEUS and HERMES detectors.

consists of 4 dipole, 2 quadrupole and correction magnets. The dipole magnets are used to bend and guide the proton bunches, whereas the quadrupole and correction magnets are used to focus the proton bunches towards the centre of the beam pipe. A bending field of approximately 4.68 T is achieved with these cells; this large field is necessitated by the large proton energies.

The electron ring consists of 416 conventional, warm, magnet cells of length 12 m, where each cell consists of 1 dipole, 2 quadrupole and 2 sextupole magnets. The bending field of 0.164 T is produced by these warm magnets. Unlike protons, the electrons lose a large fraction of their energy due to synchrotron radiation as they bend around HERA; the energy lost by the electrons per turn is 127 MeV (*cf.* 6.24×10^{-6} MeV for protons). Therefore, in order to compensate for these energy losses a series of 82 warm cavities and 16 superconducting cavities are used in the electron ring. The warm cavities accelerate electrons to about 27 GeV and the superconducting cavities, operating at 500 MHz and a RF voltage of 260 MV, enable the electrons to reach their design energy of 30 GeV.

The long straight sections on either side of the interaction regions allow the electron and proton beams to be brought together. Since the electron (or positron) beams become transversely polarized in the circular sections of HERA, it will be possible to achieve longitudinal polarized (left- or right-handed) beams by a series of magnets preceding and following the interaction region. These magnets have the effect of rotating the electron spin vector to longitudinal and rotate it back to transverse. It is expected that longitudinal polarization of up to 80% may be obtainable [28].

The injection of electrons (positrons) into the main HERA ring is based on the available accelerator complex at DESY. Electrons (positrons) from a 500 MeV linear accelerator are injected into a small storage ring. They are then injected into the DESY II ring where they are accelerated to 7 GeV before they are transferred to the PETRA II ring. Finally, the electrons (positrons) are injected into the HERA main ring.

In order to inject protons into HERA, a new complex of pre-accelerators was built. A 50 MeV linear accelerator is used to produced negatively charged hydrogen ions, which are then stripped of their electrons before the resulting protons are injected into DESY III. Here the protons are accelerated to 7.5 GeV and then transferred to PETRA II, where they are accelerated to 40 GeV before the final injection into the HERA ring.

During the first year of operation, 1992, HERA operated with 10 electron and proton bunches yielding an integrated luminosity of about 33 nb^{-1}; the bunch crossing interval was set at its design value of 96 ns. In this mode of operation, only 9 of the electron and proton were used for 'physics' collisions. The 10th bunch in both beams where separated such that they did not have a colliding partner. These 'pilot' bunches where used to study the proton beam and electron beam induced background.

By the summer of 1993, several improvements where made and HERA was able to operate with 110 bunches. By the end of 1993 it is expected that HERA will have delivered an integrated luminosity around 1 pb^{-1}. As mentioned in Section 2.1 the protons were accelerated to their design energy, whereas, the electrons were accelerated to 26.7 GeV. A detailed account describing the HERA complex together with result from the testing of its main components can be found in [32]. The performance of the HERA machine during the 1992 data runs are summarized in [70].

To detect the collisions between the electron and proton bunches, two detectors, H1 [33, 34] and ZEUS [35], have been built. Referring to Figure 3.1, the H1 detector is suited in the North hall and the ZEUS detector is suited in the South hall. In the East hall there is a third experiment, HERMES [36], currently under construction. HERMES will be used to study the collisions between polarized electron and atomic beams enabling measurements to be made of the polarized nucleon structure functions [37].

3.2 The H1 Detector: General Overview

The H1 detector [33, 34] is a general purpose detector built to study the various physics processes described in Chapter 2. The H1 detector is shown in Figures 3.2 and 3.3, which shows the detector in a cut-away view and a longitudinal view, respectively.

The asymmetric nature of the *ep* collisions is reflected in the overall design of the H1 detector. The detector is densely instrumented in the proton direction to cope with the large particle multiplicities and high energy flow emerging in this direction. The H1 coordinate system is defined such that the z-axis has it's origin at the centre of H1 (which is also the nominal vertex point) and runs along the beam-pipe, with the z co-ordinate increasing in the proton direction. The positive y-axis is vertical and the positive x-axis points towards the centre of the HERA; this is sometimes referred to as a 'right-handed' co-ordinate system.

Tracking of charged particles is carried out in a uniform, axial magnetic field by the central and forward tracking detectors. A superconducting coil together with the iron return yoke provides a uniform field of 1.15 T, varying by less than a few per cent over the central and forward tracker regions. Energy flow measurements are made by the electromagnetic and hadronic liquid argon calorimeters, the (hadronic) plug calorimeter and the backward electromagnetic calorimeter. Muon identification is performed by the forward muon detector and the instrumented iron which also acts as a secondary hadronic calorimeter. In the backward region, the time-of-flight device and the scintillator walls, shown in Figure 3.3 are used to reject background events coming from beam-gas and beam-wall interactions. To maintain beam stability a superconducting compensation magnet is used to provide a magnetic field along the beam axis which is equal and opposite to that of the main H1 magnet. The net effect is that there is a zero integrated field along the beam axis.

In the forthcoming sections, the above components of the H1 detector are briefly described. All descriptions are taken from the H1 detector reports [33, 34] unless otherwise stated.

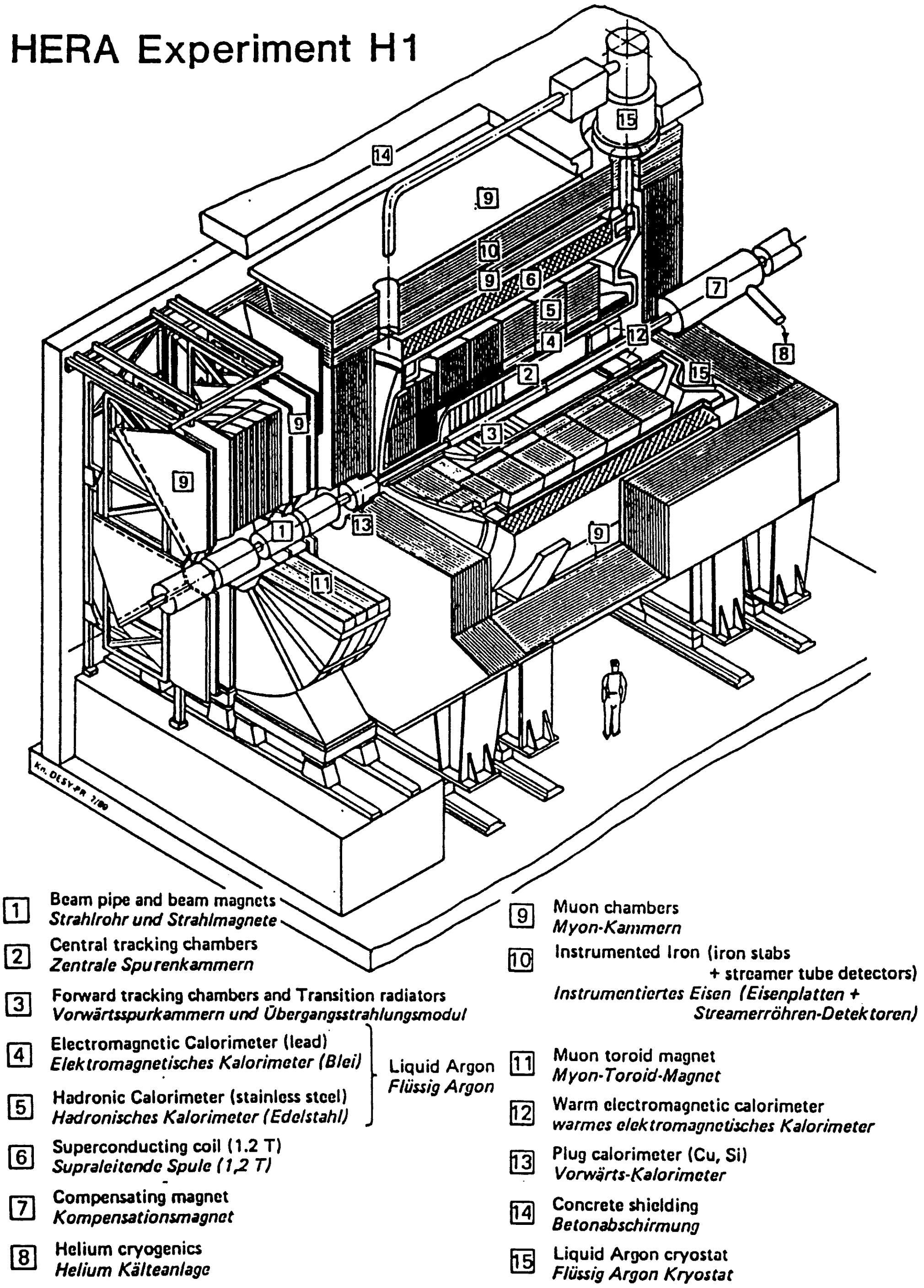

Figure 3.2: A perspective view of the H1 detector.

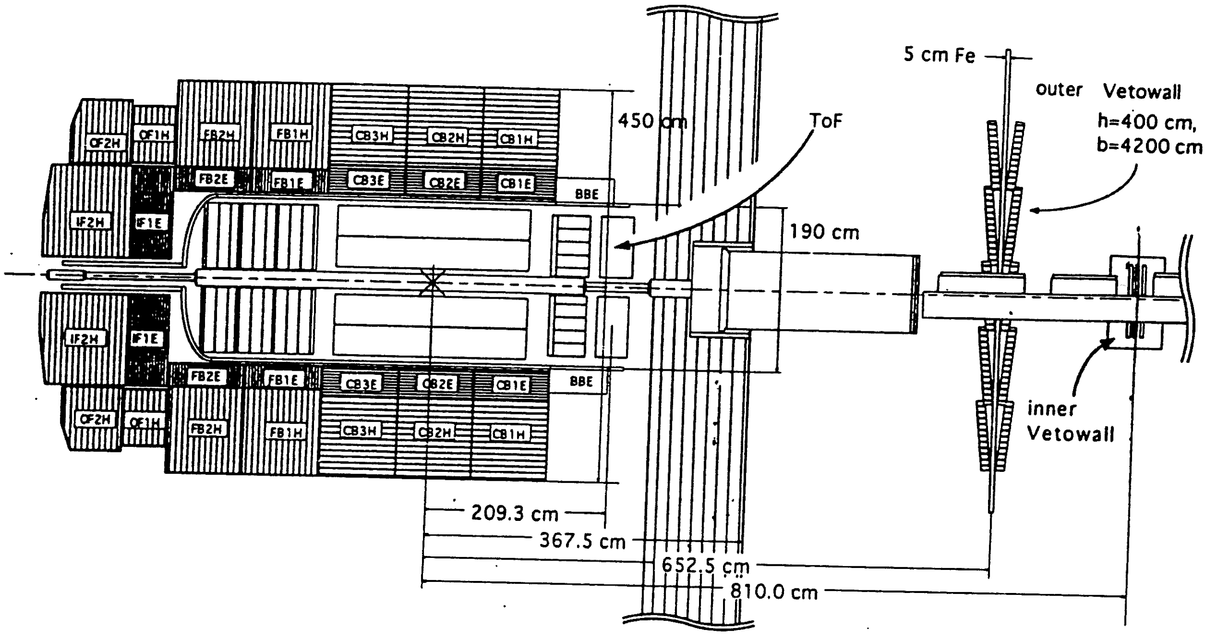

Figure 3.3: A longitudinal view of the H1 detector also showing the position of the scintillator walls.

3.3 Calorimetery: Introduction

Calorimeters measure the energy of incident particles by inducing a shower of particles in some 'absorber' material and detecting the shower development in an active medium. Shower particles lose their energy via ionisation or excitation in the active medium, and by measuring the amount of ionisation in the active medium the energy of the incident particle can be determined.

The H1 detector uses a class of calorimeters which measure the total energy of the shower (incident particle) by periodically sampling the development of the shower; these calorimeters are usually referred to as *sampling* calorimeters. The liquid argon, plug and backward electromagnetic calorimeters are all sampling calorimeters. The advantage of this measurement technique is that they allow good determination of the longitudinal and transverse profiles of the showers, which can be used to identify electrons, photons and pions.

In electromagnetic calorimeters, energetic photons and electrons (positrons) produce a shower of lower energy photons and electrons, via the Bremsstrahlung and pair production processes, on their interactions with the absorber material. An important quantity which is used in the design of electromagnetic calorimeters is the radiation length, X_o. This quantity represents the mean longitudinal length over which a electron loses all but $\frac{1}{e}$ of its energy [2, 7].

In hadronic calorimeters, hadronic showers occur through inelastic nuclear collisions producing lower energy hadrons which take part in further inelastic collisions. Another important characteristic of hadronic showers is that they take longer to develop than electromagnetic ones (with the same incident energy) and so hadronic calorimeters must be deeper than electromagnetic calorimeters. The scale for the longitudinal development of hadronic showers is given by nuclear interaction, or absorption, length, λ_I.

3.3.1 The Liquid Argon Calorimeter

The liquid argon (LAr) calorimeter covers a polar angle ranging between 4^o and 154^o, thus providing energy flow measurements over a wide kinematic region. The angular acceptance of the electromagnetic part (EMC) of calorimeter is slightly greater, in the backward region, than that the hadronic part (HAC). To gain easy access to the tracking detectors, the LAr calorimeter is not installed in the backward region.

The LAr calorimeter is situated inside the large superconducting coil to minimize both the amount of dead material in front of the EMC and the overall size and weight of the calorimeter.

The LAr calorimeter is a *non-compensating* calorimeter since the energy response for hadrons is 30% less than that for electrons of the same energy [34]. The two main reasons for non-compensation are:

- The energy deposit of hadronic showers consist of a prompt electromagnetic component due to π^o production[2] and a slower due to low energy

---

[2] π^o's are predominantly produced in the first nuclear interaction and then rapidly decay into two γ's.

hadronic activity. These energy depositions are converted to electrical signals with different efficiencies. The energy response also varies depending on the ratio of neutral pions to charged pions which fluctuates on an event-by-event basis.

- A large fraction of the incident hadronic energy is lost due to the breakup and excitation of nuclei which do not give detectable signals.

To achieve accurate energy measurements the LAr calorimeter must compensate for the non-uniformity in the energy responses. This is done at the reconstruction level where the measured cell energies are weighted according to the shape of the energy deposit and fraction of the energy observed in the EMC and HAC. This weighting procedure is non-trivial and will not be discussed further. A detailed account describing the whole energy reconstruction procedure is given in [34, 38].

The longitudinal segmentation of the calorimeter can be seen in Figure 3.3. The radial segmentation is shown in Figure 3.4. The calorimeter is longitudinally segmented into eight wheels labelled IF, OF, FB1, FB2, CB1, CB2, CB3 and BBE; the BBE wheel forms part of the EMC, it does not contain any hadronic calorimetery. As shown in the radial view, each wheel is further segmented into eight stacks (octants). The cracks between the stacks of the LAr calorimeter are classified as ϕ cracks. These ϕ cracks in the EMC point towards the interaction point (IP). In the HAC the ϕ cracks point away from the IP, in order to minimise the energy lost between cracks.

In the EMC stacks, each sampling cell consists of 2.4mm lead as the absorber material and a 2.35 mm gap filled with liquid argon as the active medium. In each gap there is one readout plane with pads and one high voltage plane. The size of the signal measured from the readout plane is proportional to energy lost by the shower in that cell[3]. The HAC sampling cells consist of a total of 19mm of stainless steel absorber plates and a double gap of 2.4 mm of active medium. In the centre of the double gap there is a plane of readout board with pads on both sides, to collect

---

[3] The particle energy is determined from a sum of cell energies.

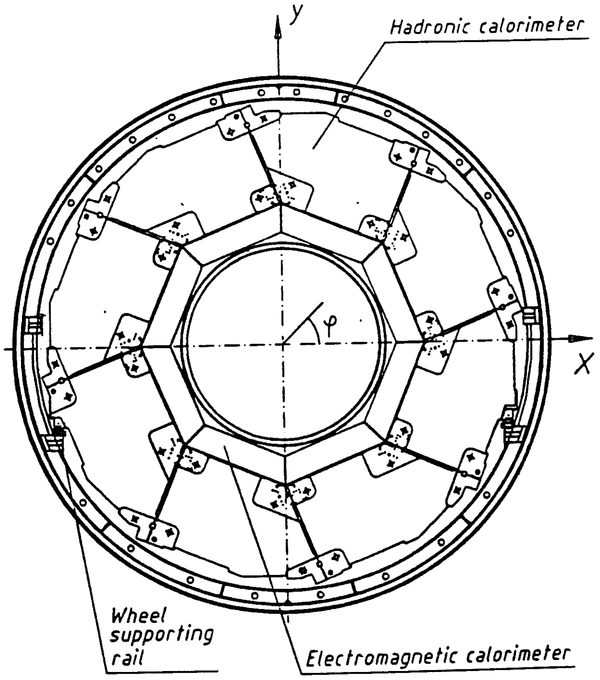

Figure 3.4: Radial view of a single wheel of the LAr calorimeter.

the charges deposited in the gaps. The high voltage planes are glued to the inner surface of the stainless steel plates. The high voltage planes used in the EMC and HAC provide an electric field of 625 Vmm^{-1}.

The size (depth) of the EMC and HAC are optimized to fully contain electromagnetic and hadronic showers, respectively. In addition, the depth of the EMC must be typically less than $1\lambda_I$ such that only a small fraction of hadronic energy is seen in the EMC. The total thickness of the EMC varies between $20X_o$ and $30X_o$. The depth of the whole LAr calorimeter varies between $5\lambda_I$ and $8\lambda_I$.

The LAr calorimeter contains a total of 45000 sampling cells, thus providing fine granularity for shower discrimination. This allows electromagnetic and hadronic showers to be identified by their different shapes, and so the correct energy weighting procedures can be applied to compensate for the different EMC and HAC responses. Also, the fine granularity will be important for particle identification, particularly for high Q^2 and exotic interactions where the electron (or positron) scatters into the LAr calorimeter. Electron identification in this calorimeter is presented in Chapter 4.

The energy resolution, $\frac{\sigma_E}{E}$, of the LAr calorimeter can be parameterised as:

$$\frac{\sigma_E}{E} = \frac{c_1}{E} \oplus \frac{c_2}{\sqrt{E}} + c_3$$

where c_2 represents the contribution from sampling fluctuations, c_1 the noise term and c_3 accounts for systematics and dispersion of the incident particle momenta.

From test beam data using energetic electrons and pions and the early H1 data (including cosmic ray runs) the above energy resolution parameters were determined as:

- $c_1 = 154\,MeV$, $c_2 = 11\%\sqrt{\mathrm{E}}$ and $c_3 = 0.6\%$ for electrons.
- $c_1 = 0.9\,GeV$, $c_2 = (50.70 \pm 0.1)\%\sqrt{\mathrm{E}}$ and $c_3 = 1.6 \pm 0.1\%$ for pions.

During the 1992 data runs the electromagnetic energy scale was subject to a 2-3% calibration uncertainty, whilst the hadronic energy scale had a 7% calibration energy[4].

A more detailed description covering all aspects of the LAr calorimeter electronic systems, cryostat and energy calibration tests can be found in [38].

3.3.2 The Backward Electromagnetic Calorimeter

The backward electromagnetic calorimeter (BEMC) has a polar angle coverage in the range $151^\circ < \theta < 177^\circ$, and is primarily used to measure the scattered electron in low Q^2 ($Q^2 < 100\,\mathrm{GeV}^2$) DIS interactions. It also has to contribute to measurements of hadronic emerging from low x/low y DIS events and photoproduction processes.

The BEMC is a lead-scintillator sampling calorimeter in which the showers produced in the lead plates cause ionisation of atoms in the scintillating material. These scintillator mediums are doped with activator centres which recombine with the liberated electrons and positive ions. These recombination processes leave the activator centres in excited states which emits light upon its return to the ground state. Detection of the light signals allow the energy of the incident particle to be determined.

The BEMC consists of 88 calorimeter stacks (cells) mounted in an aluminium barrel with a diameter of 162 cm, as shown in Figure 3.5(a). These stacks are aligned

---

[4] At the time of writing, this hadronic uncertainty was lowered to 5% as a result of more data being available for calibration studies [39].

parallel to the beam pipe and 56 of these stacks have a quadratic cross-section, the others being triangular or trapezoidal in order to fill the circular barrel.

The stacks are multilayer lead-scintillator sandwich structures with 50 active sampling layers of plastic scintillator of 4 mm thickness. The active layers are longitudinally interleaved with 49 layers of 2.5 mm lead. The entire stack corresponds to $22.5X_o$ or $0.97\lambda_I$. The light signals are carried by wavelength shifter (WLS) bars which run along the side of the stacks. Two pairs of 8 cm wide bars cover two opposite sides of a square stack extending over the full active length. The remaining two sides are covered with 16 cm wide which cover over the last 15 sampling layers, thus, giving separate access to the tails of the showers; this correspond to $6.5X_o$. The longitudinal structure of a quadratic stack is shown in Figure 3.5(b).

The lighted emitted in the wavelength shifter bars is then detected by photodiodes. Each long bar is equipped with one diode which provides one readout channel. The short bars are connected to two diodes, due to their double width, but the pair of diodes are connected to one readout channel. Special arrangements of wavelength shifters are made for the non-quadratic stacks. This is described in [53]. In total there are 472 readout channels in the BEMC.

From test beam data, the BEMC resolution due to sampling fluctuations was determined to be $10\%/\sqrt{E}$. The average noise per stack was measured to be 150 MeV implying that for an electron shower the noise contribution to the measured energy is about 450 MeV [34, 59]. The energy resolution is further affected by stack to stack intercalibration estimated to be around 4%. Thus, for an electron the BEMC resolution can be expressed as:

$$\frac{\sigma_E}{E} = \frac{\sigma_{noise}}{E} \oplus \frac{\sigma_{sampling}}{\sqrt{E}} \oplus \sigma_{const}$$

where $\sigma_{noise} = 0.45$ GeV, $\sigma_{sampling} = 0.1\ \mathrm{GeV}^{\frac{1}{2}}$ and $\sigma_{const} = 0.04$.

In addition, the BEMC resolution is subject to a calibration uncertainty of 2-3%. The energy calibration can be checked by comparing the measured (scattered) electron energy with the derived energy using the angle of the electron and the angle of the momentum vector of the hadronic final state [40]. The reconstructed position

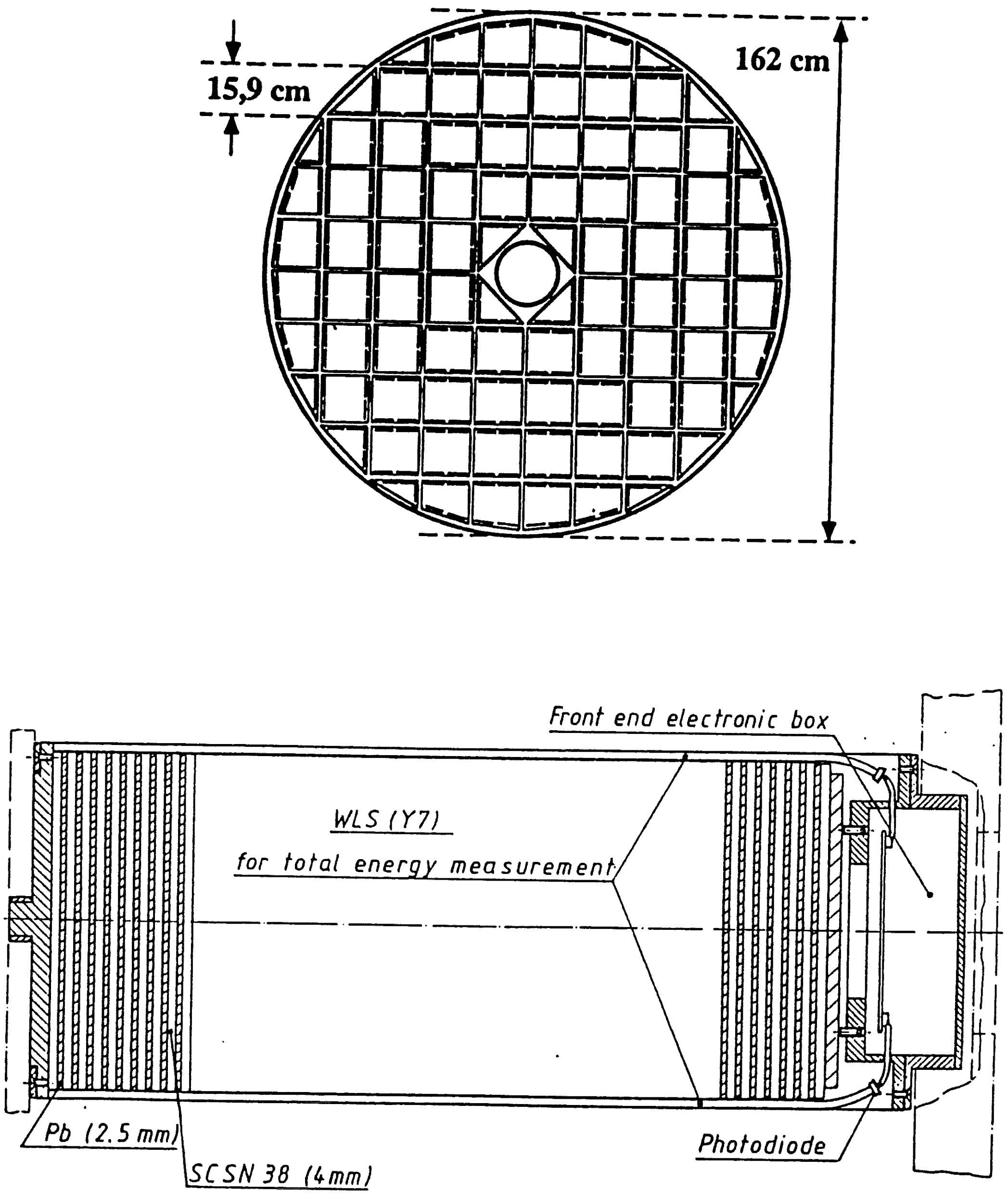

Figure 3.5: Transverse view of the BEMC (a), and a side view of a quadratic stack (b). The label SCSN 38 refers to the type of plastic scintillator used in the BEMC.

resolution for electrons has been measured to be 1.3 cm.

Since the BEMC corresponds to only 0.97 interaction lengths, about 30% of all hadrons do not interact in the BEMC, or they give very low signals which is not detectable above noise. The hadrons which do interact typically deposit about 30% of their energy in the BEMC. By combining energy measurements in the BEMC and the instrumented iron, a hadronic energy resolution of about $80\%/\sqrt{E}$ is determined from detailed simulation studies.

3.3.3 The Plug Calorimeter

The plug calorimeter is designed to fill the gap between the LAr calorimeter and the beam pipe, thus increasing the acceptance for energy flow measurements; it covers an angular range $0.6^\circ < \theta < 3^\circ$. This is very important for CC interactions where the event kinematics can only be determined from the measured hadronic final state. The plug consists of 9 layers of copper (absorber) interspersed with 8 layers of silicon detectors. The depth of the plug is roughly $4.3\lambda_I$. The showers produced in the copper produce electron-hole pairs in the silicon which are collected to give the signal.

Due to the lack of lateral and longitudinal shower containment and coarse sampling the hadronic energy resolution of the plug has been measured as $150\%/\sqrt{E}$. During the 1992 data run only four of the silicon readout plane were installed. Due to this lack of instrumentation the plug calorimeter data is not used in any part of the physics analysis presented in this thesis and will not be considered further.

3.3.4 The Instrumented Iron

As outlined in Section 3.2, one of the uses of the iron return yoke is to measure the hadronic energy flow leaking out of the LAr calorimeter, hence it is usually termed the (hadronic) tail catcher. It is also used for hadronic detection in the backward region, behind the BEMC. In order to meet these requirements the iron yoke is instrumented with streamer tubes and readout pads, placed in the gaps between alternate layers of iron.

These streamer tubes and readout pads are orientated along the beam axis in the barrel region ($25^o < \theta < 130^o$) and vertically in the forward and backward regions. The tail catcher covers the angular region $5^o < \theta < 175^o$ and has a depth of about $4.5\lambda_I$. Figure 3.6 shows the arrangement of streamer tube and readout pads in the iron yoke. Out of the 16 layers of streamer tubes, 11 are equipped with readout pads varying in size from 30 cm × 30 cm in the endcaps to 50 cm × 40 cm in the barrel region. The pad signals from the five inner and six outer layers are summed to form inner and outer towers, which give a two-fold segmentation to the hadronic energy measurements. The tail catcher hadronic energy resolution has been measured as $150\%/\sqrt{E}$.

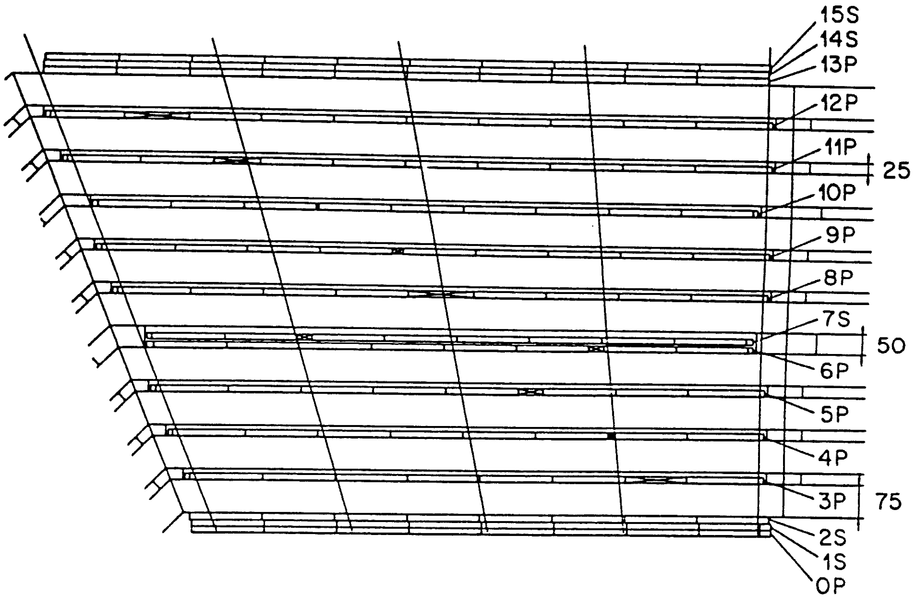

Figure 3.6: Arrangement of the streamer tubes, readout pads (P) and strips (S) in the barrel region. The point structure of the pads is also shown. The crossed elements represent dummy modules which are inserted to ensure that the dead areas are not aligned for tracks from the interaction region.

In addition to the hadronic calorimetery, the iron is also used as a muon detector. Referring to Figure 3.6, muon detection is provided by the muon boxes situated at the inner and outer radius of the iron yoke. These boxes consists of three readout layers; two strip layers with strips running perpendicular to the streamer tube wire direction and one pad layer. The forth gap in the iron yoke is twice the width of the other gaps and contains two chamber layers (one strip and one pad). Using the wire signals, the position resolution for muons was measured to be 3-4 mm, the resolutions obtained from strip hits is 10-15 mm in the perpendicular coordinate. A spatial resolution of 10 cm is obtained from the pads.

3.3.5 The Electron and Photon taggers

The H1 luminosity consists of two calorimeters (counters), an electron tagger (ET) and photon detector (PD), situated at $z = -33$m and $z = -103$ m, respectively. The two counters are placed close to the beamline in order to detect particles with very small scattering angles from the interaction point. The luminosity system is shown in Figure 3.7 [34].

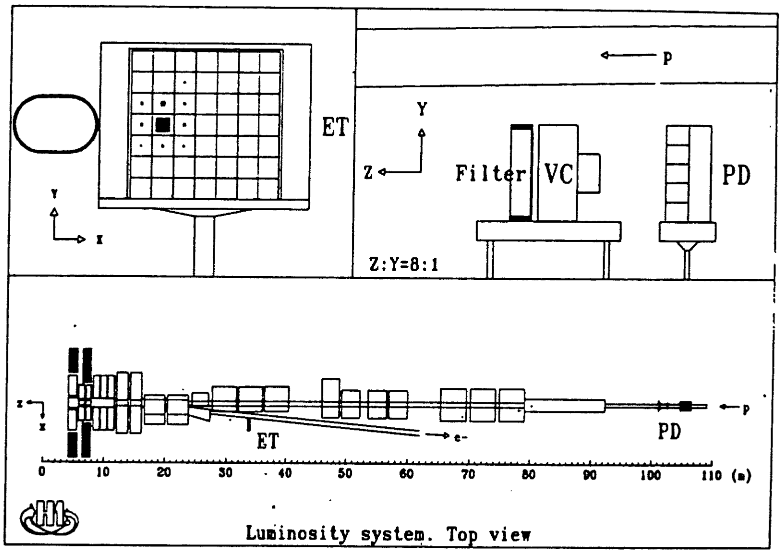

Figure 3.7: The layout of the H1 luminosity monitoring system.

The luminosity is determined from the rate of the Bethe-Heitler events $ep \to ep\gamma$, which have a large and precisely calculated cross-section. The luminosity monitor detects the outgoing electron and photons by requiring a coincidence between the two counters. The scattered electrons are deflected by a set of warm quadrupoles and a bending magnet located in the region $-5.8\,\mathrm{m} < z < -23.8\,\mathrm{m}$, such that they pass an exit window at $z = -27.3\,\mathrm{m}$ and hit the electron tagger. The bremsstrahlung photons leave the proton beam pipe at $z = -92.3\,\mathrm{m}$ (photon exit window), and hit the photon tagger.

The PD is protected from the high flux of synchrotron radiation by a lead filter ($2X_o$) and a water Čerenkov counter ($1X_o$) located in front of the photon detector. The water counter can also be used to select events where the photon passes through the filter without interacting.

Both of the counters are total absorption Čerenkov calorimeters made from an array of crystals (composition 78% TlCl and 22% TlBr) 20 cm long ($22X_o$). The energy resolution of both counters has been measured as $10\%/\sqrt{E} \oplus 1$ (E in GeV). The position resolution has been measured as 0.3 mm for the electron and 1.2 mm for the photon.

The visible cross-section for the above Bethe-Heitler processes is about 28 mb (174 mb) in the ET (PD), corresponding to a rate of about 0.4 MHz (1.3 MHz) at design luminosity. Since the two counters are used in coincidence, the rate of events seen by the luminosity monitor is 0.4 MHz. Background processes arise mainly from Bremsstrahlung interactions of electrons with gas-particles in the beam pipe and synchrotron radiation. These background processes can be estimated by using the electron pilot bunches, such that luminosity can be corrected accordingly.

The largest contribution to the systematic error in the absolute luminosity measurement comes from the uncertainty in acceptance, which is presently around 5.5%. Other contributions come from cross-section, background, calibration and trigger efficiency uncertainties. The total systematic error in the luminosity is 7%, although it is expected to be reduced to 4% in the future.

3.4 The Time-of-Flight Device and the Veto Walls

The time-of-flight (TOF) device is situated behind the BEMC at $z \simeq -2\,\mathrm{m}$ and it is used to provide timing information for the level 1 trigger in order to reject proton induced background events. The TOF consists of two scintillator walls each of which consist of a 3 cm layer of plastic scintillator sandwiched between 6.5 mm thick lead layers ($1.1X_o$). This lead is used to protect the scintillator from synchrotron radiation and to limit the number of triggers from this background. The TOF is readout by a total of 24 photomultiplier tubes.

The TOF measures the time of particles passing through it wrt. the bunch crossing time. From these time signals the TOF is able to distinguish genuine events from proton induced background events. The total time taking by the TOF to produce a trigger signal after a particle pass through it is 250 ns. The device as a whole has a resolution of 4 ns, while individual counters have a resolution around 2 ns [34].

As shown in Figure 3.3 two double scintillator veto walls are installed at $z = -6.5$ m (large veto wall) and $z = -8.1$ m (small veto wall), respectively. The larger (outer) veto wall covers a region approximately equal to the iron endcap, and has a time resolution of 8 ns. The smaller (inner) veto wall covers the region near the beam pipe down to a radius of 11 cm and has a resolution of 3 ns. These veto walls are used to identify upstream proton induced background events.

3.5 Tracking: Introduction

To compliment the energy flow measurements in the H1 detector, tracking detectors are used to give information on jets with high particle multiplicities and for particle identification. In addition, the reconstruction of particles allow accurate determination of primary and secondary interaction vertices. Tracking detectors are also extensively used for triggering, where their good timing and positional resolutions make them ideal for removing background events.

The H1 tracking system is divided into two very different tracking detectors, the

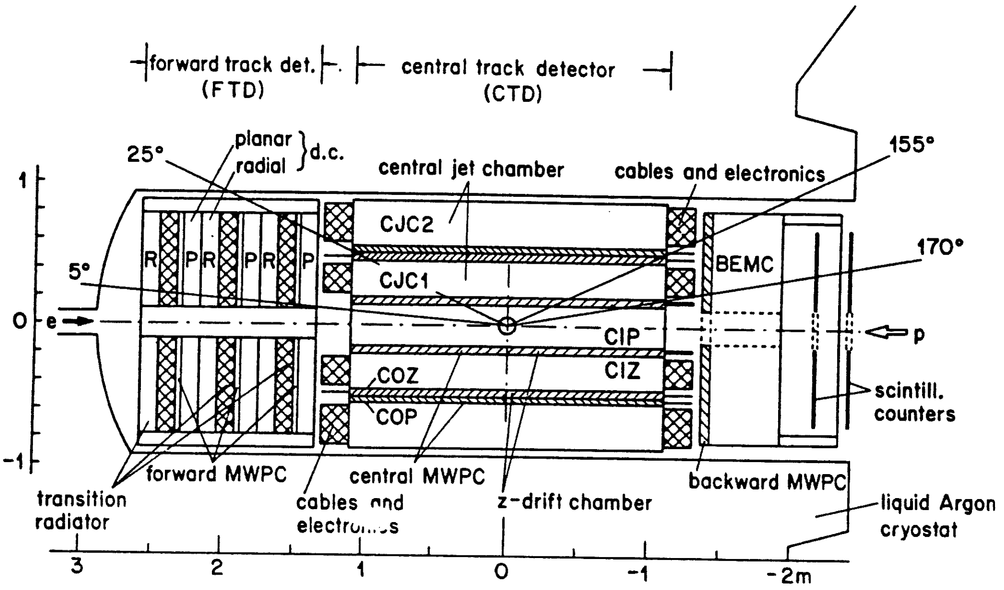

Figure 3.8: The H1 tracking system ($r - z$ view).

central tracking detector (CTD) and the forward tracking detector (FTD). Both of these detectors consist of drift chambers and multiwire proportional chambers. The tracking system is shown in Figure 3.8.

The drift chambers are used to give accurate information of charge particle trajectories from which the particle momenta can be reconstructed. The chambers contain anode (sense) and cathode wires which are used to set up a uniform drift field. As a particle traverses the gas of the tracking chamber, it causes ionization along it's path. The resulting positive ions drift towards a cathode and as the electrons drift towards the sense wire they experience a stronger electric field. This results in an avalanche of ion pairs which induce a detectable signal on the sense wires. By periodically sampling the two ends of an anode wire, the size of the pulses observed together with timing information allows the position of particle along the wire to determined.

Proportional chambers are made up of very finely spaced wires, such that a particle passing through the chamber experiences a high electric field near a anode region, irrespective of the particle's trajectory. Due to the shorter distance between anode wires the signals (pulses) are detected very quickly. The time resolution for such chambers can be of the order of tens of nanoseconds, thus providing fast triggering information [41].

3.5.1 The Central Tracking Detector

The CTD covers the angular region $25^o < \theta < 160^o$, and consists of two concentric drift (jet) chambers CJC1 and CJC2 (see Figure 3.8) which are interleaved with two planes of thin drift chambers, the central inner (CIZ) and central outer (COZ) z-chambers and two multiwire proportional chambers (CIP,COP). The jet and z-chambers are used for track reconstruction. The transverse layout of the CTD is shown in Figure 3.9.

The inner (CIP) and outer (COP) proportional chambers provide fast space point information for the Level 1 trigger. Combination of CIP and COP hits are used to trigger on tracks coming from a nominal interaction vertex. Both chambers consist of concentric double layers of chambers which are readout from cathode pads. The CIP is readout using 60 pads of length 36.6 mm in z and 8 pads in ϕ. The wires run parallel to the beam direction with 480 wires in each layer. The time resolution of the CIP was measured to be 21 ns. The COP has an inner layer with 1574 wires and an outer layer with 1615 wires. The COP has 16 pads in ϕ and 18 pads in z of length 120 mm. The time resolution of the COP was measured as 40 ns.

The two central jet chambers, CJC1 an CJC2, are similar in design with the sense wires of length 2.2 m strung parallel to the beam axis. Sampling at both ends of the sense wires provided good measurement of the position of tracks in the $r - \phi$ coordinates. Using charge division, a moderate z position measurement can be achieved.

CJC1 (CJC2) is split into 30 (60) cells in ϕ, with each cell containing a plane of 24 (34) sense wires with adjacent sense wires separated by two potential wires. The plane of wires are staggered at an angle of 30^o wrt. the radial coordinate, as shown in Figure 3.9. This arrangement ensures that the (ionisation) electrons drift perpendicular to the radial direction, thus providing optimum track momentum

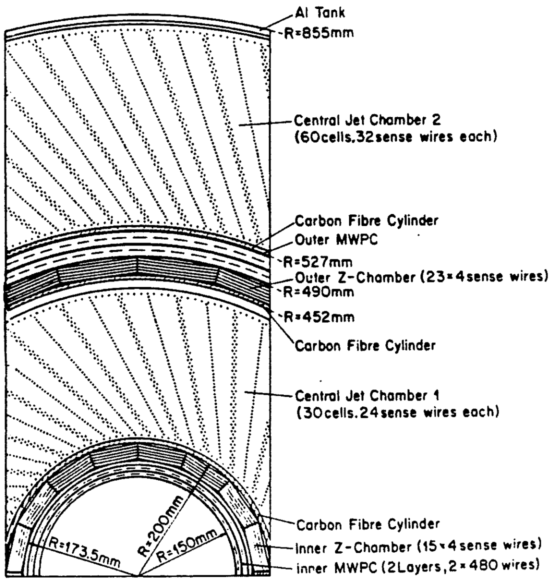

Figure 3.9: Radial view of the H1 central tracking detector.

resolution. Each cell is azimuthally limited by two cathode wire planes, and at the inner and outer radius by the field wires. The field wires ensure that the drift field remains almost uniform at the two ends of a cell. This inclination of the sense wires means that tracks with a $p_\perp$ greater than 100 MeV will always cross more than one wire plane. By connecting track segments of different cells minimises the resolution due to drift ambiguities[5]. The resolution of the two jet chambers has been measured as 170 μm in the $r - \phi$ plane and 2.2 cm in z. The design of the two chambers also allows a measurement of dE/dx, the specific energy loss, which is used for particle identification. During the 1992 run, the dE/dx resolution was measured at 10%.

The z chambers CIZ and COZ are used to complement the CJC by providing accurate z coordinate measurements, using sense wires which are strung around (*i.e.* perpendicular to) the beam axis, and a moderate ϕ measurements; the wires are readout at both end. Each sense wire in the CIZ (COZ) forms a 16 (24) sided polygon in the $r - \phi$ plane. The CIZ is divided into 15 cells in the z direction where

---

[5] Drift ambiguities arise because it is not possible, from the wire signals, to determine which side of the wire the particle passed.

each cell is made up of 4 sense wires and 3 potential wires. The COZ is divided into 24 cells where each cell consists of 4 sense wires and 6 potential wires. For each cell the 4 sense wires are separated in the radial plane. The resolution in the z coordinate determination was measured as 330 μm for the CIZ and 200 μm for the COZ. The ϕ resolutions was measured as 2.4% of the wire length for the CIZ, with an average length of 1120 mm. The corresponding COZ resolution was measured as 2% of the wire length, the COZ wires having an average length of 2970 mm.

During the 1992 and 1993 data runs, the efficiency (and acceptance) of CJC1 was degraded by the presence of dead wires due to mechanical faults. As a result of these dead wires up to 20% of the CJC1 was unable to output any signals. For more details on the performance of the CTD during the 1992 data runs and the gas mixtures used by the detectors see [34].

3.5.2 The Forward Tracking Detector

The FTD is designed to measure tracks in the forward region defined by $5^o < \theta < 30^o$. It consists of three 'supermodules', each of which is made up of a planar drift chamber, a multiwire proportional chamber (FWPC), a transition radiator and a radial drift chamber. The ordering of these chambers along the z-axis is shown in Figure 3.8.

The planar chambers are constructed from three layers of drift chambers, with the wires in each layer being parallel to each (perpendicular to the z-axis) and each layer is rotated by 60^o, in azimuth, from the previous layer. This angular ordering of the layers allows accurate determination of the x-y coordinates of the forward tracks, enabling central and forward tracks to be linked together. Each drift chamber layer contains 32 drift cells, of rectangular cross-section, containing four sense wires surrounded by four field wires on a 6 mm square matrix along the z-axis. The spatial resolution of the planar chambers has been measured as 150 μm.

In the radial chambers the wires are strung radially outwards where each chamber is azimuthally segmented into 48 drift cells. Each cell consists of 12 sense wires (separated in z by 10 mm) staggered alternately 287 μm each side of a plane which bisects the drift cell. Between adjacent sense wires, field wires are placed on this plane parallel to the sense wires. The resolution acheived in 1992 was 180-200 μm in the drift direction (ϕ). By sampling the pulses at both ends of a sense wire the radial coordinate can be determined with a resolution of 3 cm.

The FWPC's consist of two planes of wires interleaved with three cathode planes. The cathode pads are radially segmented into 20 rings and azimuthally segmented into sections covering 25^o except for the four outer rings where the pads cover 45^o. The pads have a radial width which increases with radius in a geometrical progression between 10 and 37 mm. The FWPC's provide fast track information which is useful for triggering purposes. For tracks crossing all at least two of the supermodules a timing resolution of 20 ns was measured, well below the required separation of two bunches.

The transition radiators (TR) are passive units producing X-rays when a electron passes through the TR which are an array of 400 polypropylene layers. These X-rays can then be detected in the radial chambers with signals greater for electrons than for pions, thus enabling particles to be discriminated. Tests using beams of pions and electrons have shown that a 90% electron acceptance can be acheived with less than 10% pion contamination, for energies up to 80 GeV. This will be of particular importance for leptoquark searches where the final state electron can emerge in the forward direction.

During the 1992 data run, the pattern recognition and reconstruction of the FTD was poor. For this reason the FTD data is not used in the analysis presented in this thesis. This situation has been remedied for the 1993 run. A more detailed account covering all aspects of the FTD can be found in [34].

3.5.3 The Backward Proportional Chamber

The backward multiwire proportional chamber (BPC) is used to provided accurate spatial determination for charged tracks in the region $155^o < \theta < 175^o$. The BPC is equipped with five cathode planes and four anode wire planes, where wire planes are orientated at 45^o relative to one another. In each plane the wires are parallel and seperated by 2.5 mm. The BPC is the only proportional chamber of H1 in which the cathode pads are not segmented and the anodes read out. The space points given by the BPC contribute approximately 0.5 mradians to the angular resolution, of the same order of the multiple scattering in the material in front of the it.

3.6 The Forward Muon Detector

The forward muon detector (FMD) is designed to measure high energy muons greater than 5 GeV/c in the angular range $3^o < \theta < 17^o$. This momentum cut ensures that the muon pass through iron toroid, although, the FMD will be able to measure muons with lower momentum. The FMD consists of three double layer drift chambers on either side of the toroid magnet, and is situated forward of the iron endcap; it is not affected by the axial field of the H1 magnet.

Each layer of drift chambers are made up of a number of drift cells of rectangular cross-section with the sense wires in the centre of each cell. All the drift cells have a depth of 2 cm, a width of 12 cm and length between 40 cm and 240 cm. The maximum drift distance in any cell is 6 cm. In two of the double layers (before and after the toroid) the drift cells are arranged such that the planes essentially measure the polar angle of the muon from which the muon momentum can be determined from the bending of the muon in the toroidal field. The field varies with radius, from 1.75 T at radius 0.65 m and 1.5 T at radius 2.90 m. The remaining double layer measures the azimuthal angle of the muon. In these double layers, each layer is staggered by half a cell width which enables the resolution of drift ambiguities. The total number of drift cells in the FMD is 1520 and the expected muon momentum resolution at 5 GeV/c is 24% and deteriorates slowly to 36% at 200 GeV/c. For more details see [34].

3.7 Triggering and Data Acquisition

The H1 trigger system is designed to distinguish genuine electron-proton events from the high rate of beam induced background processes. To cope with the large bunch crossing rates the H1 trigger system is 'pipe-lined'. The output signals from the H1 subdetectors are fed into front-end digitising units where they are stored (pipe-lined). The output signals from the subdetectors are also fed to the subdetector trigger where they are converted into 'trigger elements'.

These trigger elements are sent to the central trigger logic where they are collected and combined to provide the 'level 1' (L1) and 'level 2' (L2) triggers. The L1 trigger consists of nine different trigger elements and if the central trigger logic decides that the event is worth keeping it sends out an 'L1keep' signal which freezes all the detector output that is stored in the front-end pipelines; *i.e.* the detector is now disabled. The L1 trigger decision is usually made 24 beam crossings (2.5 μs) after the interactions took place. Thus, at any one time the front-end pipelines contain detector signals from the previous 24 beam crossing, which minimise the amount of 'dead time' spent by the detector waiting for trigger descision.

The L1 trigger takes the nine trigger elements and combines them to form 'sub-triggers' which can then be used to select possible physics interactions or be used to select events useful for detector studies, *e.g.* cosmic ray events for tracking and calorimeter calibration.

The L2 trigger is used to decide quickly whether the event should be kept or rejected. It analyses the event in more detail and produces a decision within 20 μs after the L1keep signal. If the event is kept then all the detector output data is read from the pipelines, otherwise the detector is re-enabled. These output signals are then passed onto the 'level 3' (L3) trigger which makes a more complex study based on event topologies and produces a descision after a few hundred μs. If the L3 accepts the event, the detector output is sent to the central data acquisition system so that a 'level 4' (L4) decision can be made.

In H1 data acquisition (DAQ) system information is read out in parallel from each subdetector system before being combined into a full event record by the event builder; these full events are passed onto the L4 trigger. Data compression is carried out online to reduce the large volume of raw data (roughly 3 Mbytes) down to event sizes ranging between 50 an 100 Kbytes.

The L4 trigger performs a simplified version of the full event reconstruction online to provide powerful discrimination on the basis of the event topology and physic classes. The accepted L4 events are then stored onto tape where they are fully reconstructed and put onto output tapes. From the original L1keep signal roughly 1 ms elapses before all the data is available to the L4 trigger after which the detector is re-enabled.

It should be noted that during the 1992 data run the H1 trigger system did not include the L2 and L3 triggers. Since the maximum rate for sending events to the DAQ is about 50 Hz, the absence of L2 and L3 meant that the L1 trigger could only accept events up to 50 Hz. Due to the low luminosity delivered in 1992, this condition was satisfied, with events being output onto tape at a rate of 8 Hz. The important L1 trigger elements used by the central trigger logic can be found in [34].

3.8 The H1 Software Chain

Once an event has passed the L4 trigger it is fully reconstructed by the H1 reconstruction software [42] H1REC. These reconstructed events are then put onto 'production output' (POT) tapes. The POT data still contain a large fraction of background events which passed the online triggers and so further event reduction is done by running software algorithm which look for certain event characteristics depending on the type of physics processes of interest. Events which pass the offline selections are assigned a (physics) class number (see Section 5.2) and are put onto data summary tapes (DST). This level of data setection is sometimes referred to as 'level 5' (L5).

The physics analysis package H1PHAN [51] uses the reconstructed data from simulated data or real data (POTs or DSTs) and converts them into meaningful 'physics' objects, such as 4-vectors. It provides a number of routines which allow determination of event kinematics, simple particle identification and jet reconstruction. The user must provide their physics analysis code which can then be used within the H1PHAN environment. The data analysis presented in the thesis has been developed within H1PHAN.

The H1 simulation program H1SIM [43] is based on the GEANT package [44]. H1SIM provides accurate detector simulation which can then be used to fine tune physics analysis programs, study trigger efficiencies and study energy flow properties in the different calorimeters. It simulates all the physics associated with the passage of particles through the various H1 subdetectors. H1SIM then outputs response banks which have the form as those produced by the real detector. The output from H1SIM can then be reconstructed using H1REC software chain.

The input to H1SIM comes from Monte-Carlo (MC) event generators, which generate the various physics processes that occur at HERA according to their calculated cross-sections. The program DJANGO [48] is an interface to the event generators HERACLES 3.1 [49] and LEPTO 5.1 [50]. HERACLES is used to generate DIS interactions including radiative corrections to $\mathcal{O}(\alpha)$. The LEPTO program is then used to simulate QCD processes and generate the hadronic final state. The DJANGO program has been extensively used in the physics analysis presented in the forthcoming sections. The MC events are generated using the input structure functions MRSD0 and MRSD$-$ [66] which give very different cross-sections in the HERA kinematic region; this is illustrated in Figure 2.13 (Section 2.3.7).

The data management for the above software packages is done by the BOS system [45]. All the data output by the above programs are stored in large tabular arrays referred to as BOS banks, which can be accessed by the use of pointers.

As mentioned in Section 3.5.1 during the 1992 and 1993 data runs the CJC1 detector contained a large fraction of dead wires. Therefore, in order to compare the real data with MC simulations these dead wires are accounted for during the reconstruction of the H1SIM data. The reconstruction of the simulated CJC data simply removes any hits on the observed dead wires. This allows the performance of the CJC1 detector to be better simulated.

Chapter 4

Electron Identification in NC DIS Events

4.1 Introduction

Experimentally, the identification of the scattered lepton in fixed target experiments has always been the most efficient way to identify and study DIS processes. Even with the unique event topologies expected for *ep* collisions at HERA, electron (and positron) identification will play a pivotal role in the analysis of NC DIS physics. Therefore, the need for an efficient software algorithm to isolate and identify the scattered electrons (e) from the reconstructed H1 data is paramount in the selection of NC DIS events.

In this chapter it will be shown how a cone-type jet finding algorithm can be adapted to identify the scattered e with high efficiency. The motivation behind the use of a jet finding algorithm for e identification can be attributed to the two-jet like structure of the NC DIS final state; in the laboratory frame, the e and quark scatter back-to-back in azimuth. Thus, the scattered e and current-jet can be treated as two separate jets with very different (reconstructed) characteristics. Hereafter, this cone-type jet algorithm will be referred to as the QJELEC algorithm.

In the first half of this chapter the expected properties of the scattered e jet, reconstructed by QJELEC, is presented from a detailed study of Monte Carlo (MC)

DIS events. From the observed e jet characteristics the criteria used by the QJELEC algorithm to select e candidates from the data is shown. In the second half, some important reconstructed properties of the scattered e is presented together with further refinements to the QJELEC algorithm needed to suppress e mis-identification coming from background processes.

In order to keep the background processes to a manageable level whilst, maintaining a high DIS acceptance rate and fully efficient Level-1 electron triggers, this analysis is restricted to electron energies greater than 8 GeV. The identification criteria presented in this chapter constitutes the main part of the forthcoming NC DIS physics analysis.

4.2 Description of the Jet-Finding Algorithm, QJELEC

The Jet-finding algorithm used in this analysis is based on the cone-type algorithm, first used by the UA1 collaboration, which defines jets as energy deposits within a cone of fixed radius in pseudo-rapidity - azimuthal space, $(\eta - \phi)$, where $\eta = -\ln\tan(\frac{\theta}{2})$.

The structure of the jet-finding algorithm is simple and consists of the following parts:

1. An η-ϕ grid is set up to match the geometry of the BEMC and LAr calorimeter. Due to the fine granularity of the LAr calorimeter a grid is set up with constant intervals in η, $\Delta\eta_{grid}$, and ϕ, $\Delta\phi_{grid}$. The much coarser granularity of the BEMC enables a η grid to be set up where the η bin size is defined by the BEMC cells; the ϕ bin size is the same as the LAr grid. The η and ϕ bin sizes are defined wrt. to the reconstructed vertex position.
2. The calorimeter cells are unpacked from the reconstructed clusters and added to their associated $\eta - \phi$ bins. The $\eta - \phi$ bins are then ordered

in increasing energy.

3. Only the $\eta - \phi$ bins above an initiator threshold, E^{in}_{thr}, are considered as possible jet initiators, *i.e.* they may initiate (start) a 'new' jet.

4. The highest energy $\eta - \phi$ bin is used to define the first jet. All the subsequent bins are added vectorially to the jet provided the distance between the jet-axis and the $(\eta - \phi)$ bin:

$$\Delta R = \sqrt{\Delta\eta^2 + \Delta\phi^2}$$

   where ϕ is in radians, is less than R_{limit}. The next highest energy $\eta - \phi$ bin which has not been associated to the first jet is used to initiate a new jet, provided the energy is greater than E^{in}_{thr}. All remaining bins are then added to this new jet provided $\Delta R \leq R_{limit}$. This procedure continues until all the $\eta - \phi$ bins have associated to a jet or the remaining bins are less than E_{thr}. Only those jets reconstructed with an energy $\geq E^{jet}_{thr}$ are accepted.

5. The reconstructed jets parameters are then stored in the H1 standard *BOS* banks.

In the forthcoming analysis, the following values are used for the above QJELEC parameters[1]:

$$R_{limit} = 1,\ E^{jet}_{thr} = 8,\ E^{in}_{thr} = 4, \text{ and } \mathrm{E_{thr}} = 0.25\,\mathrm{GeV}.$$

4.2.1 Jet Parameters and Electron Identification

For each reconstructed jet, the jet's 4-vector, $(E^{jet}_{tot}, E^{jet}_x, E^{jet}_y, E^{jet}_z)$, is constructed from the $\eta - \phi$ bins which have been associated to the jet:

$$E^{jet}_x = \sum_i E^i_x = \sum_i E^i_{tot} \sin\theta_i \cos\phi_i \tag{4.1}$$

---

[1] It should be noted that these values are tuned for reconstructing electron induced jets.

$$E_y^{jet} = \sum_i E_y^i = \sum_i E_{tot}^i \sin\theta_i \sin\phi_i \tag{4.2}$$

$$E_z^{jet} = \sum_i E_z^i = \sum_i E_{tot}^i \cos\theta_i \tag{4.3}$$

$$E_{tot}^{jet} = \sum_i E_{tot}^i \tag{4.4}$$

where the summation i is performed over the jet's $\eta - \phi$ bins. The polar and azimuthal angles correspond to the bin centre.

However, one salient feature which is inherent to this type of jet-finding algorithm, is that, the number of $\eta - \phi$ bins attributed to the jet give an indication into the lateral size, in η-ϕ, of the jet. In NC DIS events, the scattered e should appear in the H1 detector as an isolated particle such that the resulting jet should have a very small lateral size governed by the Moliere radius of the e shower.

Detailed studies into the electromagnetic shower properties of the e in the LAr calorimeter [46, 47] have shown that the e induced shower spreads out in a shape of a cone and the energy density of the shower propagates as a longitudinal cylinder within that cone, as shown in Figure 4.1(a). Figure 4.1(b) represents a typical e shower profile in the LAr calorimeter [47]. The different shadings in Figure 4.1(b) indicate the uneven distribution of the shower's energy within the cone. The darker areas correspond to the highest energy density within the shower. From Figure 4.1 it can be deduced that if the LAr cells, associated to an e induced shower, are put into an $\eta - \phi$ grid the resultant reconstructed jet would have the following characteristics:

1. The number of $\eta - \phi$ bins associated to the e jet should be small compared with the number of bins associated to the hadronic current-jet which has high particle multiplicity.
2. The e jet should have a high electromagnetic energy content.
3. The unique energy flow properties of the e shower imply that the bulk of the e jet energy should be concentrated at the centre of the jet namely, around the jet-initiator bin.

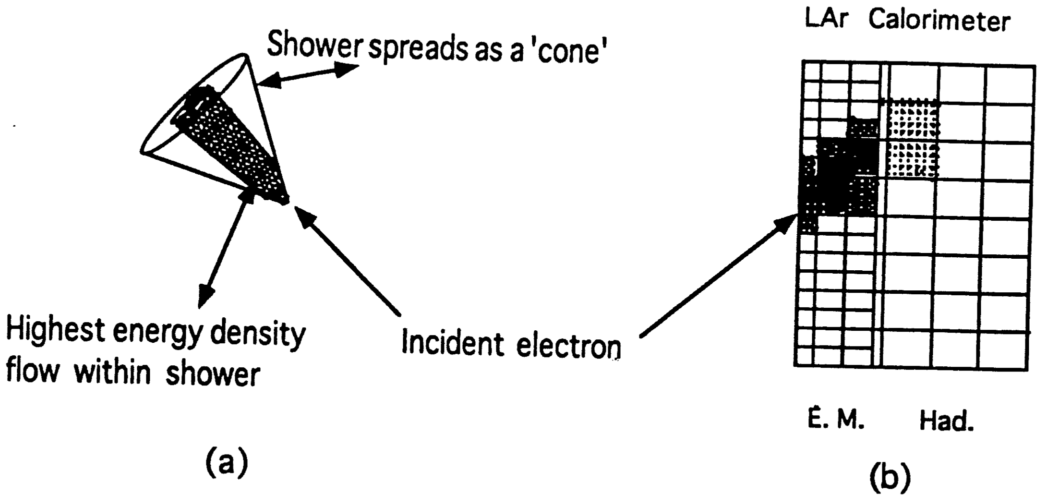

Figure 4.1: General shower properties (a) and a typical shower $r - z$ shower profile in the LAr calorimeter (b), for an electron.

However, the NC DIS event rate is dominated by low Q^2 events where the e scatters into the BEMC. Therefore, e identification must also be performed on BEMC jets. The Moliere radius for a 20 GeV e induced shower is approximately 3-4 cm within the BEMC material, which is less than the dimensions of the inner BEMC cells. Thus, a very large fraction of the incident e energy should be constrained to a single BEMC cell. However, in the case where the e enters the BEMC close to the edge of a cell, or between two cells, then the e shower (and energy distribution) can spread between two or more cells.

By treating each BEMC cell as an individual η-ϕ bin, the expected properties of the e induced reconstructed jet are similar to the above LAr cases, namely:

1. The number of η-ϕ bins associated to the e jet should be small, typically of the order of 1-3 bins.
2. The Moliere radius of the e shower imply that a high fraction of the e jet energy should be concentrated in and around the jet-initiator bin.

On the basis of the above e jet predictions, the following parameters are determined for each reconstructed jet:

1. The number of η-ϕ bins associated to the jet, N_{bin}.
2. The electromagnetic energy fraction of the jet, **EMF**.
3. The energy fraction contained in the jet-initiator bin and it's neighbouring bins, **EFN**, as shown in Figure 4.2.

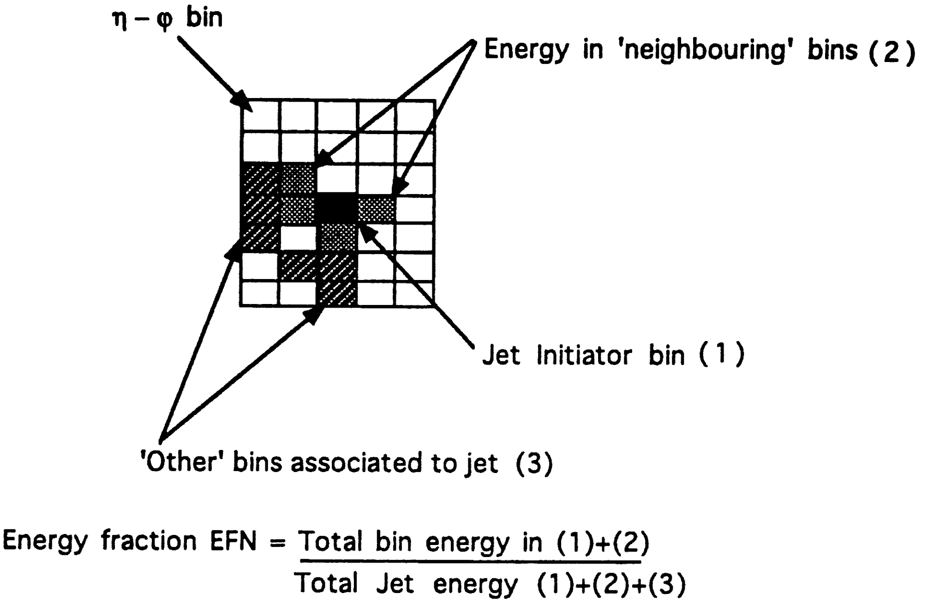

Figure 4.2: Simple diagram illustrating the meaning of the jet variable EFN.

4.3 Monte-Carlo Tuning for Electron Identification

4.3.1 MC Analysis Chain and Reconstructed Jet Profiles

To determine the potential of the above algorithm for e identification, detailed studies were made using fully simulated and reconstructed NC DIS events. The events were generated using the DJANGO [48] event generator. Only the fully reconstructed MC data is used by the QJELEC algorithm.

The method used to study the reconstructed jet profiles of the scattered e is based on the comparison between the (MC) generated e, *i.e.* true e, and it's reconstructed jet parameters. The identification of the e jet is done by determining the distance in (η,ϕ) space, ΔRe between the reconstructed jet and the generated e:

$$\Delta Re = \sqrt{(\eta_e - \eta_{jet})^2 + (\phi_e - \phi_{jet})^2}$$

Figure 4.3 shows a typical ΔRe distribution for all the jets reconstructed by QJELEC. It can be clearly seen that the highest rate of reconstructed jets is in the region $\Delta Re \leq 0.8$. Taking into account the coarse granularity of the BEMC cells, the reconstructed e jets are expected to populate this ΔRe region; visual scanning of these jets confirm that they are due to the scattered e. Hence, by looking at correlations between the jet parameters $\mathrm{N_{bin}}$, EMF and EFN and ΔRe the reconstructed profiles of the e jet should be visible.

Due to the different characteristics of the LAr and BEMC (η, ϕ) grid, the above correlations are shown separately for the LAr and BEMC jets:

1. Figure 4.4 represents the correlation between N_{bin} and ΔRe.
2. Figure 4.5 represents the correlation between EMF and ΔRe.
3. Figure 4.6 represents the correlation between EFN and ΔRe.

From Figures 4.4 and 4.5 it is evident that the jets in the region $\Delta Re \leq 0.8$ have the expected properties of the reconstructed e jet, namely, a high electromagnetic fraction (EMF ≥ 0.9), and a low number of η-ϕ bins, ($\mathrm{N_{bin}} \leq 6$). The final correlation, as shown in Figure 4.6, reveals that the jets, with $\Delta Re \leq 0.8$, have a large fraction of the jet energy concentrated in the jet-initiator bin and the neighbouring bins (EFN ≥ 0.85).

From these three correlations, the jet criteria for e identification can be derived. Thus, the following cuts are applied to the reconstructed LAr and BEMC jets in order to identify the scattered electron:

In the few cases where two or more jets satisfy the above e selection, for a given event, the jet with the highest $E_\perp$ is taken to be the scattered e candidate[2].

---

[2] This is possible since the e and current-jet scatter back-to-back in azimuth ($p_\perp$ conservation) and so the e should have the highest $E_\perp$.

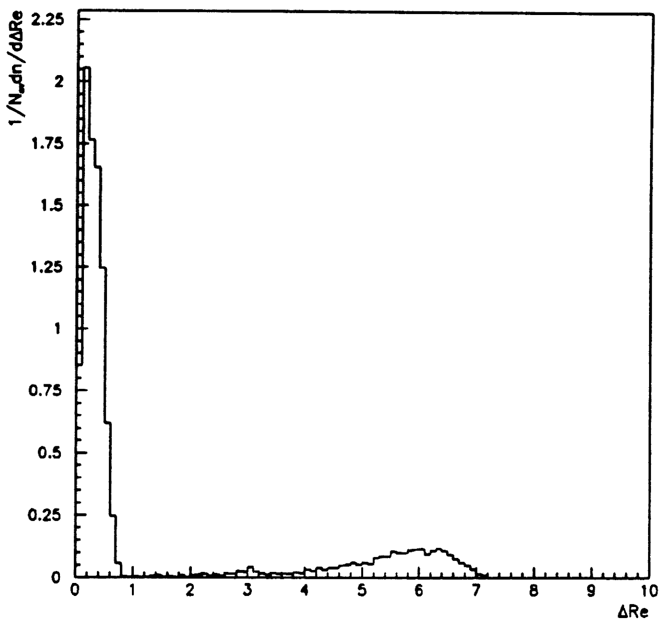

Figure 4.3: ΔRe distribution, wrt. the generated e, for all reconstructed jets.

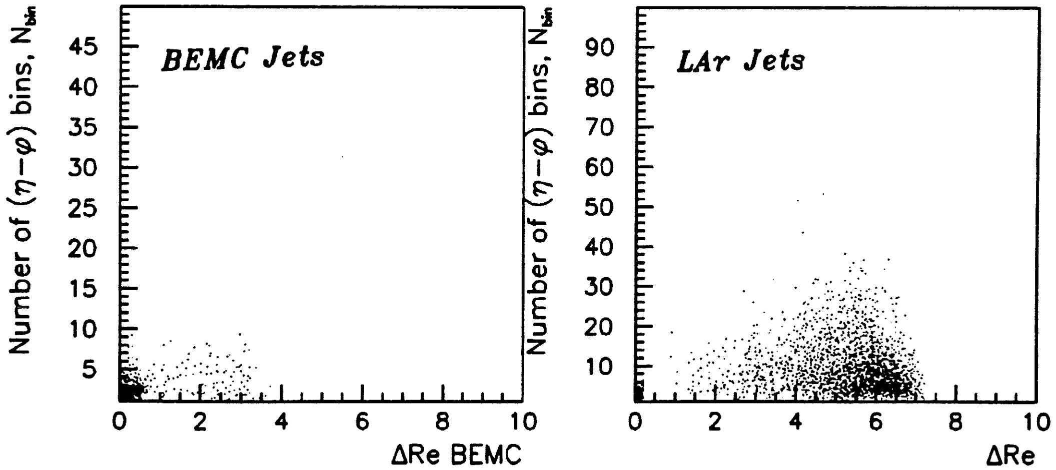

Figure 4.4: Correlation between ΔRe and the number of (η,ϕ) bins, N_{bin}, for each jet.

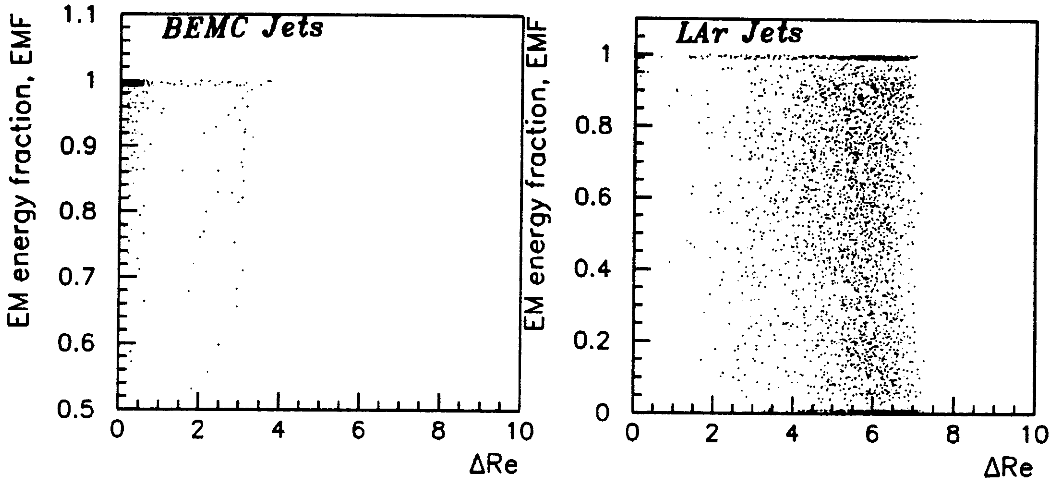

Figure 4.5: Correlation between ΔRe and the electromagnetic fraction, EMF, for each jet.

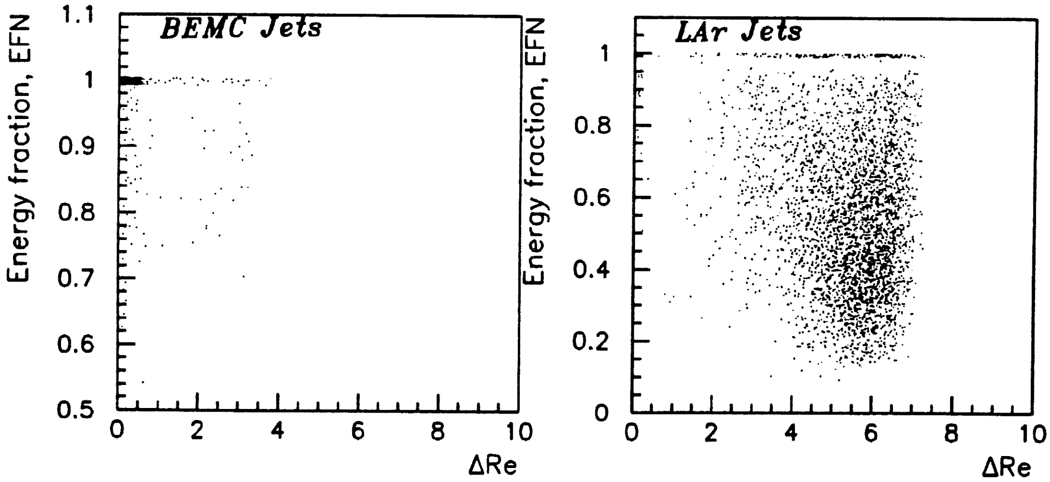

Figure 4.6: Correlation between ΔRe and the energy fraction in the jet's initiator and neigbouring bins, EFN

Jet Parameter	BEMC	LAR
$N_{bin} \leq$	4	6
EMF $\geq$	0.9	0.9
EFN $\geq$	0.95	0.85

Table 4.1: Table showing e selection cuts.

A simple method to test the efficiency of the above e selection is to study the change in the ΔRe distribution before and after e selection. This is illustrated in Figure 4.7.

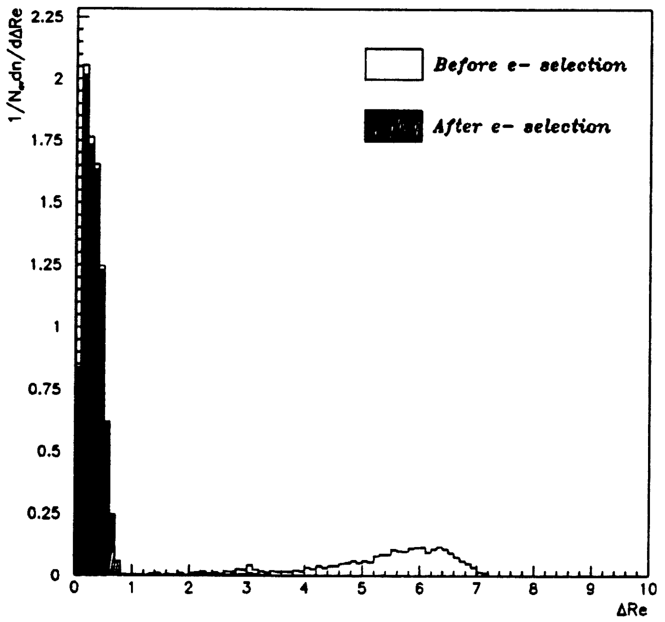

Figure 4.7: ΔRe of jets before and after e selection

From Figure 4.7, the ΔRe distribution remains almost unchanged in the region $\Delta Re \leq 0.8$ after applying the the e identification jet cuts. This simple illustration gives an an initial indication into the high e identification efficiency of the QJELEC algorithm. It can be seen that some of the selected e candidates have ΔRe values which exceed 1.2. These mis-identified e candidates are well understood and not attributed to the (true) scattered electron. The study of these the DIS events which give false e candidates is presented in section 4.6.

Unfortunately, due to various detector effects and background processes which fake e jets, further refinements have to be made to the QJELEC e identification criteria. However, before these refinements are explained some important reconstructed properties of the scattered e need to be discussed further.

4.4 Reconstructed Properties of the Selected Electron

In this section the reconstructed energy and polar angle (θ_e) profiles of the scattered electron are presented. The results originating from this study have proved to be influential in the final criteria used by QJELEC to identify the scattered e. In the following analysis only those e jets which have been correctly identified are considered. This requirement has no effect on any subsequent conclusions.

Within the H1 physics analysis environment H1PHAN, it is more convenient to refer to the identified e in terms of the associated reconstructed cluster. Once, the e cluster has been identified then additional information is linked to that cluster, such as the cluster's centre-of-gravity and reconstructed charged track data. Also, greater than 99% of the selected e jets are only associated to one cluster, which can be easily extracted[3]. For these reasons, the reconstructed cluster corresponding the selected e jet is used in the forthcoming analysis. It should be noted that the calorimeter cluster usually consists of many calorimeter cells.

4.4.1 Electron Energy Reconstruction

From chapter 3, the energy resolutions for the BEMC and LAr calorimeter including effects of noise and systematic fluctuations [52], during the first H1 data-taking periods were given as:

---

[3] In the rare cases when two clusters were attributed to the selected e jet, the highest E_t cluster is taken to be the scattered electron

$$\frac{\sigma_E}{E} = \frac{0.45}{E} \oplus \frac{0.1}{\sqrt{E}} \oplus 0.04 \quad \text{BEMC resolution} \tag{4.5}$$

$$\frac{\sigma_E}{E} = \frac{0.154}{E} \oplus \frac{0.11}{\sqrt{E}} \oplus 0.006 \quad \text{LAr resolution} \tag{4.6}$$

The last term in the BEMC resolution is the result of stack to stack intercalibration uncertainties which are not included in the H1 simulation or reconstruction chain. Therefore, in order simulate the BEMC accurately, the above uncertainly is included into the e energy as follows; the BEMC stacks which make up the identified cluster are extracted and their reconstructed energies are smeared according to a gaussian function with $\sigma = 0.04$. The e energy was then taken to be the sum of these smeared cells corrected by a factor 1.027 which compensates for energy losses in materials in front of the BEMC (about 1 X_0).

For the scattered e cluster in the LAr calorimeter, the e energy is taken to be the reconstructed energy of the cluster.

The aim of this section is to describe the energy resolutions of the scattered e predicted by realistic detector simulations. Detailed studies concerning the energy resolutions of the BEMC and LAr calorimeters can be found in [47, 54].

4.4.2 Energy Reconstruction in the BEMC

At HERA energies it is expected that radiative DIS events, with initial- and final-state photon radiation from the e, will contribute a large fraction of the selected DIS events. For final-state radiative events, the radiated photon (γ_{rad}^{FS}) is emitted almost colinear with the scattered e. Due the large BEMC cell size, it is almost impossible to separate the two particles and the selected e BEMC cluster contains the energy of the scattered e and γ_{rad}^{FS}; initial-state γ's pose no problem as the γ remains down the beam pipe.

The above statement is illustrated in Figure 4.8(a) which shows the distance in $\eta - \phi$ space, $\Delta R_{e\gamma}$, between the γ_{rad}^{FS} and scattered electron. It can be seen that the γ_{rad}^{FS} is emitted in a very narrow cone around the electron. In the lower regions of the BEMC, near the beam pipe, the difference in ϕ between the edge and centre of a BEMC stack can be as large as 0.8 radians. This implies that the e and γ_{rad}^{FS} are inseparable if $\Delta R_{e\gamma} \leq 0.8$ [4] since they both hit the same BEMC stack. In the cases where the e and γ_{rad}^{FS} enter different stacks, it transpires that they enter adjacent cells. In these cases, due to the low γ_{rad}^{FS} energies, the clustering algorithm will merge the two stacks into one cluster.

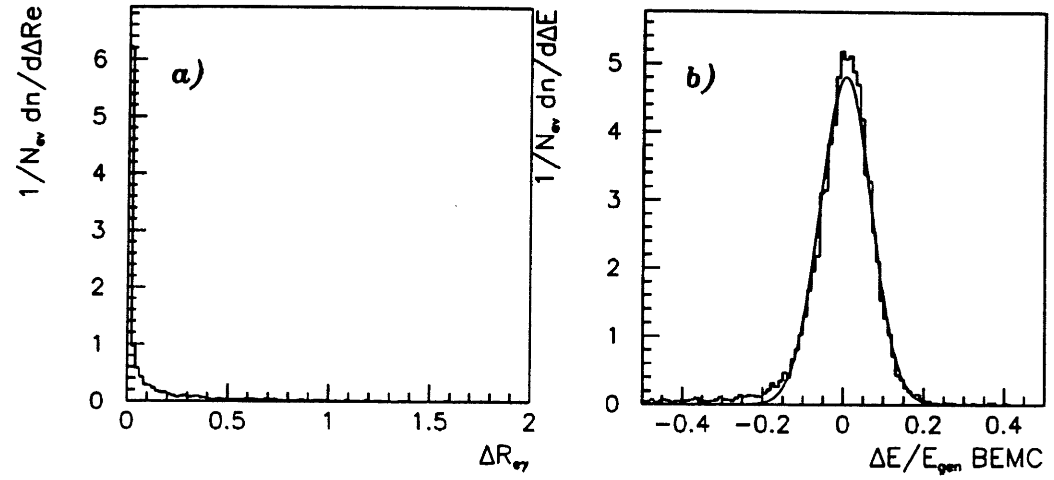

Figure 4.8: ΔR distribution between the MC scattered e and final state radiated γ (a) and the energy resolution $\frac{\Delta E}{E}$ of the selected e cluster (b).

Following the above example, the reconstructed energy resolution of the selected e cluster ($\frac{\Delta E}{E}$) can be defined as:

$$\frac{\Delta E}{E} = \frac{E_{rec}^{e} - E_{gen}^{e+\gamma}}{E_{gen}^{e+\gamma}}$$

where $E_{gen}^{e+\gamma}$ is the sum of the generated (*i.e.* true) scattered e and γ_{rad}^{FS} energies provided $\Delta R_{e\gamma} \leq 1$. E_{rec}^{e} is the reconstructed energy of the selected e cluster. In the absence of final-state radiation the above equation simply relates to the reconstructed e energy resolution.

The resulting $\frac{\Delta E}{E}$ distributions is shown in Figure 4.8. As expected the $\frac{\Delta E}{E}$ distribution has a near perfect gaussian behaviour, centred around zero. Fitting this distribution to a gaussian function leads to a gaussian mean of 0.8% and a $\sigma_{\frac{\Delta E}{E}}$

---

[4] Neglecting the η differences between the stack center and edges.

of 6%. Since the NC DIS cross-section is dominated by e scattering energies greater than 20 GeV, the $\sigma_{\frac{\Delta E}{E}}$ value agrees well with the expected BEMC resolution.

The 'tails' in the negative region of the $\frac{\Delta E}{E}$ region are a direct consequence of the deteriorated energy response of the BEMC at the edges and corners of the lower BEMC stacks. This is illustrated in Figure 4.9 which shows the correlation between $\frac{\Delta E}{E}$ and the angle θ_e (wrt. the proton direction) of the scattered electron. It can be seen that the energy resolution deteriorates at θ_e values which corresponds to the outermost and innermost BEMC stacks.

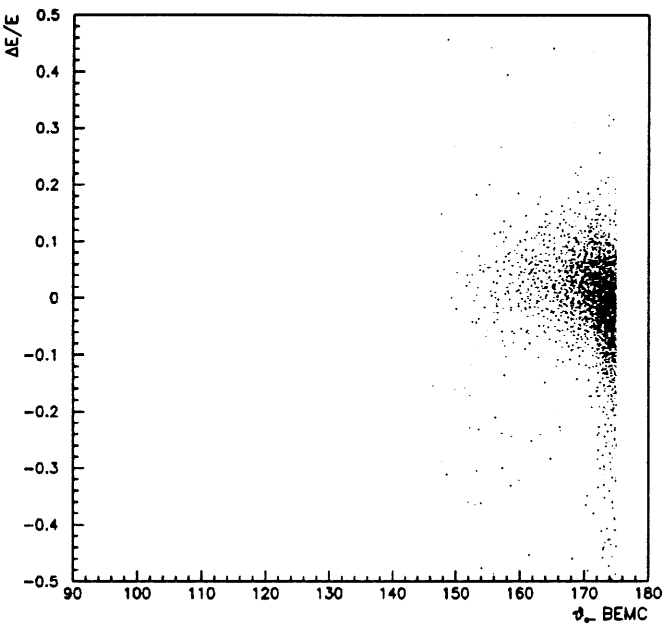

Figure 4.9: Dependence of $\frac{\Delta E}{E}$ wrt. the e scattering angle, θ_e.

The two main reasons why the energy resolution deteriorates in the lower and outer regions of the BEMC are as follows:

1. At very low scattering angles (large θ_e) the impact point of the e (IP) on the stack may lie close to or on the stack's edge. In these cases large energy losses occur in the region between single stacks (crack regions) resulting in a deteriorated energy resolution. Although, corrections are applied to account for these losses (and to render a homogeneous response), these 'crack' corrections may underestimate the energy losses when the IP is too close to a crack region. A

good account of the BEMC energy response and reconstruction can be found in [54].

2. The triangular stacks have no wavelength shifters (WLS) on the edge of the cells adjacent to the beam-pipe. Thus, no read-out is possible from these edges. As a result, the shower of the particle is not fully contained and cannot be fully read-out. A similar effect is observed when the e scatters into the outer BEMC stacks, where some stacks have no WLS on their outer edges which consequently result in lateral energy leakage and lower energy reconstruction. However, these events are not as frequent, due to the much smaller DIS cross-section in this θ_e region. For more details concerning the geometry and calibration/reconstruction of these stacks see [53, 54].

For real data, the only way to ensure a good energy resolution, and full shower containment, is to neglect the selected e clusters which have a large energy fraction in the triangular stacks. This will be discussed further in Sections 4.6 and 5.5. However, the events in which $|\frac{\Delta E}{E}|$ is large due to energy losses in the crack regions are more difficult to isolate for real data as the true IP and energy of the scattered e are not known.

4.4.3 Energy Reconstruction in the LAr Calorimeter

Unlike the BEMC, the LAr calorimeter has finer granularity in θ and ϕ [52], which implies that if the scattered e radiates a photon, the e and γ_{rad}^{FS} showers will be easily separable for $\Delta R_{e\gamma} \geq 0.1$ [5].

Therefore, the energy of the γ_{rad}^{FS} is only included in the $\frac{\Delta E}{E}$ calculation if $\Delta R_{e\gamma} \leq 0.1$. The resultant $\frac{\Delta E}{E}$ distribution, for the electromagnetic part of the LAr calorimeter, is shown in Figure 4.10(a).

Comparing this distribution with Figure 4.8 (BEMC energy resolution), it can be seen it is not centred on 0 but slightly offset in the negative region. Secondly,

---

[5] Even if $\Delta\eta$ between the γ_{rad}^{FS} and e is ≈ 0, $\Delta R_{e\gamma} \geq 0.1 \Rightarrow \Delta\phi \geq 5^o$. Taking into account the lateral shower profiles of the e and γ, the two clusters should be separable when $\Delta\phi \geq 5^o$

the distribution does not have a gaussian tail in the region $\frac{\Delta E}{E} < 0$.

To understand the origin of these tails, a correlation is plotted between $\frac{\Delta E}{E}$ and the scattering angle of the generated scattered e, θ_e. This correlation is illustrated in Figure 4.10(b), and shows that the negative tail in question dominates when $\theta_e \geq 140^o$.

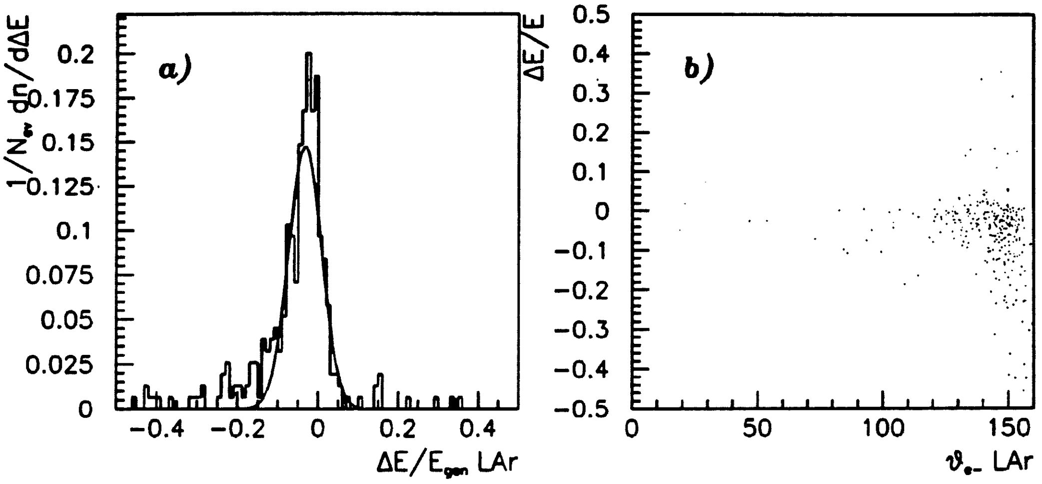

Figure 4.10: $\frac{\Delta E}{E}$ distribution (a) and dependence of $\frac{\Delta E}{E}$ wrt. θ_e (b) for LAr clusters.

Further studies into these events reveal that the origin of the 'tail' lie in the events in which the scattered e enters the extreme backward region of the BBE wheel of the LAr calorimeter; this corresponds to $\theta \approx 154^o - 156^o$. Taking in account that the simulated event vertex has a gaussian distribution between $\pm$70 cm in the z-direction, the extreme backward region now has an angular coverage $143^o \leq \theta \leq 163^o$, which explains the angular observation in Figure 4.10. The kinematic plane covered by the BBE is predominantly, $60 \leq Q^2 \leq 300\ GeV^2$, $0.1 \leq y \leq 0.7$ and $0.001 \leq x \leq 0.1$.

In this region the e enters the BBE near to the edge of the wheel, such that the some of the e shower particles escape from the edge. Hence, the resultant shower energy of e will be reduced. Clearly, as the e shower gets closer to the edge the energy losses become greater, as observed in Figure 4.10. Also, the scattered e may just scrape the outer edge of the BEMC before it enters the BBE. In these cases energy losses may occur in the BBE and the outer edges of the BEMC.

A typical MC event which highlights the above case is shown in Figure 4.11. Correcting for these type of events is non-trivial as the amount of shower energy lost via the edge is difficult to determine.

Other possible sources of shower energy losses may occur in the cracks between adjacent wheels of the LAr calorimeter and leakage of the e shower energy into the hadronic part of the calorimeter. Both sources have been extensively studied, via test beam data and MC simulations, and are well understood [55]. Although, the effect of cracks or energy leakage are corrected for in the energy reconstruction, the corrections can still be underestimated, particularly if a large fraction of the e shower energy is lost in a crack or leaked into the hadronic part.

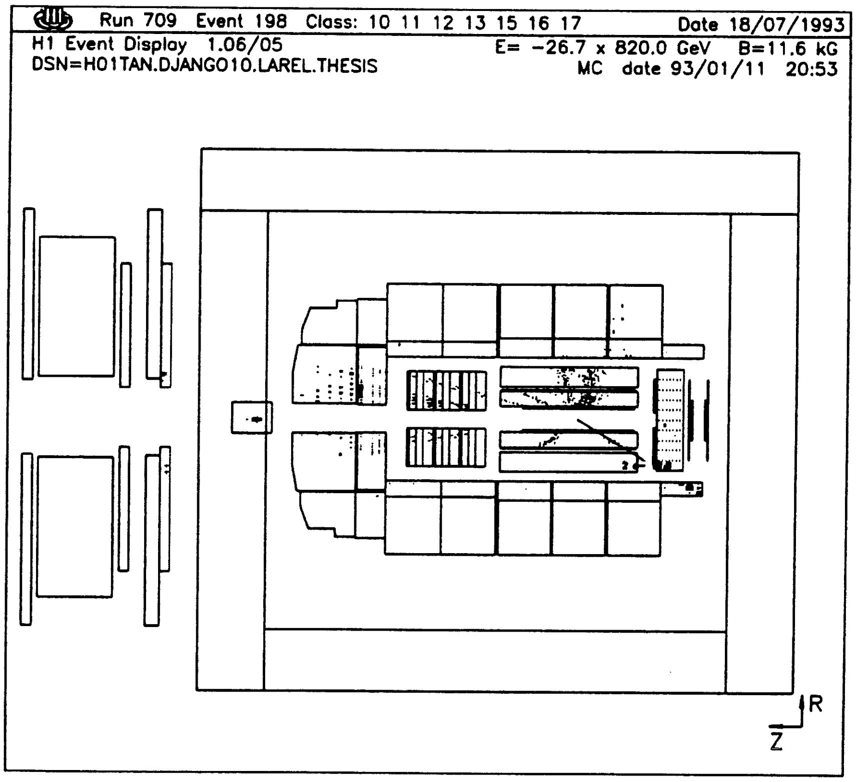

Figure 4.11: Simulated event in which the e scatters in the backward region of the BBE.

In summary, the reconstructed energy in the LAr (EM part) calorimeter for the scattered e is well understood, and the limitations of the BBE wheel have been shown.

4.4.4 θ Reconstruction

The θ angle of the scattered e can be determined either from the e clusters energy 4-vectors or from charged track data linked to the e cluster, this may be CJC tracks or BPC hits.

In the former case, when the clusters 4-vector is used, it is important to note the 4-vector is calculated using the polar and azimuthal positions of the constituent cluster cells wrt. to the reconstructed vertex. The centre of the calorimeter cells are used to define θ and ϕ for the calculation of the cell's energy vector.

For electron scattering angles in the region $22^o \leq \theta_e \leq 160^o$ the e cluster can be linked to a 'good' reconstructed CJC track[6]; here the definition of a 'good' track means that the track is reconstructed from at least 10 wire hits. Thus, for e clusters in the outermost BEMC stacks and the LAr calorimeter tracking data can be used for accurate momentum and θ_e determination. In the region $\theta_e > 160^o$ the only tracking information for the e comes from the BPC detector.

As described in Chapter 3, the BPC has an angular acceptance ranging from $155^o - 175^o$ covering a large fraction of BEMC. Only the triangular stacks and the outermost stacks are not fully covered by the BPC. The BPC hit $\leftrightarrow$ e cluster linking is done in the following way;

1. For each reconstructed BPC point, $(x, y, z)_{bpc}$, the c.o.g of the e cluster is projected on the z_{bpc} plane. A BPC hit is then linked to the cluster if the radial separation in (x,y) space between the projected c.o.g and BPC points is less then 15 cm.
2. If more then one BPC point is linked to the cluster then the average (x,y,z) co-ordinate is used to define the e angle. (Due to the amount of dead materials in front of the BEMC, the e usually liberates low energy Δ rays which accompany the e through the BPC. Thus, more than one BPC hit can be linked to the cluster.)

---

[6] The cluster - track linking is done during the data reconstruction phase.

The efficiencies for the above cluster - track (or BPC hit) linking requirements are presented in the next section.

For e clusters in the BEMC if θ_e is calculated from the clusters 4-vector the resulting $\Delta\theta_e$ distribution is shown in Figure 4.12(a). From this distribution the θ_e reconstruction resolution is determined to be 1.15 ± 0.35^o. The large resolution is mainly due to the angular difference between the e's true impact point on a stack and the stacks centre. This (polar) angular difference can be large as 4^o at very low scattering angles (*i.e.* in the triangular stacks).

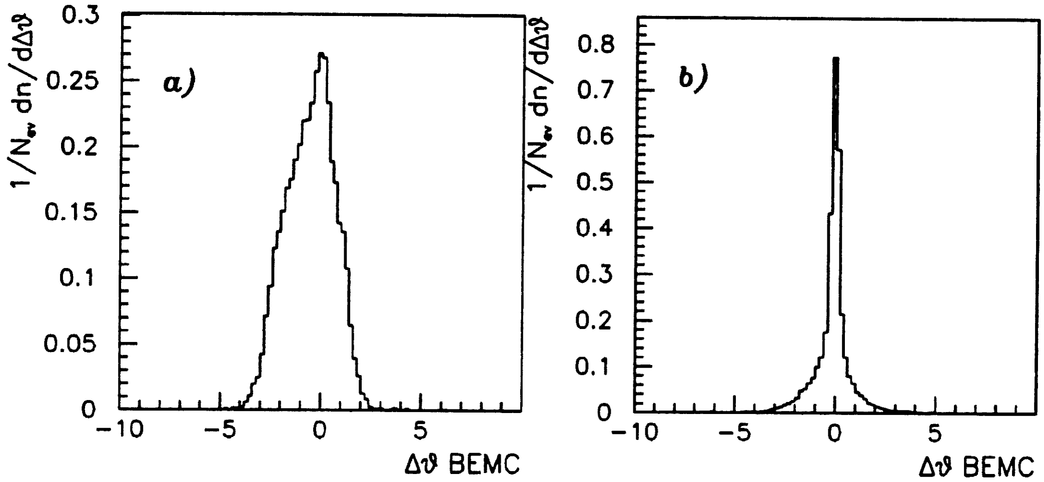

Figure 4.12: Angular resolution, $\Delta\theta$, for the BEMC clusters when θ_e is calculated from the e energy 4-vector (a) and linked tracking data (b).

By taking the BEMC clusters which have been linked to a good CJC track or a BPC hit the θ_e reconstruction is greatly improved as shown in Figure 4.12(b). If a cluster is linked to a BPC hit and a good track, θ_e is determined from the track. It should be noted that only 6% of the entries in Figure 4.12(b) are determined from linked CJC tracks. Despite the better θ_e resolution, the distribution has very striking tails. The origin of these poorly reconstructed θ_e values can be attributed to events in which no vertex position could be reconstructed for kinematic reasons. The kinematic dependence of the vertex reconstruction efficiency is discussed in Section 5.3. For these events the vertex is taken to be the nominal interaction point, $(0, 0, 0)$, which can lead to large shifts in the θ_e measurements. If Figure 4.12(b) is plotted for events with a reconstructed vertex, the tails disappear and the θ_e resolution is $\sim$ 3 mrad.

The corresponding $\Delta\theta_e$ distributions for LAr e clusters are shown in Figures 4.13(a) and 4.13(b), for 4-vector and tracking data, respectively. From these distributions the resulting θ_e resolution is determined to be 6 mrad, from the 4-vector data, and 10 mrad using the tracking data. Although, it is tempting to say that the 4-vector calculation is more accurate, it should be noted that, the track reconstruction programs will generally improve with time and so the above results should not be taken as absolute predictions[7].

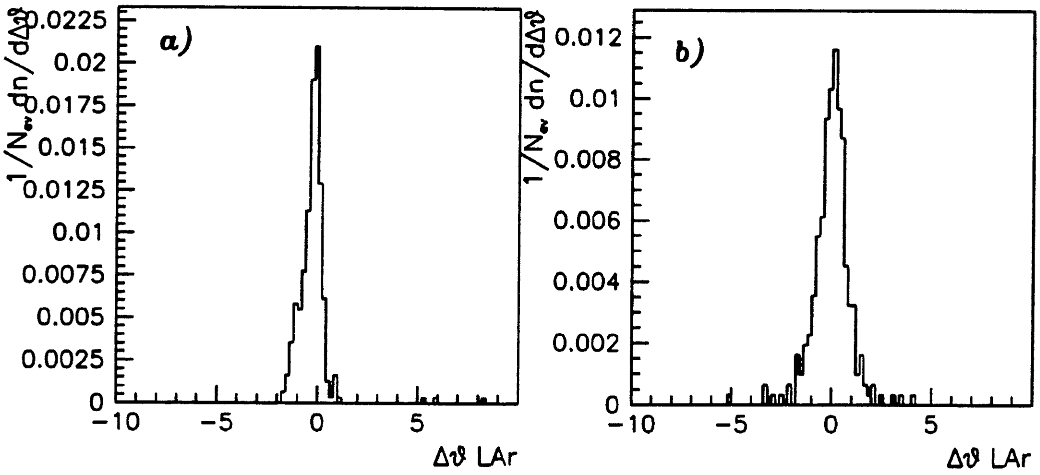

Figure 4.13: Angular resolution, $\Delta\theta$, for the LAr e clusters when θ_e is calculated from the e energy 4-vector (a) and linked CJC track (b).

The main reason for presenting this section is that the reconstruction of the event kinematics (Q^2, y and x) from the scattered e is very sensitive to $\Delta\theta_e$, particularly in the low Q^2 and low y region (see Section 5.4.1), where the e scatters into the BEMC. The results presented in this section will play an important part in the

---

[7] However, the above resolution gives a general indication into the precision of the angular reconstruction for the CJC reconstruction chain that was used for the data runs analysed in this thesis.

final e identification criteria used by the QJELEC algorithm. For high Q^2 events where the e scatters into the LAr calorimeter, the kinematic uncertainties are almost independent of $\Delta\theta_e$, thus, it is not so critical which method is used to determine θ_e.

4.5 Electron Identification Efficiencies

To determine the efficiency of the QJELEC e identification algorithm only those MC events in which the scattered e cluster is reconstructed in the BEMC or LAr calorimeter with an energy greater than 8 GeV are considered; kinematically this implies $Q^2 \geq 3\,GeV^2$, $\theta_e \leq 176^o$ and $y \geq 0.001$. Neglecting the very low Q^2 events where the e scatters down the beam-pipe avoids biasing (*i.e.* underestimating) the efficiency calculations in the low Q^2 region[8].

Applying the QJELEC algorithm on a large sample of these selected events leads to three possible outcomes:

1. The QJELEC algorithm correctly identifies the scattered e. The probability for this to happen is given by α.
2. The QJELEC algorithm selects an e candidate cluster which is not associated to the 'true' scattered e. This mis-identification probability is given by β.
3. Due to the reconstructed properties of the e cluster, the QJELEC algorithm fails to select any e candidate. The probability for this to happen is given by γ.

where, $\alpha + \beta + \gamma = 1$.

Using a sample of 20K events integrated over the kinematic plane accessible after the above event pre-selection, the above probabilities were determined as $\alpha = 0.98$, $\beta = 0.003$ and $\gamma = 0.017$. These results are found to be independent of the shape

---

[8] Over the full DIS kinematic plane accessible at HERA, approximately 70% of the total number of events would remain after the above pre-selection.

of the input structure functions and the model used to generate the hadronic final state.

Although, the above results clearly indicate the high e identification efficiency of the QJELEC algorithm it is important to note that the results are dominated by the low Q^2 events where the e scatters into the BEMC. Therefore, inorder to gain a better insight into the performance of the algorithm it is useful to recalculate the above probabilities separately for low Q^2 and high Q^2 events (e scattering into the LAr calorimeter). These new results are presented in 4.2.

QJELEC Efficiencies		
	Low Q^2	High Q^2
α	0.980	0.95
β	0.005	0.00
γ	0.015	0.05

Table 4.2: Scattered e identification probabilities in the BEMC and LAr calorimeter.

From these new results it can be concluded that the QJELEC algorithm can be efficiently used for e identification in both electromagnetic calorimeters. It should be noted that in 5% of high Q^2 events where the QJELEC fails to identify the scattered e, it is mainly due to the electronic shower penetrating into the hadronic part of the LAr calorimeter, thus failing the electromagnetic fraction cut. Although, these e can be identified by relaxing this cut it also leads to more e mis-identifications, from soft hadrons, and so no further action is taken. In these high Q^2 events, the hadronic final state contains a high $p_\perp$ current jet (hadrons) and so there is very little chance for e mis-identification.

In the case of the low Q^2 events the 1.5% of events where the QJELEC algorithm failed to identify the e is a result of the e entering close to a BEMC crack region. In these cases the cluster's energy is spread among 2 or more cells and the resulting jet fails the EFN and/or the number of $\eta - \phi$ bin criteria. The cases where the QJELEC mis-identifies the scattered e may appear to be small but it highlights the biggest limitation of the present QJELEC algorithm. The lack of hadronic calorimetry behind the BEMC results in backward going hadrons being able to fake e clusters, which as shown is very small in DIS physics but is much more important when considering photoproduction processes. It is for this reason that these events will now be discussed.

4.6 False e Candidates and Final e Selection Criteria

The most important feature of any e identification algorithm, which is used to isolate the scattered e in DIS events, is that it must have a high rejection for γ's and hadrons which can fake e signals. False e identification can lead to background processes from beam-gas, beam-wall and photoproduction events easily faking DIS events. Therefore, it is paramount that the selected event sample should be free of any non DIS events. The aim of this section is to discuss the motivation behind the final set of criteria used by the QJELEC algorithm and its implications for DIS physics.

As shown in Section 4.5, there is a small probability for e mis-identification which turns out to be mainly concentrated in the kinematic region $Q^2 \leq 30\,\mathrm{GeV}^2$ and $x \leq 10^{-3}$. In this kinematic plane the DIS events are characterized by low e scattering energies (low $p_\perp$) and backward scattered current jets, resulting in low $p_\perp$ particles from the hadronic final state entering the BEMC and the backward part of the LAr calorimeter. Consequently, the reconstructed jet (clusters) from some of these particles can satisfy the QJELEC algorithm leading to e mis-identification. False e candidates arise mainly from the poor hadronic calorimetry behind the BEMC which results in hadronic energy deposits, from π^o's and $\pi^\pm$'s, in the BEMC being treated as e type clusters. To a lesser extent γ's from the hadronic final state and hard QED radiation from the scattered e (NC DIS Compton events) also give false e candidates.

As mentioned above, the fact that hadrons (or γ's) can lead to e mis-identification subsequently results in background events dominated by photoproduction processes satisfying the QJELEC criteria, thus faking DIS events. A more detailed account of the various processes that can fake DIS events is presented in Chapter 5, in particular the subject of photoproduction background is discussed in Section 5.5. In photoproduction the final state e scatters down the beam and typically remains undetected and the hadronic final state contains low $p_\perp$ particles which give fake e candidates in the BEMC.

Due to the large photoproduction cross-sections using the present form of the QJELEC algorithm leads to a very large photoproduction acceptance rate; as indicated in Section 5.5, for a given luminosity, the photoproduction acceptance rate is expected to be to be almost 75% of the DIS acceptance rate. Clearly, this would lead a huge background contribution to the selected event sample using the present e identification criteria, thus the QJELEC algorithm needs further refinements[9].

After studying the nature of the above background events, the following extra criteria are added to the QJELEC alogorithm inorder to reduce the rate of e mis-identification:

- The selected e cluster must have less than 30% of its total energy in the triangular stacks. The criterion ensures good energy reconstruction for the scattered e and reduces the number of low $p_\perp$ fake background e candidates.

- After passing the above cut the e candidate cluster must be linked to a BPC hit if it is in the BEMC and a good CJC track if it in the LAr calorimeter. This requirement ensures that the cluster is due to a charged particle (as expected for an e) and subsequently reduces the probability for e mis-identification arising from γ's and neutral hadrons. As shown in Section 4.4.4, the BPC requirement will ensure that the reconstructed θ_e resolution will be better than 3 mrad. For e's scattering into the outermost BEMC stacks, which are only partially covered by the BPC detector, the BPC hit criterion also ensures that the energy losses from the BEMC edges is minimised.

---

[9] This background rate would be even greater if the e energy threshold is extended down to 4 GeV.

As the result of the above criteria the identification of the scattered e is restricted to the angular region $\theta_e \leq 174^{o}$[10]. For e's scattering into the BPC detector the efficiency for reconstructing and linking a BPC hit to the e cluster, using the method described in Section 4.4.4, is determined as 95±2% (97±2%) for scattering energies between 8 - 16 (16 - 28) GeV. In the case of e clusters in the LAr calorimeter the efficiency to link a reconstructed CJC track to the cluster is 93±3%.

Inevitably, the introduction of the above criteria results in reducing the DIS acceptance rate by roughly 38%, but more importantly the photoproduction background is reduced by 80%. Kinematically, the largest DIS losses occur in the very low x ($x \leq 0.001$) and low Q^2 ($Q^2 \leq 20\,GeV^2$) plane as a result of the angular cut imposed by the energy fraction and BPC hit criteria. This is illustrated in Figure 4.14 which shows the fraction of e candidates remaining after the above cuts in bins of $\log_{10} Q^2$ and $\log_{10} x$.

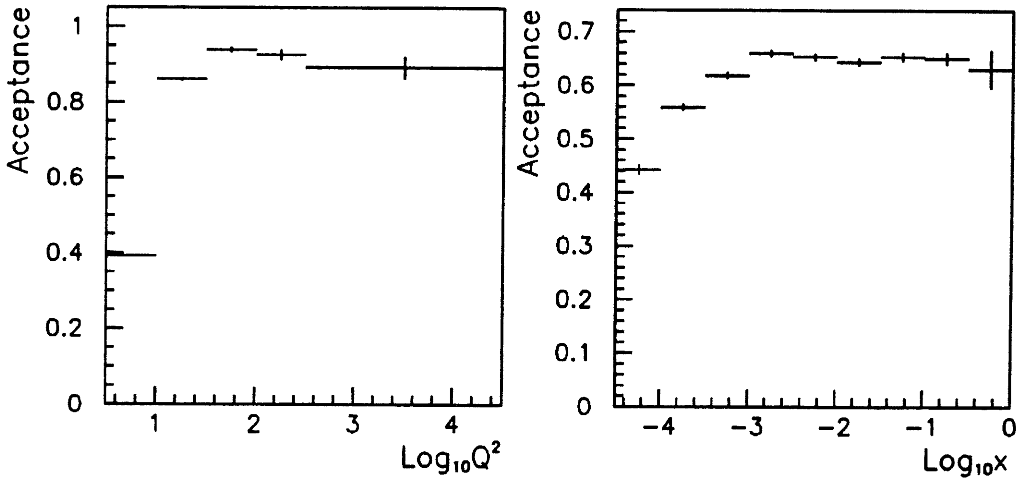

Figure 4.14: Acceptance of the refined QJELEC algorithm as a function of $\log_{10} Q^2$ (a) and $\log_{10} x$ (b). The statistical errors are also shown.

Without these extra e identification criteria the background rate from photoproduction would be so large rendering any DIS cross-section (structure function)

---

[10] Strictly speaking the angular acceptance may extend down to $\theta_e \sim 176^{o}$ depending on the z-vertex distribution of the DIS interactions.

measurements almost impossible in this region. Therefore, the DIS losses incurred by the extra cuts are compensated by the fact that the lower background rate will allow more reliable DIS measurements to be made in the new low x (high y) regime.

4.7 Concluding Remarks

In summary, the criteria used by the QJELEC algorithm to identify the scattered e from the data is as follows:

- An e candidate jet is selected based on it's reconstructed profiles, *i.e.* it must have a high electromagnetic energy fraction and the lateral size of the jet, in η-ϕ space, must be small.
- The parent cluster contributing to the selected jet is extracted; for genuine e jets there is only one reconstructed cluster contributing to the jet.
- The cluster must be linked to a reconstructed BPC point if it is a BEMC cluster and it must have less than 30% of it's energy in the triangular stacks. If the e cluster is in the LAr calorimeter then it must be linked to a reconstructed CJC track with at least 10 wire hits.

This algorithm can be considered as a 'Level 1' software trigger since it is initially used to select offline e candidates. Only the data events passing QJELEC are considered as possible NC DIS event candidates. However, since there is still some background contamination from photoproduction processes further event selection criteria are needed which are presented in the next chapter.

Chapter 5

Event Selection & Kinematic Reconstruction

5.1 Introduction

In an ideal world the most efficient method to select NC DIS events would be to identify the scattered e because of its clear signature. Unfortunately, as shown in Section 4.6, this simple selection criterion is complicated by the fact that various background processes, in which hadrons can fake e clusters, can be accepted by the QJELEC e identification algorithm, thus contaminating the DIS data sample. If these background processes are not removed from the real data, they will inevitably introduce large errors in the extraction of any DIS physics, such as the measurement of the NC DIS cross-sections and $F_2(x, Q^2)$ structure function.

The two main background processes which can be accepted by the QJELEC algorithm are; i) beam induced background originating from beam-gas and beam-wall interactions and ii) fake e clusters coming from photoproduction events.

In this chapter a detailed explanation is given for the offline criteria used to select DIS events from the H1 data taken during the Autumn 1992 run (see Section 6.1). It will be shown how simple tracking requirements and kinematic constraints can be used to efficiently suppress the background rate in the final data sample. In the last section, a few distributions of the selected DIS events are presented, together with pictures of DIS events in the new high Q^2 and low x regions.

As in the previous chapter the MRSD− [66] MC events will be used to study the efficiencies of each selection criteria.

5.2 Event Classification at the DST Level

At HERA the NC DIS interaction rate is at least three orders of magnitude smaller than the background rate resulting from the strong interactions of beam protons with either the beam-pipe or the residual gas in the beam-pipe. In order to reduce this huge background rate various levels of data selection are applied, both online and offline, before the data is finally kept and stored. In this section, a brief description is given into the data criteria used by H1 to identify and keep possible NC DIS event candidates, from the real data.

As described in Section 3.7, during 1992 only three levels of data selection and reduction (L1, L4 and L5) was used by H1. The fast trigger level (L1) is used to reject events based on their selected hardware trigger conditions. The next level of data selection/rejection is done on the filter farm (L4) which runs fast software algorithms to filter out good events based on good tracking data,vertex fits and energy cuts. Only those events which pass L4 are reconstructed (L5) and selected for the Data Summary Tapes (DST).

The real data analysed in this thesis is based on the events which have been put onto the DST. The aim of the DST is to provide a clean sample of NC DIS event candidates, which have satisfied the L4 and L5 event classification module, ECLASS [64]. The ECLASS software algorithms assign a physics class(s) to each event which is based on the reconstructed event properties. The algorithms used by ECLASS have been designed to select events which have the reconstructed properties expected for a particular physics process.

The NC DIS event candidates which have been selected for the DST data have been classified as NC low Q^2 events or NC high Q^2 events. The ECLASS definition of these classes is as follows:

At the hardware trigger level (L1), all the low Q^2 NC DIS event candidates must have satisfied the BEMC trigger (BCL2) with no TOF veto trigger. The BEMC trigger required a local cluster energy of greater 4 GeV.

For the low Q^2 classification all events must have a reconstructed energy cluster in the BEMC with a minimum energy of 4 GeV. There must be no TOF signals, or the TOF signals must occur within the physics interaction time window. After this basic selection, the low Q^2 events are then assigned to one, or both, of the following two event classes:

1. class 1: the event must have at least one good CJC track or Forward track.
2. class 2: the event must have at least one of the BEMC clusters associated to a BPC hit (see Section 4.4.4) or at least one BEMC cluster with a energy between 22 & 32 GeV.

The TOF cuts used in the low Q^2 classification are designed to reduced the background events produced in upstream proton interactions. The class 1 events are defined so that easy access can be made to events where the reconstructed vertex has been fitted from at least one track. The class 2 events account for the low Q_e^2 events where the e scatters into the lower regions of the BEMC (including the triangular stacks). However, it is important to note that in many cases an event can satisfy both classes.

The high Q^2 classification is based on events with an e candidate cluster in the LAr calorimeter. An e candidate is defined as a reconstructed cluster with an electromagnetic fraction $\geq 50\%$. In addition the event is required to balance in $p_\perp$, where the missing $p_\perp \leq 40$ GeV. An event is then classified as an high Q^2 if the event has at least one good CJC or Forward track, and an e candidate in either of the following regions:

1. $10^o \leq \theta_e \leq 45^o$ & $E_\perp^e \geq 8$ GeV.
2. $45^o \leq \theta_e \leq 160^o$ & $E_\perp^e \geq 5$ GeV.

Here it can be seen that the events are classified according to the expected event topology. The loose electromagnetic fraction and missing $p_\perp$ cuts mean that the event classification should not lose many genuine high Q^2 events due to reconstruction and detector effects.

The above DST event classifications only select possible NC DIS event candidates and do not perform any e identification. These classified events must be analysed, in order, to identify the e cluster, which is done by the QJELEC algorithm. As described in the pervious chapter the e clusters identified by QJELEC must have a minimum energy of 8 GeV.

The acceptance of the above DST selection and event classification for MC NC DIS events was found to be 77 ± 2% over the full kinematic region accessible at HERA. However, the losses are dominated by the low Q^2_e/low x events where the electron scatters down the beam pipe.

In order to calculate the efficiency of the above DST selection and event classification only those events in which the e is scattered into the BEMC or LAr calorimeter are considered. From extensive MC studies, the efficiency of the DST criteria was calculated to be 98 ± 2% for e energies greater than 8 GeV. This efficiency calculation is based on the assumption that the relevant DIS L1 triggers are fully efficient. For energy clusters greater than 8 GeV, this assumption is valid for the BEMC and LAr trigger efficiencies observed for the H1 data analysed in this thesis (see Section 5.6). In the following analysis only those events which have passed the DST event classification and satisfied the QJELEC e criteria will be analysed. However, it is important to note that if the DST event classification is used after the QJELEC algorithm, then all events accepted by QJELEC would also pass the DST classification.

5.3 Vertex Reconstruction

As part of the DIS event selection, each event selected by the QJELEC algorithm was required to have a reconstructed vertex. This selection criteria was motivated by the observation of a large number of upstream proton background events, not vetoed by the TOF, which easily satisfied the DST and QJELEC criteria. These events were characterized by having BEMC and LAr calorimeter energy deposits, but no CJC tracks, hence, no reconstructed vertex. Figure 5.1 shows a typical background event, from an upstream proton interaction, which was put onto the DST and subsequently passed the QJELEC alogorithm.

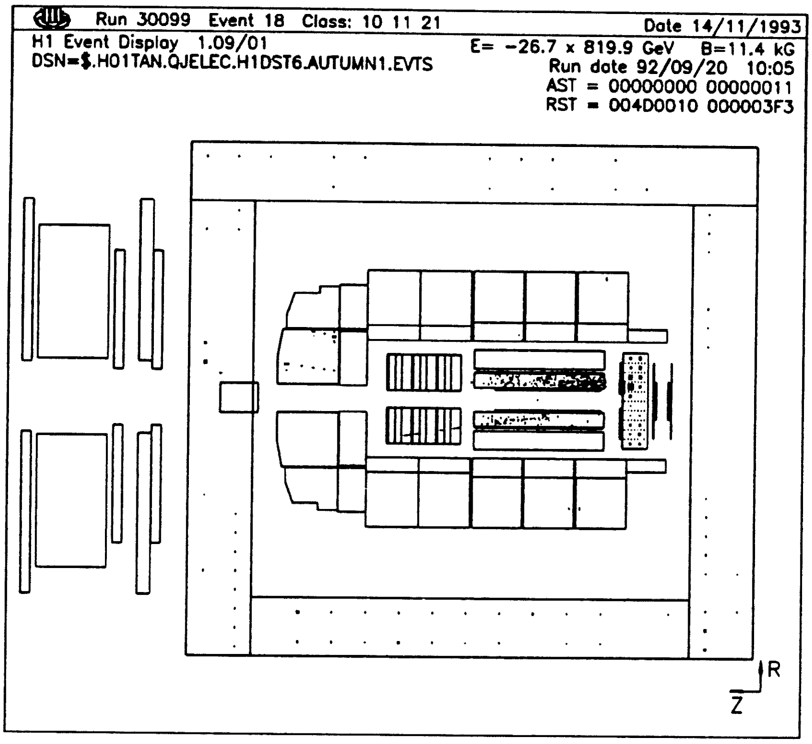

Figure 5.1: Typical background event due to an upstream proton interaction. The proton triggers the BEMC and subsequently passes the L1 and L4-L5 data selection levels.

Requiring a reconstructed vertex ensured that the background contamination rate was less than 3% of the selected data sample. This calculation was done by visually scanning events before and after the vertex requirement and studying the number events associated with the pilot bunches which satisfy the vertex cuts. The remaining background events are mainly due to beam-gas interactions within the interaction region. These events are visually indistinguishable from DIS events and their rate can only be determined from pilot bunch data. Secondly, as discussed in Section 4.4.4, the reconstructed θ_e resolution, for e's in the BEMC, is greatly improved when the events have reconstructed vertex. To ensure a good vertex resolution and that a good DIS interaction had taken place, all DST/QJELEC selected events were required to have a reconstructed vertex determined from at least two CJC tracks.

The z co-ordinate, z_{vtx}, of the reconstructed vertex was required to lie between $-50 \leq z_{vtx}(\mathrm{cm}) \leq 50$, which was compatible with the width of the z-vertex distribution of 40 cm (FWHM)[1] due to the length of the proton bunches in HERA. This z_{vtx} criteria was used to suppress the beam-induced background originating from outside the interaction region.

The efficiency for reconstructing the interaction vertex (ϵ_{vtx}) satisfying the above criteria is shown in Figure 5.2 for data and MC events. The vertex reconstruction efficiencies ϵ_{vtx} have been determined as a function of the scattered e's energy (E_e') in the angular regions $157.5^o \leq \theta_e \leq 162.5^o$, $162.5^o \leq \theta_e \leq 167.5^o$, and $167.5^o \leq \theta_e \leq 174^o$. To calculate ϵ_{vtx} only the events (data and MC) which have been classified as low Q^2 class 2 or high Q^2 and have satisfied the QJELEC alogorithm are used. These selected events have been visually scanned to remove obvious background events, similar to the one shown in Figure 5.1. The biggest background to the high Q^2 events comes from high energy cosmic ray e which pass through H1, leaving energy clusters in the LAr calorimeter and straight tracks in the CJC. The vertex reconstruction efficiency for a given E_e' and θ_e bin is determined as:

$$\epsilon_{vtx} = \frac{\text{Number of events passing vertex cuts}}{\text{Number of events selected}} \tag{5.1}$$

In the MC events the interaction vertex was simulated between $-70 \leq z_{vtx} \leq 70\,\mathrm{cm}$, thus in order not to bias the data vertex reconstruction efficiencies, the ϵ_{vtx} values are corrected for interactions occurring in the region $|z_{vtx}| \geq 70\,\mathrm{cm}$ (see Section 5.6).

The resulting uncertainties on the ϵ_{vtx} (data) points represent the statistical errors combined (added in quadrature) with the errors due to corrections made to

---

[1] FWHM = full width at half maximum; the 'tails' of the vertex distribution where observed to extend, in z, to ±90 cm.

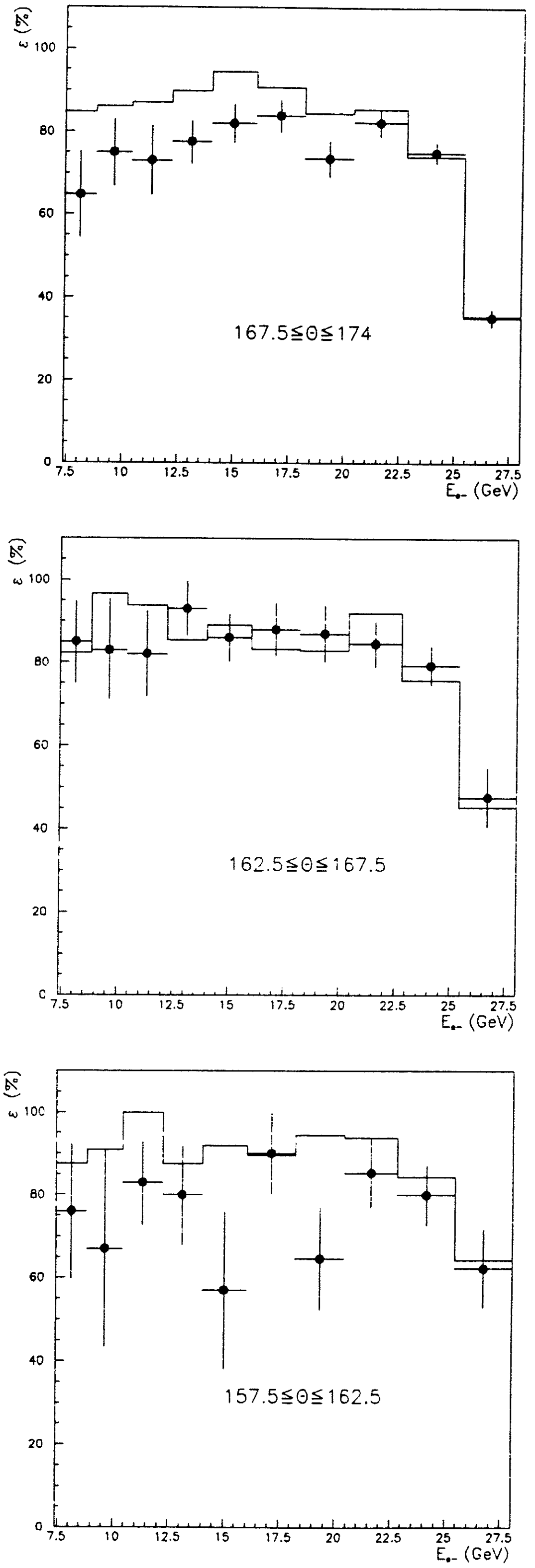

Figure 5.2: Vertex reconstruction efficiencies (ϵ_{vtx}) as a function of E'_e for the three given angular regions. The solid line indicate the MC values and the solid points correspond to the data.

remove events in the $|z_{vtx}| \geq 70\,\mathrm{cm}$ region.

From Figure 5.2 it can be seen that at large angles (top histogram) and $E'_e \leq 20\,\mathrm{GeV}$, there is a large discrepancy between the MC and data vertex reconstruction efficiencies. These observed differences lead to large shifts in the $F_2(x, Q^2)$ measurements, in the low Q^2/low x region if the acceptance corrections (see Section 6.2) are solely determined from MC events, since the efficiencies are overestimated for the MC sample. Hence, in order to accurately measure the DIS cross-sections (and $F_2(x, Q^2)$), the acceptance corrections have been modified such that they reflect the true vertex reconstruction efficiency, as observed from data. At lower scattering angles the data and MC appear to give reasonably consistent results within errors.

Aside from the above differences, it is interesting to see that, for MC and data, the ϵ_{vtx} values decrease at large E'_e ($E'_e \geq 22\,\mathrm{GeV}$) for all three θ_e regions. Kinematically, this high E'_e region corresponds to the high x/low y region (see Figure 5.7) where the current jet (or hadronic final state) is scattered into the forward regions of the CJC. As a result the CJC acceptance and reconstruction efficiencies of the final state particles drops rapidly as $x \rightarrow 1$. This explains the observed decrease in ϵ_{vtx} as E'_e increases. In the same kinematic region, it can also be seen that for fixed E'_e values the vertex reconstruction efficiencies increase with lower values of θ_e. This increase is solely due to the fact that CJC acceptance increases with decreasing θ_e.

In order to understand the origin of the ϵ_{vtx} discrepancies, various MC studies were made in which ϵ_{vtx} was calculated for MC events based on different models to simulate the hadronic final state (see Chapter 7). The resulting ϵ_{vtx} uncertainties, due to these different models, was found to be small, generally less than 5% for $E'_e \leq 20\,\mathrm{GeV}$. Hence, it can be concluded that the differences between data and MC are not attributed to the physics input, but may be due to inefficiencies in the CJC detector.

The above results can be summarized in terms of the accessible DIS kinematic plane. As a result of the characteristic DIS event topology, the event selection based on the vertex criteria inevitably results in large losses in the high x region and consequently, the DIS cross-sections cannot be accurately measured above $x = 0.01$.

However, in the more interesting low x region, the resulting event losses due to the vertex criteria are small, and do not affect any measurements in this region.

5.4 Reconstruction of the Event Kinematics

The determination of the DIS differential cross-sections strongly depends on the accuracy with which the kinematic variables, Q^2, y and x, can be measured. Thus, one of the major goals in DIS physics will be the accurate measurement of the event kinematics. This problem, over the past decade, has resulted in the development of various kinematic reconstruction methods. To date the following methods have been proposed and studied [62]:

1. Electron-only method: Q^2 and y are determined from the scattered e's energy and polar angle.
2. Hadrons-only method (Jacquet-Blondel): Q^2 and y are calculated from **all** the DIS final state hadrons.
3. Mixed method : Q^2 is determined from the e and y is calculated from the Jacquet-Blondel method.
4. Double-angle method: Q^2 and y are determined from the polar angles of the scattered e and current jet (struck quark).
5. Double-energy method: The energy of the scattered e and current jet are used to calculate Q^2 and y.

It is beyond the scope of this chapter, and thesis, to present detailed studies into the advantages and disadvantages of all the proposed methods, since this would diverge from the main essence of this chapter. It is worth mentioning that the latter two methods, double-angle & energy, are relatively new and are still under extensive studies. Results using these method have be presented in [62].

By far the most popular and widely used methods for kinematical reconstruction, to date, have been the Jacquet-Blondel and electron-only methods. It turns out that the comparisons between these two methods provides a good framework for the rejection of background photoproduction events which fake DIS events. Also, the event kinematics can be determined from a combination of the Jacquet-Blondel and electron- only methods. This combination is referred to as the 'mixed' method, and it's main advantage over the other two methods, is that the resultant kinematic resolutions remain approximately constant over a wide kinematic plane.

The aim of this section is to show the expected kinematic profiles for the Jacquet-Blondel, electron-only and mixed methods. The latter two methods have been used to extract the F_2 structure function from the data.

5.4.1 Reconstruction from the Scattered Electron

Using the leptonic kinematic definitions given in Section 2.2, the kinematic reconstruction from the reconstructed scattered e can be evaluated as:

$$y_e = 1 - \frac{E_f}{E_i}\sin^2\frac{\theta_e}{2} \quad Q^2_e = 4E_iE_f\cos^2\frac{\theta_e}{2} \tag{5.2}$$

where E_f (E_i) represents the energy of the scattered (incoming) e, and θ_e corresponds to the e scattering angle wrt. the proton direction (calculated from the BPC hit(s) or CJC track linked to the e cluster), and E_i = 26.7 GeV. The kinematic variable x_e can then be determined from the relation $Q^2_e = sx_ey$.

Differentiating the above equations, the expected Q^2, y and x resolutions can be derived as:

$$\begin{aligned}
\frac{\delta Q^2_e}{Q^2_e} &= \frac{\delta E_f}{E_f} \oplus \tan\frac{\theta_e}{2}\cdot\delta\theta_e && (5.3)\\
\frac{\delta y_e}{y_e} &= (1-\frac{1}{y_e})\cdot\frac{\delta E_f}{E_f} \oplus (\frac{1}{y_e}-1)\cdot\cot\frac{\theta_e}{2}\cdot\delta\theta_e && (5.4)\\
\frac{\delta x_e}{x_e} &= \frac{1}{y_e}\cdot\frac{\delta E_f}{E_f} \oplus (\tan\frac{\theta_e}{2}+(\frac{1}{y_e}-1)\cdot\cot\frac{\theta_e}{2}\cdot\delta\theta_e && (5.5)
\end{aligned}$$

It is obvious from the above equations that the y_e and x_e measurements can not extend far below $y_e \sim 0.1$ because the resolutions diverges as $y_e \rightarrow 0$. The resolutions are made worse by the fact that any mis-measurements of the e energy is amplified by the $\frac{1}{y}$ factor. The Q_e^2 values are well measured except in the kinematic regions where the e scattering angles are large, typically $\theta_e \geq 175^0$. In these cases the Q_e^2 resolution is dominated by the $\tan\frac{\theta}{2}$ term. However, the fact that the QJELEC criteria requires a BPC hit to be linked to the e cluster implies that $\theta_e \leq 174^o$. Thus for the e's that will be used in the forthcoming analysis, the $\tan\frac{\theta}{2}$ is relatively small except in a few cases, and the Q_e^2 resolution will be dominated by the e energy resolution.

Using equation 5.4 and the energy and θ_e resolutions observed in Sections 4.4.2 and 4.4.4[2] respectively, the y_e resolution is calculated to be 50% at $y_e = 0.1$ and better than 30% for $y_e \geq 0.15$. The Q_e^2 resolution, corresponding to $\theta_e \sim 174^o$, will generally be better than 10%; at lower scattering angles, the resolution will be better than 7%.

The above predictions are clearly confirmed in Figures 5.3(a)-(d), which show the correlations between the reconstructed (rec) and generated (gen) kinematic variables, y_e and Q_e^2. In order to highlight the above predictions and to appreciate the importance of the vertex criteria, described in Section 5.3, the figures labelled (a) and (c) contain all events selected by QJELEC (and H1DST) and the figures labelled (b) and (d) contain the selected events satisfying the vertex criteria.

From Figure 5.3(a) the rapid deterioration in the y_e resolution as $y_e^{mc} \rightarrow 0$ can be clearly seen. This effect is strongly suppressed by the vertex criteria, illustrated in Figure 5.3(b), which, as expected removes events in this troublesome low y_e region. Using these events, the y_e resolution, $\frac{\delta y_e}{y_e}$, is found to be 60±4% for $y_e \leq 0.1$, 34±2% for $0.1 \geq y_e \geq 0.2$ and 9% for $y_e > 0.2$. In general as y_e increases the resulting resolution is better than 9%.

Using the same y_e regions as above, the x_e resolutions were found to be 65±5%, 44±3% and 19%, respectively. In the latter two regions the x_e resolutions are larger than the corresponding y_e resolutions due to the presence of the extra $\tan\frac{\theta_e}{2}$ term in equation 5.5.

---

[2] Recall, $\frac{\delta E}{E} \sim 6\%$ and $\delta\theta_e \sim 3$ mrad for e in the BEMC.

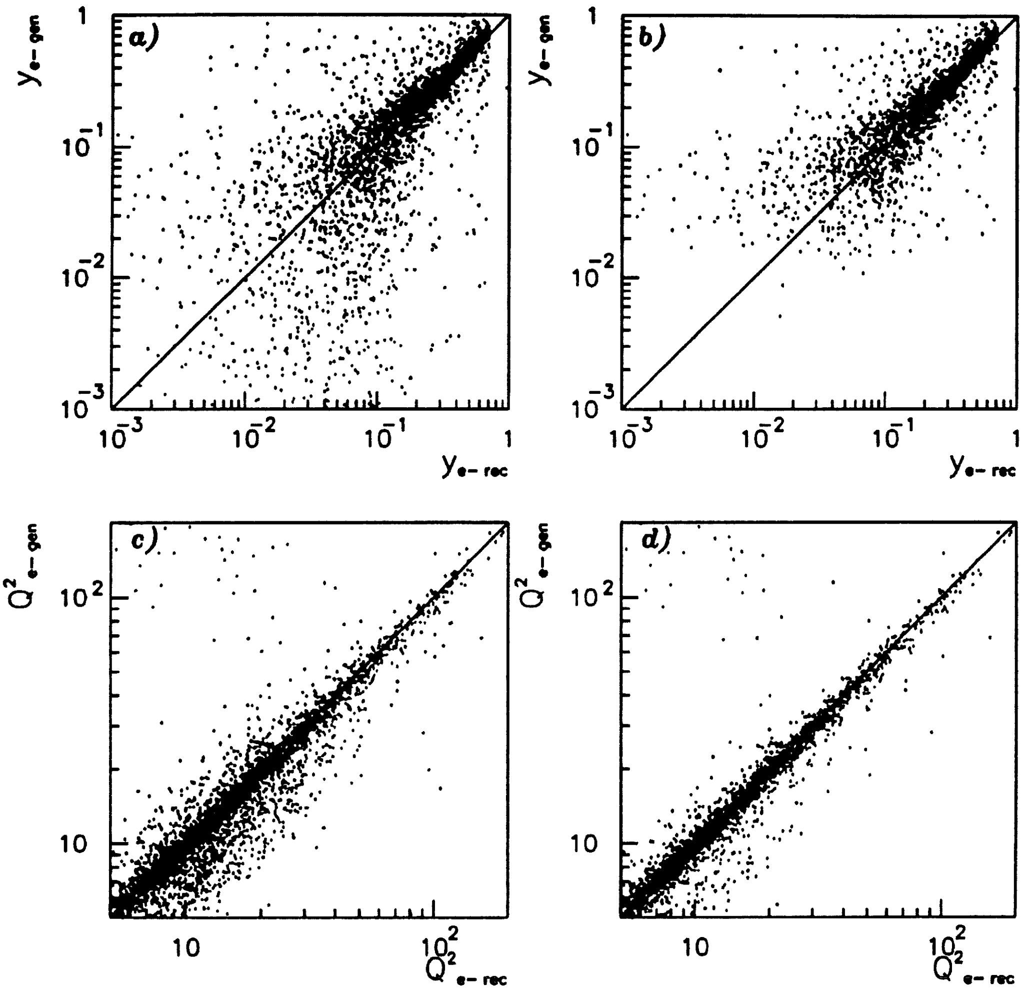

Figure 5.3: Correlation between the reconstructed and generated variables y_e ((a)-(b)), and Q_e^2 ((c)-(d)). The y_e resolution can be seen to deteriorate as $y_e \rightarrow 0$, and the Q_e^2 resolution can be seen to remain approximately constant.

On the other hand, from Figures 5.3(c) and Figures 5.3(d) the Q_e^2 correlation is observed to be very good over the full accessible kinematic range. Comparing these two figures it turns out that the vertex requirement remove the events in which $\frac{\delta Q_e^2}{Q_e^2} \geq 20\%$. Hence, the resulting Q_e^2 resolution is found to be less than 9%. The isolated events where $\frac{\delta Q_e^2}{Q_e^2} \geq 30\%$ are a direct result of energy losses in the BEMC and LAr calorimeter cracks or edges. In addition to these energy losses, the false e candidates from the DIS hadronic final state (see Section 4.6), introduce large shifts in the $\frac{\delta Q_e^2}{Q_e^2}$ determination. These false e candidates correspond to less than 1% of the total event sample, and are observed in the region $Q^2_{erec} > 100\mathrm{GeV}^2$ for $Q^2_{egen} < 40\,\mathrm{GeV}^2$.

The excellent resolutions obtained from the e kinematics, particularly in the high y_e region, indicate the motivation behind the use of the inclusive measurements. In addition, the clear signature of the scattered e eases all the systematic error studies.

5.4.2 Reconstruction from the Hadronic Final State

To enable the event kinematics to be reconstructed in Charged Current DIS events, where the scattered neutrino goes undetected, a method was devised to determine the event kinematics from the DIS hadronic final state (DHFS). This 'Jacquet-Blondel' method [69] is based on energy-momentum conservation between the 'invisible' neutrino, or the e in NC DIS, and the hadronic system, *i.e.* the vector sum of all outgoing hadrons. The kinematic relations are then derived from the definitions of Q^2 and y at the hadronic vertex (see Section 2.2):

$$y_{JB} = \frac{\sum_h (E_h - p_{zh})}{2E_i} \qquad Q^2_{JB} = \frac{(\sum_h p_{x\,h})^2 + (\sum_h p_{yh})^2}{1 - y_{JB}} \tag{5.6}$$

where, the above sum is performed **over all the outgoing hadrons**. As before E_i is the incoming e energy, 26.7 GeV.

Clearly, this method makes no assumption on the internal structure of the incoming proton or of the final hadronic system. In fact by using all the hadrons it avoids the difficult problem of hadronic jet definition. Another subtle feature of this method, is that it is independent of final-state radiative events, provided the e and

γ_{rad}^{FS} are removed from the DHFS.

As shown in the Section 4.4.2, the γ_{rad}^{FS} will generally be masked into the e cluster. However, the measured y_{JB} can be subject to large shifts, wrt. the interaction kinematics, for initial-state radiative events as $E_i \leq 26.7\,\mathrm{GeV}$.

By expanding the y_{JB} equation, it follows that each hadron produced at the interaction vertex contributes to y_{JB} by $\sin^2(\frac{\theta_h}{2}) \cdot \frac{E_h}{E_i}$. Thus for the particles along the proton direction, which are likely to be lost in the beam pipe, $sin^2\frac{\theta_h}{2} \sim 0$ implies that their contribution to y_{JB} will be very small. However, the final accuracy is determined by these particle losses. In fact these losses rapidly cause a deterioration in the kinematic resolution especially when the current jet is close to the beam pipe. The effects of these losses in the proton (forward) direction are increased by the exclusion of the plug calorimeter data.

In order to derive the Jacquet-Blondel resolution expressions, the variable y_{JB} and Q_{JB} are expressed as:

$$y_{JB} = \frac{(E_{hfs} - p_{zhfs})}{2E_i} \sim \frac{E_{hfs}}{E_i}\sin^2\frac{\theta_{hfs}}{2} \tag{5.7}$$

$$Q^2_{JB} = \frac{p^2_{\perp hfs}}{1 - y_{JB}} \sim \frac{E^2_{hfs}\sin^2\theta_{hfs}}{1 - y_{JB}} \tag{5.8}$$

here the subscript *hfs* refers to the total hadronic final state; *i.e.* summation over all hadrons. The variable θ_{hfs} is determined from the 4-vector corresponding to the hadronic final state.

Using these new expressions, the y_{JB} and Q^2_{JB} resolutions are derived as:

$$\frac{\delta Q^2_{JB}}{Q^2_{JB}} = \frac{2 - y_{JB}}{1 - y_{JB}} \cdot \frac{\delta E_{hfs}}{E_{hfs}} \oplus (2\cot\theta_{hfs} + \frac{y_{JB}}{1 + y_{JB}} \cdot \cot(\frac{\theta_{hfs}}{2})) \cdot \delta\theta_{hfs} \tag{5.9}$$

$$\frac{\delta y_{JB}}{y_{JB}} = \frac{\delta E_{hfs}}{E_{hfs}} \oplus \cot(\frac{\theta_{hfs}}{2}) \cdot \delta\theta_{hfs} \tag{5.10}$$

The experimental determination of the Jacquet-Blondel (JB) variables can be done either by summing over all calorimeter cells or over a combination of tracks and calorimeter cells. Due to the fact that the Plug calorimeter was not fully instrumented and operational during the data taking periods analysed in this thesis, the Plug data was not used for any part of the DIS analysis. Thus in order to present results that will accurately describe the expected resolutions from the H1 detector, the Plug data is excluded in the all the following MC studies.

It has been shown in [62] that the latter combined method is more precise, particularly at low Q^2 where the events are characterised by low particle energies and multiplicities. With this is mind, the combined method was used to determine the JB kinematical variables, since the low $p_\perp$ hadrons can be more accurately determined using the CJC data. In this combined method adapted in the forthcoming analysis only the LAr and BEMC calorimeter data are used together with reconstructed tracks which meet the following requirements (standard tracking criteria used by the H1 DIS groups):

- They must be measured in the CJC with a least 10 wire hits and $22^o \leq \theta_{trk} \leq 160^o$.

- After being constrained to the average beam position in the transverse (r-ϕ) plane and to the reconstructed z-vertex, the track must have $p_\perp \geq 0.1$ GeV and a fractional momentum error, $\frac{\sigma(p)}{p}$, of less than 0.5.

Double counting of energy is avoided by masking off calorimeter cells behind a CJC track in a cylinder of 15 (25) cm in the electromagnetic (hadronic) part of the LAr calorimeter. The contribution of the CJC tracks to the y_{JB} measurement was to found to vary between 40-50%. The use of the tracking data not only improved the y_{JB} resolution but minimised the systematic effects due to calorimeter energy scale uncertainties.

As before, the JB kinematic resolutions are shown as 2-dimensional correlations with the generated JB kinematics, Q^2_{JBgen} and y_{JBgen}. The corresponding reconstructed variables are denoted as Q^2_{JBrec} and y_{JBrec}. The correlations are shown for all events, Figures 5.4(a) and (c), and for events with a reconstructed vertex, Figures 5.4(b) and (d).

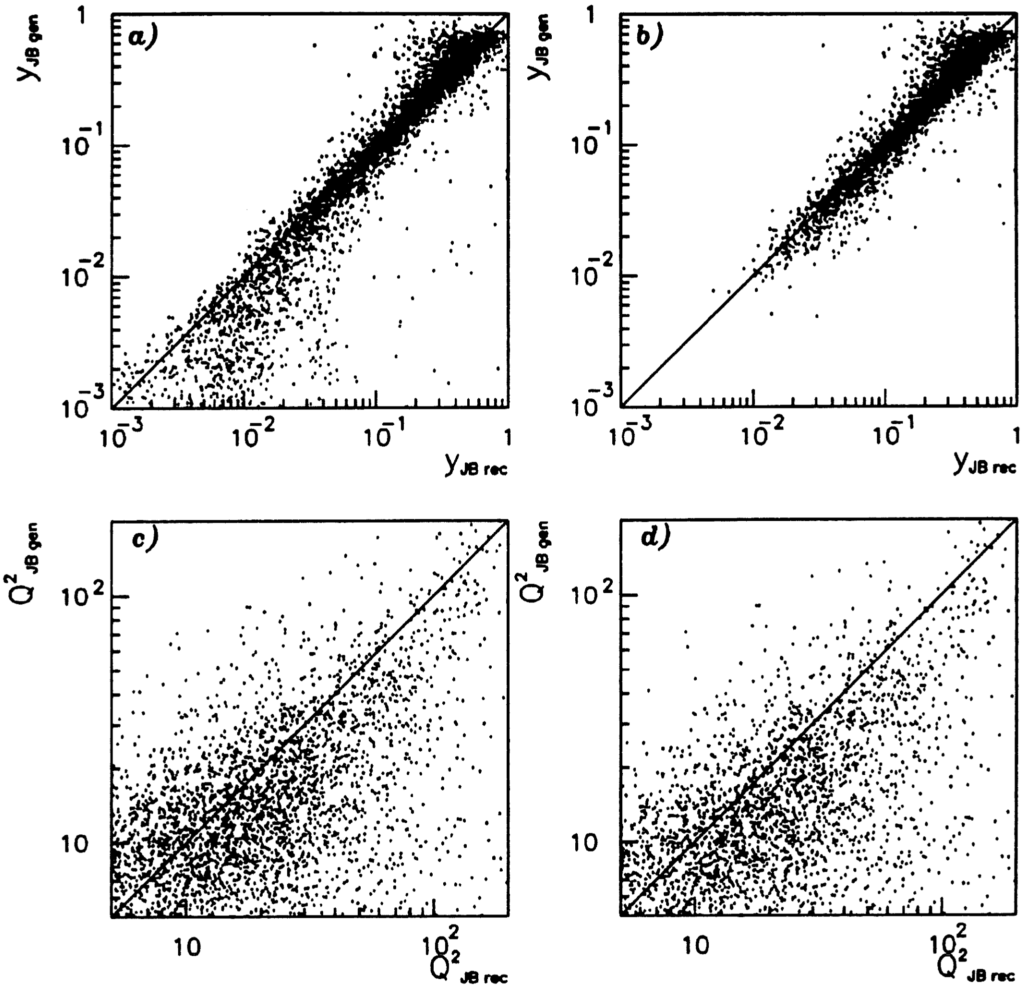

Figure 5.4: Correlation between the reconstructed and generated Jacquet-Blondel variables y_{JB} and Q^2_{JB}, for all events ((a) and (c)) and events with a reconstructed vertex ((b) and (d)).

It is immediately visible from Figure 5.4(a) that the y_{JBrec} resolution starts to deteriorates when $y_{JBgen} \leq 0.01$; ie. the kinematic region where the current jet gets more forward scattered as y_{JBgen} decreases. In this kinematic region particle losses down the beam pipe and the poor track acceptance in this forward region can introduce large biases in the y_{JBrec} measurement, as seen in Figure 5.4(a). A detailed study of this effect can be found in [65].

The y_{JBrec} correlation for the events which have passed the reconstructed vertex criteria, is shown in Figure 5.4(b). As expected, the vertex criteria removes the poorly determined y_{JBrec} events (observed in Figure 5.4(a)) and ensures that the y_{JBrec} will always be better than 30% for $y_{JBgen} \geq 0.01$. It can be seen the y_{JB} remains roughly constant over all y_{JB}.

The vertex criteria guarantees that some fraction of the outgoing hadronic energy is seen in the H1 detector. This implies that the y_{JB} resolution will be dominated by the $\frac{\delta E_{hfs}}{E_{hfs}}$ term, since the error on θ_{hfs} will have a small effect for these events. The effects of beam pipe loses is small, due to the larger angles of the hadrons, and so this energy resolution term will dominated by the calorimeter resolutions. This explains why the y_{JB} correlations observed in Figure 5.4(b) appears to be roughly constant.

Using the events in Figure 5.4(b), $\frac{\delta y_{JB}}{y_{JB}}$ is found to be 25±1% for $y_{JB} \leq 0.1$, 18% for $0.1 \leq y_{JB} \leq 0.3$ and 22% when $y_{JB} > 0.3$. Comparing these results with the $\frac{\delta y_e}{y_e}$ values, it is easy to conclude that in the low y region Jacquet-Blondel method is much more accurate than y_e. In the latter y_{JB} region the y_{JB} resolution is degraded by the poor hadronic calorimetry in the backward region.

The corresponding Q^2_{JB} correlations are shown in Figures 5.4(c) and (d). Clearly, the Q^2_{JBrec} determination using the Jacquet-Blondel method is extremely poor, particularly at low Q^2_{JB}. Referring, to the $\frac{\delta Q^2_{JB}}{Q^2_{JB}}$ expression, the largest error in the Q^2_{JB} determination, at low y_{JB}, is attributed to the large particle losses in the beam pipe. However, at higher y_{JB}, where a large fraction of the DHFS is seen by the H1 detector, the $\frac{2-y_{JB}}{1-y_{JB}}$ term rapidly increases degrading the Q^2_{JB} measurement. In the kinematic region $Q^2_{JB} \leq 50\,\mathrm{GeV}^2$ the Q^2_{JB} resolution was observed to be 79±5%.

Similarly, the x^{JB} resolution was found to be 64±2% over all x.

The results shown in this section clearly indicate the importance of the Plug calorimeter in the determination of the event kinematics, particularly Q^2_{JB}, from the hadronic final state. The absence of the Plug from this MC analysis gives a good indication into the expected kinematic resolutions for the early HERA data. From these results it can be concluded that in order to achieve accurate kinematical reconstruction the Jacquet-Blondel method cannot be used with the present state of the H1 detector.

5.4.3 Reconstruction using the Mixed Method

Comparing the results in the previous two sections, it is clear that both the JB and electron kinematics have some major shortcomings. It has been shown that, as a result of particle losses down the beam pipe, the Q^2 (and x) resolutions obtained using the JB method are extremely poor, whereas, the y resolution remains fairly constant. On the other hand, using the inclusive e measurements the Q^2 resolution was found to be better than 9%, whereas the y and x resolutions rapidly deteriorate as $y \longrightarrow 0$.

Forced with the above predicament, the mixed method was devised such that the event kinematics can be determined from the variables which are relatively insensitive to detector and reconstruction effects. In this method Q^2 measured from the scattered e and y is determined using the JB method. To appreciate the motivation behind the mixed variables, it is worth referring back to equations 5.3 and 5.10 which give the expressions for Q^2_e and y_{JB} resolutions, respectively. It can be seen that both expressions do not contain the divergent terms of the form $\frac{1}{y}$ or $\frac{1}{1-y}$. It is the absence of these troublesome terms that make the mixed method such an attractive way to determine the event kinematics, since the x variable x_{mix} $(\frac{Q^2_e}{sy_{JB}})$ can be accurately determined over full kinematic plane.

Since the Q^2_e and y_{JB} resolutions have already been shown in Figures 5.3 and 5.4, only the resulting x_{mix} resolution is presented in Figure 5.5. As before, the kinematic resolution is illustrated as a correlation between the reconstructed and generated x_{mix}.

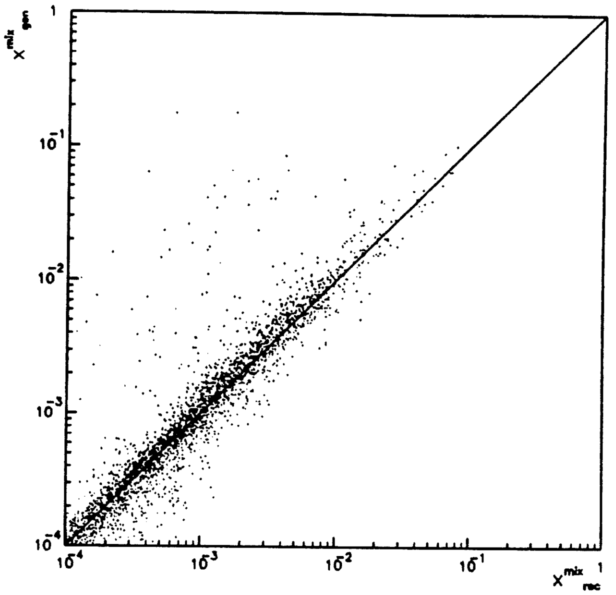

Figure 5.5: Correlation between reconstructed and generated x^{mix}. Only the events satisfying the vertex criteria are plotted.

The correlation between the reconstructed and generated x_{mix} appears to be good over the full x_{mix} range accessible after the vertex cut. The overall resulting resolution was found to be better than 10%. In the low x_{mix} the resolution was observed to deteriorate as a result of the poorer y_{JB} resolution when $y_{JB} \geq 0.3$.

However, aside from this slight deterioration in the x_{mix} resolution it is easy to see why the mixed method is used to determine the event kinematics. Unlike the inclusive e measurements the x_{mix} resolution remains relatively constant over the accessible kinematic region, thus, making it more favourable to use.

5.5 Study of Photoproduction Background

Early results from the HERA experiments [60, 70] have shown that the total photoproduction (γp) cross-section is at least two orders of magnitude greater than the expected DIS cross-sections. Consequently, the DIS background rates from the various γp processes, described in Section 2.4, are expected to be high and greater than the beam induced background.

Unlike the beam gas or beam wall interactions, which can be easily suppressed by stringent vertex cuts (and visual scanning), the DIS background from γp events are difficult to suppress. Typically, these events contain a low $p_\perp$ e candidate in the BEMC and a reconstructed vertex from the outgoing hadrons, thus easily faking a low Q_e^2, low x DIS event. The rejection of this background is paramount to any DIS cross-section ($F_2(x, Q^2)$) measurement in this kinematic region.

In order to accurately study the γp background the following MC programs were used to generate the different γp subprocesses:

- The soft processes of the non-diffractive part of the total γp cross-section were generated according to the vector-meson dominance model using the RAYVDM generator [68]. The generated cross-section for these VDM events is 8.32 μb.
- For the hard scattering processes the PYTHIA 5.6 generator [67] was used. This MC generator has also been adapted to generate the elastic and diffractive γp events which contribute to the diffractive component of the total γp cross-section. The input proton structure function was parameterised using the MRSD0 parton distributions [66][3], and the photon structure function was parameterised with the GRV distribution [87]. The generated cross-section for the PYTHIA events was 6.739 μb.

The γp analysis presented in [60] show that the RAYVDM and PYTHIA MC datasets give a good agreement with the observed data distributions.

As before, these generated events are passed through the H1 detector simulation and reconstruction chains. The RAYVDM and PYTHIA events which are analysed by the QJELEC algorithm have been selected as DIS event candidates (DST level) by the H1 event classification algorithm, described in Section 5.2.

As mentioned in Section 4.6, apart from meeting the desired energy and θ resolutions, the final QJELEC e identification criteria were also motivated by the presence

---

[3] At the time of writing this thesis only the MRSD0 datasets were available for these γp studies.

of false e candidates from these γp events. Using the basic QJELEC e identification based on jet shapes, it transpired that a large fraction of fake e candidates came from low $p_\perp$ π's and γ's. Thus, the requirement that the e candidate must be linked to a CJC and/or BPC track removed any fake e candidates originating from these neutral particles. The low $p_\perp$ fake e candidates are removed by the cut based on the energy fraction in the BEMC's triangular stacks.

The effect of the above e identification criteria on the rejection of γp events is summarized in Table 5.1. The results presented in Table 5.1 show the number of MC DIS and γp events accepted by the QJELEC algorithm before and after the CJC/BPC and triangular stack cuts. The last column show the number of events which, in addition to the above criteria, pass the reconstructed vertex requirement. Due to the different kinematics of the soft and hard γp processes, the RAYVDM and PYTHIA results are shown separately. The total γp background is determined as the sum of the RAYVDM and PYTHIA events which have passed the above selection. All datasets correspond to an integrated luminosity of 120 nb^{-1}.

	QJELEC e selection		
	Before	After	With Rec. VTX
NC DIS	32482	20038	14072
RAYVDM	18076	2065	2003
PYTHIA	6345	2842	2671

Table 5.1: Table summerizing the expected rate of e candidates from DIS and γp events.

The numbers shown in Table 5.1 clearly show the importance of the extra QJELEC criteria. Without, these cuts the background rate from γp events can be seen to be 75% of the DIS acceptance rate. This number is only meant to give an indication into the different acceptance rates, since the number of DIS events is strongly dependent on the shape of input parton distribution functions. In fact, if the DIS events are generated using the MRSD0 parton distributions then this background rate would be at least 27% greater than the DIS rate. In the DIS kinematic range accessible at HERA ($Q^2 \geq 3\,\mathrm{GeV}^2$ and $10^{-4} \leq x \leq 1$), the MRSD0 DIS cross-section (including first order electroweak corrections) is approximately 44% lower than the MRSD− cross-section.

The γp events remaining after the final e identification criteria contain e candidates which are predominately due to charged hadrons, mainly $\pi^{\pm}$, and to a lesser extent $e^{\pm}$ originating from the semi-leptonic decays of photoproduced c and b quarks. From the numbers shown in Table 5.1 it can be easily seen that after the final QJ-ELEC requirements the γp background rate is roughly 25%.

Due to the different events topologies of the accepted DIS and γp events it can be seen that for these background physics processes the vertex requirement has little impact in the rejection of these γp events. After the vertex requirement, due to the large DIS event losses in the high x (low y) region, the γp background rate rises to 33%. Therefore, the only other way to reduce this background is to make use of the different kinematic properties between DIS and γp events.

In contrast to DIS events observed by H1 which occur at Q^2_e values greater than 5 GeV^2, γp events occur at very low Q^2_e, $Q^2_e \leq 4\,\mathrm{GeV}^2$, in which the e scatters down the beam pipe. For events where $Q^2_e \approx 0$, the scattering angle ($\theta_e \leq 5$ mrad wrt. the electron beam direction) is such that the energy of the e can be measured in the H1 electron tagger. Therefore, one possible way to reduce the number of γp events is to check for energy measurements in the electron tagger.

However, the γp rejection efficiency of this criteria is restricted by the limited acceptance of the electron tagger, which is about 20 % of the γp events. By rejecting events in which the electron tagger energy is greater than 3 GeV[4] the remaining PYTHIA events are reduced by 60% and the RAYVDM events reduced by only 10%.

Since the e scatters down the beam pipe the γp events should have no kinematic correlation between y measured from the fake e candidate (y_e^{rec}) and the hadronic final state (y_{JB}^{rec}). This is due to the fact that the fake e candidate is itself part of

---

[4] For the data used in this thesis, the e tagger noise threshold was found to be 2-3 GeV, thus, by rejecting events with an energy > 3 GeV avoided possible DIS event losses due to this noise.

the hadronic final state, so removing this cluster from the y_{JB}^{rec} determination will introduce large errors in the correlation. This is not the case for DIS events in which the scattered e is identified and, as shown in the last section, the y variable can be accurately determined from the e or the hadronic final state.

The above kinematic correlations for the γp and DIS events are shown in Figures 5.6(a)-(b) and 5.6(c), respectively. As expected for the DIS data, Figure 5.6(c) shows a clear correlation between y_e and y_{JB} particularly in the region $y_e \geq 0.1$, where $\frac{\delta y}{y}$ is found to be better than 12%. This is not the case for the background γp events. From Figures 5.6(a) and (b) it can be seen that, independently of y_{JB}, there appears to be an accumulation of events in the region $y_e \geq 0.6$; *i.e.* low e energies. In contrast to the DIS correlation, this accumulation of high y_e events is more predominant for the γp events.

Based on this observation, and on the badly correlated DIS events, events were rejected if:

- $y_{JB} < \frac{1}{2}y_e$, for $y_e \geq 0.6$. The events removed by this cut are indicated on Figures 5.6(a)-(c) by the dashed line.
- $|y_{JB} - y_e| > 0.4$

For the large majority of γp events the above y cuts are correlated together, *i.e.* the event can be rejected by both criteria. However, the first of these two criteria is designed to remove the γp events which are observed in the high y_e region, and the second cut is designed to remove those events which fail the first cut, but nevertheless, have a poor $y_{JB} - y_e$ correlation.

The background rejection of these y cuts is better than 75% for the PYTHIA events and 88% for the RAYVDM events. The γp events remaining after these cuts are kinematically indistinguishable from DIS events. Reduction of the remaining γp event would inevitably result in large losses in DIS events due to further cuts. It is for this reason that the no further rejection criteria are applied. It is worth mentioning, that these remaining events have no e tagger signal.

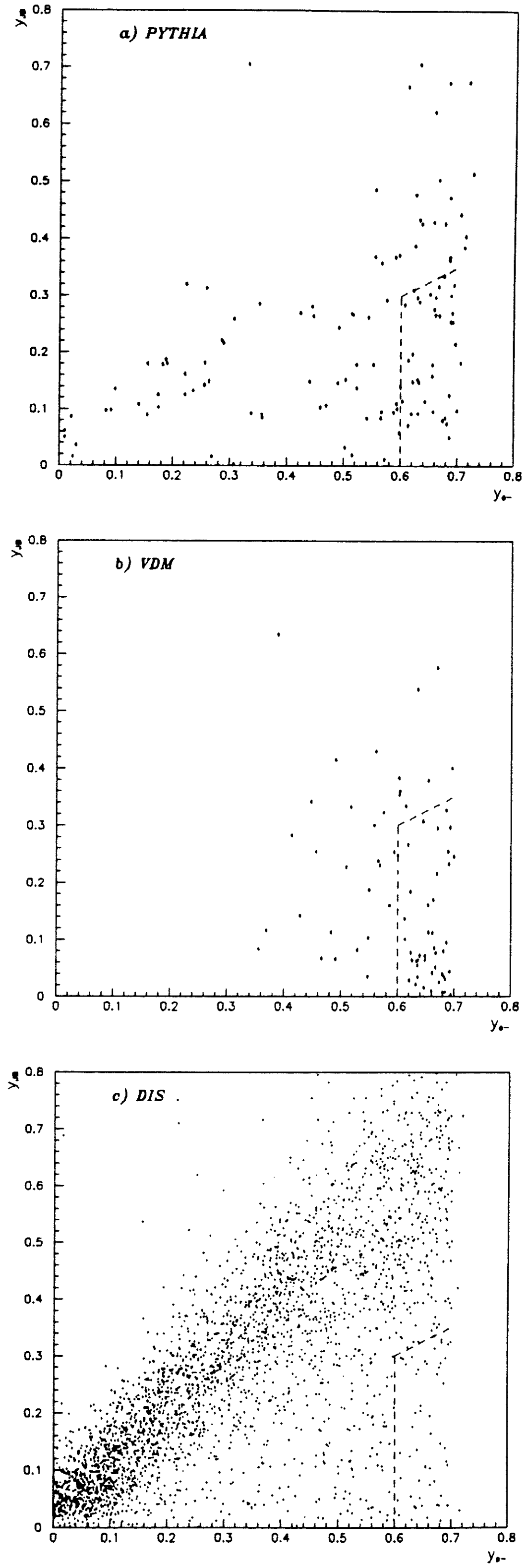

Figure 5.6: Correlation between kinematic variables y_{JB} and y_e for MC γp (a)-(b) and DIS (c) events. The dashed lines mark the region where events are rejected by the y cut; $y_{JB} < \frac{1}{2}y_e$ for $y_e \geq 0.6$.

To conclude this section a summary of the above cuts applied to γp and DIS events are presented in Table 5.2. Each column represents the number of DIS, RAYVDM and PYTHIA events remaining after the application of each rejection criteria. The columns are ordered in the following way:

- Column A: Number of events which satisfy the H1DST and QJELEC algorithms and have a reconstructed vertex.
- Column B: Events remaining after removing the events with electron tagger energy.
- Column C: Final number of events which remain after both y cuts.

MC data	A	B	C
NC DIS	14072	14072	13570
RAYVDM	2003	1803	213
PYTHIA	2672	1069	271

Table 5.2: Expected number of DIS and γp events remaining after each rejection criteria have been applied

The results presented in Table 5.2 show a significant decline in the γp background rate after the kinematic cuts based on the y variable. Inevitably, as a results of detector and reconstruction effects, the kinematic cuts also reduce the DIS acceptance but this is a small effect compared to the γp losses. The γp events remaining can be further reduced if the DIS physics analysis is restricted to the kinematic region $y_e < 0.6$. This requirement has the important advantage of avoiding the effects of large radiative corrections to the measured cross-sections. More details will be given Section 6.2.4.

Based on the event numbers shown in Table 5.2, the event selection described in this chapter has a γp rejection efficiency of 90±2%. The 2% error represents the uncertainty in the efficiency calculation due to possible energy mis-calibrations of 2% and shifts in the θ_e determination of 3 mrad (see Section 5.6). However, this rejection efficiency may be subject to a larger uncertainty due to the effects of different input parton structure functions in the MC data. It is expected that this uncertainty should only be at the few percent level. Aside from this uncertainty, the conclusions remain the same, in that the expected γp background rate is calculated to be less than 5%, which is a substantial improvement on the expected rate observed in Table 5.1. The remaining γp events can then be subtracted statistically from the DIS data sample.

5.6 Event Selection Summary & Global Uncertainties

In this section a brief summary is given for each of the criteria used to select the NC DIS event candidates from the H1 DST data, together with the relevant H1 detector and trigger efficiencies.

Using the H1DST event data, NC DIS candidates are selected offline by the following requirements:

1. A BEMC or LAr energy cluster must be selected by the QJELEC e identification criteria.
2. The event must have a reconstructed vertex which has been determined from at least 2 CJC tracks. Also, the z vertex position must lie between ± 50 cm from the nominal interaction point.
3. Events are rejected if a signal greater than 3 GeV is observed in the electron tagger.
4. There has to be a good correlation between the y_e and y_{JB} kinematic variables; the difference between these two variables must be less than 0.4 and $y_{JB} \geq \frac{1}{2} y_e$ for $y_e \geq 0.6$.

It is important to note that the use of cuts (3) and (4) on DIS events do not affect the results presented in Sections 5.4.1, 5.4.2 and 5.4.3; the kinematic resolutions remain unchanged.

The efficiencies for cuts (1) and (2) have been determined directly from the data and were found to be:

- Cut (1): By taking the events in which a BEMC cluster was linked to a CJC track, the efficiency for selecting e candidates in the BEMC by requiring a BPC hit was found to be 92±5% at low e energies and 95±3% at high energies. These efficiencies are in excellent agreement with MC predictions. In this calculation it has been assumed that the BPC efficiency is independent of the e impact point (angle).
- Cut (2): The efficiency for reconstructing an interaction vertex was determined to be 76±8% at large θ_e and 86±6% at lower θ_e, for e energies less than 22 GeV. As shown in 5.3 this is in sharp contrast to the MC predictions of 88±4% at large angles and 90±3% at lower angles.

The relevant L1 BEMC and LAr electron triggers were fully efficient for e energies greater than 8 GeV. However, the TOF trigger was found to veto genuine DIS events which lead to event losses of 4±3% [71]. As a result of the vertex requirement, it was found that 10±2% of the DIS event candidates put on DST were being lost due to the z_{vtx} position cut. These event losses were due to DIS events occuring in the tails of the z_{vtx} distributions, and were not simulated in the MC event files. The largest event losses, approximately 6%, were attributed to interactions originating from 'satellite' proton bunches.

During the injection of proton bunches into the HERA proton ring, it was found that for each main proton bunch there was a smaller proton bunch trailing by 8 ns. Once the bunches are in HERA, they are compressed into a smaller z region, however, if some bunches are too long, during the compression the protons in the tail of the bunch gets split from the original bunch, and forms a stable satellite bunch. These satellite bunches contributed around 6% of the DIS event sample. As a result of this 8 *ns* difference, the interaction vertex for the satellite bunch events was found to be around $z_{vtx} \sim -130\,\text{cm}$, well outside the limits of cut (2).

Since the L1 trigger efficiencies and events losses due the z_{vtx} position are independent of the event kinematics they correspond to the global detector efficiency, ϵ_{H1}. Using the above information it can be seen that for the data analysed in this thesis $\epsilon_{H1} \sim 0.86$. This global efficiency factor can be can be conveniently used as a weighting factor in the MC distributions, in order to simulate these event losses.

The uncertainty in the L1 trigger efficiencies and DIS event losses together with a 7% error in the luminosity measurement, leads to a global normalization uncertainty of 8%; all error sources are added in quadrature.

The following reconstruction uncertainties contribute to the systematic errors on the cross-section and $F_2(x, Q^2)$ measurements:

- Based on $p_\perp$ balance in DIS events where the current jet and e are detected, the hadronic energy scale is known to within 7%. By comparing $e^\pm$ tracks in the CJC with the corresponding LAr cell energies the electromagnetic energy scale is known to an accuracy of 2%.
- Using the double angle formula, the e energy can be calculated from the reconstructed e angle and the angle of the hadronic final state. Comparisons between the measured and calculated leads to an energy scale uncertainty of 2%.
- The uncertainty in the θ_e determination was found to be 3 mrad for events in which the e angle was calculated from the BPC point and CJC track.

5.7 First Look at the Selected Data

To conclude this chapter a brief discussion is presented for the DIS events selected, using the offline cuts defined previously, from the Autumn 1992 data. Detailed analysis of this data will be presented in the forthcoming chapters.

During this data taking period roughly 50000 DIS event candidates were put on the DST of which only 1809 events survived the offline selection criteria. Figure 5.7 shows the distribution of the selected DIS event candidates in the $x - Q^2$ plane. As expected the majority of the data can be seen to accumulate in the low x and low Q^2 region, as a result of the $\frac{1}{Q^4 x}$ dependence of the cross-section (see Section 6.2).

From the remaining 1809 events only 34 high Q^2 events were observed in which the e scatters into the LAr calorimeter. The highest Q^2 event was found to be $Q^2 = 1935\,\mathrm{GeV}^2$, and is shown in Figure 5.8. In this event, the current jet can be clearly seen to scatter into the forward region of the LAr calorimeter, with the e scattering into the lower barrel region. Using the simple parton model formulae, the scattering angle (θ_{jet}) of the struck quark is calculated to be 75^o. However, hadronization between the struck quark and the proton remnant has the effect of pulling the resulting current jet towards the proton direction, thus, reducing θ_{jet}. This smearing effect explains the situation in Figure 5.8 where $\theta_{jet} \sim 25^o$.

On the other hand, from the 1775 events in which the e scatters into the BEMC calorimeter, the lowest x event was found to be $x = 0.000038$. This event is shown in Figure 5.9, for θ_{jet} was calculated to be $\sim 176^o$. As above, the effect of hadronization between the struck quark and proton remnant, results in particles emerging at lower angles. However at low Q^2 and low x, the energy of the current jet is small and so little energy is seen in the calorimeter, as can be seen in this event.

The kinematics for both figures are determined from the e kinematic variables. For both events some energy flow in the very forward part of the LAr calorimeter can be seen. This is due to the particles from the proton remnant. The hits in the first two planes of the forward muon system are due to secondary particles originating from the proton remnant interactions in the Plug calorimeter and the HERA magnets.

One salient feature of the good $y_e - y_{JB}$ correlation for DIS events is that the ratio $\frac{y_e}{y_{JB}}$ should peak around 1. Comparisons of this ratio between MC and data provide a fast, but simple, method to check the accuracy by which the hadronic final state is simulated in the CJC and H1 calorimeters. This ratio is shown is in

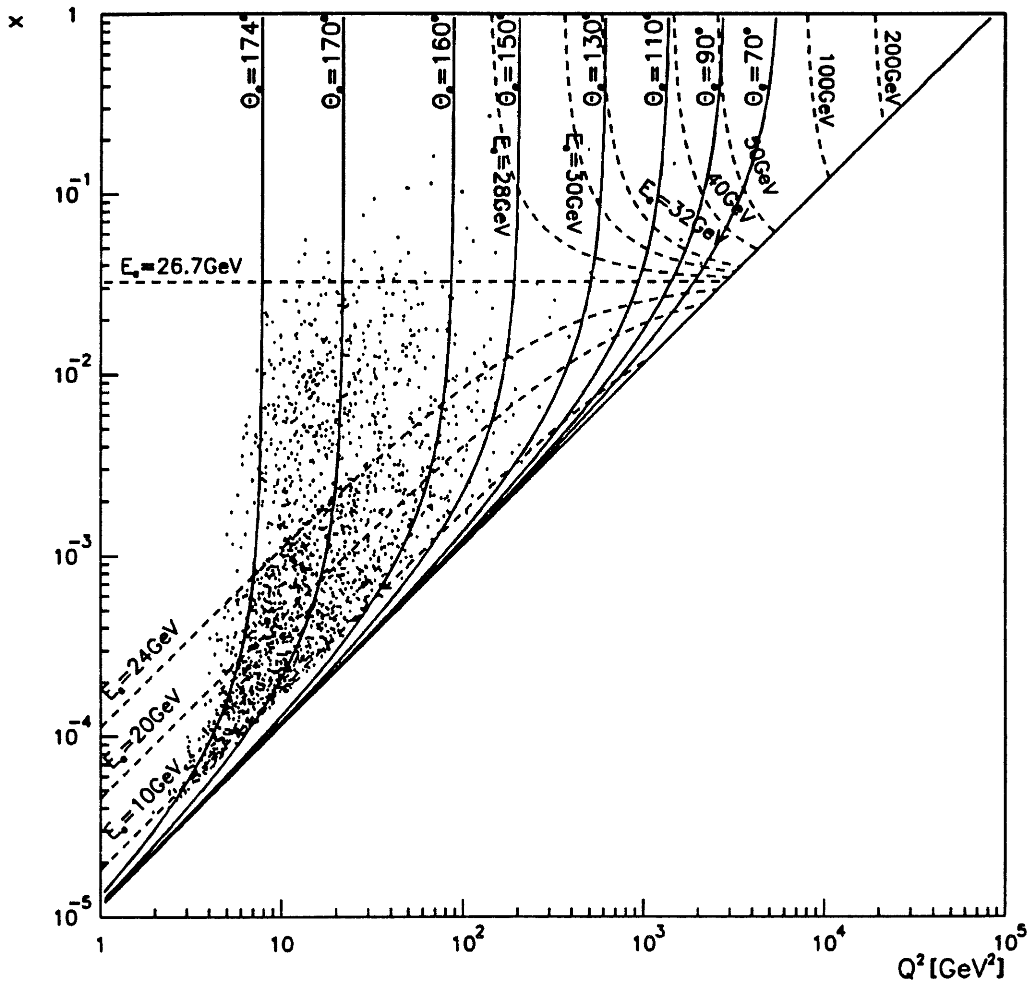

Figure 5.7: $x - Q^2$ distribution of the 1809 DIS event distributions. Also shown on the figure are the lines of constant E'_e and θ_e.

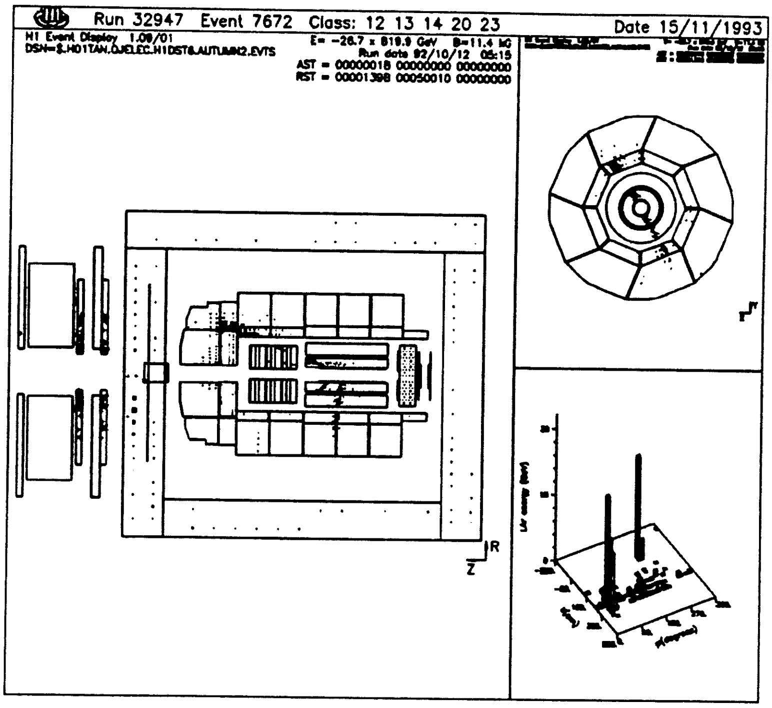

Figure 5.8: A deep inelastic scattering event at $Q^2 = 1935\,\mathrm{GeV}^2$ and $x = 0.046$, as seen in the H1 detector. Also shown are the radial view of the central tracking detector and LAr calorimeter, together with the LAr energy flow in $\eta - \phi$ space.

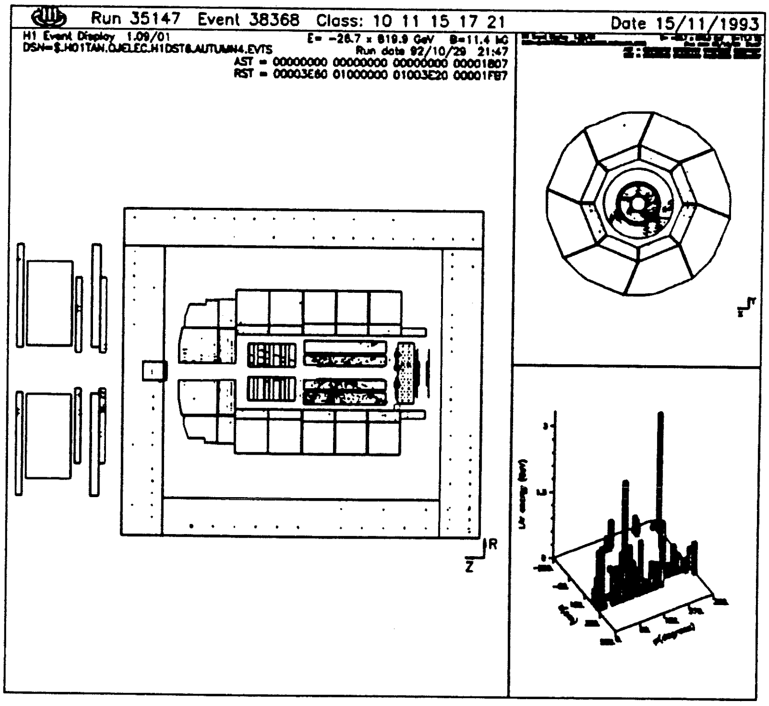

Figure 5.9: This figure shows the deep inelastic scattering event that was recontructed with the lowest x value. The kinematics of this event are $Q^2 = 1.95\,\mathrm{GeV}^2$ and $x = 0.000038$.

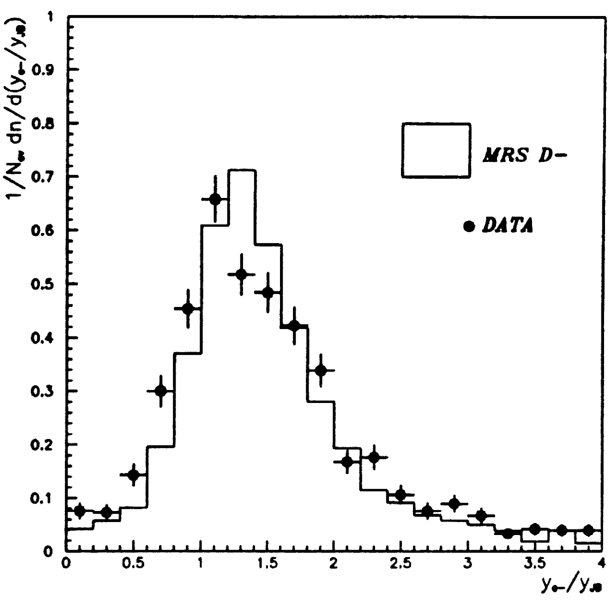

Figure 5.10: Distribution of the ratio $\frac{y_e}{y_{JB}}$. The solid histogram corresponds to the Monte Carlo prediction. Both the data and MC points have been normalised to 1.

Figure 5.10, for the 1809 selected events together with the MC prediction. It can be seen that the resulting resolution, or width, of the distribution is well described by the MC event sample, and both distributions peak around 1. Hence, the MC event sample can be reliably used to study the affects of event migration between kinematic regions, due to mis-measurements of y_{JB}, and thus, be used to determine the acceptance corrections needed to measure $F_2(x, Q^2)$.

Finally, Figure 5.11 shows the z_{vtx} distribution for the selected data and MC events. Once again, there is a good agreement between the two event samples, clearly indicating that the vertex distribution, in the region $|z_{vtx}| \leq 50\,\text{cm}$, is well simulated.

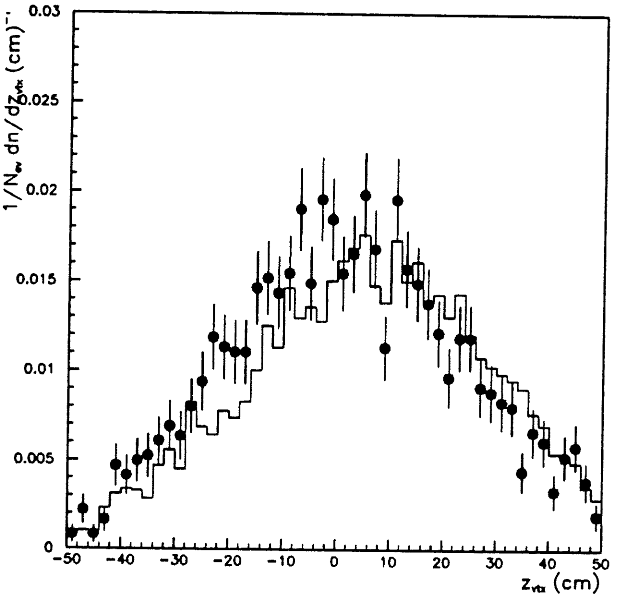

Figure 5.11: Reconstructed z_{vtx} distribution for MC and data. As before, the solid histogram represents the MC distribution and the solid point corresponds to data.

Chapter 6

Measurement of the Total Cross-section(s) & the Proton Structure Function $F_2(x, Q^2)$

6.1 Introduction

This chapter is devoted to the extraction of the F_2 structure function from the data taken by the H1 detector during the first year of physics collisions at HERA. In 1992 the H1 detector recorded data corresponding to an integrated luminosity of 1.5 nb^{-1} during the July data run, and 22.5 nb^{-1} during the period September-November. The results presented in this chapter are based on the data taken during the Sept.-Nov. period, due to the larger event statistics available. The DIS analysis of the July data has been performed by H1 and can be found in [59, 61].

The first half of this chapter is dedicated to the relevant theoretical and experimental information needed for the cross-section and structure function measurements. In the latter half, the extracted results are presented and compared with up-to-date theoretical predictions. The $F_2(x, Q^2)$ analysis is based on two independent methods in which the kinematics are determined from the leptonic and mixed variables, thus allowing accurate measurements to be over the full x range. In concluding this chapter a discussion is presented concerning the observed cross-section and F_2 measurements.

6.2 Cross-section and Structure Function Determination

In Section 2.3.2 it was shown that the observed NC DIS cross-section is given by:

$$\frac{d^2\sigma_t}{dxdQ^2} = \frac{d^2\sigma_o}{dxdQ^2} + \frac{\alpha}{2\pi}\frac{d^2\sigma_1}{dxdQ^2} + \mathcal{O}(\alpha^2) \tag{6.1}$$

where, the first term on the right hand side denotes the Born cross-section and the other terms represent the electroweak radiative radiative corrections in first and second order. Referring back to Section 2.3.2, it was shown that in the low x region, the Born cross-section can be expressed in terms of the F_2 structure function and the photoabsorption cross-section ratio, R:

$$\frac{d^2\sigma_o}{dxdQ^2} = \frac{2\pi\alpha^2}{Q^4x}\left(2(1-y) + \frac{y^2}{1+R(x,Q^2)}\right)F_2(x,Q^2) \tag{6.2}$$

for $Q^2 \ll M_Z$ where the contribution due to the xF_3 term can be neglected.

In the analysis of the DIS data, the Born cross-section is derived from the experimentally observed cross-section and then the F_2 structure function is extracted using equation 6.2. In order to extract the Born cross-section it is convenient to rewrite equation 6.1 as:

$$\frac{d^2\sigma_t}{dxdQ^2} = \frac{d^2\sigma_o}{dxdQ^2} \cdot (1 + \delta(x,Q^2)) \tag{6.3}$$

where, the term $\delta(x,Q^2)$ is known as the radiative corrections and accounts for the QED contributions to the measured DIS cross-sections.

Thus, in order to determine the Born cross-sections and F_2 both the radiative corrections and the photoabsorption ratio have to be known. However, the ratio $R(x,Q^2)$ has not been measured at HERA[1], so $R(x,Q^2)$ has to be calculated according to an assumed QCD prescription and input parton distributions. In the F_2

---

[1] To measure $R(x,Q^2)$ would require HERA to run at lower energies.

analysis, $R(x,Q^2)$ $\left(= \frac{F_L(x,Q^2)}{F_2(x,Q^2)-F_L(x,Q^2)}\right)$ is calculated using the $\mathcal{O}(\alpha_s)$ QCD prediction for F_L[78]:

$$F_L = \frac{\alpha_s(Q^2)}{4\pi}\left(\frac{16}{3}I_F + (8\sum_{i=1}^{4} Q_i^2)I_G\right) \tag{6.4}$$

where

$$I_F = \int_x^1 \frac{dz}{z}\left(\frac{x}{z}\right)^2 F_2(x,Q^2) \tag{6.5}$$

$$I_G = \int_x^1 \frac{dz}{z}\left(\frac{x}{z}\right)^2 \left(1-\frac{x}{z}\right) zg(z,Q^2) \tag{6.6}$$

here, Q_i refers to the quark's electric charge and the summation is over the four flavours, **u**, **d**, **c**, **s**, and $zg(z,Q^2)$ refers to the gluon structure function.

For a given kinematic bin of size Δx ΔQ^2, the experimentally observed cross-section can be expressed as:

$$\sigma^{obs}_{\Delta x \Delta Q^2} = \sigma^{t}_{\Delta x \Delta Q^2} + \sigma^{bck}_{\Delta x \Delta Q^2} \tag{6.7}$$

where σ^t corresponds to the total radiative DIS cross-section (equation 6.1) and σ^{bck} represents the correction term which allows for fake DIS events coming from background processes.

The relative contribution of each of the above cross-sections to the experimentally observed cross-section depends on the experimental cuts used to select the data and the kinematic region in which the cross-section (F_2) measurements are made. It is also important to mention that the radiative corrections needed to extract the Born cross-sections are also strongly coupled to the measurable kinematic regions. In the previous chapter it was shown that the beam-induced background is strongly suppressed by the vertex criteria, whilst the larger γp background can be reduced by stringent kinematic correlations. However, the observed cross-section may still contain a sizeable contribution from the γp background, particularly in the low x/low Q^2 region.

On the basis of the above information, the total DIS cross-section in a given (x,Q^2) bin is experimentally determined by:

$$\sigma^t_{\Delta x \Delta Q^2} = \frac{N^{tot}_{\Delta x \Delta Q^2} - N^{bck}_{\Delta x \Delta Q^2}}{\epsilon_{H1} \cdot A(\Delta x, \Delta Q^2) \cdot \mathcal{L}} \tag{6.8}$$

where $N^{tot}_{\Delta x \Delta Q^2}$ is the number of selected events in the kinematic bin and $N^{bck}_{\Delta x \Delta Q^2}$ is the expected number of background events in that bin. $A(\Delta x, \Delta Q^2)$ is known as the smeared acceptance of the bin (see below). The global variable ϵ_{H1} represents the overall efficiency of the H1 detector, and in general accounts for trigger inefficiencies and event loses at the L1 stage which are not included in the MC simulations. $\mathcal{L}$ corresponds to the total integrated luminosity of the data sample recorded by H1 from which the DST data were created.

Due to measurement errors and the acceptance of the H1 detector, the observed event rate in a given kinematic bin will, in practice, not be the true event rate, since events can get lost down the beam pipe and migrate into and out of the bin. To determine the true cross-section in a given bin, the observed cross-section is divided by a discontinuous function, known as the 'smeared acceptance' $A(\Delta x, \Delta Q^2)$ of the bin. The smeared acceptance is a convolution between the detector acceptance and measurement/reconstruction effects, and is defined as:

$$A(\Delta x, \Delta Q^2) = \frac{N^{rec}_{\Delta x, \Delta Q^2}}{N^{gen}_{\Delta x, \Delta Q^2}} \tag{6.9}$$

where, the numerator represents the number of events reconstructed in the bin (after event selection cuts), and the denominator corresponds to the number of MC events generated in that bin.

This function can only be precisely determined from accurate simulations of the H1 detector and it is dependent on the chosen bin size, cross-sections in that bin, and on detector acceptance/resolutions and event selection. Therefore, the MC from which the smeared acceptances are calculated, and used for the measurement of σ_t, must accurately reproduce the distributions observed for the data, particularly in the new, unexplored, low x region.

6.2.1 Bin Centre Corrections

The experimentally observed bin cross-section, $\sigma^t_{\Delta x \Delta Q^2}$, corresponds to the total integrated cross-section in that bin. Therefore, in order to extract F_2 at a chosen (x, Q^2) point within that bin, the integrated cross-section must be converted to give the differential cross-section at that (x, Q^2) point (equation 6.3). For convenience, the chosen point is usually the centre of the bin, although, any point within that bin can be used. This conversion is achieved by multiplying the measured cross-section $(\sigma^t_{\Delta x \Delta Q^2})$ by a factor known as the bin centre correction $(BCC(x, Q^2))$.

Each bin centre correction is determined from MC studies and is simply the ratio between the differential cross-section at the bin centre (or chosen (x, Q^2) point) and the total integrated bin cross-section. However, computing the total integrated cross-section is extremely time consuming as it requires the determination of the Born and radiative cross-sections at every integration step. By neglecting the radiative contributions and calculating the corrections using the Born terms only, the $BCC(x, Q^2)$ values change by less than 2%. Hence, the bin centre correction is defined as:

$$BCC(x, Q^2) = \frac{\left.\frac{d^2\sigma_o}{dxdQ^2}\right|_{x}^{Q^2}}{\int_{\Delta x}\int_{\Delta Q^2}\frac{d^2\sigma_o}{dxdQ^2}dxdQ^2} \qquad (6.10)$$

where, the cross-section formula corresponds to the Born cross-section given by equation 6.2. The numerator is evaluated at the bin centre and the denominator is evaluated by integrating over the kinematic limits of the bin. These limits are defined by the x and Q^2 bin boundaries and may also be defined by y and θ_e cuts (see Section 6.2.3).

It is important to note that the (x, Q^2) points chosen for the F_2 measurements are also the points at which the radiative corrections and photoabsorption ratios are determined.

In Section 6.3, the measured cross-sections are presented in bins of Q^2 and $\log_{10}(x)$. Similarly, the differential cross-sections $\frac{d\sigma_t}{dQ^2}$ and $\frac{d\sigma_t}{d\log_{10}(x)}$ are determined from the bin cross-sections ($\sigma_t^{\Delta Q^2}$ and $\sigma_t^{\log_{10}(x)}$) by applying factors which correct for finite bin sizes and kinematic constraints. These factors, known as the bin size corrections, are defined as:

$$BSC(\Delta Q^2) = \frac{\int_x \frac{d^2\sigma_o}{dx dQ^2}\Big|_{Q_c^2}}{\int_x \int_{\Delta Q^2} \frac{d^2\sigma_o}{dx dQ^2} dx dQ^2} \tag{6.11}$$

$$BSC(\Delta \log_{10}(x)) = \frac{\int_{Q^2} \frac{d^2\sigma_o}{dx dQ^2}\Big|_{x_c}}{\int_{Q^2} \int_{\log_{10}(x)} \frac{d^2\sigma_o}{dx dQ^2} dx dQ^2} \tag{6.12}$$

The denominators evaluate the integrated Born cross-section for a given ΔQ^2 or $\Delta \log_{10}(x)$ bin, by integrating over the allowable cross-section (after kinematic cuts) for that bin. The numerators are simply the integrated cross-section at the bin center, Q_c^2 or x_c

6.2.2 Comparison between Monte Carlo and Data

To decide which MC data set should be used to calculate the smeared acceptances, detailed comparisons were made between, fully simulated and reconstructed, MC events and real data. Both event samples were selected using the same event selection criteria summarized in Section 5.6, and the resulting data sample consisted of 1809 DIS event candidates.

The MC datasets used in this comparison were generated using the MRSD− and MRSD0 parton distributions [66], which give distinctive predictions for $F_2(x, Q^2)$ in the low x region, as shown in Figure 2.13 (Section 2.3.7); the low x evolution of the gluon density varies as $\frac{1}{\sqrt{x}}$ for MRSD− (steep rise in F_2) and is constant for MRSD0 (slow rise in F_2). This difference in the F_2 predictions lead to clear differences in the number of MC events selected, for a given luminosity, in the low x region.

In order to accurately describe the data, the MC distributions have been modified to include the expected contribution due to background γp events which survived the event selection criteria. The background contamination from γp events was determined from detailed MC studies based on the PYTHIA [67] and RAYVDM

[68] generators, which describe the hard and soft processes, respectively (Section 5.5).

Figures 6.1(a) and 6.1(b) show the energy and theta (θ_e) distributions of the selected e candidates compared with the MC predictions normalized to the data luminosity ($22.48\,\text{nb}^{-1}$). These MC distributions have been modified to account for the observed vertex reconstruction efficiencies between MC and data, and global event losses due to TOF inefficiencies and vertex position cuts (see Section 5.6). The overall normalization differences between the two MC distributions can be clearly seen.

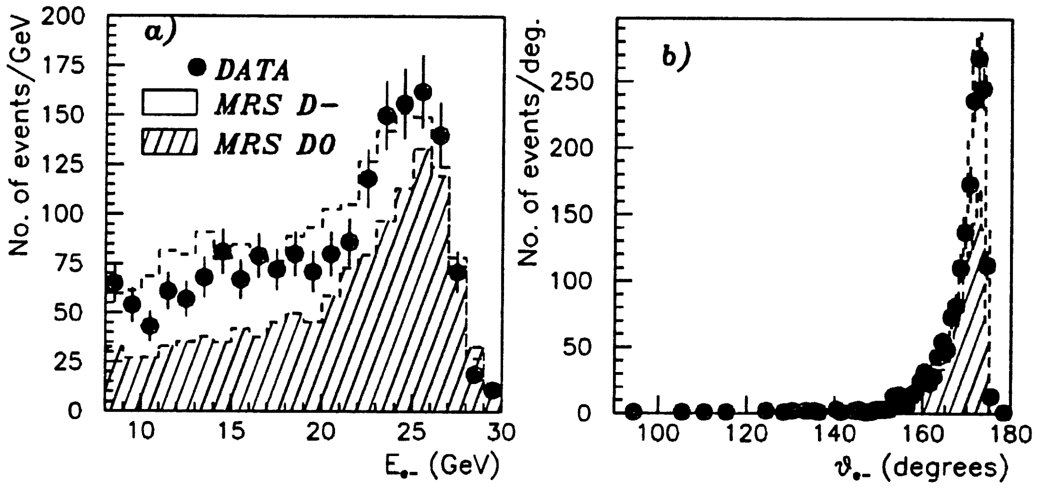

Figure 6.1: Distributions of the scattered electron's energy E'_e and (b) polar angle θ_e for Monte Carlo and data. The Monte Carlo distributions have been normalised to the data luminosity, and also include the predicted background due to photoproduction events.

From both figures it can be seen that, within errors, the MRSD− distributions appear to describe the data better than the MRSD0 distributions, in shape and overall normalization, particularly in the low x region ($E'_e \leq 22\,\text{GeV}$). Systematic effects due to energy scale and θ_e uncertainties have little impact on the distributions shown in Figures 6.1(a) and 6.1(b), and can be neglected. It is interesting to see that the energy distribution in the kinematic peak region ($E'_e \geq 25\,\text{GeV}$) is similar for both types of parton distributions, although the MRSD− peak is slightly larger.

This is expected since the kinematic peak corresponds to the high x region $x \geq 0.02$ where the differences between the two F_2 distributions are small.

Based on the above observation, the MRSD− MC was used to determine the values for $A(\Delta x, \Delta Q^2)$, although, the MRSD0 MC was used to study the behaviour of $A(\Delta x, \Delta Q^2)$ between these two extreme F_2 distributions. This will be discussed further in Section 6.3.

6.2.3 The Measurable Kinematic Domain and Bin Sizes

Due to the presence of background γp events which survived the event selection criteria the differential cross-sections and F_2 measurements are restricted to the following kinematic boundaries:

1. $Q_e^2 \geq 5$GeV and $\theta_e \leq 174^o$
2. $0.025 \leq y \leq 0.6$ where y is a generic variable corresponding to y_e or y_{JB}, depending on the variables used for the kinematic measurements.

The angular cut imposed in (1) simply reflects the angular acceptance of the BPC detector. The Q_e^2 criteria is partly due to the θ_e cuts but it also minimises the sensitivity of the radiative corrections due to different parton distributions[72].

In the case of the y variable (2) the lower limit reflects the accessible y region after the vertex criteria (see Section 5.3) and the upper limit restricts the measurements to the region where the γp background rates are expected to be to be less than 15% in the low x region. This latter statement is illustrated in Figures 6.2(a) and 6.2(b) which show the predicted γp contamination in the data sample in bins of y_e and $\log_{10} x$, respectively. It can be seen that if no y_e cut is imposed the background fraction can be as large as 40% in the high y_e region.

Secondly, this upper y limit reduces the systematic uncertainty on the value of $\delta(x, Q^2)$ due to the different methods available to calculate the radiative corrections (see Section 6.2.4).

For the F_2 measurements that have been based on the mixed variables (Q_e^2,y_{JB}), the y variable in criteria (2) refers to y_{JB} and y_e. The reason for applying the

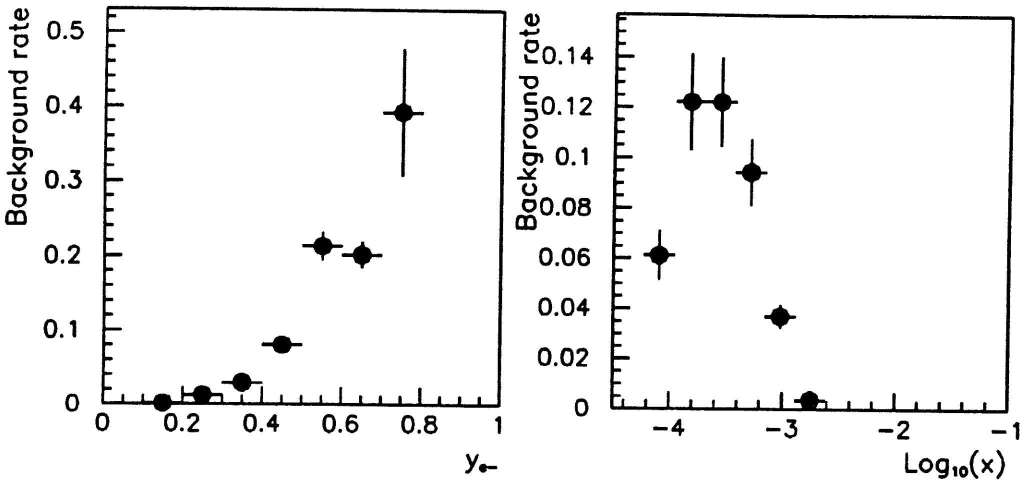

Figure 6.2: Predicted γp background rates in the selected data sample in bins of y_e (a) and $\log_{10} x$ (b).

additional y_e criteria in this case is twofold: (i) the γp events tend to accumulate in the high y_e independently of y_{JB}, therefore, the y_e cut is better at rejecting γp events, (ii) for DIS events the $y_{JB} - y_e$ correlation is good, so both y cuts will in effect reject the same DIS events.

The estimated background rates after the above kinematic constraints will be given in the forthcoming sections.

The corresponding (Q^2,x) bin sizes depend not only on the above x, Q^2 cuts but also on the limited event statistics due to the non-uniform distributions in x and Q^2 and the observed reconstruction resolutions of the kinematic variables (refer back to Sections 5.4.1 and 5.4.3). In order to reasonably determine the x evolution of F_2, at fixed Q^2, whilst minimising the migration rate between bins, the kinematic bins used for the F_2 measurements are defined as follows:

1. The Q^2 bins are: 5 - 10, 10 - 20, 20 - 40, 40 - 80, 80 - 120 and 120 - 200 GeV^2.
2. The x bins are defined in $\log_{10} x$ and the upper (lower) limits in $\log_{10} x$ are -4 (-1). The $\log_{10} x$ bins are split into 4 bins per decade, that is, the bin widths are 0.25; *i.e.* -4 - -3.75, -3.75 - -3.5 and -3.5 - -3.25 etc.

The varying Q^2 bins reflect the limited cross-sections in the higher Q^2 region; recall that the Born cross-sections varies as $\frac{1}{Q^4}$ [2].

The advantage of using the same bins for the analysis based on the mixed and inclusive e variables, is that it allows a direct comparison to be made between the two sets of F_2. Thus, an important cross check can be made in the kinematic regions where both methods are observed to be inaccurate. Also, with the large systematic uncertainties and low event statistics, it makes no sense to use different bins. However, in the future, with much greater statistics and systematic uncertainties at the few per cent level, the F_2 measurements will be more accurate when the chosen bin sizes are optimized for the different kinematic reconstruction methods.

In the measurement of the total cross-section, Section 6.3, the cross-section measurements are made in bins of Q^2 and $\log_{10} x$, the so-called single differential cross-sections ($\frac{d\sigma_t}{dQ^2}$ and $\frac{d\sigma_t}{d\log_{10} x}$). For these measurements, the Q^2 and $\log_{10} x$ bins are defined as follows:

- The Q^2 bins are: 5 - 10, 10 - 15, 15 - 20, 20 - 25 etc. in bins of $5\,\mathrm{GeV}^2$ upto $60\,\mathrm{GeV}^2$, and 60 - 100, 100-200, 200-500 and 500-1000 GeV^2.
- The $\log_{10} x$ limits are defined by the upper (lower) boundaries -4.25 (-0.75), and the bins are defined by a constant width of 0.5.

6.2.4 Radiative Corrections, $\delta(x, Q^2)$

Radiative corrections to the lowest Born cross-section originate, first of all, from emission of additional photons in conjunction with virtual QED corrections and secondly, due to the emission of hard photon(s) off the lepton and quark lines, the so-called bremsstrahlung events. A few of the diagrams contributing to the radiative corrections are shown in 6.3. The radiative corrections are dominated by the leptonic bremsstrahlung diagrams and the size of the corrections depend on the kinematic variables chosen to determine the Born cross-section. A detailed

---

[2] Due to the very poor event statistics in the region $Q^2 \geq 200\,\mathrm{GeV}^2$, the F_2 measurements are restricted to the above Q^2 bins.

discussion on radiative corrections can be found in [74]. It is a well known fact that radiative corrections to the cross-section as a function of the leptonic variables are larger than the corresponding corrections based on the true hadronic variables, since the hadronic variables as less sensitive to leptonic bremsstrahlung corrections.

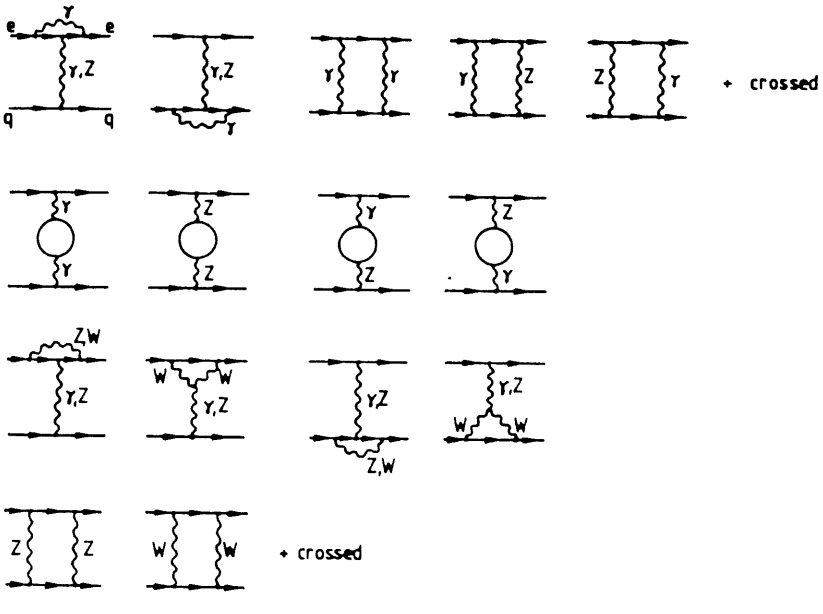

(a) 1-loop diagrams for neutral current lepton–quark scattering.

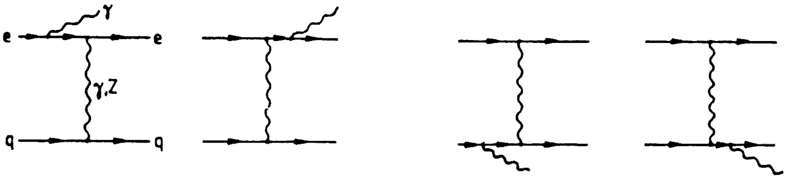

(b) Single-photon bremsstrahlung diagrams for neutral current lepton–quark scattering.

Figure 6.3: One-loop (a) and single-photon bremsstrahlung (b) diagrams showing the $\mathcal{O}(\alpha)$ corrections to the NC DIS cross-section.

Over the past decade various semi-analytical programs and MC generators which calculate radiative corrections have been developed and presented in [73, 74]. One of these programs, the MC generator HERACLES [49], has been used to generate events, at the parton level, for the MC data samples. The HERACLES program allows the calculation of the total cross-section over the kinematic regions given by the leptonic variables x_e,y_e and Q_e^2. The calculations include contributions from the complete one-loop virtual corrections using the results of [75], as well as the contributions due to γ radiation from the leptonic and quark line (see Figure 6.3).

An important test of the accuracy of the theoretical calculations of the initial state bremsstrahlung radiative correction can be made by comparing the energy distributions seen by the photon tagger calorimeter (see Section 3.3.5). Figure 6.4 shows the reconstructed energy distribution of radiated γ's compared with MC predictions using the MRSD− and MRSD0 parton distributions; both MC plots have been normalised to 22.48 nb^{-1}. Within the limited statistics, a good agreement is observed in shape and overall normalization, suggesting that, to a first approximation, the radiative corrections are correctly calculated. However, a complete test can only be made with greater statistics.

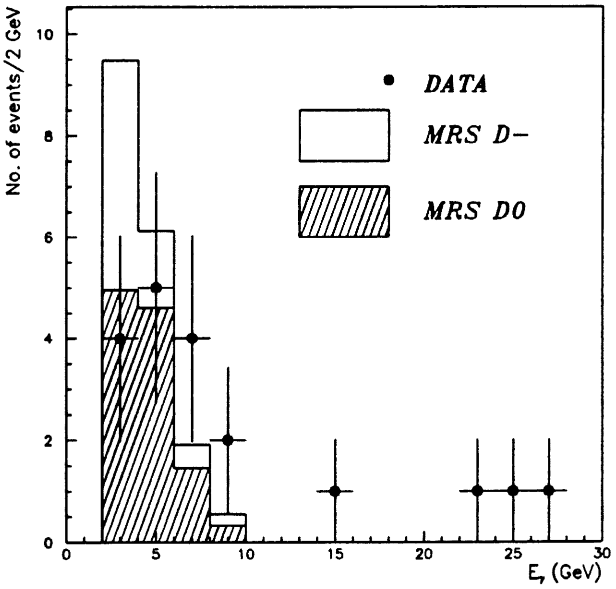

Figure 6.4: Photon energy E_γ spectrum for DIS events with colliner initial-state bremsstrahlung, as detected by the photon tagging calorimeter. The two MC predictions are normalized to the integrated luminosity of the data sample.

Thus, the ideal way to calculate the leptonic radiative corrections would be to use the HERACLES generator. However, using this program requires a lot of computer time which is very impractical, and secondly, radiative corrections using the mixed variables cannot be calculated with the present version of HERACLES.

The semi-analytical program TERAD91 [76] and a model based on the HELIOS program [77] which calculate radiative corrections to $\mathcal{O}(\alpha)$ have also been studied. Unlike the TERAD91 program which calculates the complete 1-loop QED and weak corrections, the HELIOS program only calculates the electromagnetic corrections due to leptonic bremstrahlung diagrams in the leading logarithmic approximation. The HELIOS program is based on the fact the major radiative corrections originate from the leptonic bremsstrahlung diagrams; in this approximation the quarkonic corrections are negligible and result in a small modification of the Q^2 dependence of the parton distribution functions.

Although, the TERAD91 program is the more accurate, similarly to the HERACLES program it requires a lot of computer time to complete the full set of corrections. On the other hand, the HELIOS model is only an approximation for the complete corrections but it allows a fast way to the calculate the leading radiative corrections. Since the radiative corrections are introduced into the F_2 calculations by the term $\frac{1}{1+\delta(x,Q^2)}$ (see equation 6.15), the resulting error on F_2 due the different $\delta(x,Q^2)$ values are found to be less than 6% for the leptonic corrections and less than 1% for the mixed corrections. These differences between the two programs are found to be roughly independent on the input structure functions, although, the size of the corrections are very much dependent on the shape of the input structure functions.

Figure 6.5 shows the complete x ($\log_{10}(x)$) dependence of the leptonic and mixed corrections, as determined from the TERAD91 and HELIOS programs; in both cases, the MRSD$-$ structure functions have been used. For clarity, the x dependence has been illustrated for the Q^2 values, 7.5, 30, 60 and 100 GeV^2, which correspond to the Q^2 values at which $F_2(x,Q^2)$ will be measured. The corresponding $F_2(x,Q^2)$ uncertainties, due to the difference between the two programs, are shown in Figure 6.6.

It can be seen that for the mixed corrections, the agreement between the two programs is excellent and the resulting uncertainty on the F_2 is always better than 1%. However, for the leptonic corrections, it can be that the leading logarithmic

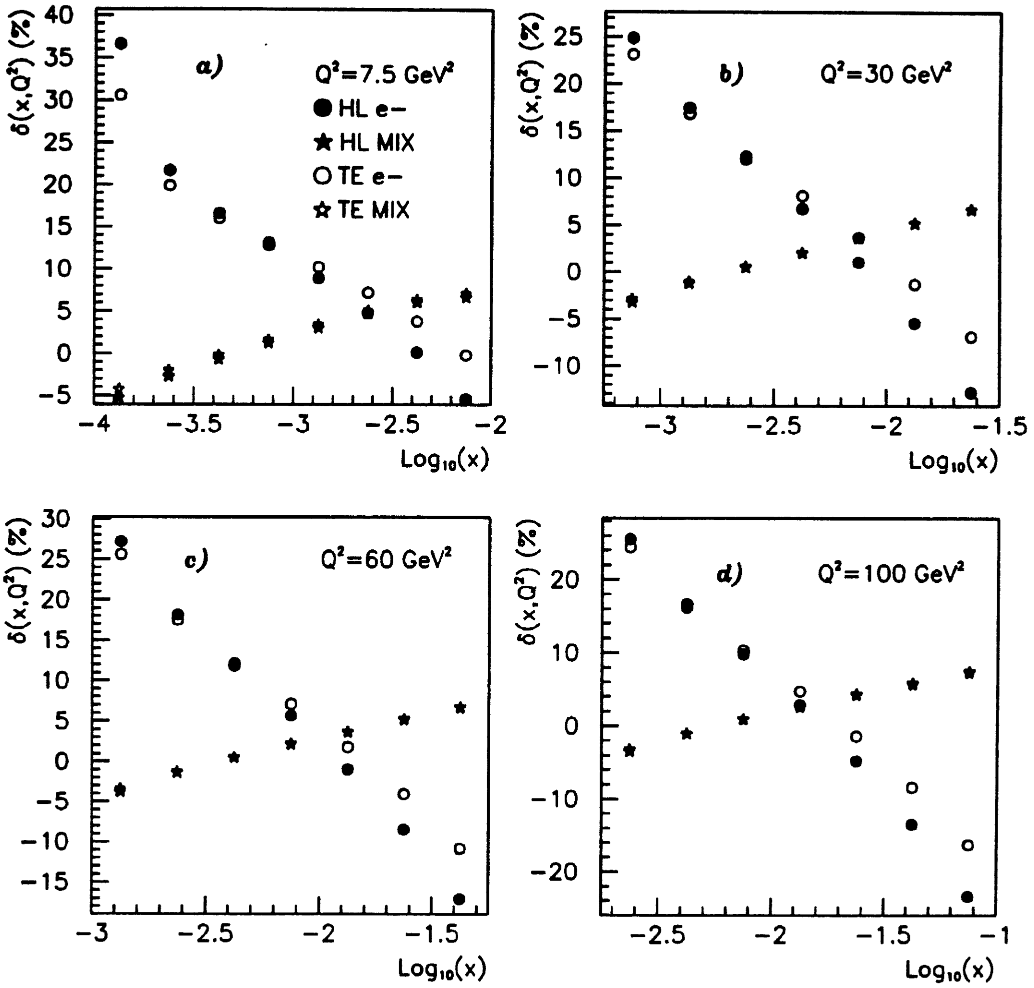

Figure 6.5: Kinematic dependence of the leptonic and mixed radiative corrections using the TERAD91 (TE) and HELIOS (HL) programs for Q^2 = 7.5 (a), 15 (b), 30 (c) and 60 GeV^2 (d).

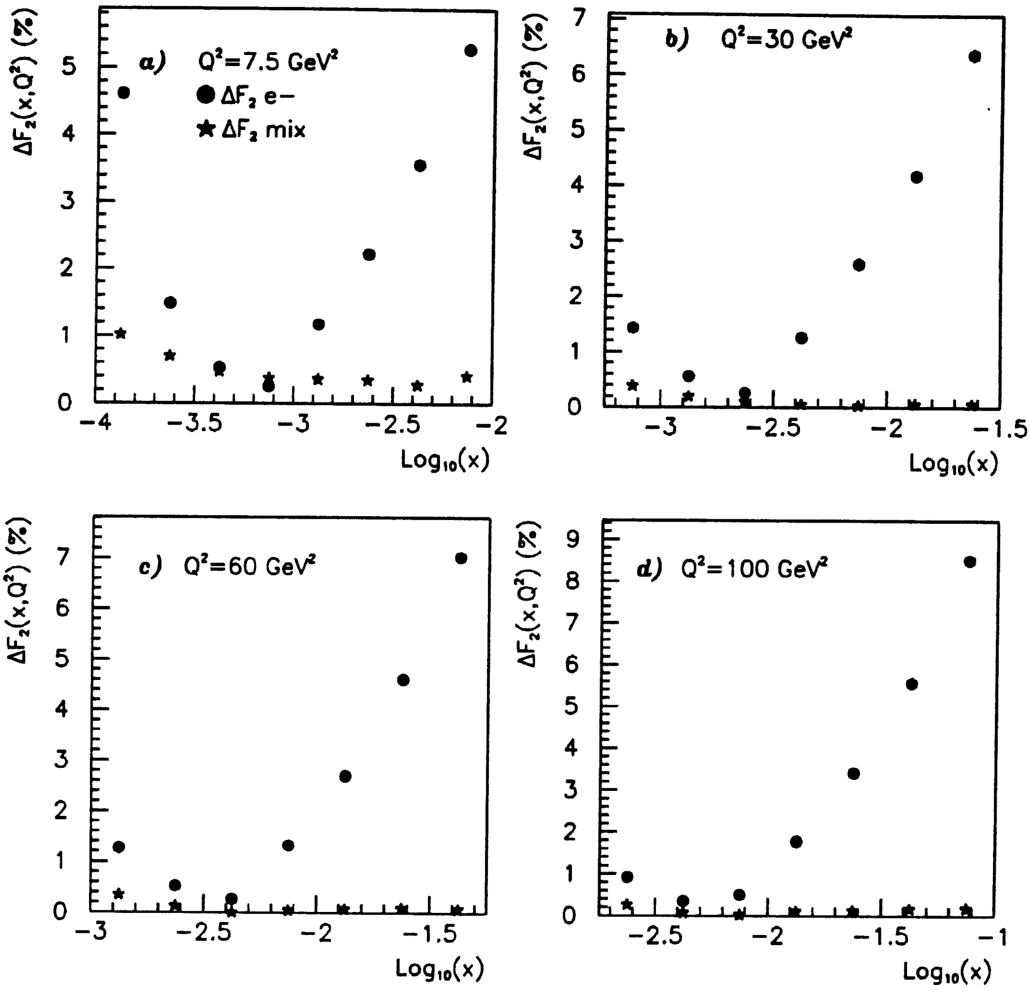

Figure 6.6: F_2 measurement uncertainty due to the difference between the TERAD91 and HELIOS radiative corrections at four Q^2 values. In the case of the leptonic corrections, the resulting $F_2(x, Q^2)$ errors are significant only in the high x region.

method (HELIOS) starts to deteriorate in the high x (low y) region, and these difference tend to increase with increasing Q^2. In this region the uncertainty on F_2 is always better than 6% except in the very high x regions where the error can be around 7-9% for at high Q^2. However, these high x points will generally correspond to $y_e < 0.025$, and so will not be included in the F_2 analysis.

It is clear from the above results, the resulting uncertainty of F_2 due to the different leptonic corrections is always better than 6%, which is relatively small in comparison with the systematic effects observed due to MC model dependence, reconstruction and detector uncertainties (see later). Secondly, these correction uncertainties are only significant in the high x region, where the statistic uncertainties will be large. On the other hand, for the mixed corrections the agreement between the two programs is excellent and resulting F_2 errors are negligible.

On the basis of the observed F_2 errors, the HELIOS model was used to determine the radiative corrections, since the computing time used by this program was significantly less than the TERAD91 program. Also, in the light of the other systematic uncertainties no clear advantage is gained by using the TERAD91 program.

In this model [77], the contributions due to initial and final state lepton bremsstrahlung to the logarithmic corrections are derived from:

$$\frac{d^2\sigma^{rad}}{dxdy} = \frac{\alpha}{2\pi}\ln\left(\frac{Q^2}{m_e^2}\right)\int_0^1 dz\frac{1+z^2}{1-z}\left\{\theta(z-z^0)|J(x,y,s)|\left.\frac{d^2\sigma_o}{dxdy}\right|_{x=\hat{x},y=\hat{y},s=\hat{s}} - \frac{d^2\sigma_o}{dxdy}\right\} \tag{6.13}$$

where $\frac{d^2\sigma_o}{dxdy}$ denotes the respective Born cross-section (equation 6.2) for a particular set of kinematic variables x, y (e.g leptonic or mixed). The integration variable z represents the fraction of the e's energy taken by the radiated photon, and z^o is the lower limit of the integration. The kinematic variables $\hat{x}, \hat{y}$ and $\hat{s}$ are the so-called *rescaled variables* which account for the kinematic changes due to the radiated photon. $J(x,y,s)$ is the Jacobian matrix relating the variables x, y to $\hat{x}, \hat{y}$:

$$J(x,y,s) = \begin{vmatrix} \frac{\delta\hat{x}}{\delta x} & \frac{\delta\hat{x}}{\delta y} \\ \frac{\delta\hat{y}}{\delta x} & \frac{\delta\hat{y}}{\delta y} \end{vmatrix} \tag{6.14}$$

The Compton contribution to the NC cross-section can be neglected in measurable kinematic domain.

The size of the radiative corrections play an important part in the determination of the smeared acceptance function $A(x,Q^2)$, since $A(x,Q^2)$ is calculated from the radiative and Born events. This implies that for a given MC event sample, $A(x,Q^2)$ is related to the size of $\delta(x,Q^2)$ used in the generation of the total event sample. Therefore, when calculating $F_2(x,Q^2)$, the radiative corrections and smeared acceptances must be determined from the same set of parton distributions (MRSD−) and the $(1+\delta(x,Q^2)) \cdot A(x,Q^2)$ term, which appears in the $\frac{\sigma^t_{\Delta x \Delta Q^2}}{1+\delta(x,Q^2)}$ term of equation 6.15, can be treated as one variable, say, $\bar{A}(x,Q^2)$. This implies that the systematic uncertainties on the $F_2(x,Q^2)$ measurements due to the assumed form of input parton distributions are equal to the uncertainties observed in the $\bar{A}(x,Q^2)$ values. This avoids overestimating the systematic errors by treating the structure function dependence of the radiative corrections and smeared acceptances as independent sources of systematic errors.

6.3 Measurement of the Total DIS Cross-section σ_t

Unlike the extraction of the Born cross-section, the measurement of σ_t requires no prior knowledge and application of radiative corrections, which implies that any method can be used to reconstruct the event kinematics. Based on the observed kinematic resolutions shown in Sections 5.4.1 and 5.4.2, for the measurement of σ_t, the following variables were used to define the event kinematics:

- Q^2 was determined from the e only.
- y was determined from y_e only when $y_e \geq 0.1$, and y_{JB} when $y_e < 0.1$.

The above y criteria ensures that the resulting y resolution will always be better than 30%, and avoids the observed y divergences as $y_e \rightarrow 0$. Out of the 1809 selected DIS event candidates, only 1275 events survived the kinematic cuts; the largest event losses being attributed to the $Q_e^2 \geq 5\,\mathrm{GeV}^2$ criteria.

The total differential cross-sections have been determined in bins of Q^2 and $\log_{10}(x)$, so that the individual Q^2 and x distributions can be calculated. Calculating the single differential cross-sections has the added advantage of minimising the systematic uncertainties due to event migration between bins and also reducing the statistical uncertainties. These effects can be large when the double differential cross-sections, in bins of (Q^2,x), are calculated for the F_2 analysis (see next section).

The bin-by-bin cross-sections $\sigma_t^{\Delta Q^2}$ and $\sigma_t^{\Delta \log_{10}(x)}$ are calculated according to cross-section formulae 6.8 given in Section 6.2. The differential cross-sections $\frac{d\sigma_t}{dQ^2}$ and $\frac{d\sigma_t}{d\log_{10}(x)}$ are then determined from the bin cross-section by applying the bin size correction defined in Section 6.2.1.

As described in Section 6.2.2 the smeared acceptances for the Q^2 and $\log_{10}(x)$ bins are determined from the MRSD$-$ MC datasets. The smeared acceptance for each bin is defined wrt. the generated leptonic kinematics, since the HERACLES MC program calculates the total cross-section(s) by integrating over the e kinematics. After accounting for the observed discrepancies between data and MC vertex reconstruction efficiencies, the total acceptance corrections varied between 80%-40% for the Q^2 bins and 61%-32% for the $\log_{10}(x)$ bins. Globally, the total acceptance correction in the measureable kinematic region is 48% (the systematic errors on these acceptances are discussed below).

In Section 6.2.3 it was shown that within the measurable kinematic plane the γp background contamination is deemed to be less than 10% in the low x region $x \leq 0.001$; this was illustrated in Figure 6.2(b). In the Q^2 region $Q^2 \leq 60\,\mathrm{GeV}^2$, the bin-by-bin contamination is less than 5%. These small residual contaminations are then subtracted statistically from the number of events observed in each kinematic bin.

The background contribution from beam-gas and beam-wall events was estimated by looking for events which pass the event and kinematic criteria, but originate from the pilot electron or proton bunches[3]. Only one event was selected from the pilot proton bunch, corresponding to a background of around 10 events, which is approximately 1% of the total event sample. This contamination was subtracted from the two lowest Q^2 and $\log_{10}(x)$ bins.

In order to determine the systematic errors due to detector and reconstruction uncertainties, detailed MC studies were made, in which the acceptance variations due to each systematic effect was determined. These acceptance uncertainties correspond to the overall bin-by-bin systematic errors on the cross-section measurements. The systematic uncertainty is determined from the following contributions, all added in quadrature:

- **Uncertainty in the determination of the smeared acceptance due to possible shifts of the e energy scale by 2%, in the BEMC and LAr calorimeter, and an 2% uncertainty in the BEMC energy resolution.**

  These energy scale/resolution uncertainties lead to acceptance (and cross-section) errors of less than 6% (3%) in the lowest Q^2 ($\log_{10}(x)$) bins, and increase to 22% for the higher bins; in the highest $\log_{10}(x)$ bin the systematic uncertainty is 50%. In the region $Q^2 > 60\,\mathrm{GeV}^2$ where the Q^2 bin size is increased, the resulting error is better than 10% and decreases with increasing bin size.

- **Uncertainty due to possible shifts of θ_e by 3 mrad.**

  As above, the systematic uncertainties, for the uniform Q^2 bins increase with Q^2 and is less than 5% in the lower Q^2 bins, and about 21% for the higher bins. For the larger Q^2 bins the systematic uncertainty is less than 10%. The corresponding $\log_{10}(x)$ errors are roughly uniform and better than 4%, except in the highest bin where it is 7%.

- **Uncertainty in the acceptance calculation due to measurements of y_{JB} which is dominated by the 7% uncertainty in the absolute scale**

---

[3] Recall, that these pilot bunches are unpaired bunches with no associated colliding partner. They are mainly used for background studies.

of the hadronic energy measurement (LAr calorimeter).

Also included in this uncertainty are effects arising from the 2% uncertainty in the electromagnetic energy scale, and the treatment of calorimetric noise. The resulting uncertainty on the cross-section measurements are small, since y_{JB} is calculated from tracking and calorimeteric data, and it is only used when $y_e \leq 0.1$. In the low Q^2 region the systematic error is around 4% and less than 2% for $Q^2 \geq 10\,\mathrm{GeV}^2$. Since Q^2 is determined from the scattered e, the above error is simply the result of acceptance changes due to events satisfying or failing the y cut. However, this is not the case for the $\log_{10} x$ bins, since x may determined from y_{JB}, in which case the error may be due to event migrations between $\log_{10} x$ bins. In the region where a sizeable fraction of the current jet is seen by the CJC and LAr calorimeter, the resulting systematic error does not exceed 1%; this corresponds to the region $-3.75 \leq \log_{10}(x) \leq -2.25$. However, in the very low x (high x) region where the current jet is backward (forward) scattered, the systematic errors are approximately 16% (7%); these large errors are partly due to the absence of accurate tracking data in these two detector regions.

- **Uncertainty in the event selection efficiency.**

  This systematic uncertainty reflects the possible cross-section errors due to uncertainties in the BPC and vertex reconstruction efficiency calculations. The largest contribution comes from the vertex reconstruction efficiency errors which range from 12-7%; the BPC uncertainties are approximately 4% (2%) at low (high) scattering angles. These errors are added in quadrature to give the total event selection uncertainty. The resulting errors range from 10% in the lowest Q^2 and $\log_{10}(x)$ bins to 7% in the higher kinematic bins.

- **Uncertainty in the background contamination from γp and beam induced background.**

  The uncertainty in the γp background contamination was determined by studying the variation in the number of γp events with the above energy scale, θ and event selection uncertainties. The observed variations are added in quadrature to determine the total γp uncertainty. Also included in this calculation is the statistical uncertainty on the background events which is taken to represent possible errors due to structure function dependence of the γp contamination. The resulting systematic uncertainty on the cross-section measurements, is determined by studying the statistical changes due to the total background uncertainties. Thus, the systematic uncertainties are determined to be better than 4% for the bins in the region $Q^2 \leq 60\,\mathrm{GeV}^2$ and can be neglected in the higher Q^2 bins. In the lowest $\log_{10}(x)$ bin the systematic uncertainty is 8% and steadily decreases from 3% to 1% as x increases; in the high x region, $\log_{10}(x) \geq -2.25$ the uncertainty is negligible.

- **Uncertainty in the smeared acceptance calculation due to the chosen form of the input parton distributions (MRSD−).**

  This uncertainty is the result of the assumption that the MRSD− parton distributions describe the true structure functions, which in practice is unknown. Therefore, the measured cross-section is subject to an uncertainty which is related to the structure function dependence of the bin-by-bin acceptances; the MRSD− smeared acceptances are observed to be greater than the corresponding MRSD0 values; *i.e.* the smeared acceptance increases with increasing structure functions. From the distributions shown in Figures 6.1(a) and 6.1(b) (Section 6.2.2) it is clear that if the MRSD0 MC is used to determine this effect, the uncertainty would be grossly overestimated, in the low x region, as it does not agree with the data. However, it is easy to see that a MC data sample generated using a parameterization in which, at a fixed Q^2, F_2 rises faster than F_2^{MRSD0} and less (or slightly greater) than $F_2^{\mathrm{MRSD-}}$, can also give a good agreement with data. In the absence of this type of MC data sample, the systematic uncertainties were taken as 50% of the differences between the MRSD− and MRSD0 acceptance values, such that the resulting errors are of the same size as expected from the above hypothetical F_2 shape. In fact, this method is justified by acceptance differences observed using the KMRSB0 and

KMRSB- MC data samples[4]. The KMSRB- distributions predict a comparatively slow rise in F_2 compared to the KMSRB0 predictions, and the their acceptance errors are between 50-30% lower than the corresponding MRS errors. Based on the above arguments, the resulting systematic uncertainties are determined to be better than 13% (15%) in the low Q^2 ($\log_{10}(x)$) bins and gradually decrease to better than 6% (4%) as Q^2 ($\log_{10}(x)$) increase; this systematic drop can be attributed to the convergence of $F_2^{\mathrm{MRSD-}}$ and F_2^{MRSD0} with increasing x.

- **Possible uncertainties due to different fragmentation models.**

  This systematic uncertainty originates from the fact that various models exist for the simulation of QCD processes in DIS events (see next chapter), which can lead to differences in the simulated hadronic final state, and thus y_{jb}^{rec}. Hence, this effect leads to additional systematic uncertainties generally less than 6% over the Q^2 range. As before, in the $\log_{10}(x)$ plain where the current jet scatters into the more central regions of H1, the resulting uncertainty is always better than 4%. However, as x increases, the difference between the models leads to errors of about 15% in the highest $\log_{10}(x)$ bins.

- **Uncertainty in the bin size correction due to chosen form of the input parton distributions.**

  This contribution has been determined by comparing the correction obtained using the MRSD− parton distribution set with the corrections obtained using the MRSD0 set, the MRSD′ [85], KMRS [82], and MTB [83] structure function parameterizations. As expected, the resulting uncertainty is only significant in the low x, Q^2 regions due to the different cross-sections (F_2) predicted in this new kinematic region. In the lowest Q^2 ($\log_{10}(x)$) bins the systematic error is 4% (8%) and better than 2% in the higher kinematic bins.

- **Statistical uncertainty in the acceptance calculations.**

---

[4] These two MC data samples are not used because the event vertex distribution has been incorrectly simulated and the CJC efficiency has not been deteriorated.

Due to the large MC data sample used for these acceptance studies the resulting systematic uncertainties are better than 2% in the low Q^2 and $\log_{10}(x)$ bins. In the higher bins the uncertainty is generally better than 5%.

- **Global normalization uncertainty of 8%.**

It is important to note that the systematic errors due to energy scale and θ_e uncertainties are roughly independent of the MC datasets; the same systematic effects are observed for the MRSD− and MRSD0 datasets. Thus, these errors can be treated separately from the uncertainty due to the structure function dependence of the smeared acceptance.

Globally, within the kinematic region the overall systematic uncertainty (sys) on the total cross-section is dominated by the event selection and global normalization uncertainties which are both 8%. The next largest contributions comes from the structure function dependence of the total acceptance calculation (6%) and the hadronization/fragmentation model dependence (3%); the other uncertainties each contribute between 1-2% to the overall systematic uncertainty.

Using the information given in this section, the total cross-section, not corrected for radiative effects, in the defined kinematic region, was measured as $\sigma_t = 130 \pm 24(sys.) \pm 4(sta.)$ nb.

This measurement together with the corresponding MC cross-section calculations based on the HERACLES program using the MRS, MTB and KMRS parton distribution sets, is shown in Table 6.1; recall, that these parameterizations differ in assumptions of the parton distribution functions at low x.

The extracted differential cross-sections together with their systematic, statistical and total errors are tabulated in Tables 6.2 and 6.3 for the Q^2 and $\log_{10} x$ bins, respectively; the total error is determined from the systematic and statistical errors added in quadrature. These results are also illustrated in Figures 6.7(a) and 6.7(b) which show measured points, for the Q^2 and $\log_{10}(x)$ bins respectively, superimposed with the corresponding theoretical predictions.

In this new and previously unexplored kinematic region, the cross-section measurements shown in Table 6.1 and Figure 6.7 appear to agree well with the theo-

Total Cross-sections from Data and Monte Carlo								
DATA			Monte Carlo F_2 Parameterizations					
(nb)			MRS (nb)		MT (nb)		KMRS (nb)	
σ_t	$\pm\Delta\sigma_t(sys)$	$\pm\Delta\sigma_t(sta)$	D0	D-	B1	B2	B0	B-
130	24	4	91	130	66	149	64	81

Table 6.1: The total cross-sections, determined from the Autumn 1992 data (σ_t) and the HERACLES event generator, in the kinematic region $Q_e^2 \geq 5\,\mathrm{GeV}^2$, $\theta_e \leq 174^o$ and $0.025 \leq y_e \leq 0.6$. The systematic (sys) and statistical (sta) measurement errors are also shown. The statistical error on the different Monte Carlo cross-section calculations is better than 1%. Within errors the measured cross-section agrees well with the MRSD− and MTB2 predictions.

retical cross-sections based on the MRSD− structure function set, to within a few percent. However, the calculations based on the MTB2 also agrees within one standard deviation from the measured cross-section(s). Both these parameterizations predict a rapid rise in F_2 with decreasing x, due to the rise of the gluon distribution function at small x. The cross-sections based on the MRSD0, MTB1 and KMRS parameterizations, which all assume a moderate growth of F_2 (or gluon density), are greater than two standard deviations from the measured values and do not appear to accurately describe the data points.

It is important to note that in the calculation of the model cross-sections, the HERACLES program assumed the photoabsorption ratio $R(x, Q^2)$ to be zero. This leads to an overestimation of the theoretical cross-section by no more than 2% if the leading order QCD expression for $R(x, Q^2)$ is used; thus, the above observations remain valid.

It is interesting to see that the first measurements of the total cross-sections, in this new low x region, although not corrected for radiative effects, suggest a form for F_2 which rises at low x. This leads nicely to the next section and no further discussion will be presented here.

Differential Cross-sections				
Q^2 bin (GeV^2)	$\frac{d\sigma_t}{dQ^2}$ (nb)	$\pm\Delta\frac{d\sigma_t}{dQ^2}$ (sys) (nb)	$\pm\Delta\frac{d\sigma_t}{dQ^2}$ (sta) (nb)	$\pm\Delta\frac{d\sigma_t}{dQ^2}$ (tot) (nb)
5 - 10	12.2	2.4	0.7	2.5
10 - 15	4.6	0.8	0.3	0.9
15 - 20	2.2	0.4	0.2	0.5
20 - 25	1.6	0.3	0.2	0.3
25 - 30	1.0	0.2	0.1	0.2
30 - 35	0.9	0.2	0.1	0.2
35 - 40	0.5	0.1	0.1	0.1
40 - 45	0.4	0.1	0.1	0.1
45 - 50	0.4	0.1	0.1	0.1
50 - 55	0.3	0.1	0.1	0.1
55 - 60	0.3	0.1	0.1	0.1
60 - 100	0.1	0.02	0.01	0.02
100- 200	0.03	0.01	0.01	0.01
200- 500	0.002	0.001	0.001	0.001
500-1000	0.0007	0.0001	0.0003	0.0004

Table 6.2: Measured cross-sections in bins of Q^2. The third and fourth columns indictate the systematic (sys) and statistical (sta) contributions to the total error (tot) shown in the last column.

$\log_{10}(x)$ bin	$\frac{d\sigma_t}{d\log_{10}(x)}$ (nb)	$\pm\Delta\frac{d\sigma_t}{d\log_{10}(x)}$ (sys) (nb)	$\pm\Delta\frac{d\sigma_t}{d\log_{10}(x)}$ (sta) (nb)	$\pm\Delta\frac{d\sigma_t}{d\log_{10}(x)}$ (tot) (nb)
-4.25 - -3.75	19.3	5.9	2.4	6.3
-3.75 - -3.25	74.2	14.0	4.0	14.6
-3.25 - -2.75	74.6	11.7	3.8	12.3
-2.75 - -2.25	55.2	8.5	3.4	9.2
-2.25 - -1.75	19.5	3.7	1.7	4.1
-1.75 - -1.25	2.5	0.7	0.6	0.9
-1.25 - -0.75	0.9	0.4	0.5	0.6

Table 6.3: Measured cross-sections in bins of $\log_{10}(x)$. As above, the third and fourth columns show the respective systematic (sys) and statistical (sta) contributions to the total error (tot) shown in the in the last column.

6.4 Extraction of the $F_2(x, Q^2)$ Structure Function

To extract $F_2(x, Q^2)$ from the measured bin cross-section $\sigma^t_{\Delta x \Delta Q^2}$, the differential Born cross-section ($\frac{d\sigma_t}{dx dQ^2}$) is determined by multiplying $\sigma^t_{\Delta x \Delta Q^2}$ with the bin center and radiative corrections, and then $F_2(x, Q^2)$ is calculated using equation 6.2. The full expression is:

$$F_2(x, Q^2) = BCC(x, Q^2) \cdot \frac{\sigma_{\Delta x \Delta Q^2}}{1 + \delta(x, Q^2)} \cdot \frac{Q^4 x}{2\pi\alpha^2} \cdot \frac{1}{\left(2(1-y) + \frac{y^2}{1+R(x,Q^2)}\right)} \tag{6.15}$$

On the basis of the excellent agreement observed between the measured σ_t and the MRSD− predictions, the bin centre corrections $BCC(x, Q^2)$ and photoabsorption ratio $R(x, Q^2)$ have been calculated using the MRSD− parton distributions. The $BCC(x, Q^2)$ have only a small dependence on the shape of the input structure functions, and $R(x, Q^2)$ contributes to the differential cross-section mainly in the high y region. In fact, in the lowest x bins, the $F_2(x, Q^2)$ values are reduced at most

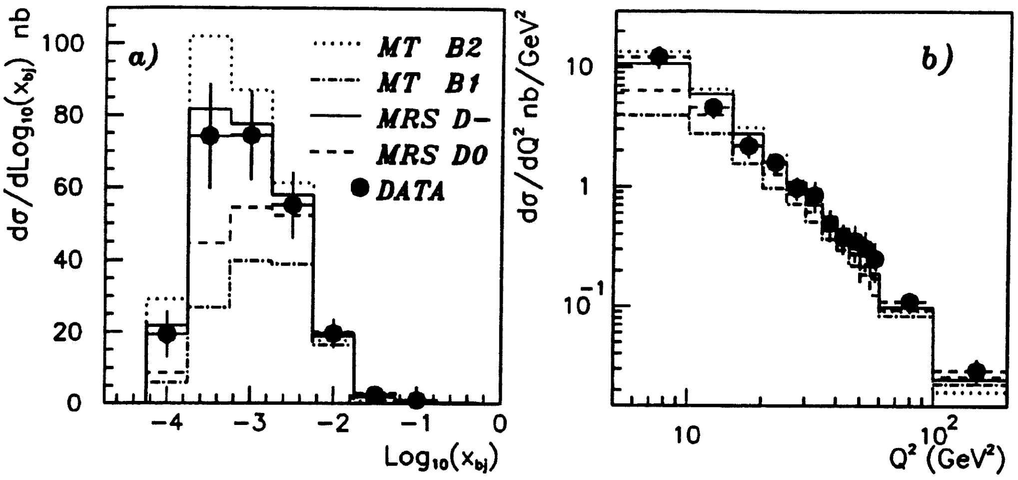

Figure 6.7: Differential cross-sections $\frac{d\sigma_t}{d\log_{10}(x)}$ (a) and $\frac{d\sigma_t}{dQ^2}$ (b) in the kinematic region $Q_e^2 \geq 5\,\mathrm{GeV}^2$, $\theta_e \leq 174^o$ and $0.025 \leq y_e \leq 0.6$. The full and dashed lines show the HERACLES cross-section calculations for different parton distribution parameterizations. The full error bars correspond to the total measurement uncertainties.

by 10%, if the calculated $R(x, Q^2)$ values are replace by $R(x, Q^2) = 0$.

The differential cross-sections have been measured using the inclusive e (analysis I) and mixed (analysis II) kinematic variables. As stated before, comparisons between these two independent $F_2(x, Q^2)$ measurements allow an important cross check between the two measurements, since each method will, to a large degree, be subject to different systematic effects. This comparison is particularly important in the low y (high x) region where the respective kinematic resolutions are vastly different.

In the majority of cases the differential cross-section is measured at the (x, Q^2) point corresponding to the centre of the kinematic bin. However, for a few kinematic bins which lie close to the kinematic limits, the y variable at the bin centre (y_c) may lie just outside the y limits, $y_c < 0.025$ or $y_c > 0.6$, although, the bin may still contains a sizable cross-section. For these bins, the differential cross-section is calculated at the (x, Q^2), which corresponds to the y limit, provided this point lies within the bin. In other words, the Q^2 point still corresponds to the bin centre (Q_c^2), and $x = \frac{Q_c^2}{s0.6}$ or $x = \frac{Q_c^2}{s0.025}$. This slight rearranging of the F_2 points ensures that all the $F_2(x, Q^2)$ measurements are within the designated kinematic limits.

Out of the 1809 DIS event candidates only 1190 events survived the kinematic cuts for analysis I and 1218 for analysis II. The lower event for analysis I reflects the large losses in the high x region as a result of the poor y_e resolutions in the low y_e region. Due to the very low event rates in the high Q^2 region, only the events with $Q^2 \leq 200\,\mathrm{GeV}^2$ were binned leading to a final data sample consisting of 1176 events for analysis I and 1208 for analysis II.

The bin-by-bin acceptances $A(\Delta x, \Delta Q^2)$ were found to vary between 45-80% for analysis I and 40-90% for analysis II. In the low x (high y) bins the analysis I acceptance values were found to be greater than the analysis II values, as a result of the better y_e resolution. However, in the higher x (lower y) bins, due to the superior y_{JB} accuracy, the acceptances were better for analysis II. In general, for the bins that contained a sizeable cross-section (after kinematic cuts) the acceptances decreased with increasing x, due to the vertex criteria in the event selection[5].

As in the previous section, the background contamination from γp was determined from simulation studies using the PYTHIA and RAYVDM event generators. The total background rate was predicted to be 42 events for analysis I and 40 events for analysis II, and as expected, these events accumulated in the low (x, Q^2) bins, for both methods. In the contaminated bins, the background rate was generally better than 10% and decreased with increasing x. As before these background events were subtracted statistically from the bins. The 10 events predicted in the last section from the beam related background was subtracted uniformly from the two lowest (x, Q^2) bins.

The systematic uncertainties have been determined in the same manner as the differential cross-section uncertainties, discussed in the last section; in most cases, the observed uncertainties in the smeared acceptance are translated to $F_2(x, Q^2)$ errors. As before, the overall bin-by-bin uncertainty is determined from the same sources, all added in quadrature:

---

[5] Recall, that for increasing x the current jet gets more forward scattered and the vertex reconstruction efficiency rapidly deteriorates.

- **Uncertainty due to possible shifts on the e energy scale by 2% and an BEMC energy resolution uncertainty of 2%.**

  This affects mainly analysis I, in which the kinematics are calculated only from the scattered e. This leads to uncertainties as large as 25% in the high x region and decreases to around 5-7% at lower x. This is due to the rapid deterioration in the x resolution as $y_e \rightarrow 0$. For analysis II, the errors are better than 10% in the high x region and as x decreases the errors remain less than 5%; the use of y_{JB} drastically reduces the effect of e energy mis-measurements.

- **Uncertainy due to possible shifts of θ_e by 3 mrad.**

  As above, this effect leads to larger uncertainties in analysis I than analysis II. In the lowest Q^2 bin, the resulting errors are 4% in the lower x bins and increase to around 25% in the higher x bins. However, for the other Q^2 bins, which have a bigger width, the resulting uncertainties do not exceed 12% in the high x bins. For analysis II, the resulting systematic uncertainties are smaller and do not exceed 10% in the high x bins. In the low x bins, the error is generally better than 5%.

- **Uncertainty in the measurement of y_{JB} due to the uncertainties in the hadronic energy scale (7%), electromagnetic energy scale (2%) and the treatment of calorimeter noise in the LAr calorimeter.** This affects only analysis II, and the largest errors are observed in the very lowest x bins (high y) for each Q^2 region. These large errors arise due to the poor y_{JB} resolutions in these low x regions. In general, the systematic uncertainties do not exceed 10% in the lowest x bins, and decrease to values better than 5% as x increases. For the very high Q^2 bins ($Q^2 \geq 100\,\mathrm{GeV}^2$), where the current jet scatters into the central regions of H1, the systematic errors are negligible. The use of tracking data in the calculation of y_{jb} greatly reduces the systematic errors, as shown above.

- **Uncertainty in the event selection efficiency.**

This effect leads to 12-10% uncertainties in the two lowest x bins for both analysis I and II. As x increases the uncertainties are dominated by the vertex efficiency uncertainties of 7%.

- **Uncertainty in the background contamination from γp and beam induced background.**

  This uncertainty was determined in the same way as the corresponding cross-section errors, and the resulting errors were only significant in the low (Q^2-x) bins. For analysis I, this background uncertainty lead to errors of around 8% for the lowest x bins in the first two Q^2 bins. In the other x bins, the errors do not exceed 5%. The background contamination in the high Q^2 bins is negligible. For analysis II, the uncertainties are generally better than 5% in the low x bins.

- **Uncertainty in the $(1 + \delta(x, Q^2))A(\Delta x, \Delta Q^2)$ calculation due to the chosen form of the input parton distributions.**

  As in the previous section, this uncertainty is due to the fact that the radiative corrections and smeared acceptances have been calculated using the MRSD− Monte Carlos. Although, the total cross-section measurements were seen to give a good agreement with the MRSD− predictions, the results may still be compatible with a F_2 shape which rises slighter faster or lower than $F_2^{\mathrm{MRSD-}}$. As before, the systematic uncertainties were taken to be 50% of the residual differences between the MRSD− and MRSD0 $\bar{A}(\Delta x, \Delta Q^2)$ values. The resulting errors were found to be slightly greater for analysis II in the low x bins, and in general the errors were better than 10% for I and II. As expected, the uncertainties decreased with increasing x, and on average, in the high x region the errors did not exceed 6% (8%) for analysis I (II).

- **Possible uncertainties due to different models for simulation of the hadronic final state.**

  This systematic uncertainty only effects analysis II, since y_{JB} is determined from the hadronic final state particles. The largest effects are seen in the low x bins, were the errors tend to vary between 14-25%. At fixed Q^2, the systematic uncertainties, on average, tend to decrease with increasing x to values around 10-14%.

- **Uncertainty in the bin size correction due to chosen form of the input parton distributions.**

  Comparing the bin centre corrections for the MRS and MTB distributions leads to errors of less than 3% in the low x region. These errors diminish with increasing x and become negligible at high x.

- **Uncertainty due to the size of the radiative corrections.**

  This uncertainty arises from the fact that the size of the radiative corrections are sensitive to the model used to calculate the corrections, and was discussed in Section 6.2.4. For analysis I this model dependence gave errors upto 6% in the very lowest and highest x bins, and less than 3% elsewhere. The resulting uncertainties for analysis II are around 1%.

- **Statistical uncertainty in the acceptance calculations.**

  For both sets of analysis, the statistical errors on the acceptance values do not exceed 6% for $Q^2 \leq 60\,\mathrm{GeV}^2$ and 9% for the higher Q^2 bins. On average, in the low x bins, the resulting $F_2(x, Q^2)$ uncertainties are better than 2% and gradually increase to around 6% for the higher x bins. In the two highest Q^2 bins, the uncertainty varies between 6-9%.

- **Global normalization uncertainty of 8%.**

The uncertainty on the $F_2(x, Q^2)$ measurements due to the assumption made for the $R(x, Q^2)$ values are not included, since $F_2(x, Q^2)$ can be easily recalculated when more precise information about $R(x, Q^2)$ becomes available.

The $F_2(x, Q^2)$ measurements for analysis I and II are presented in Figure 6.8 for the six Q^2 values, together with predictions obtained using the recent MRSD′ [85]

parameterizations. In these plots all the $F_2(x, Q^2)$ measurements are shown irrespective of their systematic or statistical uncertainties. The errors bars correspond to the bin-by-bin statistical and systematic errors added in quadrature. The $F_2(x, Q^2)$ points with the largest errors correspond to the kinematic bins which have a small cross-section due to the kinematic constraints placed on the events. For these bins both the systematic and statistical uncertainties can be large ($\geq 30\,\%$). These two sets of $F_2(x, Q^2)$ values are tabulated in Appendix A.

Although the $F_2(x, Q^2)$ measurements from analysis I and analysis II are subject to different systematic uncertainties, the two sets of results can be seen to be in good agreement. It is interesting to see that in this new kinematic region, both sets of measurements show a rise in F_2 with decreasing x, which is expected within the framework of perturbative QCD (see next section). The fact that this rise is consistent for both sets of analysis, indicates that rise is purely physical and not attributed to normalization or systematic effects.

In order to study the x evolution of the measured results, a unique set of $F_2(x, Q^2)$ measurements was derived from the results of analysis I and II, by taking the systematically more accurate values and also requiring that the statistical error be better than 70%. This latter requirement ensures that some of the high Q^2 ($Q^2 \geq 100\,\mathrm{GeV}^2$) will be kept. In the kinematic region $y \leq 0.15$ where the y_{JB} resolution is far superior than the y_e resolution, the F_2 values are taken from analysis II. Similarly, in the high y region where the y_e resolution is observed to be better, the F_2 points are taken from analysis I. By taking the best measurements from analysis I and analysis II ensures that the x evolution of F_2 is accurately determined in the full x range.

The final set of $F_2(x, Q^2)$ measurements are presented in Tables 6.4 and 6.5, together with the $\delta(x, Q^2)$ and $R(x, Q^2)$ values used for the measurements. The total error contributions from the systematic (σ_{sys}) and statistical (σ_{sta}) uncertainties are also shown. The individual $F_2(x, Q^2)$ values from the two analysis are given the appendix, together with their associated errors. The $F_2(x, Q^2)$ values are in good agreement with the results published by the H1 [79] and ZEUS [80] collaborations.

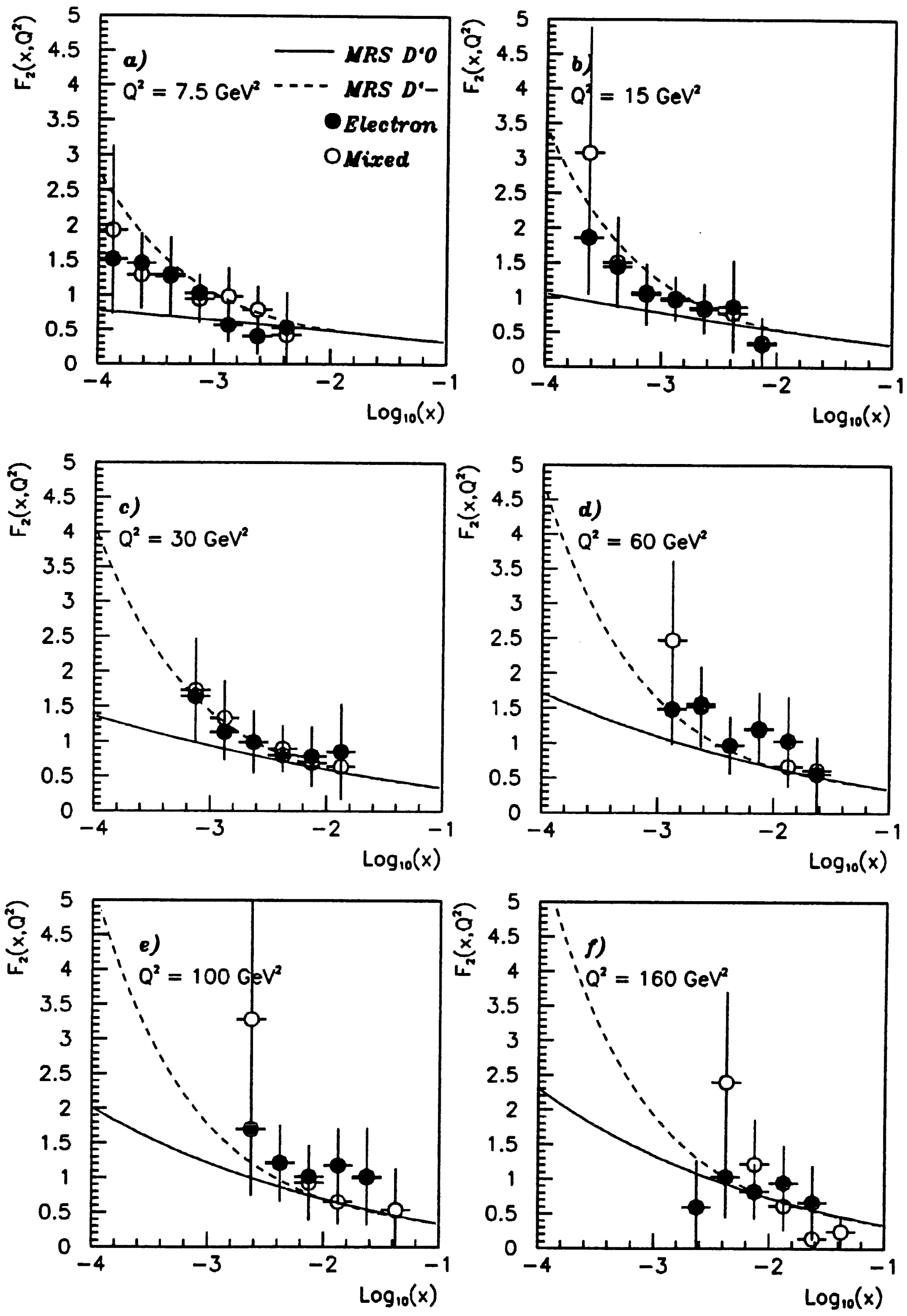

Figure 6.8: $F_2(x, Q^2)$ measurements, from analysis I and II, for six values of Q^2. The full circles correspond to the e measurements (analysis I) and the open circles correspond to the mixed variable measurements (analysis II). The error bars show the total errors obtained by adding the systematic and statistical errors in quadrature.

Measured $F_2(x, Q^2)$ values							
Q^2 (GeV^2)	x	y	$F_2(x, Q^2)$	σ_{sys}	σ_{sta}	$R(x, Q^2)$	$\delta(x, Q^2)$
7.5	0.00014	0.606	1.52	0.74	0.19	0.64	0.32
7.5	0.00025	0.349	1.46	0.40	0.14	0.74	0.21
7.5	0.00044	0.196	1.29	0.29	0.15	0.68	0.16
7.5	0.00078	0.110	0.94	0.32	0.13	0.63	0.02
7.5	0.00138	0.062	0.98	0.38	0.15	0.58	0.04
7.5	0.00245	0.035	0.79	0.30	0.14	0.49	0.05
7.5	0.00339	0.025	0.42	0.23	0.16	0.46	0.06
15	0.00029	0.594	1.87	0.78	0.28	0.52	0.31
15	0.00044	0.392	1.45	0.38	0.14	0.50	0.23
15	0.00078	0.221	1.07	0.33	0.11	0.47	0.17
15	0.00138	0.124	0.99	0.30	0.10	0.43	0.01
15	0.00245	0.070	0.83	0.33	0.09	0.39	0.03
15	0.00437	0.039	0.78	0.29	0.10	0.35	0.04
15	0.00692	0.025	0.35	0.13	0.13	0.31	0.06
30	0.00078	0.441	1.64	0.44	0.21	0.38	0.25
30	0.00138	0.248	1.13	0.37	0.15	0.35	0.17
30	0.00245	0.140	0.99	0.43	0.13	0.33	0.01
30	0.00437	0.078	0.90	0.31	0.12	0.29	0.02
30	0.00776	0.044	0.69	0.23	0.12	0.26	0.04
30	0.01380	0.025	0.64	0.26	0.17	0.22	0.06

Table 6.4: The proton structure function $F_2(x, Q^2)$, as measured from the first HERA data, for $Q^2 \leq 30\,\mathrm{GeV}^2$. The last two columns give the values of the photoaborption ratio and the radiative corrections used to calculate $F_2(x, Q^2)$. The statistical (σ_{sta}) and systematic (σ_{sys}) contribution to the total errors are given separately.

Measured $F_2(x, Q^2)$ values							
Q^2 (GeV^2)	x	y	$F_2(x, Q^2)$	σ_{sys}	σ_{sta}	$R(x, Q^2)$	$\delta(x, Q^2)$
60	0.00138	0.496	1.49	0.40	0.31	0.30	0.27
60	0.00245	0.279	1.56	0.32	0.27	0.28	0.18
60	0.00437	0.157	0.97	0.36	0.19	0.25	0.11
60	0.00776	0.088	1.19	0.40	0.20	0.22	0.02
60	0.01380	0.050	0.67	0.25	0.15	0.19	0.04
60	0.02455	0.028	0.61	0.41	0.20	0.16	0.09
100	0.00245	0.465	1.70	0.66	0.70	0.25	0.26
100	0.00437	0.262	1.22	0.33	0.43	0.23	0.16
100	0.00776	0.147	0.93	0.38	0.38	0.20	0.01
100	0.01380	0.083	0.65	0.20	0.25	0.17	0.03
100	0.02455	0.047	1.00	0.49	0.33	0.14	0.04
160	0.00437	0.419	1.03	0.27	0.52	0.21	0.22
160	0.00776	0.235	0.82	0.24	0.31	0.18	0.14
160	0.01380	0.132	0.61	0.17	0.31	0.16	0.02

Table 6.5: Similar to previous table, except that the $F_2(x, Q^2)$ measurements are made at $Q^2 \geq 60\,\mathrm{GeV}^2$.

6.5 DIS Events with Large Rapidity Gaps

In the analysis of the DIS hadronic final state (see next chapter), a large fraction of the events have a significant energy flow in the forward part (proton direction) of the LAr calorimeter. This energy flow is consistant with models that include fragmentation of the proton remnant as well as the fragmentation between the current jet and remnant. However, approximately 65 events were selected for the cross-section and $F_2(x, Q^2)$ analysis in which very little energy was observed outside the current jet region (very little energy flow in the forward direction)[6]. These events correspond to around 5% of the binned data sample which is in sharp contrast to the MC[48] prediction of 0.2%. These so-called 'rapidity gap' events have also been observed by the Zeus collaboration [81].

It turns out that the events do not depend too strongly on x or Q^2 and so do not effect the observed rise in $F_2(x, Q^2)$ at low x. However, it will be interesting to study these events, since they may be linked to diffractive *ep* scattering where the proton scatters down the beam pipe and does not break up. These events are characterized by very little forward energy and may be due to the exchange of a Pomeron, thus giving information on the nature (constituents) of the Pomeron. A typical 'rapidity gap' event candidate is shown in Figure 6.9, where the e scatters into the BEMC calorimeter and virtually no energy is seen in the forward region. The resulting e kinematic distributions, Q^2 and $\log_{10}(x)$, are shown in Figure 6.10.

6.6 Discussion

For the first time the proton structure function $F_2(x, Q^2)$ has been measured in the very low x region, $x \leq 10^{-3}$, nearly two orders of magnitude lower than the existing fixed target data. As discussed in Chapter 2, the predicted behaviour of the parton distributions in this new x regime have been subject to various theoretical scenarios. Within the framework of perturbative QCD, the standard linear evolution

---

[6] For these events, the total energy in the forward region corresponding to $\eta \geq 1.8$ (puesdo-rapidity), was taken to be less than 0.6 GeV.

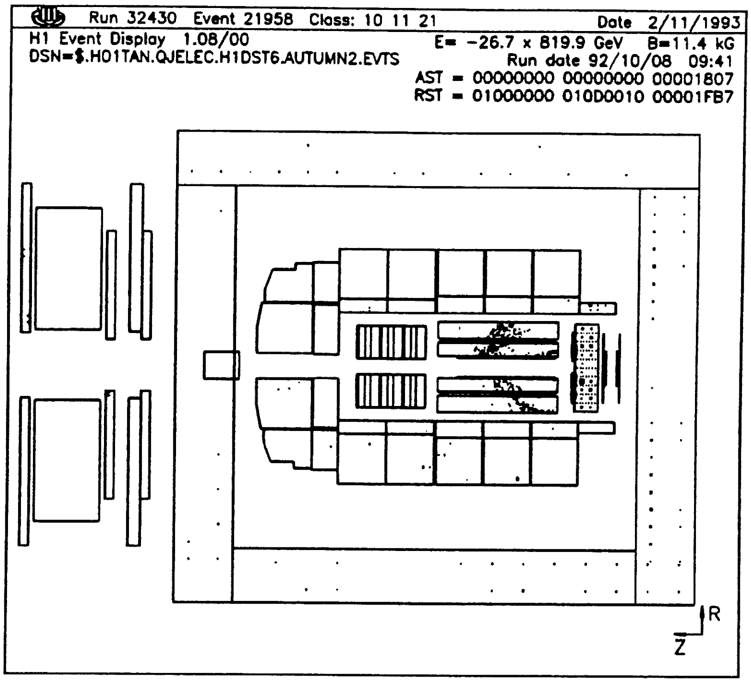

Figure 6.9: A typical 'rapidity gap' event candidate as seen in the H1 detector. The kinematics of this event are found to be $Q_e^2 = 5.12\,\mathrm{GeV}^2$, $y_e = 0.43$ and $x = 0.000136$.

equations of Gribov, Lipatov, Alterelli and Parisi (GLAP) [14, 15], and Balitskiǐ, Kuraev, Fadin and Lipatov (BFKL) [16, 17] both predict a fast growth of the gluon density $xg(x, Q^2)$ towards small x. The evolution equations of BFKL which have been adapted to study the very small x region, predict a very characteristic $x^{-\lambda}$ behavior of the gluon density at small x, where $\lambda \sim 0.5$. On the other hand, this increase in $xg(x, Q^2)$, has to be compared to the results of the Regge-parton model which predicts that the gluon density remains approximately constant, as $x \rightarrow 0$.

Since, the low x sea quark distributions are coupled to the gluon distributions, due to $g \rightarrow q\bar{q}$ decays, the evolution of $F_2(x, Q^2)$ at low x is expected to reflect the assumptions made on $xg(x, Q^2)$. This implies, that if $xG(x, Q^2)$ evolves as $\sim x^{-0.5}$ then $F_2(x, Q^2)$ rapidly grows as x decreases. Similarly, if the gluon density remains constant, then $F_2(x, Q^2)$ will evolve (rise) very slowly towards low x.

In this discussion, the measured $F_2(x, Q^2)$ points will be compared with parton distributions which have all been fitted to the recent NMC data [84], but differ in their assumptions on the low x behaviour of the parton distributions. The parton distributions that have been used are the MRSD$'$ [85], the CTEQ [86] and GRV

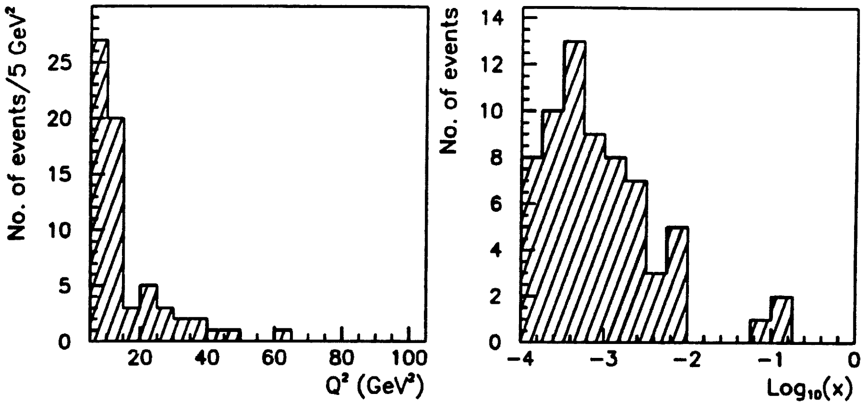

Figure 6.10: (a) Q^2 and (b) $\log_{10}(x)$ distributions for the 65 'rapidity gap' event candidates.

[87] sets. In the first two parameterizations, the parton structure functions are parameterized for all x at one value of Q^2, typically around 4 GeV^2. These structure functions are then evolved in Q^2 using the GLAP evolution equations of Chapter 2. For the MRSD$'$ distributions the gluon density, at $Q_o^2 = 4\,\mathrm{GeV}^2$, is assumed to be singular, $x^{-0.5}$ (Lipatov behaviour), for the MRSD$'-$ parameterization and is constant for the the MRSD$'$0 parameterization (Regge behaviour). Similary, for the CTEQ distributions, the CTEQ1MS parameterization is based on the singular gluon, and the CTEQ1M parameterization assumes a constant gluon distribution. However, unlike the MRSD$'$ distributions, in the CTEQ parameterizations the sea quark density is not strongly coupled to the gluon density, which results in a slower rise of $F_2(x,Q^2)$ for the CTEQ1MS set, as x decreases. In the case of the GRV parameterization, the parton distributions are taken to be 'valence like' at a Q^2 scale of $0.3\,\mathrm{GeV}^2$; *i.e.* the parton densities vanish as $x \rightarrow 0$. The low x behaviour of the parton distributions at larger Q^2 is then dynamically generated using the GLAP evolution equations. In the Q^2 region of the data, the gluon distribution mimics a $x^{-0.4}$ behaviour [88] in the low x region.

The above parameterizations together with the final set of $F_2(x,Q^2)$ points are shown in Figure 6.11 for the six Q^2 values. It can be seen that the measured values are consistant with the GRV and MRSD$'-$ parameterizations, which both predict a rapid rise in the gluon density towards low x. However, the sharp rise in the GRV distribution is due to the fact that the Q^2 evolution is started at a very low Q_o^2 scale of 0.3 GeV^2. At such a low Q^2 scale non-perturbative effects may need to be accounted for, thus destroying the $x^{-0.4}$ behaviour.

Therefore, a plausible explanation for the observed rise of $F_2(x, Q^2)$ is that it is due to the Lipatov (or BFKL) resummation of soft gluon radiation. A precise test will only be possible with much greater statistics and a better understanding of the detector and event systematics.

Finally, Figure 6.12 shows the Q^2 dependence, at fixed x, for the measured $F_2(x, Q^2)$ points. It can be seen that $F_2(x, Q^2)$ increases slowly with Q^2, as expected from perturbative QCD where the GLAP evolution equations predict a logarithmic dependence of F_2 with Q^2 (scaling violations).

6.7 Summary

Within the limited statistics, the first precise measurements of deep inelastic scattering in the low x region have produced some very interesting physics. In the kinematic region $Q^2 \geq 5\,\mathrm{GeV}^2$, $0.025 \geq y \geq 0.6$ and $\theta_e \leq 174^\circ$, the total cross-section (not corrected for radiative events) was measured to be $\sigma_t = 130 \pm 24(sys.) \pm 4(sta.)$ nb. Although the cross-section and structure function measurements were dominated by large systematic uncertainties, both sets of measurements clearly confirmed that F_2 agreed with theoretical models that predicted a strong rise towards low x. The consequences of this observed rise are very exciting as it means that at some very small x value, the gluon density must be damped, in order to keep the total cross-section finite. This means that interesting QCD effects such as *screening* and *saturation*, may become detectable at HERA.

Also, the observation of DIS events with large rapidity gaps may allow a better understanding of diffractive interactions, thus providing a new insight into the partonic nature of the Pomeron.

In summary, the kinematic window has been opened for the first time and the preliminary results indicate a very exciting, and challenging, future for the HERA

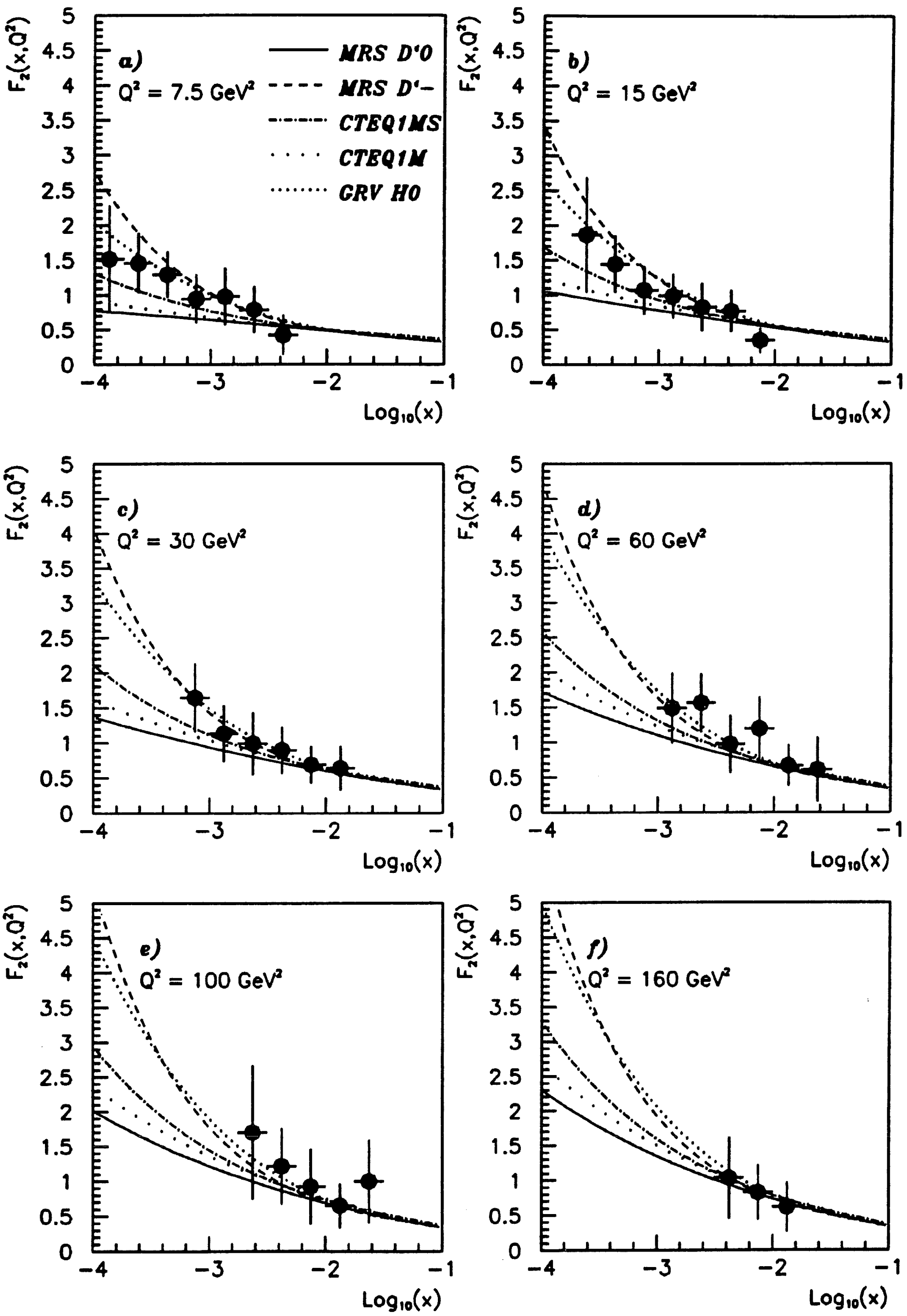

Figure 6.11: The $F_2(x, Q^2)$ measurements for six values of Q^2, compared to several parameterizations which are fitted to recent low energy data from the muon proton scattering experiments. The error bars show the total measurement errors obtained by adding the statistical and systematic errors in quadrature.

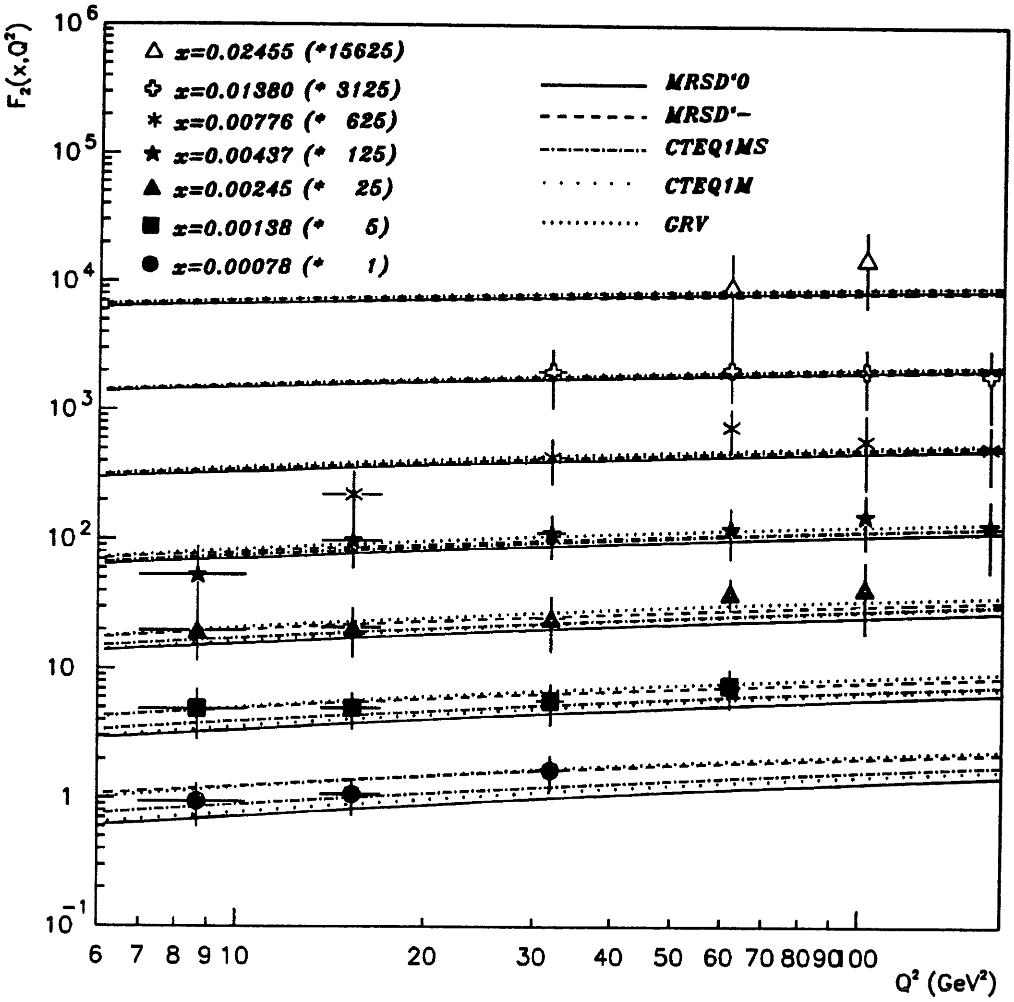

Figure 6.12: The $F_2(x, Q^2)$ measurements as a function of Q^2 for fixed values of x, compared to several recent structure function parameterizations. As expected from pertubative QCD, $F_2(x, Q^2)$ can be seen to rise slowly with Q^2.

DIS physics program.

Chapter 7

Measurements of the Hadronic Final State

7.1 Introduction

It is now well established from the analyses of lower energy fixed target DIS experiments, that QCD corrections are needed to the naive quark-parton model to explain the topological characteristics of the observed hadronic final state. As discussed in Section 2.3.3 QCD corrections are needed to explain the scale breaking nature (*i.e.* the Q^2 dependence) of $F_2(x, Q^2)$. The large phase space available at HERA for QCD processes makes HERA an ideal testing ground for perturbative QCD tests. Such tests can be made by comparing the observed hadronic final state from DIS interactions (DHFS) with perturbative QCD model predictions.

In this chapter, a brief study is presented comparing the observed DHFS from data with various MC predictions based on different QCD models. This study is presented in order to clarify the (systematic) uncertainty calculations on σ_{tot} and $F_2(x, Q^2)$, presented in Chapter 6, due to the particular model used to simulate the QCD processes for DIS events.

The MC events used in the following comparisons have gone through the full H1 simulation and reconstruction chain. The MC and data events used in this study have all satisfied the event selection criteria described in Chapter 5 and lie within the kinematic range defined in Section 6.2.3. In addition the events must have $W^2 \geq 3000\,GeV^2$, where W is the invariant mass of the hadronic final state; the event kinematics are determined using the mixed method. The 65 'rapidity gap' events in the data sample are removed in this analysis, although their presence does not affect the DHFS distributions too strongly. This is done because the DIS event generators that are used in this study do not simulate events with large rapidity gaps.

The above W cut ensures that a large fraction of the DHFS is seen in the H1 detector. Also limiting the events to $Q^2 \geq 5\,GeV^2$ and $y \leq 0.6$ reduces the background rate from photoproduction events and minimises the radiative corrections.

7.2 QCD Models and Simulation

In this study the DHFS from data is compared with three different theoretical used models used to simulate QCD processes in deep inelastic scattering. The three QCD models are follows:

- Leading logarithmic parton showers (PS): In this model [89, 90] radiation is described by two parton cascades, one from the time-like scattered parton, and one from the space-like initial parton. The evolution of the parton cascades can be derived from the Alterelli-Parisi splitting kernels. The amount and hardness ($p_\perp$) of parton radiation depends on the virtuality of the of the parton before and after the electroweak vertex. In this study the scale for the maximum allowed virtuality, which determines the phase space available for parton showers, is taken to be Q^2, W^2 and an intermediate scale $W.Q$. The distributions for each of these scales is denoted by PS(Q^2), PS(W^2) and PS($W.Q$), respectively. At low x, W^2 can be much larger than Q^2 giving rise to vast differences in the amount of parton radiation; these two scales define the two extreme scales for the PS model.

- $\mathcal{O}(\alpha_s)$ matrix element and parton showers (MEPS): In this model the first order QCD processes $\gamma q \rightarrow qg$ or $\gamma q \rightarrow q\bar{q}$ are simulated according to their exact $\mathcal{O}(\alpha_s)$ matrix element calculations and additional softer emissions are added using PS model[1]. In this model the maximum virtuality scale for the parton showers is kinematically constrained by the matrix element calculations.

- Colour dipole model (CDM): The CDM model does not distinguish between initial and final state parton radiation. In this model gluon emission can be described by a chain of radiating 'colour' dipoles starting with an initial dipole formed between the scattered point-like quark and the extended proton remnant. In the case of $\mathcal{O}(\alpha_s)$ QCD processes, such as $\gamma q \rightarrow q\bar{q}$, gluon radiation occurs from the two dipoles formed between the proton and quark and between the proton and anti-quark. By treating the proton as an extended coloured object (in one dimension) small wavelength gluon emission can be suppressed in the target region. This is implemented in the MC by involving only a fraction of the proton in the dipole radiation of a gluon with transverse momentum $p_\perp$; this fraction being inversely to $p_\perp$. In the CDM the scale for gluon radiation is only dependent on W^2 of the DIS interaction and the maximum $p_\perp^2$ proportional to $W^{\frac{4}{3}}$.

The PS model is incorporated into the DJANGO [48] MC generator which has been extensively used throughout this thesis. The MC datasets, that were used to calculate the bin-by-bin smeared acceptances in Chapter 6 were generated using W^2 as the scale for the parton showers. The MEPS model is incorporated into the LEPTO 6.1 [91] MC generator which generates electroweak DIS interactions without leptonic radiative corrections. The CDM model is implemented in the program ARIADNE [92] which is interfaced with LEPTO 6.1. In this study the distributions labelled with CDM are based on events with LEPTO 6.1 for the electroweak and $\mathcal{O}(\alpha_s)$ processes, followed by ARIADNE for parton emissions in CDM.

All the above event generators used the LUND string model as implemented in JETSET [93] to simulated the non-perturbative soft parton fragmentation (or

---

[1] In these first order events, the two final state partons define the hardest emission and so only softer ones can be added.

hadronization) process. On the basis of the cross-section and $F_2(x, Q^2)$ presented in Chapter 6 all the following MC distributions are generated with the MRSD$-$ parton distributions, except the PS($W.Q$) distributions which have been simulated using the MRSD0 parton distributions. However, specific studies have shown that the hadronic final state is not too dependent on the choice of input parton distributions [94], and so it will not affect the resulting conclusions.

7.3 Results and Discussion

In the following distributions the error bars shown on the data point are purely statistical. The data point uncertainties due to energy scale uncertainties are not included since they are small compared with the differences between the models. In this study the reconstructed energy cluster of the scattered electron is removed from the hadronic final state.

The distributions shown in Figures 7.1 and 7.2 shows the transverse energy flow[2] as a function of pseudo-rapidity, η ($\eta = -\tan\frac{\theta}{2}$), and of the azimuthal angle, ϕ, defined wrt. the scattered electron. In Figure 7.1 the forward region is given by positive η.

From both figures it can be seen that the PS(W^2) and PS(Q^2) predictions do not agree with the data. As expected the energy flow is much greater for the PS(W^2) predictions. The PS(Q^2) predicts too little energy simply due to the fact that dominant low Q^2 interactions restricts the phase space for parton showers if Q^2 is used as the scale parameter. The MEPS and CDM predictions appear to give distributions which are consistent with the data to within 20%. The PS($W.Q$) model give too much energy flow in the central regions and too little in the forward regions.

However, in Figure 7.2 the energy flow in the ϕ plane can be seen to be well described by the CDM and PS($W.Q$) models. From this figure, the distribution clearly shows the presence of a current jet from the collimated energy balancing the

---

[2] Reconstructed in the LAr calorimeter, the BEMC and iron tailcatcher.

$p_\perp$ of the scattered at $\phi = \pi$.

It is interesting to see from both distributions that the observed energy flow appears to lie between the MEPS and CDM predictions. Referring to Figure 7.1 it can be seen that in the very forward region ($\eta > 2$) all the models then to predict to little $E_\perp$ in this region. Detailed studies have shown that this is not the result of an insufficient understanding of the detector simulation in that region, but may be due to a poor description of the fragmentation of the proton remnant in the present models [95]. Possible model dependence on the input parton distributions or the presence of background events can be neglected.

One of the best ways to compare the accuracy of the different QCD models is to study the energy flow in the hadronic centre-of-mass (CMS) frame where large differences can be observed between the models. In the CMS frame, the z^* axis[3] is defined as the direction of the virtual boson. Thus, in the naive quark parton model the current jet points in the $+z^*$ region and the proton remnant jet points in $-z^*$ direction. The lorentz transformation to the CMS frame is performed using the mixed kinematic variables (Q^2_e and y_{JB}) since this combination is relatively insensitive to QED radiation from the electron.

Figure 7.3 shows the CMS energy (E^*) as a function of θ^*, where θ^* is the angle, of the calorimeter cells, wrt. the $+z^*$ direction. It can be seen that the data and different models predicts a large energy flow in the in the direction of the current jet. It can be seen that the data distribution is well described by the CDM and PS($W.Q$) predictions, in the overall width and energy flow. The MEPS model also gives a good agreement in the jet direction but tends to underestimate the energy flow at larger θ^*.

The final distribution to be shown is that of the 'seagull' plot, which shows the distribution of the mean transverse momentum squared $< p_\perp^{*2} >$ as a function of Feynman-x ($x_F = 2p_z^*/W$, where p_z^* is the z component of the charged particle's CMS momentum). This distribution is shown in Figure 7.4 for good CJC tracks within the acceptance of the CJC (see Section 5.4.2). It can be seen that the

---

[3] All variables in the CMS frame are denoted with a $*$ as superscript.

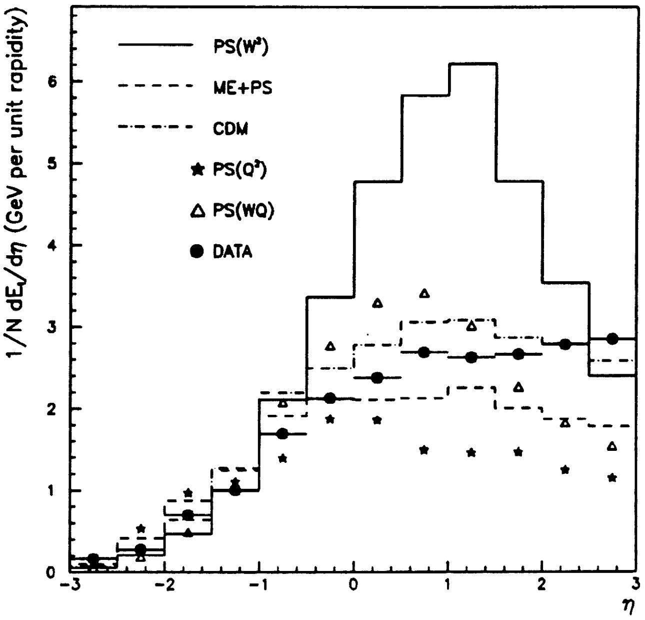

Figure 7.1: Transverse energy flow ($E_\perp$) as a function of the pseudo-rapidity (η) for the data. Also shown are the fully reconstructed QCD model predictions.

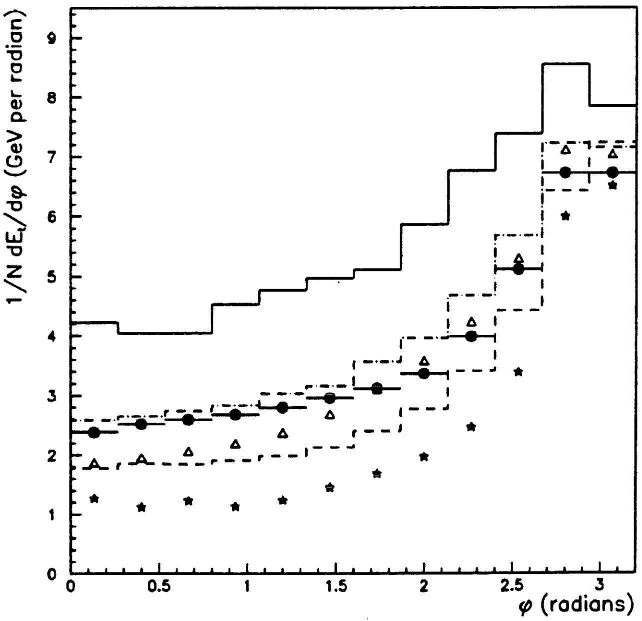

Figure 7.2: Transverse energy flow ($E_\perp$) as a function of the azimuthal angle (ϕ) defined wrt. the scattered electron, for data and QCD model predictions.

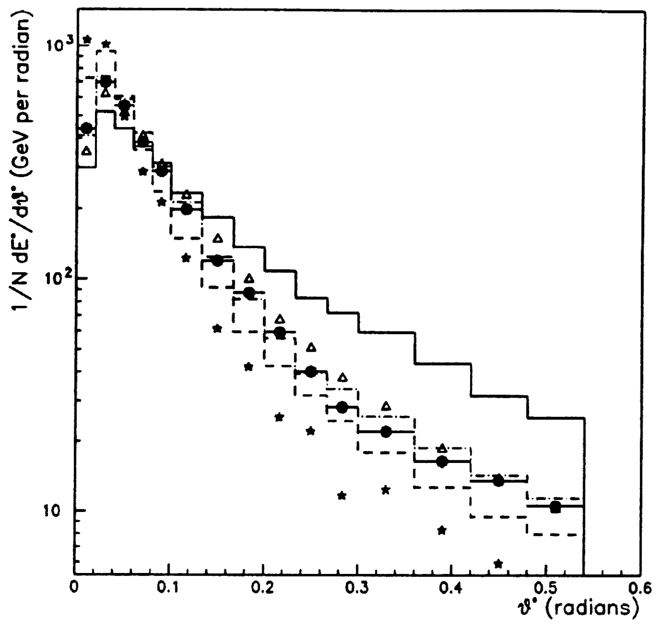

Figure 7.3: Energy flow (E^*) in the hadronic centre-of-mass frame as a function of θ^*, for data and the model predictions. A well collimated current jet can be observed.

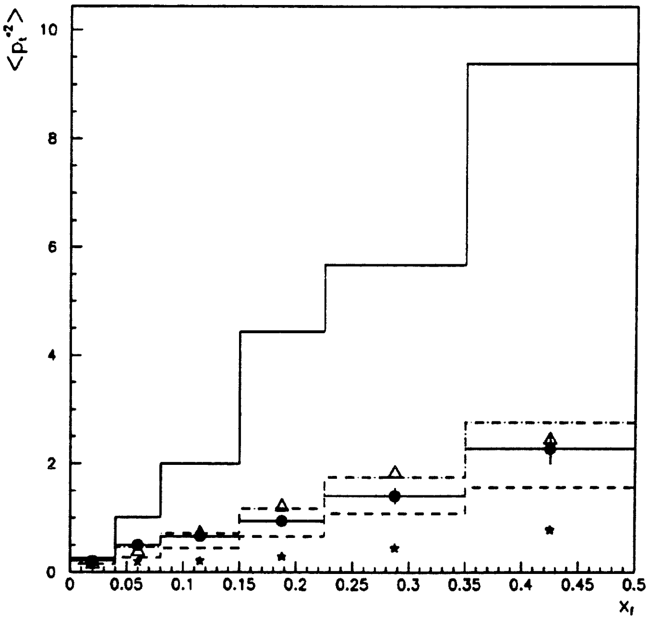

Figure 7.4: Seagull plot showing the mean $p_\perp^2$ in the hadronic centre-of-frame ($< p_\perp^{*2} >$) as a function of Feynman-x (x_F), for data and model predictions.

PS($W.Q$) and CDM predictions are in good agreement with the data. Due to to the angular cuts imposed on the reconstructed CJC tracks, the above distribution is not sensitive to negative x_F.

7.4 Concluding Remarks

In this section a very brief discussion has been presented comparing the observed DHFS with model predictions. It has been shown that the DHFS is sensitive the particular model used to simulated the perturbative QCD processes in the proton. The predictions based on the PS(W^2) model have clearly shown that it does not reproduce the observed distributions, which lead to additional uncertainties being included in the measurements of σ_{tot} and $F_2(x, Q^2)$. This particular MC was used to determine the smeared acceptances because of the large event sample available at DESY.

From the few distributions shown in this chapter it can be concluded that with the different MC available at DESY only the CDM model is able to reproduce the observed DHFS distributions to within an accuracy of around 20% in all distributions. The MEPS and PS($W.Q$) models also give good results comparable with the data, although the PS($W.Q$) model fails somewhat to describe the transverse energy flow as a function of η (in the laboratory frame). Although, the LEPTO 6.1 event generator cannot be used for cross-section (or $F_2(x, Q^2)$) studies, since it does not included radiative corrections, the results from this chapter suggest that if the MEPS or CDM is incorporated into the framework of the DJANGO program, the systematic uncertainties on the $F_2(x, Q^2)$ measured can be significantly lowered. However, with the present DJANGO program, the DHFS can be better simulated if the PS($W.Q$) scale is used.

From these simple distributions, the uncertainties in the DHFS has been lowered, but more work is still needed in order to get a better agreement between data and theory. In particular the observation of excess transverse energy flow in the very forward region will need to addressed.

Chapter 8

Summary & Conclusions

In this thesis a detailed discussion has been presented describing the perturbative QCD predictions for the evolution of $F_2(x,Q^2)$ at HERA. The total cross-section and $F_2(x,Q^2)$ measurements extracted from the first data collected by H1 have shown that the results are consistent with the standard perturbative QCD prediction of the gluon density increasing as $x \rightarrow 0$. Initial results show that the x evolution of $F_2(x,Q^2)$ is in good agreement with the Lipatov (or BKFL) evolution equations, described in Section 2.3.5, in which the x evolution is described by a summation over gluon ladders. The Q^2 evolution of the measured $F_2(x,Q^2)$ is observed to rise as Q^2 increases, which is in good agreement with the GLAP evolution equations.

The observation of a strong rise in $F_2(x,Q^2)$ with decreasing x suggests that new QCD effects, such as parton saturation, may be detectable at HERA. With greater event statistics and lower event systematics a more quantative study will be possible on the behaviour of $F_2(x,Q^2)$ in the very low x region. Nevertheless, the first $F_2(x,Q^2)$ measurements have narrowed down the theoretical uncertainties that were predicted in the HERA kinematic range.

The observation of 'rapidity gap' events has been one of the major surprises from the first HERA data. Traditionally, these events are associated with an exchange of a Pomeron, although the radiation of a pion from the proton can also give rise to events with large rapidity gaps. In addition, rapidity gap events can occur through the VDM process, where the photon dissociates into a heavy vector meson, which is also a colourless object, resulting a in large rapidity gap between the proton and parton jet. Thus, the large rate of such events observed by H1 will allow a better understanding into the nature of these events and may be give an important insight into the partonic nature (composition) of the poorly understood Pomeron.

Finally, the very preliminary measurements of the hadronic final state have shown that the simulation of QCD processes using the PS, MEPS and CDM prescriptions do not accurately reproduce the experimentally observed hadronic final state. However, the CDM models appears to give the best agreement out of the three models. However, with a better understanding of the detector more precise tests will be possible.

To conclude this thesis, the physics potential at HERA is immense, the results presented in this thesis is only the beginning, the best is yet come. *Consummatum est.*

Tirez le rideau; la farce est jouée.

Appendix A

$F_2(x, Q^2)$ Values

The $F_2(x, Q^2)$ values determined from the electron (analysis I) and mixed (analysis II) kinematic variables are shown in the following tables. The bin-by-bin errors shown, correspond to the total uncertainty on the $F_2(x, Q^2)$ values determined from the systematic and statistical errors added in quadrature. Also shown are the respective radiative corrections $\delta(x, Q^2)$ used in the extraction of $F_2(x, Q^2)$ from the measured radiative (total) cross-sections.

Measured $F_2(x, Q^2)$ values

			Electron Kinematics		Mixed Kinematics	
Q^2	x	y	$F_2^e(x, Q^2)$	$\delta^e(x, Q^2)$	$F_2^m(x, Q^2)$	$\delta^m(x, Q^2)$
7.5	0.00014	0.606	1.52±0.58	0.32	1.93±1.20	-0.04
7.5	0.00025	0.349	1.46±0.65	0.21	1.29±0.49	-0.02
7.5	0.00044	0.196	1.29±0.32	0.16	1.27±0.56	0.00
7.5	0.00078	0.110	1.02±0.25	0.13	0.94±0.34	0.02
7.5	0.00138	0.062	0.57±0.24	0.09	0.98±0.17	0.04
7.5	0.00245	0.035	0.40±0.27	0.04	0.79±0.33	0.05
7.5	0.00339	0.025	0.53±0.50	0.02	0.42±0.28	0.06
15	0.00029	0.594	1.87±0.82	0.31	3.08±1.81	-0.05
15	0.00044	0.392	1.45±0.40	0.23	1.51±0.65	-0.03
15	0.00078	0.221	1.07±0.35	0.17	1.05±0.44	0.01
15	0.00138	0.124	0.97±0.26	0.12	0.99±0.31	0.01
15	0.00245	0.070	0.86±0.34	0.07	0.83±0.34	0.03
15	0.00437	0.039	0.87±0.66	0.02	0.78±0.30	0.04
15	0.00692	0.025	0.33±0.39	-0.02	0.35±0.18	0.06
30	0.00078	0.441	1.64±0.49	0.25	1.73±0.74	-0.03
30	0.00138	0.248	1.13±0.40	0.17	1.33±0.53	-0.01
30	0.00245	0.140	0.99±0.27	0.12	0.99±0.45	0.01
30	0.00437	0.078	0.80±0.22	0.06	0.90±0.33	0.02
30	0.00776	0.044	0.78±0.42	0.01	0.69±0.26	0.04
30	0.01380	0.025	0.85±0.46	-0.06	0.64±0.31	0.06

Measured $F_2(x, Q^2)$ values

			Electron Kinematics		Mixed Kinematics	
Q^2	x	y	$F_2^e(x,Q^2)$	$\delta^e(x,Q^2)$	$F_2^m(x,Q^2)$	$\delta^m(x,Q^2)$
60	0.00138	0.496	1.49±0.50	0.27	2.47±1.14	-0.04
60	0.00245	0.279	1.56±0.42	0.18	1.52±0.57	-0.01
60	0.00437	0.157	0.97±0.41	0.11	0.97±0.33	0.01
60	0.00776	0.088	1.21±0.50	0.05	1.19±0.45	0.02
60	0.01380	0.050	1.03±0.63	-0.01	0.67±0.29	0.04
60	0.02455	0.028	0.57±0.53	-0.09	0.61±0.46	0.06
100	0.00245	0.465	1.70±0.96	0.26	3.28±2.06	-0.04
100	0.00437	0.262	1.22±0.54	0.16	1.21±0.55	-0.01
100	0.00776	0.147	1.02±0.42	0.09	0.93±0.53	0.01
100	0.01360	0.083	1.18±0.52	0.02	0.65±0.31	0.03
100	0.02455	0.047	1.02±0.70	-0.05	1.00±0.59	0.04
160	0.00437	0.419	1.03±0.58	0.22	2.40±1.31	-0.03
160	0.00776	0.235	0.82±0.39	0.14	1.22±0.65	0.00
160	0.01380	0.132	0.95±0.53	0.06	0.61±0.35	0.02
160	0.02455	0.074	0.66±0.53	-0.02	0.14±0.15	0.03

Bibliography

[1] F. Halzen and A.D. Martin, *Quark and Leptons: An Introductory Course in Modern Particle Physics*, John Wiley and Sons (1984).

[2] D.H. Perkins, *Introduction to High Energy Physics*, Third edition, Addison Wesley (1987).

[3] I.J.R. Aitchison and A.J.G. Hey, *Gauge Theories in Particle Physics*, Second edition, Adam Hilger (1989).

[4] S.L. Glashow, Nucl. Phys **22** (1961) 579,
S. Weinberg, Phys. Rev. Lett. **19** (1967) 1264,
A. Salam,*Elementary Particle Theory*, ed. N. Svartholm, (Almqvist and Wilkell, Stockholm, 1968).

[5] I.O.P., *High Energy Physics 1990*, Proceedings of the Annual Conference of the HEPP Group of the Institute of Physics, ed. F.H. Crombley, Sheffield University (1990).

[6] G.'t Hooft,
Nucl. Phys. **B33** (1971) 173.
Nucl. Phys. **B35** (1971) 167.

[7] *Review of Particle Properties*, Phys. Rev. **D47** (1992) Number 11 Part II.

[8] P.W. Higgs,
Phys. Rev. Lett. **13** (1964) 508.
Phys. Rev. **145** (1964) 1156.

[9] LEP collaborations, *Updated Parameters of the Z^o Resonance from Combined Preliminary Data of the LEP Experiments*, CERN/PPE/93-157 (1993).

[10] G. Ingelman et al., *Monte-Carlo Study of Structure Function Measurements*, Proceedings of the HERA workshop, ed. R.D. Peccei, Hamburg, Germany (1987) Vol. 1 107.

[11] J. Feltesse, *HERA the New Frontier*, Lectures presented at the SLAC Summer Institute Stanford, California, 5 - 16 August 1991, DAPNIA/SPP 92-01.

[12] M.W. Krasny et al., *Determination of the Longitudinal Structure Function at HERA from Radiative Events*, Proceedings of the Workshop "Physics at HERA", ed. W. Buchmüller and G. Ingelman, Hamburg, Germany, (1991) Vol. 1 171.

[13] D.H. Perkins, *Deep Inelastic Lepton - Nucleon Scattering*, Techniques and Concepts of High-Energy Physics, ed. T. Ferbel (1981) 279.

[14] G. Alterelli et al., Nucl. Phys. **126B** (1977) 298.

[15] V.N. Gribov et al., Sov. J. Nucl. Phys. **15** (1972) 438.
Sov. J. Nucl. Phys. **15** (1972) 675.

[16] E.A. Kuraev et al, Phys. Lett. **60B** (1975) 50.
Sov. Phys. JETP **45** (1977) 199.

[17] Y.Y. Balitskiǐ et al., Sov. J. Nucl. Phys. **28** (1978) 822.

[18] A.H. Mueller, J. Phys. G: Nucl. Part. Phys. **19** (1993) 1463.

[19] L.V. Gribov et al., Nucl. Phys. **B188** (1981) 555.
Phys. Rep **100** (1983) 1.

[20] E.M. Levin, *Parton Density at Small x_B*, DESY 92-122 (1992).

[21] J. Bartels, $F_2(x, Q^2)$ *scaling violations at very small x*, Proceedings of the Workshop "Physics at HERA", ed. W. Buchmüller and G. Ingelman, Hamburg, Germany, (1991) Vol. 1 193.

[22] J. Kwiecinski et al., *Deep-Inelastic Events Containing a Measured Jet as a Probe of QCD Behaviour at Small x*, DTP/92/04 (1992).

[23] J. Bartels et al., *Measurements of Hot Spots at HERA*, Proceedings of the Workshop "Physics at HERA", ed. W. Buchmüller and G. Ingelman, Hamburg, Germany, (1991) Vol. 1 203.

[24] M.G. Ryskin, Nucl. Phys. **B** (Proc. Suppl.) **18C** (1990) 162.
Heavy Photon Dissociation in Deep Inelastic scattering, Proceedings of the Workshop "Physics at HERA", ed. W. Buchmüller and G. Ingelman, Hamburg, Germany, (1991) Vol. 1 215.

[25] H. Jung et al., *J/ψ-Production Mechanism and Determination of the Gluon Density at HERA*, DESY 92-028 (1992).

[26] S. Levonian et al., *Photoproduction*, Proceedings of the Workshop "Physics at HERA", ed. W. Buchmüller and G. Ingelman, Hamburg, Germany, (1991) Vol. 1 459 - 666.

[27] A. Levy, J. Phys. G: Nucl. Part. Phys. **19** (1993) 1489.

[28] J.B. Dainton, *Physics at HERA*, RAL 90-038 (1990).

[29] G.A. Schuler, *Perspective on Physics at HERA*, DESY 89-075 (1989).

[30] W. Buchmüller et al., *Electroweak Physics*, Proceedings of the Workshop "Physics at HERA", ed. W. Buchmüller and G. Ingelman, Hamburg, Germany, (1991) Vol. 2 919 - 1028.

[31] W. Buchmüller et al., *Physics Beyond the Standard Model*, Proceedings of the Workshop "Physics at HERA", ed. W. Buchmüller and G. Ingelman, Hamburg, Germany, (1991) Vol. 2 1027 - 1151.

[32] B.H. Wiik, *HERA status*, Proceedings of the Workshop "Physics at HERA", ed. W. Buchmüller and G. Ingelman, Hamburg, Germany, (1991) Vol. 1 1 - 16.

[33] H1 Collaboration, Technical Proposal for the H1 Detector, DESY, Hamburg (1986).

[34] H1 Collaboration, The H1 Detector at HERA, DESY 93-103 (1993).

[35] ZEUS Collaboration, Technical Proposal for the ZEUS Detector, DESY, Hamburg (1986).

[36] M. Düren et al., *Polarized Electron Nucleon Scattering at HERA: the HERMES Experiment*, Proceedings of the Workshop "Physics at HERA", ed. W. Buchmüller and G. Ingelman, Hamburg, Germany, (1991) Vol.1 427 - 446.

[37] G. Alterelli, *Polarized Structure Functions at HERA: Introduction and Overview*, Proceedings of the Workshop "Physics at HERA", ed. W. Buchmüller and G. Ingelman, Hamburg, Germany, (1991) Vol. 1 379 - 388.

[38] H1 Calorimeter Group, *The H1 Liquid Argon Calorimeter System*, DESY 93-078 (1993).

[39] V. Shekelyan, *Simulation and Reconstruction in H1 Liquid Argon Calorimetry.*, H1 note H1-04/93-288 (1993).

[40] M. Goldberg, *Energy Calibration and Reconstruction in BEMC*, H1 note H1-05/93-292 (1993).

[41] C.D. Hilton, *Forward Muon Detection in H1 and Hadronic Energy Flow in Deep Inelastic Scattering*, Ph.D thesis, University of Manchester (1993).

[42] G. Bernardi et al., *Guide to the Reconstruction Program H1REC*, H1 document.

[43] S. Egli et al., *Guide to the Simulation Program H1SIM*, H1 document (1991).

[44] R. Brun et al., *GEANT long writeup*, CERN Program Library, W5103 (1989).

[45] V. Blobel, *The BOS System: Dynamic memory managment*, H1 document (1987).

[46] Y. Sirois, *H1 LAr Calorimeter Group*, private communication.

[47] B. Andrieu et al., *Electron Identification in H1 LAr Calorimeters*, H1 note H1-01/93-266, Proceedings of the 3rd International Conference on Advanced Technology and Particle Physics, Como, Italy (1992).

[48] G.A. Schuler et al., *DJANGO: the interface for event generators HERACLES and LEPTO*, Proceedings of the Workshop "Physics at HERA", ed. W. Buchmüller and G. Ingelman, Hamburg, Germany, (1991) Vol. 3 1419.

[49] A. Kwiatkowski et al., Comp. Phys. Commun. **69** (1992) 155.

[50] G. Ingelman, *LEPTO 5.2*, unpublished program manual, see also H. Bengtsson et al., Nucl. Phys. **B301** (1988) 554.

[51] H.Albrecht et al., *H1PHAN - H1 physics analysis program*, H1 document (1991 onwards)

[52] G.Cozzika, H1 collaboration, *The H1 Detector* , Proc. 3rd International Conference on Calorimetry in High Energy Phyics (Corpus Christi, Texas, 1992), to be published.

[53] H1 BEMC group, *The H1 Backward Electromagnetic Calorimeter (BEMC)*, H1 note H1-08/92-233 (1992).

[54] H1 BEMC group, *Calibration and Reconstruction of the BEMC*, H1 note H1-08/92-234 (1992).

[55] J. Gaylor, H1 collaboration, *Performance of the H1 Liquid Argon Calorimeter*, Proc. 3rd International Conference on Calorimetry in High Energy Phyics (Corpus Christi, Texas, 1992), to be published.

[56] G. Raedel,*H1 Central Tracker Group*, private communication.

[57] M. Besançon, *Photoproduction background in low x DIS events in H1*, H1 note H1-04/93-285 (1993).

[58] M. Besançon, *Experimental study of the background in low x QCD at HERA*, Proceedings of the Workshop "Physics at HERA", ed. W. Buchmüller and G. Ingelman, Hamburg, Germany (1991) Vol. 1 181.

[59] T.Ahmed et al., H1 Collaboration, Phys. Lett. **B299** (1993) 385.

[60] T. Ahmed et al., H1 Collaboration, Phys. Lett. **B299** (1993) 374.

[61] T. Ahmed et al., H1 Collaboration, Phys. Lett. **B298** (1993) 469.

[62] U. Bassler et al., *Progress on kinematical variable reconstruction. Consequences for D.I.S. physics analysis at low x*, H1 note H1-03/93-274 (1993).

[63] A. De Roeck, *H1 Electron Analysis & DIS working group*, private communication.

[64] H. Hufnagel, *H1REC - L5 Event Classification* , H1 document (1992 onwards).

[65] G. Bernardi et al., *A detailed simulation of F_2 measurability at HERA*, Proceedings of the Workshop "Physics at HERA", ed. W. Buchmüller and G. Ingelman, Hamburg, Germany (1991) Vol. 1 79.

[66] A.D. Martin et al., Phys. Rev. **D43** (1991) 3648.

[67] T. Sjöstrand, *PYTHIA 5.6 - PYTHIA at HERA*, Proceedings of the Workshop "Physics at HERA", ed. W. Buchmüller and G. Ingelman, Hamburg, Germany (1991) Vol. 3 1405 (references therin).

[68] N.H. Brook et al., *RAYPHOTON 2.0 - An interface for HERA photoproduction physics*, Proceedings of the Workshop "Physics at HERA", ed. W. Buchmüller and G. Ingelman, Hamburg, Germany (1991) Vol. 3 1453 (references therin).

[69] G. Ingelman, *Deep Inelastic Physics at HERA*, DESY 87-144 (1987).

[70] G. Wolf, *First Results from HERA*, DESY 92-190 (1992).

[71] J. Heatherington et al., *Studies of TOF efficiency during Autumn 1992 run*, H1 note H1-08/93-306 (1993).

[72] M. Klein, *H1 Electron Analysis & DIS working group*, private communication.

[73] G. Kramer et al., *Radiative corrections to ep scattering, a survey*, Proceedings of the Workshop "Physics at HERA", ed. W. Buchmüller and G. Ingelman, Hamburg, Germany (1991) Vol. 2 789.

[74] H. Spiesberger et al., *Radiative corrections at HERA*, Proceedings of the Workshop "Physics at HERA", ed. W. Buchmüller and G. Ingelman, Hamburg, Germany (1991) Vol. 2 798.

[75] M.Böhm et al., Nucl. Phys. **B294** (1987) 1081.

[76] A. Akhundov et al., *TERAD91 2.10 - A program package for the calculation of cross-sections of deep inelastic NC and CC scattering at HERA*, Proceedings of the Workshop "Physics at HERA", ed. W. Buchmüller and G. Ingelman, Hamburg, Germany (1991) Vol. 3 1285.

[77] J. Blümlein, *HELIOS 1.00 - A program to calculate leading order log QED corrections to ep scattering*, Proceedings of the Workshop "Physics at HERA", ed. W. Buchmüller and G. Ingelman, Hamburg, Germany (1991) Vol. 3 1270.

[78] A.M. Cooper-Sarker et al., *Measurement of $F_L(x, Q^2)$ at low-x & Extraction of the Gluon Distribution*, Proceedings of the Workshop "Physics at HERA", ed. W. Buchmüller and G. Ingelman, Hamburg, Germany (1991) Vol. 1 155.
Measurement of the Longitudinal Structure Function and the Small x Gluon Density of the Proton, Proceedings of the HERA workshop, ed. R.D. Peccei, Hamburg, Germany (1987) Vol. 1 231.

[79] I. Abt et al., H1 Collaboration, Nucl. Phys. **B407** (1993) 515.

[80] M. Derrick et al., ZEUS Collaboration, DESY 93-110 (1993).

[81] M. Derrick et al., ZEUS Collaboration, *Observation of events with a Large Rapidity Gap in Deep Inelastic Scattering at HERA*, DESY 93-093 (1993).

[82] J. Kwiecinski et al., Phys. Rev. **D42** (1990) 3645.

[83] J. Morfin et al., Z. Phys. **C52** (1991) 13.

[84] P. Amaudruz et al., NMC Collaboration, Phys. Lett. **223B** (1992) 159.

[85] A.D. Martin et al., Phys. Lett. **306B** (1993) 145.,
Phys. Lett. **309B** (1993) 492.

[86] J. Botts et al., Phys. Lett. **298B** (1993) 159.

[87] M. Glück et al., Z. Phys. **C53** (1992) 127.

[88] A.M. Cooper-Sarker et al., J. Phys. G: Nucl. Part. Phys. **19** (1993) 1601.

[89] M. Bengtsson et al., *Parton Cascade Evolution and Event Structure at HERA*, Proceedings of the HERA workshop, ed. R.D. Peccei, Hamburg, Germany (1987) Vol. 1 149.

[90] Yu.L. Dokshitzer, V.A Khoze, A.H. Mueller and S.I. Troyan, *Basics of Perturbative QCD*, Editions Frontières (1991).

[91] G. Ingelman, *LEPTO 6.1 - The Lund Monte Carlo for Deep Inelastic Scattering at HERA*, Proceedings of the Workshop "Physics at HERA", ed. W. Buchmüller and G. Ingelman, Hamburg, Germany (1991) Vol. 3 1366 (references therin).

[92] L. Lönnblad, *ARIADNE version 4*, Proceedings of the Workshop "Physics at HERA", ed. W. Buchmüller and G. Ingelman, Hamburg, Germany (1991) Vol. 3 1440 (references therin).

[93] T. Sjöstrand, Comp. Phys. Commun. 39 (1986) 347.
T. Sjöstrand et al., Comp. Phys. Commun. 43 (1987) 367, and for JETSET 7.3, CERN-TH. 6488/92 (1992).

[94] P. Lanius, *H1 Hadronic Final State & DIS working group*, private communication.

[95] A. De Roeck, *Deep Inelastic Scattering at Low-x. Results from the H1 Experiment*, DESY 93-087.
J. Phys. G: Nucl. Part. Phys. **19** (1993) 1549.